Topics in Gravitational Physics: Tidal Coupling in Gravitational Wave Searches and Mach's Principle

Thesis by

Hua Fang

In Partial Fulfillment of the Requirements
for the Degree of
Doctor of Philosophy

California Institute of Technology
Pasadena, California

2007
(Defended January 9, 2007)

Acknowledgements

Foremost, I would like to thank my advisor, Kip Thorne, for being a great mentor. He introduced me to the science of relativity and gravitational waves, and to a group of enthusiastic, talented Kiplings with whom I have a lot of valuable interactions. I thank Kip for suggesting interesting research topics to me, for inspiring discussions and constant encouragement, and for patiently demonstrating and urging me to a clear, well-organized presentation of ideas.

I am also very thankful to my former advisor, Thomas Prince, for supporting my study and research for two years when I first came to Caltech, and for introducing me to the exciting field of gravitational-wave physics. I am thankful to Massimo Tinto, for introducing me to LIGO-related data analysis and for interesting discussions on numerical techniques such as Markov chain Monte Carlo methods.

I am thankful to Jonathan Gair, who assisted me in coding up the Press formula for numerical kludge (NK) waveforms. He was also kind enough to educate me a lot on geodesic integrators and on practical concerns in template counting, waveform comparison, etc. In addition, I must thank my other collaborators on our NK paper, Stanislav Babak, Kostas Glampedakis, and Scott Hughes, for helpful discussions.

I wish to thank Geoffrey Lovelace, with whom I studied the black hole perturbation theory and applied it to the tidal coupling problem we jointly worked on. The collaboration was based on our genuine quest to seek the truth, so there was never a lack of critical debates and earnest discussions. I thank Geoffrey for this very rewarding experience and for the finishing of our tidal coupling paper.

I am thankful to everyone who participated in the LIGO-IMRI project: Duncan Brown, Jonathan Gair, Chao Li, Geoffrey Lovelace, Ilya Mandel, Kip Thorne, Jeandrew Brink, Yanbei Chen, Teviet Creighton, Curt Cutler, Steve Drasco, Yi Pan, Cole Miller, and Sterl Phinney, for helpful inputs and comments, and for the final submission of the IMRI paper.

In addition to the above, I would like to thank Yasushi Mino, Shane Larson, Frans Pretorius, Rob Owen, Luisa Buchman, Harald Pfeiffer, Mark Scheel, Lee Lindblom, and all others who attend Kip and Lee's group meetings, where a lot of interesing presentations and discussions are made. I am very grateful to Chris Mach, who has helped me solve many computer problems, and to JoAnn Boyd, Shirley Hampton, and Donna Driscoll for helping me with administrative matters.

There are people outside my research group who have influenced me during my time as a graduate student. I thank Pengpeng Sui, Delores Bing, Qun Cao, Jian Wu, Zhimei Yan, Xin Liu, and Loredana Prisinzano, for

their enlightenment and for sharing great moments.

Last, I am deeply grateful to my family, who have been supportive all through the years. I owe them for their love and kindness.

The research presented in this thesis was supported in part by NASA grants NAG5-12834, NAG5-10707, and NNG04GK98G, and by NSF grants PHY-0099568 and PHY-0601459.

Abstract

The gravitational waves emitted by a compact object inspirling into a massive central body (e.g., a massive black hole) contain exquisite information about the spacetime geometry around that body and the tidal interaction (energy and angular momentum transfer) between the body and the inspiraling object's orbit. The first part (chapters 2–4) of this thesis presents (i) an analysis of tidal coupling between a massive, nonrotating black hole with circularly orbiting moon; (ii) an estimate of tidal-coupling measurement accuracy—in the context of using ground-based interferometers (e.g., Advanced LIGO) to detect gravitational waves from intermediate-mass-ratio inspirals (IMRIs); and (iii) an efficient and effective algorithm to generate "kludge" gravitational waveforms, which could be useful in real graviational-wave data analysis for the space-based LISA (Laser Interferometer Space Antenna) mission. More specifically:

- In chapter 2 (research in collaboration with Geoffrey Lovelace), we use first-order perturbation theory to study a simplified model: a Schwarzschild black hole of mass M is tidally perturbed by a "moon" moving along a circular orbit with angular velocity Ω; the moon's perturbing tidal field $\mathcal{E}_{ij}$ gives rise to an induced quadrupole moment $\mathscr{I}_{jk}$ in the hole's external gravitational field at large radii. Much to our surprise, we find that the induced quadrupole moment is proportional to *the time derivative* of the moon's tidal field, $\mathscr{I}_{ij} = (32/45)M^6\dot{\mathcal{E}}_{ij}$, instead of being proportional to the field itself (as one might expect from a Newtonian analogy)! This time-varying induced quadrupole moment is gauge-invariant, and its gravitational force acting back on the moon is responsible for the orbital energy and angular momentum loss to the hole's horizon. We discuss the implication of this result in the static limit and conclude that the static induced quadrupole moment for a black hole is inherently ambiguous. We also show that the orbiting moon's tidal field induces a tidal bulge on the hole's horizon, and that the horizon *shear* (i.e., the rate of change of the horizon shape) *leads* the perturbing tidal field at the horizon by an angle $4M\Omega$.

- In chapter 3 (research largely by the author alone), we give a survey of initial explorations of the prospects for using Advanced LIGO to detect gravitational waves from *intermediate*-mass-ratio inspirals (IMRIs)—analogous to the *extreme*-mass-ratio inspirals (EMRIs) targeted by LISA. We describe initial estimates of the detection range and the number of IMRI wave cycles in the Advanced LIGO band. Motivated by the possibility of using IMRI waves to probe the properties of its central body, e.g, to constrain its deviation from a Kerr black hole, we give a detailed analysis of Advanced LIGO's

accuracy for measuring the tide-induced energy transfer $\dot{E}_H$ between the central black hole and the orbit.

Our study shows that at signal-to-noise ratio 10, the accuracy of measuring tidal coupling $\dot{E}_H$ is roughly a few percent of the gravitational energy flow to infinity. This suggests that Advanced LIGO, working together with a network of detectors, will be able to put a modest but interesting constraint on a source's deviation from a Kerr black hole in terms of its tidal response.

- In chapter 4 (research in collaboration with Stanislav Babak, Jonathan Gair, Kostas Glampedakis, and Scott Hughes), we describe a new waveform-generating scheme in the context of LISA's data analysis for EMRI waves. Our scheme involves combining flat-spacetime wave-emission formulas (i.e., quadrupole, quadrupole-octupole, and the Press formula) with a full relativistic treatment of the orbiting object's motion. The result is a family of "Numerical Kludge" (NK) waveforms. We compare our NK waveforms with the corresponding canonical, but more computational-intensive Teukolsky-based waveforms, and find remarkable agreement between the two.

The second part (chapter 5) of this thesis (research in collaboration with Kip Thorne) discusses another prediction from general relativity, the dragging of inertial frames, in connection with Mach's principle. Specifically:

- We first explain frame dragging outside the rotating Earth by two physical descriptions, gravitomagnetism and a fluid like space-drag, and demonstrate the equivalence between the two. Then we study frame dragging inside a rotating universe, i.e., Mach's principle, by a simple model. We idealize our universe as a homogeneous, isotropic expanding, and slowly rotating sphere, surrounded by vacuum. We find that as the universe expands, the frame dragging weakens at its center; and that at later times inertia at the center completely breaks free of the grip of the universe's rotating matter.

Contents

List of Figures

List of Tables

Chapter 1

Introduction

Gravitational waves (GWs), fundamentally different from electromagnetic waves, are ripples of spacetime curvature, carrying information from motions of mass-energy and propagating through intervening media with almost no interactions [1]. By contrast with traditional astronomical observations based on the electromagnetic spectrum, gravitational wave searches are expected to reveal the properties of strong-gravity regions such as those around a massive black hole, hence opening up a new window onto the universe and bringing profound changes to our current understanding of nature. We are entering an exciting age of "*gravitational wave astronomy*".

Large-scale scientific facilities for gravitational wave observations are being constructed or proposed for commissioning in the near future. These include:

(i). The high-frequency band (1–10^4Hz), ground-based interferometric detectors such as LIGO and VIRGO, targeting GWs from (among other things) stellar mass binaries that are composed of black holes (BHs) and/or neutron stars (NSs). First-generation ground-based detectors are targeting NS binaries with masses $\sim 1\text{–}3 M_\odot$, BH binaries with masses $\sim 3\text{–}40 M_\odot$, and NS-BH binaries with components in these mass ranges [2, 3]. For Advanced LIGO [4, 5, 6] and its partners, gravitational waves from an inspiraling compact object (e.g. a NS) into a intermediate-mass black hole (IMBH) with $M \sim 50\text{–}350 M_\odot$ [7] will be detectable. These *intermediate-mass-ratio inspirals* (IMRIs) will be the subject of chapter 3 of this thesis.

(ii). The low-frequency band (10^{-4}–1Hz), space-based Laser Interferometer Space Antenna (LISA) [8], targeting GWs (among other things) from binaries with massive black holes ($M \sim 10^3\text{–}10^9 M_\odot$) or other massive exotic objects. One of the most interesting and promising GW sources for LISA is the inspiral of a stellar mass compact object into a massive black hole. Gravitational waves from these *extreme-mass-ratio inspirals* (EMRIs) will be the subject of chapter 4 of this thesis.

Due to the small mass ratio between the components of an EMRI or IMRI, the trajectory of the compact object (CO) at any given moment can be approximated by a geodesic in the central black hole's background metric. As a result, the emitted EMRI/IMRI waves can be shown to encode exquisitely accurate information about the black hole spacetime geometry [9], as well as information about the energy and momentum transfer (*tidal coupling*) between the black-hole horizon and the CO's orbit [10]. The first part (chapters 2-4) of this thesis presents research relevant to tidal coupling and the modeling of EMRI/IMRI waves. Specifically,

- *The tidal interaction between a non-rotating black hole and orbiting body*. The tidal coupling between a black hole and inspiraling compact object is usually described as a perturbation to the horizon's 2-metric [11, 12], or as gravitational radiation going down to the horizon [13]. In Sec 1.1.2 and chapter 2, we discuss an alternative description—a description that is independent of the existence of a horizon. As an analogy to the Newtonian tidal torquing between the earth and the moon, we explore the possibility to parameterize tidal coupling in terms of the central body's induced multiple moments, in a body-independent manner.

- *Extracting tidal coupling information from IMRI waveforms*. The Advanced LIGO interferometers, with their much improved sensitivity, will be able to detect gravitational waves from an IMRI and perform interesting tests to probe the properties of the IMRI's central body, e.g., constrain its deviation from a Kerr black hole. Section 1.2 and chapter 3 discuss the prospects for using Advanced LIGO to detect IMRI waves and the related parameter estimations. In particular we are concerned with the measurability of the tidal coupling, to determine whether it is in accordance with that of a Kerr black hole.

- *Modeling EMRI waveforms*. EMRI waves are among the most interesting targets for the proposed LISA mission. Within the LISA band, the orbiting compact object will spend its last few years at distances from the central hole that are less than or of order the black hole's circumference, emitting $\sim 10^5$ gravitational wave cycles. These will enable unprecedented, high-precision tests of black hole properties and strong-field of relativity. Extensive research has been done (and is still under way) on the computation of EMRI waveforms [14, 15, 16, 17, 18], and on the computation of the radiation-reaction-induced evolution of the CO's orbit [19]. Section 1.3 and chapter 4 describe a new waveform-generating scheme, which combines flat-spacetime wave-emission formulas with a full relativistic treatment of the CO's motion. The resulting "kludge" waveforms are much easier to generate than the canonical Teukolsky-based waveforms, and are proved to be effective for data analysis studies and possibly also for LISA's actual wave searches.

Besides research on gravitational waves (with emphasis on tidal coupling), this thesis (chapter 5) also studies another prediction of general relativity—frame dragging. This study is motivated by the test of frame-dragging being carried out by Gravity Probe B [20] , a set of four superconducting gyroscopes in an Earth-orbting satellite. Specifically, we discuss

- *Frame dragging and Mach's principle*. Gravity Probe B aims to measure the angular velocity of local inertial axes with respect to distant starts, a frame-dragging effect caused by the spin of the Earth. In chapter 5, we explain frame dragging *outside* the rotating Earth (or any other rotating body) through two equivalent descriptions: gravitomagnetism and a dragging of space into motion. We further study frame dragging *inside* a rotating universe, i.e. Mach's principle and its relation to general relativity, via a simple and pedagogically illuminating model. In this model, we give an outer edge to a spatially homogeneous, expanding, slowly rotating universe, and examine the time evolution of the spin of a local inertial-guidance gyroscope at the center. We discuss our results in terms of Mach's principle [21], which states that inertial axes are tied to the mean rotational motion of the matter that fills the distant universe.

1.1 Tidal interaction between compact objects and massive black holes

One of the primary scientific requirements for LISA is to perform high-precisoin mapping of the spacetime geometries of massive black holes (and, if they exist, other massive, compact bodies) using EMRI waves. The possibility of making such maps was speculated by Thorne in the early 1990s (e.g., in Refs. [22, 23]). In 1995 Ryan [9] laid the first detailed foundation for such mapping: he showed that, when the massive, central body is general relativistic, axisymmetric, and reflection-symmetric, and the orbiting object is in a near-equatorial, near-circular orbit in the vacuum region surrounding the body, the full details of the central body's metric are encoded in (i) the phase evolution of the waves and also in (ii) the evolution of the frequencies (or phases) of wave modulation produced by orbital precessions.

However, Ryan's proof ignored completely the influence of tidal coupling between the central body and the orbiting object. Finn and Thorne [10] have shown that, for values of the body and object masses in the range relevant to LISA, the tidal coupling can have an influence as large as a few percent on the evolution of the waves' inspiral phase—a phase that should be measurable to a fraction of a cycle out of tens or hundreds of thousands of cycles (see Sec. 3.2.4 of this thesis for a similar analysis for IMRIs in the Advanced LIGO band). Thus, the influence of the tidal coupling may be measurable with rather high precision. It is reasonable to expect that *both* the spacetime map and details of the central body's tidal response will be individually extractable.

To permit information extraction, we must describe the tidal coupling in a manner that can encompass all possible types of central bodies—in a body-independent manner. To draw intuition and physical insight from a most familiar scenario, we shall first describe the tidal coupling between the earth and moon and argue that the same type interaction must occur between any compact object and a massive central body, including a black hole.

1.1.1 Tidal coupling between Earth and Moon

Tidal coupling is a well understood phenomenon in the case of the earth and the moon [24, 25]. The moon's tidal gravitational field $\mathcal{E}_{jk} = \partial^2\Phi_{\rm moon}/\partial x^j\partial x^k$ (where $\Phi_{\rm moon}$ is the moon's Newtonian potential) stretches and squeezes the earth, thereby deforming it and inducing a mass quadrupole moment $\mathscr{I}_{jk}$, which gives rise to $\delta\Phi_{\rm earth} = \frac{3}{2}\mathscr{I}_{jk}x^j x^k/r^5$ in the earth's exterior gravity. The induced quadrupole moment is related to the moon's tidal field by $\mathscr{I}_{jk} = -\mathcal{P}_2\mathcal{E}_{jk}$, in which the proportionality constant $\mathcal{P}_2$ can be thought of as the earth's *mass-quadrupole polarizability*. It is of order the radius R of the earth to the fifth power, $\mathcal{P}_2 = \gamma_2 R^5$ with $\gamma_2 \sim 1$.

Because the earth's rotation is not synchronous with the moon's orbital motion, the induced tide moves through the earth's material dynamically. Energy is dissipated in the tide's dynamical rise and fall (largely via viscous heating in sloshing of the oceans), and this dissipation causes a *lag* of the direction of the tidally induced $\mathscr{I}_{jk}$ relative to the direction of the imposed $\mathcal{E}_{jk}$, by a tidal lag angle $\Delta\varphi_2 = 1/\mathcal{Q}_2$ where $\mathcal{Q}_2$ is the so-called tidal quality factor or tidal $\mathcal{Q}$. This lag enables the induced tide to exert a torque $N_2 \propto \Delta\varphi_2\mathscr{I}_{jk} \propto \mathcal{P}_2/\mathcal{Q}_2$ on the moon. This tidal torque N_2 has caused the moon to spiral outward in its orbit in historical times, by a well measured amount [26].

Noticeably different from the case of the earth and moon, the tidal coupling in the case of a black hole has always been described in terms of the influence of the orbiting object's gravitational field on the hole's horizon—the perturbation of the horizon's 2-metric (e.g. [11, 12]), or the conversion of the tidal field into gravitational radiation at the horizon by gravitational blue-shifting and the energy and angular momentum carried inward by those waves [13].

It is conceivable that one tidal feature in common between a black hole, the earth, a boson or soliton star, and all other central bodies, is the body's tidally induced multipole moments and multipolar gravitational fields. It is these induced fields, acting back on the orbiting object, that change the object's orbital energy and angular momentum, secularly change its orbit, and thereby alter the emitted gravitational waves. For this reason, Thorne [27] has proposed that we adopt these induced multipole fields (or, more precisely, the polarizability and lag angle) as our body-independent description of tidal coupling when analyzing LISA data.

The next subsection summarizes my research on using this multipole-moment language to describe black-hole tidal couplings, as presented in chapter 2. In this research (performed jointly with Geoffrey Lovelace), I have (i) calculated the induced quadrupole moment of a non-rotating black hole due to the perturbing tidal field from an orbiting moon; (2) verified that the time-varying piece of the induced quadrupole moment is gauge-invariant and is responsible for the orbital energy and angular momentum loss down to the horizon; (3) showed that the black hole's static induced quadrupole moment and polarizability are gauge-dependent and thus inherently ambiguous; (4) defined and computed a tidal lead angle at the horizon, which is in agreement with Hartle's result for a rotating black hole accompanied by a static, distant moon.

1.1.2 Black hole tidal coupling

In chapter 2, we analyze the tidal response of a non-rotating black hole (with mass M) to a distant, circularly orbiting moon (with mass μ; $\mu \ll M$). We assume that the distance b between the black hole and the moon is large enough ($b \gg M \gg \mu$), that in between there exists an intermediate region, where the spacetime is nearly flat and the moon's external quadrupolar tidal field $\mathcal{E}^{\rm ext}_{ij} \equiv -3\mathscr{Q}_{ij}$ is approximately constant. This region is referred to as the black hole's local asymptotic rest frame (LARF). The full tidal field in the LARF, including the moon's (external) tidal field $\mathcal{E}^{\rm ext}_{ij}$ and the the central hole's induced field, can be written (in Cartesian coordinates) to linear order and in each multipole moments as [28]

$$\mathcal{E}_{ij} \equiv R_{0i0j} \quad = \quad -\sum_{\ell=0}^{\infty} \frac{(-1)^\ell}{\ell!} \mathscr{I}_{A_\ell}\Big(\frac{1}{r}\Big)_{,ijA_\ell} - \sum_{\ell=2}^{\infty} \frac{(2\ell-1)!!}{(\ell-2)!} \mathscr{Q}_{ijA_{\ell-2}} X_{A_{\ell-2}}. \tag{1.1}$$

Here $\mathscr{I}_{A_\ell}$ and $\mathscr{Q}_{A_\ell}$ are the ℓ-th internal and external moments; they are symmetric and trace free (STF) in their tensor indices $A_\ell \equiv a_1...a_\ell$ [29]. The "internal moments" $\mathscr{I}_{A_\ell}$ characterize the central body, while the "external moments" $\mathscr{Q}_{A_\ell}$ characterize the gravitational fields of distant sources (in our case the moon) that perturb the central body. In our problem, the tidally induced quadrupole moment of the black hole can be read off from the terms of the form $\sim \mathscr{I}_{a_1a_2}(1/r)_{,ija_1a_2}$; and the tidal field $\mathcal{E}^{\rm ext}_{ij}$ can be identified as equivalent to the external quadrupole moment $\mathscr{Q}_{ij}$—they differ only by a constant scaling factor, $\mathcal{E}_{ij} = -3\mathscr{Q}_{ij}$.

In Sec. 2.2, we decompose the moon's external tidal field into tensor spherical harmonics. The quadrupolar result is a static piece $\mathcal{E}^{\rm ext,20}_{ij}$ ($\ell = 2, m = 0$), and two time-dependent pieces conjugate to each other $\mathcal{E}^{\rm ext,2\pm2}_{ij}$ ($\ell = 2, m = \pm 2$). In Sections 2.3 and 2.4, we solve for the corresponding static and time-dependent metric perturbations in the Regge-Wheeler gauge, with outer boundary conditions such that the $\mathcal{O}(r^0)$ terms in the resulting tidal field $\mathcal{E}_{ij}$ go to $\mathcal{E}^{\rm ext}_{ij} = -3\mathscr{Q}_{ij}$ in the LARF [to be in agreement with Eq. (1.1)].

Our results from Sec. 2.3 and Sec. 2.4 show that: (i) the static induced quadrupole moment of the black hole *vanishes* in Regge-Wheeler gauge; (ii) the total induced quadrupole moment is proportional to *the time derivative* of the moon's tidal field,

$$\mathscr{I}^{\rm ind}_{ij} = (32/45) M^6 \dot{\mathcal{E}}_{ij}\,, \tag{1.2}$$

and hence is precisely out of phase with the external tidal field. In Sec. 2.3.2, we prove that this out-of-phase induced moment is gauge-invariant and is responsible for the tidal torque that changes the orbital energy and angular momentum. We show in Sec. 2.4.2 that the static induced quadrupole moment is inherently ambiguous. If there had been an unambiguous piece of $\mathscr{I}^{\rm ind}_{ij}$ in phase with $\mathcal{E}^{\rm ext}_{ij}$, then we would be able to define an unambiguous polarizability and tidal lag angle in the same way as in the earth and moon; but our result shows we cannot do so. The polarizability and lag angle are inherently ambiguous in the case of a black hole.

Although the tidal angle is ambiguous in the LARF, we calculate a quadrupolar horizon phase shift in Sec. 3.5 as a partial analog of a result derived by Hartle for a spining hole and a static distant moon [12]. We define our horizon phase shift to be the angle between the perturbing tidal field at the horizon and the shear (i.e., the rate of change of shape) of the horizon, and we find that the shear of the horizon *leads* the perturbing tidal field at the horizon by

$$\delta_{\rm Horizon} = 4M\Omega\,. \tag{1.3}$$

This tidal lead angle is the same (nicely!) for both situations: a stationary moon perturbing a rotating hole (Hartle's analysis) and an orbiting moon perturbing a non-rotating hole (our analysis).

1.2 IMRI waves for Advanced LIGO

Evidence from ultra-luminous X-ray sources and from the dynamics of globular clusters suggests that there exists a population of intermediate mass black holes (IMBHs) with masses in the range $\sim 10^2$–$10^4\,M_\odot$ [30]. Gravitational waves from the inspiral and coalescence of a NS or small BH into an IMBH with mass $\sim$ 50–$350M_\odot$ will lie in the frequency band of Advanced LIGO and its partners. These *intermediate-mass-ratio inspirals* (IMRIs) are analogous to the extreme-mass-ratio inspirals (EMRIs) targeted by LISA, the planned space-based gravitational wave observatory [31].

In a recent letter [32], my coauthors and I report on our initial explorations of the prospects for Advanced LIGO to detect IMRI waves, and on initial studies of using IMRI waves to probe the properties of the massive central body. Chapter 3 summarizes my research that underlines a portion of our joint publication. Specifically, I do the following:

(i). *Estimate the detection range and number of IMRI wave cycles in the Advanced LIGO band for circular equatorial orbits* (Sec. 3.2). Using the leading order quadrupole radiation formula, we compute the sky-averaged signal-to-noise ratio (SNR) for IMRI waves from a source ($1.4M_\odot$ NS inspirling into an IMBH) at a distance of 100Mpc. We find the SNR reaches $\sim$ 20 for slowly rotating holes ($a \lesssim 0.3M$) and $\sim$ 50 for rapid rotating holes ($a \gtrsim 0.9M$), suggesting that Advanced LIGO can reliably detect IMRIs if there is a sufficient population of IMBHs and captures. We estimate the number of IMRI wave cycles by using results from the Teukolsky formalism [10]. We find that for a $1.4M_\odot$ NS inspiraling into an IMBH with mass $\sim 50M_\odot$ to $200M_\odot$, the emitted gravitational waves will spend $\sim$ 200 to 1000 cycles in the Advanced LIGO band, high enough to promise at least moderate accuracy parameter extraction.

(ii). *Implement a variant of the so-called Manko-Novikov metric with an arbitrary mass quadrupole moment and compute the periapse precession rate in this spacetime* (Appendix 3.A in chapter 3). We consider the possibility that the central body of an IMRI deviates from a black hole, but its surrounding spacetime is still Stationary, Axisymmetric, Reflection Symmetric about an equatorial plane, and Asymptotically Flat (SARSAF). The relativistic multipole moments that characterize any SARSAF metric are two families of scalars: the "mass moments" $\{M_0, M_2, M_4, \ldots\}$ and the "current moments"

$\{S_1, S_3, S_5, \ldots\}$. In the case of a Kerr black hole, they are given by

$$M_\ell + i S_\ell = M(ia)^\ell, \qquad \ell = 0, 1, 2, \ldots, \tag{1.4}$$

where $a \equiv S_1/M_o$ = spin angular momentum divided by mass $M_o = M$. Equation (1.4) is the black-hole no hair theorem, which states that the entire multipole-moment structure of a black hole spacetime is determined solely by the mass and spin of the black hole. The leading order deviation from a black hole in an arbitrary SARSAF spacetime will be an anomalous mass quadrupole M_2—one that violates $M_2 = -Ma^2$. Due to the anomalous M_2, the separability of the geodesic equation for an orbiting object (which holds in the Kerr spacetime) may no long exist and the orbit may become ergodic. A substantial amount of research, based on either small quadrupolar perturbations [33, 34] or exact SARSAF solutions [35, 36, 37], has been carried out to analyze the imprints of an anomalous M_2 on the orbital dynamics and on the observational features of the gravitational waves emitted by the orbiting object. The Manko-Novikov spacetimes [38] belongs to a family of exact SARSAF solutions that possess an arbitrary set of mass multipole moments. In Appendix 3.A, we compute the Manko-Novikov metric functions parameteried by M_o, S_1, and M_2, and calculate the periapse precession rate for equatorial orbits in order to show the effects of M_2. We compare our results to previous studies by Collins and Hughes [33].

(iii). *Construct 3.5PN-Teukolsky IMRI waveforms for both circular equatorial and circular inclined orbits and perform parameter estimation to scope out Advanced LIGO's measurement accuracy for tidal coupling* (Sec. 3.3). The existence of an event horizon is one defining property of black holes. The gravitational-wave "plunge frequency" can be used to indicate the existence and location of the horizon, thereby distinguishing a massive black hole from a massive boson star [39]. The black-hole horizon also interacts dynamically with the inspirling orbit via tidal coupling, i.e., via the energy and angular momentum transfer ($\dot{E}_H$, $\dot{L}_H$) between the two. To assess the measurability of tidal coupling and use it as a means to probe the tidal properties of the IMRI's central body, we model the energy flow into the central body as $\dot{E}_{\rm body} = \varepsilon \dot{E}_H$ and seek to measure any deviation from the black-hole absorption, parameterized by ε. We then construct precessional waveforms by the techniques of Apostolatos et al. [40], using the 3.5PN orbital energy loss $\dot{E}_\infty$ (to infinity) [41] and $\dot{E}_H$ (to the horizon) [42] for circular equatorial orbits from with corrections for small inclination angles from [43]. We use the Fisher matrix analysis to quantify the measurement error $\Delta\varepsilon$ for tidal coupling (together with the error for the other wave parameters). Our results are listed in Tables 3.2–3.4. For rapidly spinning intermediate-mass central bodies, we find interestingly small values for $\Delta\varepsilon$ at SNR = 10. However, $\Delta\varepsilon$ grows quite large when the spin decreases, because (i) the tidal coupling becomes weaker for smaller spins [$\dot{E}_H \propto (a/M)v^5 \dot{E}_{\rm body}$ at leading order in a], (ii) there are fewer wave cycles in the Advanced LIGO band (if other parameters remain the same), and (iii) weakened precession causes a growing degeneracy between ε and other parameters.

1.3 Template waveforms for EMRI waves

Astronomical observations give very strong evidence for the the existence of massive black holes ($M \sim 10^6$ to $10^9 M_\odot$) in the nuclei of galaxies. Gravitational waves emitted from stellar-mass compact objects inspirling into massive black holes (extreme-mass-ratio inspirals or EMRIs) carry detailed information about the highly nonlinear relativistic regime and are among the most interesting targets for the LISA mission. Preliminary estimates suggest LISA could see as many as $\sim 10^3$ EMRI events during its lifetime [44, 45], using a suitable "semi-coherent" matched filtering search algorithm and provided that "confusion noise" (produced by unresolved galactic binaries [46] and many weak EMRIs) can be efficiently reduced in the real data.

Theoretical EMRI waveform templates with sufficient accuracy are needed in order to "filter out" the GW signal from the detector's noisy data. The extreme mass ratio $\mu/M \ll 1$ of the binary system implies that EMRI waveforms can be computed accurately using black-hole perturbation theory; it also guarantees that orbital parameters evolve on a much longer time scale than the orbital periods (adiabatic condition). As a result, within the radiation reaction time scale, the inspiral waveform can be well approximated by "snapshot" waveforms, i.e. waveforms calculated by assuming that the compact object moves along a geodesic. Accurate snapshot waveforms have been calculated by numerical integration of the Teukolsky equation for circular-inclined orbits [14], equatorial-eccentric orbits [15, 16, 17], and a number of generic orbits [18]. However, one practical constraint that prevents Teukolsky-based (TB) waveforms from being readily applicable to scope out LISA data analysis issues (e.g. template counting and initial parameter estimation) is that they are computationally expensive to generate—the numerical integration of the Teukolsky equation involves summing over a large number of multipole modes. This has motivated the development of alternative algorithms to generate EMRI waves.

In chapter 4, adapted from a paper I wrote in collaboration with Stanislav Babak, Kostas Glampedakis, Jonathan Gair, and Scott Hughes, I describe a quick way to generate EMRI waveforms. In Sec. 4.2, we first give a brief overview of the development of TB waveforms, as well as other available (but less accurate) wave-generation schemes including the "analytic kludge" [47]. This survey of the current waveform inventory motivates the need to develop an alternative approach, one that is both efficient (time-saving) and sufficiently accurate.

In Sec. 4.3, we describe the generation of "Numerical Kludge" (NK) waveforms in two steps. (i) Compute the trajectory of the compact object. Currently we are mainly focusing on computing geodesics at this step. A proper prescription for the evolution of the constants of motion will be needed to produce accurate inspiral trajectories (hence inspiral waveforms) [19]. (ii) From the trajectory, compute the gravitational waveforms according to the weak-field emission formula, e.g. the quadrupole, the quadrupole-octupole, or the Press formula. In particular, the Press formula is not restricted to slow-motion or small sources, and contains contribution from all harmonics including quadrupole and octupole.

In Sec. 4.4, we compare our various NK waveforms (quadrupole, quadrupole-octupole, and Press) to the corresponding TB waveforms, both in the time domain and the frequency domain. We find that the NK waveforms generally have overlaps with the TB waveforms of 95% or higher over most of the parameter space. The Press waveforms consistently outperform the quadrupole and quadrupole-octupole waveforms, but the improvement is not large. We therefore conclude that in a large part of parameter space, the quadrupole-octupole waveform model is sufficient; and that NK waveforms are accurate—yet very quick to generate—substitutes for TB waveforms.

In the research presented in this chapter, I am mostly responsible for developing of the Press NK waveforms.

1.4 General relativity and Mach's Principle

General relativity predicts that the spin of the Earth drags nearby inertial axes into inhomogeneous rotation relative to asymptotic Minkowski space. This frame dragging effect is being tested by Gravity Probe B (GPB) [20], using a reference telescope pointing towards a distant guide star and superconducting gyroscopes flown in an Earth-orbiting satellite. One underlying assumption of GPB's test, as noted by Schmid [48], is that the local asymptotic Minkowski space near Earth (which is merely vacuum) is *nonrotating* with respect to distant stars ("Mach 0"). This motivates us to ask the question: if this assumption is relaxed, i.e. if relative rotations between the asymptotic Minkowski space and distant stars do exist, then how will the local inertial-guidance gyroscope respond? It is expected that the answer to this question should give insight into the relationship between Mach's principle and general relativity.

Mach's principle, in its simplest and most straightforward form, states that when there are no nearby massive spinning bodies, inertial axes are tied to the mean rotational motion of the matter that fills the distant universe. Einstein [49] has stated that this idea of Mach was one of his principal motivations in formulating general relativity. To date, many cosmological models have been developed to explore how and to what extent general relativity embraces Mach's principle [48, 50, 51, 52, 53, 54]. Chapter 5 of the thesis presents a pedagogical variant of these studies. This chapter is a draft of a pedagogical paper to be submitted to American Journal of Physics.

In Sec. 5.2, which is largely contributed by my coauthor Kip Thorne, we explain frame dragging outside the spinning Earth (or any other massive spinning object) via two equivalent descriptions: the fluid like space-drag, and gravitomagnetism; and we elucidate the relationship between them.

In Sec. 5.3, under the guidance of Thorne, I study frame dragging inside model universes (i.e. Mach's principle). In Sec. 5.3.2, we treat our universe as being spatially homogeneous and filled with pressureless matter—i.e., a spatially flat Friedmann-Robertson-Walker (FRW) universe. We set the universe into slow, rigid rotation relative to local inertial axes (homogeneous vorticity). We find that as the universe expands, the vorticity of the matter decays in magnitude, but it does not vanish. This indicates that the inertial axes are *not* tied into lock-step rotation with the matter.

In Sec. 5.3.3, to explore the influence of the rotating matter more closely, we give our model universe an outer edge, beyond which is vacuum and asymptotically flat spacetime. We examine the time evolution of frame dragging at the center of the universe. We find that at very early times when the big-bang expansion just begins, the universe's matter completely controls the inertial axes. As the universe expands, the inertial influence of the external vacuum space gradually wins over and the inertial axes become increasingly aligned with inertia at radial "infinity" at later times. In Sec. 5.3.4, we add dark energy (in the form of a cosmological constant) into our universe-with-edge model. Despite the radical change in spacetime geometry, we find the evolution of the frame dragging behaves qualitatively the same.

Bibliography

[1] K. S. Thorne, gr-qc/9704042.

[2] B. Abbott et al., Phys. Rev. D **72**, 082001 (2005).

[3] B. Abbott et al., Phys. Rev. D **73**, 062001 (2006).

[4] K. S. Thorne, The Scientific Case for Mature LIGO Interferometers. `http://www.ligo.caltech.edu/docs/P/P000024-00.pdf`.

[5] P. E. Lindquist, Advanced LIGO—the next generation. `http://www.ligo.caltech.edu/docs/P/P030019-00/P030019-00.pdf`.

[6] T. Creighton, Advanced LIGO: Sources and astrophysics. `http://www.ligo.caltech.edu/docs/P/P030017-00.pdf`.

[7] R. M. O'Leary, F. A. Rasio, J. M. Fregeau, N. Ivanova, and R. O'Shaughnessy, Astrophys. J. 637, 937 (2006), astro-ph/0508224.

[8] K. Danzman et al, *LISA—Laser Interferometer Space Antenna, Pre-Phase A Report*, Max-Planck-Institute fur Quantenoptic, Report MPQ 233 (1998).

[9] F. D. Ryan, Phys. Rev. D **52**, 5707 (1995).

[10] L. S. Finn and K. S. Thorne, Phys. Rev. D **62**, 124021 (2000).

[11] J. B. Hartle, Phys. Rev. D **8**, 1010 (1973).

[12] J. B. Hartle, Phys. Rev. D **9**, 2749 (1974).

[13] S. A. Teukolsky, Phys. Rev. Lett. **29**, 1114 (1972).

[14] S. A. Hughes, Phys. Rev. D **61**, 084004 (2000); Phys. Rev. D **64**, 064004 (2001).

[15] K. Glampedakis and D. Kennefick, Phys. Rev. D **66**, 044002 (2002).

[16] C. Cutler, D. Kennefick, and E. Poisson, Phys. Rev. D **50**, 3816 (1994).

[17] T. Tanaka, M. Shibata, M. Sasaki, H. Tagoshi, and T. Nakamura, Prog. Theor. Phys. **90**, 65 (1993).

[18] S. Drasco and S. A. Hughes, Phys. Rev. D **73** 024027 (2005).

[19] J. R. Gair and K. Glampedakis, Phys. Rev. D **73**, 064037 (2006).

[20] `http://einstein.stanford.edu`

[21] E. Mach, *Die Mechanik in ihrer Entwickelung: Historisch-kritisch dargestellt*, (Brockhaus, Leipzig, 1883); English translation *The Science of Mechanics: A Critical and Historical Account of its Development* (Open Court, La Salle, IL, 1960).

[22] A. Abramovici, K. S. Thorne, et. al., LIGO: The Laser Interferometer Gravitational Wave Observatory. Science, 256, 325–333 (1992).

[23] K. S. Thorne, in *Proceedings of the Snowmass 94 Summer Study on Particle and Nuclear Astrophysics and Cosmology*, edited by E. W. Kolb and R. Peccei (World Scientific, Singapore, 1995), p. 398, gr-qc/9506086.

[24] G. H. Darwin, Philos. Trans. R. Soc. (Pt. I) **170**, 1 (1879).

[25] C. D. Murray and S. F. Dermott, *Solar System Dynamics*, Cambridge University Press, 1999.

[26] The first two paragraphs of Sec. 1.1.1 are adapted from Kip Thorne's NASA proposal in July, 2003.

[27] K. S. Thorne, private communication.

[28] W. M. Suen, Phys. Rev. D **34**, 3633 (1986).

[29] K. S. Thorne, Rev. Mod. Phys. **52**, 299 (1980).

[30] M. C. Miller and E. J. M. Colbert, Int. J. Mod. Phys. **D13**, 1 (2004). astro-ph/0308402.

[31] J. R. Gair et al., Class. Quant. Grav. **21**, S1595 (2004).

[32] D. A. Brown, H. Fang, J. R. Gair, C. Li, G. Lovelace, I. Mandel, and K. S. Thorne, gr-qc/0612060.

[33] N. A. Collins and S. A. Hughes, Phys. Rev. D **69**, 124022 (2004).

[34] K. Glampedakis and S. Babak, Class. Quant. Grav. **23**, 4167 (2006).

[35] Guéron and Letelier, Phys. Rev. E **66**, 046611 (2002).

[36] J. R. Gair, C. Li, G. Lovelace, I. Mandel, and H. Fang (2006), in preparation.

[37] E. Barausse, L. Rezzolla, D. Petroff, and M. Ansorg, gr-qc/0612123.

[38] V. S. Manko and I. D. Novikov, Class. Quant. Grav. **9**, 2477 (1992).

[39] M. Kesden, J. Gair, and M. Kamionkowski, Phys. Rev. D **71**, 044015 (2005).

[40] T. A. Apostolatos, C. Curtler, G. J. Sussman, and K. S. Thorne, Phys. Rev. D **49**, 6274 (1994).

[41] H. Tagoshi, M. Shibata, T. Tanaka, and M. Sasaki, Phys. Rev. D **54**, 1439 (1996).

[42] H. Tagoshi, S. Mano, and E. Takasugi, Prog. Theor. Phys., **98**, 829-850 (1997).

[43] M. Shibata, M. Sasaki, H. Tagoshi, and T. Tanaka, Phys. Rev. D **51**, 1646 (1995)

[44] S. Sigurdsson and M. J. Rees, Mon. Not. R. Astron. Soc. **284**, 318 (1997).

[45] J. R. Gair, L. Barack, T. Creighton, C. Cutler, S. L. Larson, E. S. Phinney and M. Vallisneri, Class. Quant. Grav. **21**, S1595 (2004).

[46] G. Nelemans, L. R. Yungelson and S. F. Portegies Zwart, Astron. and Astrophys. **375**, 890 (2001).

[47] L. Barack and C. Cutler, Phys. Rev. D **69**, 082005, (2004).

[48] C. Schmid, Phys. Rev. D **74**, 044031 (2006).

[49] See Sec. 2 of A. Einstein, Annalen der Physik, 1916, p. 49; English translation in H. A. Lorentz, A. Einstein, H. Minkowski, and H. Weyl, *The Principle of Relativity* (Methuen, London, 1923), Reprinted (Dover, New York, 1952).
See also chapter 4 of J. Eisenstaedt, *The Curious History of Relativity* (Princeton University Press, Princeton NJ, 2006).

[50] D. R. Brill and J. M. Cohen, Phys. Rev. **143**, 1011 (1966).

[51] L. S. Kegeles, Phys. Rev . D **18**, 1020 (1978).

[52] R. J. Wiltshire, Gen. Rel. Grav. **35**, 175 (2003).

[53] D. Lynden-Bell, J. Katz, and J. Bicak, Mon. Not. R. Astron. Soc. **272** 150 (1995); 1600(E) (1995).

[54] J. Bicak, D. Lynden-Bell, and J. Katz, Phys. Rev. D **69**, 064011 (2004).

Chapter 2

Tidal Coupling of a Schwarzschild Black Hole and Circularly Orbiting Moon

We describe the possibility of using LISA's gravitational-wave observations to study, with high precision, the response of a massive central body to the tidal gravitational pull of an orbiting, compact, small-mass object (a white dwarf, neutron star, or small-mass black hole). Motivated by this LISA application, we use first-order perturbation theory to study tidal coupling for a special, idealized case: a Schwarzschild black hole of mass M, tidally perturbed by a "moon" with mass $\mu \ll M$ in a circular orbit at a radius $b \gg M$ with orbital angular velocity Ω. We investigate the details of how the tidal deformation of the hole gives rise to an induced quadrupole moment $\mathscr{I}_{ij}$ in the hole's external gravitational field at large radii. In the limit that the moon is static, we find, in Schwarzschild coordinates and Regge-Wheeler gauge, the surprising result that *there is no induced quadrupole moment*. We show that this conclusion is gauge dependent and that *the static, induced quadrupole moment for a black hole is inherently ambiguous*, and we contrast this with an earlier result of Suen, which gave, in a very different gauge, a nonzero static induced quadrupole moment with a sign opposite to what one would get for a fluid central body. For the orbiting moon and the central Schwarzschild hole, we find a time-varying induced quadrupole moment that is proportional to the time derivative of the moon's tidal field, $\mathscr{I}_{ij} = (32/45)M^6\dot{\mathcal{E}}_{ij}$ and that therefore is out of phase with the tidal field by a spatial angle $\pi/4$ and by a temporal phase shift $\pi/2$. This induced quadrupole moment produces a gravitational force on the moon that reduces its orbital energy and angular momentum at the same rate as the moon's tidal field sends energy and angular momentum into the hole's horizon. As a partial analog of a result derived long ago by Hartle for a spinning hole and a static distant companion, we show that the orbiting moon's tidal field induces a tidal bulge on the hole's horizon, and that the rate of change of the horizon shape (i.e. the horizon shear) *leads* the perturbing tidal field at the horizon by an angle $4M\Omega$. We discuss the implications of these results for LISA's future observations of tidal coupling, including the inappropriateness of using the concepts of *tidal polarizability* and *tidal lag or lead angle*, for the massive central body, when discussing LISA's observations.

Originally published as H. Fang and G. Lovelace, Phys. Rev. D **72**, 124016 (2005). Slightly revised.

2.1 Introduction and summary

2.1.1 Motivations

One of the primary scientific requirements for LISA (the Laser Interferometer Space Antenna) is to map, in exquisite detail, the spacetime geometries of massive black holes (and, if they exist, other massive, compact bodies) by using the gravitational waves emitted by inspiraling white dwarfs, neutron stars, and small-mass black holes. This emission process has come to be called "Extreme Mass Ratio inspiral" (EMRI, pronounced emm-ree). The possibility of making such maps from EMRI waves was discussed by Thorne in the early 1990s (e.g., in Refs. [1, 2]). In 1995 Ryan [3] laid the first detailed foundation for such mapping: he showed that, when the massive, central body is general relativistic, axisymmetric, and reflection-symmetric, and the orbiting object is in a near-equatorial, near-circular orbit in the vacuum region surrounding the body, the full details of the central body's metric are encoded in (i) the phase evolution of the waves and also in (ii) the evolution of the frequencies (or phases) of wave modulation produced by orbital precession. Phinney [4] has given the name "bothrodesy" to the mapping of a black hole's metric via EMRI waves, and bothrodesy has been identified, by the LISA International Science Team (LIST), as one of the prime goals for LISA [5]. The initial phase of scoping out LISA's data analysis challenges for EMRI waves is now underway [6].

Ryan's proof that the EMRI waves carry a map of the central body's metric ignored completely the influence of tidal coupling between the central body and the orbiting object. Finn and Thorne [7] have shown that, for values of the body and object masses in the range relevant to LISA, the tidal coupling can have an influence as large as a few percent on the evolution of the waves' inspiral phase—a phase that should be measurable to a fraction of a cycle out of tens or hundreds of thousands of cycles. Thus, the influence of the tidal coupling may be measurable with rather high precision. Because, in Ryan's analysis, the map is encoded redundantly in the EMRI waves' inspiral phase and in their modulations, it is reasonable to hope that the tidal coupling will break that redundancy in such a manner as to permit extraction of both the map and details of the central body's response to the tidal gravitational pull of the orbiting object [8].

Thorne [9] has argued that if we are to keep an open mind about the physical nature of the central body from the outset [e.g., if we are to allow for the possibility that it is a boson star (e.g. [10, 11]) or a soliton star (e.g. [12]) rather than a black hole], then we must describe the tidal coupling in a manner that can encompass all possible types of central bodies—a body-independent manner.

In the case of the earth and moon, the tidal coupling is normally described in terms of the rise and fall of the earth's surface or ocean's surface, and in terms of energy dissipation in the earth's oceans. Noticeably different from this, the tidal coupling in the case of a black hole has always, until now, been described in terms of the influence of the orbiting object's gravitational field on the hole's horizon—the perturbation of the horizon's 2-metric (e.g. [13, 14]), or the conversion of the tidal field into gravitational radiation at the horizon by gravitational blue-shifting and the energy and angular momentum carried inward by those waves (e.g., [15]).

One tidal feature in common between a black hole, the earth, a boson or soliton star, and all other conceivable central bodies, is the body's tidally-induced multipole moments and multipolar gravitational fields. It is these induced fields, acting back on the orbiting object, that change the object's orbital energy and angular momentum, secularly change its orbit, and thereby alter the emitted gravitational waves. For this reason, Thorne [9] has proposed that we adopt these induced multipole fields or moments as our body-independent description of tidal coupling when analyzing LISA data.

As a first step in exploring Thorne's proposal, we compute, in this paper, the tidally induced quadrupole moment and its back reaction on the orbiting object, in the special case where the central body is a Schwarzschild black hole, and the object is a distant, circularly orbiting moon.

2.1.2 Framework and results

Consider a moon of mass μ orbiting around a massive central body at a large distance. When the central body is a planet [16] (see Sec. III of Ref. [14] for a review), the external tidal field produced by the moon, denoted by $\mathcal{E}^{\rm ext}_{ij}$, raises a tide on the central body and induces a quadrupole moment $\mathscr{I}^{\rm ind}_{ij}$ that is proportional to $\mathcal{E}^{\rm ext}_{ij}$. The proportionality constant is the body's polarizability. Because of viscous dissipation, the induced quadrupole moment $\mathscr{I}^{\rm ind}_{ij}$ will be slightly out of phase with $\mathcal{E}^{\rm ext}_{ij}$; it will have a small phase lag with respect to the applied field. This phase lag is generally referred to as the tidal lag angle, and can be defined equivalently as the ratio of the tangential and radial component of the tidally induced force acting back on the moon. One objective of this paper is to explore whether this type of characterization via polarizability and lag angle is also reasonable when the central body is a black hole.

To explore this, we study a model problem where the moon is orbiting circularly around a massive Schwarzschild black hole of mass M ($\gg \mu$) at large distance b ($\gg M$). We assume the separation b is large enough that there exists an intermediate region between the hole and moon where (i) gravity is weak so space is nearly flat; (ii) the moon's tidal field does not vary appreciably. This region is referred to as the black hole's local asymptotic rest frame (LARF) [17]. Because the spacetime is nearly flat, one can write down the full tidal field in the LARF (in Cartesian coordinates) to linear order in each multipole moment as [18]

$$\mathcal{E}_{ij} \equiv R_{0i0j} \quad = \quad -\sum_{\ell=0}^{\infty} \frac{(-1)^{\ell}}{\ell!} \mathscr{I}_{A_\ell} \left(\frac{1}{r}\right)_{,ijA_\ell} - \sum_{\ell=2}^{\infty} \frac{(2\ell-1)!!}{(\ell-2)!} \mathscr{Q}_{ijA_{\ell-2}} X_{A_{\ell-2}}. \tag{2.1}$$

Here $\mathscr{I}_{A_\ell}$ and $\mathscr{Q}_{A_\ell}$ are the ℓ-th internal and external moments; they are symmetric and trace free (STF) in their tensor indices $A_\ell \equiv a_1...a_\ell$ [19]. The "internal moments" $\mathscr{I}_{A_\ell}$ characterize the central body, while the "external moments" $\mathscr{Q}_{A_\ell}$ characterize the gravitational fields of distant sources that perturb the central body. In our problem, the tidal field $\mathcal{E}^{\rm ext}_{ij}$ is physically the same as the external quadrupole moment $\mathscr{Q}_{ij}$; they differ only by a constant scaling factor, $\mathcal{E}_{ij} = -3\mathscr{Q}_{ij}$. The internal quadrupole moment is induced by the applied tidal field and characterizes the tidal deformation of the central body.

Equation (2.1) is the gravitational analogy to the multipole expansion of an electromagnetic field. It will be sufficiently accurate for our purpose, since we shall compute the nonspherical parts of the Riemann curvature tensor by solving the linearized Einstein field equations. It will be shown in Sec. 2.2 that only multipole moments with $\ell = 0, 2$ are relevant to our problem. Dropping all other terms in Eq. (2.1) and contracting with the unit spatial vector yields

$$\mathcal{E}_{ij} n^i n^j = -\frac{2M}{r^3} + \mathcal{E}^{\rm ext}_{ij} n^i n^j - \frac{18 \mathscr{I}^{\rm ind}_{ij} n^i n^j}{r^5}, \tag{2.2}$$

where we have identified $\mathscr{I}$ in Eq. (2.1) as the total mass of the black hole and substituted the external tidal field $\mathcal{E}^{\rm ext}_{ij}$ for $\mathscr{Q}_{ij}$. In the last term, $\mathscr{I}^{\rm ind}_{ij}$ represents the quadrupole moment induced on the black hole by the external tidal field.

In Secs. 2.3 and 2.4.1 of this paper we compute the induced quadrupole moment in Regge-Wheeler gauge, obtaining

$$\mathscr{I}^{\rm ind}_{ij} = \frac{32}{45} M^6 \dot{\mathcal{E}}^{\rm ext}_{ij}. \tag{2.3}$$

The same result was recently derived by Poisson from calculating the averaged rate of change of mass and angular momentum of the perturbed black hole [20]. Note that $\mathscr{I}^{\rm ind}_{ij}$ is proportional to the time derivative of $\mathcal{E}^{\rm ext}_{ij}$ (a time derivative caused by the moon's motion) and is therefore completely out of phase with the external tidal field (by 90 degrees in time and 45 degrees in space). As we will show in Sec. 2.5, this out-of-phase induced moment is gauge invariant and is responsible for the torque that changes the orbital energy and angular momentum. Thus it is also responsible for the tidally induced portion of the orbital evolution and the phase evolution of the gravitational waves.

The piece of the induced quadrupole moment that is proportional to and in-phase with the applied tidal field is ambiguous (in a sense that we shall discuss in Sec. 2.4.2); in Schwarzschild coordinates and Regge-Wheeler gauge, it *vanishes*. If there had been an unambiguous piece of $\mathscr{I}^{\rm ind}_{ij}$ in phase with $\mathcal{E}^{\rm ext}_{ij}$, then this in-phase piece would have defined a polarizability, and the ratio of out-of-phase piece to the in-phase piece would have been, in a certain well-defined sense, the small tidal lag angle. Thus, our result can be regarded as saying that both the polarizability and the lag angle of a black hole are ambiguous (in the sense discussed in Sec. 2.4.2).

Although we find that the tidal lag angle in the LARF, in the case of a Schwarzschild black hole, is ambiguous, we can still define and calculate an angular tidal shift on the horizon (as opposed to in the LARF or out at the moon). We study this horizon phase shift in Sec. 2.5. Hartle [14] has calculated[1] the tidal lag angle for the problem of a bulge raised on *slowly rotating* hole's horizon by a *stationary moon*, and he has shown it to be *negative*: the horizon's tidal bulge *leads* the applied tidal field due to the horizon's teleological definition (i.e., a definition in terms of the future fate of null rays). As in Hartle's case, we can compare the phase of the shape of our *nonrotating* horizon to our *moving* moon's position by mapping the moon to the horizon with an ingoing, zero-angular momentum, null geodesic. In Sec. 2.5, we find that this prescription

---

[1] We review the principal results of Hartle's investigation in Sec. 2.5.2.1.

leads to a *lead* angle between the moon and the horizon

$$\delta_{\text{null map}} = \frac{8}{3}M\Omega + \Omega b^*, \tag{2.4}$$

where Ω is the orbital angular frequency of the moon and b^* is the moon's tortoise coordinate $b^* \equiv b + 2M\log(b/2M - 1)$.

For comparison, Hartle's result [14] for the tidal lead angle in the case of the rotating hole and distant, stationary moon in the equatorial plane, is (after correcting a sign error, as discussed in footnote [6] of this chapter)

$$\delta^{\text{H}}_{\text{null map}} = \frac{2a}{3M} + \frac{a}{b} = \frac{8}{3}M\Omega_H + 4\frac{M^2\Omega_H}{b}, \tag{2.5}$$

Here a is the hole's specific angular momentum, and Ω_H is the horizon angular velocity. The radius of the moon's position b is sufficiently large that the moon is essentially stationary. Throughout this paper, we use the superscript "H" to indicate results corresponding to Hartle's system, i.e., to a system with a stationary moon and rotating horizon. Other results (without the subscript "H") correspond to our system of a distant moon, orbiting at frequency Ω, which perturbs a Schwarzschild black hole).

Our result (2.4) differs from Hartle's (2.5)—even though we initially expected that the tidal phase shift should depend only on the difference in angular velocities of the applied tidal field and the horizon generators, so the results would be the same. The terms that differ arise from the particular choice to map the moon to the horizon using an ingoing, zero-angular momentum null ray.

We prefer an alternative definition of the tidal lead angle, one that is independent of b^*; we prefer to define the tidal phase shift as the angle between the perturbing tidal field at the horizon and the shear (which is the rate of change of the shape) of the horizon [21]. This definition avoids introducing null connections between the moon (which, at radius $b \ll \Omega^{-1}$, is in the near zone) and the horizon. Using this definition, we find that the shear of the central hole *leads* the perturbing tidal field at the horizon by an angle

$$\delta_{\text{Horizon}} = \delta^{\text{H}}_{\text{Horizon}} = 4M\Omega. \tag{2.6}$$

The tidal lead angle is the same whether one considers a stationary moon perturbing a rotating hole or an orbiting moon perturbing a non-rotating hole.

The rest of paper is organized as follows. In Sec. 2.2, we decompose the applied tidal field in the LARF into a time-dependent part and a static part. In Sec. 2.3 we analyze fully the time-dependent part and deduce the dynamical part of the induced quadrupole moment [Eq. (2.23)]. In Sec. 2.4, we solve for the static perturbation and discuss the ambiguity in defining the static part of the induced quadrupole moment. In Sec. 2.5, we study the phase shift between the deformation of the horizon and the applied tidal and compare the result with the phase shift as defined by Hartle. A brief conclusion is made in Sec. 2.6. Throughout the paper, we use geometrized units with $G = c = 1$.

2.2 Problem setup

We study small perturbations of a non-spinning black hole caused by an orbiting moon. The unperturbed background metric is the Schwarzschild metric:

$$ds^2 = -\left(1 - \frac{2M}{r}\right)dt^2 + \frac{dr^2}{1 - 2M/r} + r^2(d\theta^2 + \sin^2\theta d\phi^2), \tag{2.7}$$

where M is the mass of the central hole. At large radii (i.e., in the LARF), we will study the perturbations in a notation that treats the Schwarzschild coordinates (r, θ, ϕ) as though they were flat-space spherical coordinates. These coordinates are related to the Cartesian coordinates $(x, y, z) = (x^1, x^2, x^3)$ by

$$(x^1, x^2, x^3) = r(\sin\theta\cos\phi, \sin\theta\sin\phi, \cos\theta).$$

We will denote the radial vector with length r by $\mathbf{x}$, the unit radial vector by $\mathbf{n}$, and their components by x^j and n^j, respectively.

Let a moon of mass μ move along a circular orbit with radius b in the equatorial plane ($b \gg M \gg \mu$). The moon's position is specified by

$$\mathbf{x}^{\mathrm{s}} = b\,\mathbf{n}^{\mathrm{s}} = b\,(\cos\Omega t, \sin\Omega t, 0), \tag{2.8}$$

where the superscript "s" stands for the "source" of the perturbation and $\Omega = \sqrt{M/b^3}$ is the moon's orbital angular frequency, satisfying $\Omega b \ll 1$. The moon's tidal field $\mathcal{E}^{\mathrm{ext}}_{ij}$ is the double gradient of the moon's Newtonian gravitational potential. Its value in the LARF (at $r \ll b$ but $r \gg M$) is well approximated by

$$\mathcal{E}^{\mathrm{ext}}_{ij} = -\left.\left(\frac{\mu}{|\mathbf{x} - \mathbf{x}^{\mathrm{s}}|}\right)_{,ij}\right|_{r=0} = \frac{\mu}{b^3}\left(\delta_{ij} - 3n^{\mathrm{s}}_i n^{\mathrm{s}}_j\right). \tag{2.9}$$

Note that although the applied tidal field is defined in the LARF, the induced quadrupolar field $\mathscr{I}^{\mathrm{ind}}_{ij}$ of greatest interest is not in the LARF, but further out in the vicinity of the moon's orbit, where it interacts with the moon.

The tidal field (2.9) can be decomposed into spherical, harmonic modes [22]. The result of the decomposition is

$$\mathcal{E}^{\mathrm{ext}}_{ij} = \frac{\mu}{b^3}\sqrt{\frac{6\pi}{5}}\left(\sqrt{\frac{2}{3}}\mathscr{Y}^{20}_{ij} - \mathscr{Y}^{22}_{ij}e^{-i\omega t} - \mathscr{Y}^{2-2}_{ij}e^{i\omega t}\right) \equiv \mathcal{E}^{\mathrm{ext},20}_{ij} + \mathcal{E}^{\mathrm{ext},22}_{ij} + \mathcal{E}^{\mathrm{ext},2-2}_{ij}, \tag{2.10}$$

with $\omega \equiv 2\Omega$ and $\mathcal{E}^{\mathrm{ext},2m}_{ij}$ ($m = 0, \pm 2$) equal to the corresponding $\mathscr{Y}^{2m}_{ij}$ term. Here the $\mathscr{Y}^{2m}_{ij}$ are position-independent, rank-2, symmetric trace-free (STF) tensors defined in Eqs. (2.67)–(2.68) and are related to the familiar $\ell = 2$ spherical harmonics $Y^{2m}(\theta, \phi)$ by Eq. (2.66). (See Eqs. (2.7)–(2.14) of Ref. [22] for the general mapping between order ℓ spherical harmonics and rank-ℓ STF tensors). The explicit values of the tidal field components are

$$\mathcal{E}_{ij}^{\text{ext},20} = -\frac{\mu}{2b^3}\begin{pmatrix} 1 & 0 & 0 \\ 0 & 1 & 0 \\ 0 & 0 & -2 \end{pmatrix}, \tag{2.11a}$$

$$\mathcal{E}_{ij}^{\text{ext},2\pm2} = -\frac{3\mu}{4b^3}\begin{pmatrix} 1 & \pm i & 0 \\ \pm i & -1 & 0 \\ 0 & 0 & 0 \end{pmatrix} e^{\mp i\omega t}\,. \tag{2.11b}$$

The tidal field $\mathcal{E}_{ij}^{\text{ext}}$ [Eq. (2.10)] is the source of perturbations of the central hole; it is an even-parity $\ell = 2$ external tidal field. We shall therefore perform our calculation in the even-parity Regge-Wheeler gauge, mode by mode ($\ell = 2, m = 0, \pm 2$). The tidal field $\mathcal{E}_{ij}^{\text{ext}}$ also sets the outer boundary condition for the problem: the $O(r^0)$ terms in the perturbed tidal field $\mathcal{E}_{ij}$ must go to $\mathcal{E}_{ij}^{\text{ext}}$ in the LARF [Eq. (2.2)].

The inner boundary condition is set differently, depending on whether the perturbations are static or time-dependent. For the static perturbations generated by $\mathcal{E}_{ij}^{20}$, we impose a “regularity boundary condition”: the perturbations must be physically finite at $r = 2M$. For the time-dependent perturbations generated by $\mathcal{E}_{ij}^{\text{ext},2\pm2}$, we impose the “ingoing-wave boundary condition”: the perturbations have the asymptotic behavior $\sim e^{\mp i\omega r^*}$ when approaching the horizon. Here r^* is the tortoise coordinate $r^* \equiv r + 2M\log(r/2M - 1)$.

2.3 Time-dependent part of the perturbation

2.3.1 The perturbed metric

We will specialize to $(\ell, m) = (2, 2)$ in solving for the time-dependent part of the metric perturbation. The $(\ell, m) = (2, -2)$ results can be obtained by complex conjugating the $(2, 2)$ results. For briefness, a superscript “22” will not be added to quantities calculated in this harmonic mode in this section, unless a distinction is needed. Throughout this section, we refer to Appendix 2.B for details of the perturbation calculation.

In the standard Regge-Wheeler gauge, the $(\ell, m) = (2, 2)$ time-dependent perturbations take the form [23]

$$\begin{aligned} h_{ab}^{(22)} &= Y^{22}(\theta,\phi)e^{-i\omega t} \\ &\times \begin{vmatrix} H(1-\frac{2M}{r}) & H_1 & 0 & 0 \\ H_1 & H(1-\frac{2M}{r})^{-1} & 0 & 0 \\ 0 & 0 & r^2 K & 0 \\ 0 & 0 & 0 & r^2 K\sin^2\theta \end{vmatrix}. \end{aligned} \tag{2.12}$$

Here H, H_1 and K are functions of r alone. These radial functions are solutions of the perturbed Einstein equations; they can be constructed from the Zerilli function $\mathbb{Z}(r)$ [24], which satisfies a second order ordinary differential equation [Eq. (2.73)]. Specifically, H_1, K and H are given in terms of $\mathbb{Z}(r)$ by Eqs. (2.69)–(2.72). Instead of solving for $\mathbb{Z}$(r) directly, one may obtain the Zerilli function from its odd-parity correspondent, the Regge-Wheeler function $\mathbb{X}(r)$, which obeys a simpler differential equation [23, 25] that is easier to solve [Eq. (2.75)]:

$$\left[\frac{d^2}{dr^{*2}} + \omega^2 - \left(1 - \frac{2M}{r}\right)\left(\frac{\ell(\ell+1)}{r^2} - \frac{6M}{r^3}\right)\right]\mathbb{X}(r) = 0,$$

where $d/dr^* = (1 - 2M/r)d/dr$. The Zerilli function $\mathbb{Z}(r)$ is expressed in terms of $\mathbb{X}(r)$ by Eq. (2.76). Thus, the metric perturbation is determined by the single radial function $\mathbb{X}(r)$, by way of Eq. (2.76) to get $\mathbb{Z}(r)$ and then Eqs. (2.69)–(2.72) to get H_1, K, and H.

The analytic solution for $\mathbb{X}$(r) with the ingoing-wave boundary condition at horizon was derived by Poisson and Sasaki [26]. Their solution, X^H in their notation and for the limiting case $\omega r \ll 1$, is what we have used in our analysis. With our slow motion assumption $\Omega b \ll 1$, $X^H(\omega r \ll 1)$ will be sufficient to cover the region inside the moon's orbit—including the LARF, where we read out the induced quadrupole moment. Following Poisson and Sasaki's notation, we define the dimensionless quantity

$$\varepsilon \equiv 2M\omega. \tag{2.13}$$

We then combine Eqs. (3.4), (3.11), and (3.12) of Ref. [26] to obtain

$$X^H(\omega r \ll 1) \quad = \quad \mathcal{A}\left(\frac{r}{2M}\right)^3 e^{i\omega(r-2M)} \times F(c_1, c_2; c_3; 1 - \frac{r}{2M})e^{-i\omega r^*}, \tag{2.14a}$$

where $\mathcal{A}$ is an overall scaling factor that did not appear in Ref. [26] but will be determined by the outer boundary condition in our problem; F is the hypergeometric function with parameters [Eq. (3.11) of Ref. [26] with $\ell = 2$]

$$c_1 \quad = \quad -i\varepsilon + O(\varepsilon^2), \tag{2.14b}$$

$$c_2 \quad = \quad 5 - i\varepsilon + O(\varepsilon^2), \tag{2.14c}$$

$$c_3 \quad = \quad 1 - 2i\varepsilon. \tag{2.14d}$$

Note that expression (2.14a) for X^H is only accurate to first order in ε. We then expand Eq. (2.14a) in large r and keep terms to first order in ε

$$X^H = \mathcal{A}\left[\left(1 + \frac{13}{12}i\varepsilon\right)\tilde{r}^3 + \sum_{n=5}^{\infty} \frac{i\varepsilon}{n\tilde{r}^{n-3}} + O(\varepsilon^2)\right], \tag{2.15}$$

where $\tilde{r} \equiv r/2M$ is the dimensionless radius. Next, we use Eq. (2.76) to get $\mathbb{Z}(r)$. Then the perturbed metric components can be constructed using Eqs. (2.69)–(2.72). In the following all quantities will be calculated up to first order in ε and we will suppress "$O(\varepsilon^2)$" in our expressions.

2.3.2 Induced quadrupole moment in the LARF

Once the perturbed metric is known, it is straightforward to calculate the full Riemann tensor and extract from it the first-order tidal field in the LARF:

$$\mathcal{E}^{(1)}_{ij} \equiv R^{(1)}_{0i0j} = R_{0i0j} - R^{(0)}_{0i0j}, \tag{2.16}$$

where a superscript of "(0)" or "(1)" indicates the quantity is of zeroth or first order in the perturbation. In our calculation, we found it convenient to look at the $0r0r$ component of the first-order Riemann tensor in the LARF, since

$$R^{(1)}_{0r0r} = R^{(1)}_{0i0j} n_i n_j = \mathcal{E}^{(1)}_{ij} n_i n_j. \tag{2.17}$$

From this equation we can read off $\mathcal{E}^{(1)}_{ij} = R^{(1)}_{0i0j}$, the first-order tidal field in Cartesian coordinates in the LARF, from the Riemann tensor in Schwarzschild coordinates. By the procedure outlined in this paragraph we have deduced the following $(\ell, m) = (2, 2)$ part of $\mathcal{E}^{(1)}_{ij}$ in the LARF:

$$\mathcal{E}^{(1),22}_{ij} = -\frac{3\mathcal{A}}{4M^3}\left[1 + \frac{4}{3}i\varepsilon + \sum_{n=5}^{\infty}\frac{i\varepsilon}{n\tilde{r}^n}\right]\mathscr{Y}^{22}_{ij} e^{-i\omega t}. \tag{2.18}$$

The outer boundary condition states that the $O(r^0)$ [i.e. $O(\tilde{r}^0)$] term of $\mathcal{E}^{(1),22}_{ij}$ must equal $\mathcal{E}^{\text{ext},22}_{ij}$ [Eq. (2.11b)]. This determines the scaling factor to be

$$\mathcal{A} = \frac{4\mu M^3}{b^3}\sqrt{\frac{2\pi}{15}}\left(1 - \frac{4}{3}i\varepsilon\right). \tag{2.19}$$

Inserting Eq. (2.19) into Eq. (2.18), we can write $\mathcal{E}^{(1),22}_{ij}$ as

$$\mathcal{E}^{(1),22}_{ij} = \mathcal{E}^{\text{ext},22}_{ij} - \frac{\mu}{b^3}\sqrt{\frac{6\pi}{5}}\sum_{n=5}^{\infty}\frac{i\varepsilon}{n\tilde{r}^n}\mathscr{Y}^{22}_{ij} e^{-i\omega t}. \tag{2.20}$$

Here the $O(1/\tilde{r}^5)$ term, by Eq. (2.2), contains the induced quadrupole moment. The $O(1/\tilde{r}^6)$ and higher terms are proportional to the $O(1/\tilde{r}^5)$ term and contain no new information; they represent the non-linear coupling between the induced quadrupole and the black hole's monopole moment.

Comparing the $O(1/\tilde{r}^5)$ term in Eq. (2.2) and the $O(1/r^5)$ term in Eq. (2.20), we find that

$$\mathscr{I}^{22}_{ij} = \frac{32}{45}M^6\dot{\mathcal{E}}^{\text{ext},22}_{ij}. \tag{2.21}$$

Complex conjugating this equation yields the $(\ell, m) = (2, -2)$ part of the induced quadrupole moment:

$$\mathscr{I}_{ij}^{2-2} = \frac{32}{45} M^6 \dot{\mathcal{E}}_{ij}^{\text{ext},2-2}. \tag{2.22}$$

Thus, the time dependent part, i.e. the dynamical part (DP), of the induced quadrupole moment is given by

$$\mathscr{I}_{ij}^{\text{ind, DP}} = \frac{32}{45} M^6 \Big(\dot{\mathcal{E}}_{ij}^{\text{ext},22} + \dot{\mathcal{E}}_{ij}^{\text{ext},2-2}\Big) = \frac{32}{45} M^6 \dot{\mathcal{E}}_{ij}^{\text{ext}}. \tag{2.23}$$

This agrees with the result recently obtained by Poisson [20] by a very different method. Note that the induced quadrupole moment is proportional to the time derivative of the applied tidal field. Hence the induced quadrupole moment and the applied tidal field are completely out of phase with each other ($\pi/4$ phase shift in space, $\pi/2$ in time). This leads to a dissipative force acting back on the moon.

From the induced quadrupole moment (2.23), we define a corresponding Newtonian potential in the LARF and out to the moon's orbit:

$$\Phi = -\frac{3}{2} \mathscr{I}_{ij}^{\text{ind, DP}} \frac{n^i n^j}{r^3}. \tag{2.24}$$

Then the force acting back on the moon can be found by evaluating the gradient of Φ at the moon's position:

$$\mathbf{F} = -\nabla\Phi|_{\mathbf{x}^s} = -\frac{32}{5}\left(\frac{\mu}{b}\right)^2 \left(\frac{M}{b}\right)^{13/2} \mathbf{e}_\phi. \tag{2.25}$$

Equation (2.25) shows that the force is tangential and opposite to the moon's motion. The energy loss from the moon's orbital motion is then

$$\dot{E} = -\mathbf{F}\cdot\mathbf{v} = \frac{32}{5} M^4 \mu^2 \Omega^6, \tag{2.26}$$

where $\mathbf{v} = \Omega b \mathbf{e}_\phi$. It is straightforward to show that there is also an angular momentum loss of magnitude $\dot{E}/\Omega$. Equation (2.26) agrees with Poisson and Sasaki's calculation of the rate at which the perturbation carries energy into the black hole's horizon at the leading post-Newtonian order [26].

2.4 The static, axisymmetric part of the perturbation

2.4.1 Static induced quadrupole moment

We now specialize to the even-parity, static part of the moon's perturbation: $(\ell, m) = (2, 0)$. The Regge-Wheeler metric for this type of perturbation has the form [23]

$$h_{ab}^{(20)} = \text{Diag}\Big[\Big(1 - \frac{2M}{r}\Big)\hat{H}_2,\ \frac{\hat{H}_2}{1 - 2M/r},\ r^2\hat{K}_2,\ r^2\hat{K}_2\sin^2\theta\Big] \times Y^{20}(\theta, \phi)\,, \tag{2.27}$$

where "Diag" is short for diagonal matrix and $\hat{H}_2$ and $\hat{K}_2$ are functions of r only. The general solution to the field equation governing $\hat{H}_2$ can be expressed in terms of the associated Legendre functions [13]:

$$\hat{H}_2(r) = \alpha_2 P_2^2\left(\frac{r}{M} - 1\right) + \beta_2 Q_2^2\left(\frac{r}{M} - 1\right), \tag{2.28}$$

where α_2 and β_2 are constants to be determined. The solution to $\hat{K}_2$ can then be obtained from that of $\hat{H}_2$ (Appendix C). As r approaches $2M$, we have [27]

$$Q_\ell^2(r/M - 1) \sim (r/M)^{-1/2},$$

so the Q_2^2 term in Eq. (2.28) becomes divergent at $r = 2M$ and we must set the coefficient β_2 to be zero in order for the perturbation to be finite there. As r goes to infinity,[2]

$$P_\ell^2(r/M - 1) \sim (r/M)^\ell.$$

Therefore the remaining P_2^2 term in Eq. (2.28) keeps growing quadratically as r becomes large, corresponding to the non-asymptotic flatness due to the presence of the moon.

With the metric perturbation $h_{ab}^{(20)}$, we compute the Riemann tensor from the full metric and series expand the result up to linear order in α_2 (i.e., first order in the perturbation). The $0r0r$ component of the resulting first-order Riemann tensor is found to be

$$R^{(1)}_{0r0r} = \frac{3\alpha_2}{M^2}\, Y^{20}(\theta, \phi). \tag{2.29}$$

From this and from Eq. (2.10), we obtain the first-order tidal field in the Cartesian basis

$$\mathcal{E}^{(1)}_{ij} = \frac{3\alpha_2}{M^2}\, \mathscr{Y}^{20}_{ij}. \tag{2.30}$$

The static, first-order tidal field thus contains *only* an $O(r^0)$ term, which should be identified as the static part of the applied external field $\mathcal{E}^{\mathrm{ext},20}_{ij}$ [Eq. (2.11a)]. The coefficient α_2 is determined from this identification to be $\alpha_2 = \sqrt{4\pi/45}\,\mu M^2/b^3$. Since there is no $O(1/r^5)$ term present in Eq. (2.30), we infer that there is no static induced quadrupole moment:

$$\mathscr{I}^{20}_{ij} = 0. \tag{2.31}$$

This is quite a counter-intuitive result. It is worth pointing out, however, that the absence of negative powers of r in Eq. (2.30) follows directly from the regularity condition we imposed at $r = 2M$. If the radius $r = 2M$ were well inside the central body itself, which naturally is the case for any nonrelativistic body with weak self-gravity, then the Q_2^2 term in Eq. (2.28) would survive and give rise to an induced quadrupole

---

[2] Valid for all Re $\ell > -1/2$.

moment. Equation (2.31) may also be the consequence of the gauge (Regge-Wheeler) we choose to work in. Is it possible to give a gauge-invariant definition of static, induced multipole moment in a non-asymptotically-flat spacetime? This is the question we shall investigate in the next subsection.

We now summarize and conclude that the total induced quadrupole moment *in our chosen gauge* is

$$\mathscr{I}^{\rm ind}_{ij} = \mathscr{I}^{20}_{ij} + \mathscr{I}^{22}_{ij} + \mathscr{I}^{2-2}_{ij} = \frac{32}{45} M^6 \dot{\mathcal{E}}^{\rm ext}_{ij}, \tag{2.32}$$

which is proportional to the time derivative of the external tidal field—not the field itself as one would expect for Newtonian tidal couplings.

Lastly, we move from the LARF to the perturbed horizon and examine the effect of the static perturbation there. Hartle has shown [13] that to first order in the perturbation, the coordinate location of the event horizon of a slowly rotating black hole perturbed by a stationary distribution of matter is still at $r = 2M$. This is also true for a Schwarzschild black hole under static perturbations. Evaluating the full metric at $r = 2M$, we find the horizon metric is given by

$$ds^2_H = 4M^2\Big[1 - 2\mu(M^2/b^3)P_2(\cos\theta)\Big]\Big(d\theta^2 + \sin^2\theta d\phi^2\Big), \tag{2.33}$$

where P_2 is the Legendre function. From this metric the scalar curvature of the horizon is obtained as

$$\mathscr{R} = \frac{1}{2M^2}\Big[1 - 4\mu(M^2/b^3)P_2(\cos\theta)\Big]. \tag{2.34}$$

So it is clear that the shape of the horizon does acquire a small quadrupolar component. But this deformation is *not* accompanied by an induced quadrupole moment in the LARF, at least in our chosen gauge.

2.4.2 Ambiguity of the static induced quadrupole moment

In the previous subsection, we found that a Schwarzschild black hole has a vanishing static induced quadrupole moment (SIQM) in response to the external tidal field $\mathcal{E}^{\rm ext,20}_{ij}$. To see that this vanishing of the SIQM might possibly be a gauge effect, imagine replacing the radial coordinate r in the expression $\Phi = (1/2)\mathcal{E}^{\rm ext,20}_{ij} n^i n^j r^2$ for the external tidal Newtonian potential by $r = \bar{r}(1 + \chi M^5/\bar{r}^5)^{1/2}$, where χ is some dimensionless number of order unity. The result is $\Phi = (1/2)\mathcal{E}^{\rm ext,20}_{ij} n^i n^j \bar{r}^2 + (\chi/2)M^5\mathcal{E}^{\rm ext,20}_{ij} n^i n^j/\bar{r}^3$. By comparing this expression with Eq. (2.2) we read off a SIQM $\mathscr{I}_{ij} = (\chi/18)M^5\mathcal{E}^{\rm ext,20}_{ij}$. In Newtonian theory this procedure would obviously be naive, but in general relativity, where the unperturbed black hole metric can be expanded in powers of M/r and the coefficients in that expansion depend on one's choice of radial coordinate and that choice is a "gauge" issue, this type of procedure is not obviously naive at all.

From our point of view, the best way to explore the gauge dependence of the SIQM is to ask whether it is physically measurable. If (as we shall find) physical measurements give a result that is ambiguous at some level, then that ambiguity constitutes a sort of gauge dependence of the SIQM.

In this section we shall study a thought experiment for measuring the SIQM, one based on coupling to a small, static external "test" octupole field $\mathcal{E}_{ijk}$ (proportional to the symmetrized and trace-removed gradient of some fiducial external quadrupolar tidal field). For simplicity we take $\mathcal{E}_{ijk}$ to be axisymmetric around the same z-axis as our static external tidal field $\mathcal{E}^{\rm ext,20}_{ij}$, i.e. we take it to be proportional to a tensor spherical harmonic of order $(\ell, m) = (3, 0)$:

$$\mathcal{E}_{ijk} \sim \mathscr{Y}^{30}_{ijk}.$$

The analysis in Ref. [28] says that, any SIQM $\mathscr{I}_{ij}$ (created in the black hole by $\mathcal{E}^{\rm ext,20}_{ij}$) will couple to the external octupole moment to produce a force that gradually changes the hole's momentum:[3]

$$\dot{P}^i = -\frac{1}{2}\,\mathcal{E}^i{}_{jk}\mathscr{I}_{jk}. \tag{2.35}$$

(Eq. (1.12) of Ref. [17]; Eq. (4b) of Ref. [28]). The same will be true if the central black hole is replaced by a neutron star or any other spherical body. The rate of change of momentum $\dot{P}^i$ can also be evaluated by a surface integral of the Landau-Lifshitz pseudotensor $t^{ij}_{\rm LL}$ in the LARF [17]:

$$\dot{P}^i = -\oint (-g)\, t^{ij}_{\rm LL}\, dS_j. \tag{2.36}$$

Equations (2.35) and (2.36) for the coupling-induced force on the hole actually have ambiguities that arise from nonlinearities in the Einstein field equations. The origin of those ambiguities is discussed with care in Sec. I of Thorne and Hartle [17]. In this subsection we use Eq. (2.36) to calculate the force on the hole, and shall identify the ambiguities as those terms in which the force depends on the location of the integration surface. The result of our calculation will tell us, by comparison with Eq. (2.35), the SIQM and the amount by which it is ambiguous.

To compute the pseudotensor for insertion into Eq. (2.36), we must solve for the metric perturbation containing both the quadrupole and octupole terms:

$$h_{ab} = h^{(20)}_{ab} + h^{(30)}_{ab} \quad = \quad \sum_{\ell=2,3} {\rm Diag}\Big[\,(1-2M/r)\,\hat{H}_\ell,\ \frac{\hat{H}_\ell}{1-2M/r}\,,\ r^2\hat{K}_\ell,\ r^2\hat{K}_\ell\sin^2\theta\Big] \times Y^{\ell 0}(\theta,\phi)\,. \tag{2.37}$$

When $\ell = 2$, the general solution to $\hat{H}_2$ is given in Eq. (2.28). For $\ell = 3$, we have

$$\hat{H}_3(r) = \alpha_3 P^2_3\Big(\frac{r}{M}-1\Big) + \beta_3 Q^2_3\Big(\frac{r}{M}-1\Big). \tag{2.38}$$

In order that both types of perturbation be finite at $r = 2M$, β_2 and β_3 must be set to zero [see Eq. (2.29)]. In order to deal with more general cases, however, we keep *non-vanishing* values for β_2 and β_3 in Eqs. (2.28) and (2.38) so the following analysis will be valid for stars as well as black holes. [For central bodies other

---

[3] The test octupole field may also induce a static octupole moment $\mathscr{I}_{ijk}$ in the central black hole, which will couple to the external quadrupolar tidal field. This coupling, as we shall show, contributes to the ambiguities in the definition of the SIQM.

than black holes, β_2 and α_2 (and similarly β_3 and α_3) are not independent of each other: β_2 is proportional to α_2 with a proportionality constant that depends on the body's internal physical properties]. Having specified the metric perturbation, we then insert the full metric into the expression for the pseudotensor (Eq. (20.22) of Ref. [29])

$$\begin{aligned}(-g)t^{\alpha\beta}_{\mathrm{LL}} &= \frac{1}{16\pi}\Big\{\mathfrak{g}^{\alpha\beta}{}_{,\lambda}\mathfrak{g}^{\lambda\mu}{}_{,\mu} - \mathfrak{g}^{\alpha\lambda}{}_{,\lambda}\mathfrak{g}^{\beta\mu}{}_{,\mu} + g_{\lambda\mu}g^{\nu\rho}\mathfrak{g}^{\alpha\lambda}{}_{,\nu}\mathfrak{g}^{\beta\mu}{}_{,\rho} - \left(g^{\alpha\lambda}g_{\mu\nu}\mathfrak{g}^{\beta\nu}{}_{,\rho}\mathfrak{g}^{\mu\rho}{}_{,\lambda} + g^{\beta\lambda}g_{\mu\nu}\mathfrak{g}^{\alpha\nu}{}_{,\rho}\mathfrak{g}^{\mu\rho}{}_{,\lambda}\right) \\ &+ \frac{1}{2}g^{\alpha\beta}g_{\lambda\mu}\mathfrak{g}^{\lambda\nu}{}_{,\rho}\mathfrak{g}^{\rho\mu}{}_{,\nu} + \frac{1}{8}\left(2g^{\alpha\lambda}g^{\beta\mu} - g^{\alpha\beta}g^{\lambda\mu}\right)\times\left(2g_{\nu\rho}g_{\sigma\tau} - g_{\rho\sigma}g_{\nu\tau}\right)\mathfrak{g}^{\nu\tau}{}_{,\lambda}\mathfrak{g}^{\rho\sigma}{}_{,\mu}\Big\}\,, \qquad (2.39)\end{aligned}$$

and evaluate the surface integral at some radius $r = R$ in the LARF. Because of the axisymmetry of the perturbed spacetime, only the z-component of $\dot{P}^i$ is nonzero. The result, up to first-order coupling and with uninteresting numerical coefficients being suppressed, has the following form:

$$\dot{P}^z = \alpha_3\alpha_2\left[\frac{R^4}{M^4}\ \&\ \frac{R^3}{M^3}\ \&\ \frac{R^2}{M^2}\ \&\ \frac{R}{M}\ \&\ 1\ \&\ ...\right] + \alpha_3\beta_2\left[1\ \&\ \frac{M}{R}\ \&\ ...\right] + \beta_3\alpha_2\left[\frac{M^3}{R^3}\ \&\ \frac{M^4}{R^4}\ \&\ ...\right]\,, \qquad (2.40)$$

where "&" is to be read "and a term of the order".

The constant terms in Eq. (2.40) [i.e., the "1"s] that are independent of the integration radius R are the ones to be compared with Zhang's result (2.35) so as to deduced the gauge-invariant SIQM. Other terms that depend on R constitute ambiguities.[4] Terms with positive power(s) of R/M appear because the spacetime is not asymptotically flat, and they prevent us from minimizing the ambiguities by simply pushing the integration surface to infinity.

Let us step back and write down the most general form that the SIQM can take. By order of magnitude analysis of the response of any physical body (black hole, star, planet, moon, etc) to a tidal field, we must have

$$\mathscr{I}_{ij} \sim L^5(1+\xi)\,\mathcal{E}^{\mathrm{ext},20}_{ij}. \qquad (2.41)$$

Here L is the size of the body ($L \sim M$ for a black hole) and ξ is a dimensionless number describing the SIQM's dependence on the integration radius R—deviations from being well defined. From Eq. (2.30), we know the external tidal field scales as $\sim \alpha_2/M^2$. Similarly for the external octupole field, $\mathcal{E}_{ijk} \sim \alpha_3/M^3$. Using these relations, Eq. (2.35) becomes

$$\dot{P}^i \sim L^5(1+\xi)\,\mathcal{E}^{\mathrm{ext},20}_{jk}\,\mathcal{E}^i{}_{jk} \sim \alpha_2\alpha_3\left[\frac{L^5}{M^5} + \frac{\xi L^5}{M^5}\right]. \qquad (2.42)$$

---

[4] The M^2/R^2 term includes the effect of any octupole moment induced on the central body by the test octupole field. Note that $\dot{P}^i$ is a dimensionless vector. On dimensional grounds, the coupling between any induced octupole moment and the external tidal field must take the form $\mathscr{I}^{ijk}\mathcal{E}_{jk}/R^2$ to contribute to $\dot{P}^i$. (Nonlinear coupling to the monopole moment can lead to similar terms that scale as higher, but not lower, powers of $1/R$.)

Here the first term in the square bracket should be identified as the "1"s in Eq. (2.40) (note again that β_2 and α_2 are not independent of each other for stars); and the second term should be identified as the sum of all R-dependent terms:

$$\frac{\xi L^5}{M^5} = \frac{R^4}{M^4} \,\&\, ... \,\&\, \frac{R}{M} \,\&\, \frac{M}{R} \,\&\, ... \,. \tag{2.43}$$

In the case of a black hole we have $L \sim M$ and the smallest the right hand side of Eq. (2.43) can be is ~ 1 (for $R \sim M$), so $\xi \gtrsim 1$, i.e. *the SIQM for a Schwarzschild black hole is ambiguous by an amount* $\gtrsim M^5 \mathcal{E}^{\mathrm{ext},20}_{ij}$, i.e. *totally ambiguous*, since the largest we could expect $\mathscr{I}_{ij}$ to be is $\sim M^5 \mathcal{E}^{\mathrm{ext},20}_{ij}$.

For central objects with $L \gg M$ (e.g., the Earth) we must choose $R > L$. The right hand side of Eq. (2.43) is then minimized by setting $R \simeq L$, giving $\xi \sim M/L \ll 1$ ($\sim 10^{-9}$ in the case of the Earth) for the fractional ambiguities in the SIQM.

We comment that our result for a Schwarzschild black hole differs from what Suen has derived. Suen has given an unambiguous prescription to read out static multipole moments in non-asymptotically-flat spacetimes, which is based on transforming coordinates into a particular set of de Donder coordinates [30]. He has used his prescription to calculate the induced quadrupole moment of a Schwarzschild black hole when it is perturbed by a static, equatorial matter ring at large distances [18]. According to his prescription, the SIQM does *not* vanish. It is proportional to the tidal field produced by the ring:

$$\mathscr{I}_{ij} = -\frac{4}{21} M^5 \mathcal{E}^{\mathrm{ring}}_{ij}. \tag{2.44}$$

The incompatibility between this result and the vanishing SIQM that we derived in Sec. 2.4.1 in Regge-Wheeler gauge and Schwarzschild coordinates illustrates the ambiguities of the SIQM. Both results, zero and $(-4/21) M^5 \mathcal{E}_{ij}$ are less than or of order the ambiguity.

2.5 The tidal phase shift

In the LARF, the time-dependent induced quadrupole moment is $\pi/4$ out of phase with the perturbing tidal field (Sec. 2.3.1). This large phase shift is quite different from the small phase lag angle, caused by viscous dissipation, between a planet's induced quadrupole moment and the perturbing tidal field. A closer black-hole analogy to a planet's viscous phase lag may be found by considering the tide raised on the hole's horizon by an orbiting moon.

In this section, we compute the tidal phase shift on the horizon for our perturbed Schwarzschild black hole. We will discuss in what sense it is and is not analogous to the fluid-planet's viscous phase lag. To calculate this phase shift, it is convenient to use the Newman-Penrose formalism [31] (see, e.g., chapter 1 of Ref. [32] for a review of the Newman-Penrose formalism). Appendix 2.D summarizes some details of the Newman-Penrose formalism that are relevant for our purpose.

We consider two approaches to defining the tidal phase shift. In Sec. 2.5.1, we define the phase shift only in terms of quantities on the horizon (following the method suggested in Sec. VIIC of Ref. [21]), while in Sec. 2.5.2, we define a phase between the tide raised on the horizon and the "retarded" position of the moon (following the method used by Hartle in Ref. [14]).

2.5.1 Phase of the tidal bulge on the horizon

For Sec. 2.5 and Appendix 2.D only, we use ingoing Eddington-Finkelstein coordinates $(\tilde{V}, r, \theta, \phi)$ and a $(+ - - -)$ signature of the metric. The Schwarzschild metric in these coordinates is

$$ds^2 = \left(1 - \frac{2M}{r}\right) d\tilde{V}^2 - 2d\tilde{V}dr - r^2 \left(d\theta^2 + \sin^2\theta d\phi^2\right). \tag{2.45}$$

The ingoing Eddington-Finkelstein null time coordinate $\tilde{V}$ is related to the Schwarzschild time coordinate t and radial coordinate r by the following equation (Eq. (1b) of Box 32.2 of Ref. [29]):

$$\tilde{V} = t + r^* = t + r + 2M \ln |r/2M - 1| \,, \tag{2.46}$$

and the Eddington-Finkelstein radial and angular coordinates $\{r, \theta, \phi\}$ are identical to those of Schwarzschild.

Our slowly orbiting moon deforms the Schwarzschild event horizon. By analogy with Newtonian tides, we would like to describe the horizon deformation as a perturbation that co-rotates (at a slightly different phase) with the tidal field that drives it. But this viewpoint inherently envisions the perturbed event horizon as a two-dimensional, evolving surface, rather than as a three-dimensional, global surface in spacetime. Therefore, before we can consider the *phases* of quantities on the horizon, we must first specify what we mean by *time* on the horizon.

Begin by considering the Schwarzschild event horizon (which is, of course, the three-surface $r = 2M$). There is a preferred way to slice the horizon into a single-parameter family of two-surfaces; this preferred slicing uses two-surfaces that are orthogonal to the Schwarzschild Killing vector $\partial_t = \partial_{\tilde{V}}$ that is timelike at the moon and null on the horizon. Following Hartle [14], we call this family of two-surfaces the "instantaneous horizon". The instantaneous horizon can be pictured as an evolving two-surface defined by $r = 2M$ and $\tilde{V}$ = constant, so that $\tilde{V}$ plays the role of a "time" coordinate. Throughout this section, we use the terms "horizon" and "instantaneous horizon" interchangeably unless otherwise indicated.

We now consider how the horizon's perturbation evolves with time $\tilde{V}$. The moon's tidal field, characterized in the LARF by [Eq. (2.10)]

$$\mathcal{E}^{\text{ext}}_{ij} = \mathcal{E}^{\text{ext},20}_{ij} + \mathcal{E}^{\text{ext},22}_{ij} + \mathcal{E}^{\text{ext},2-2}_{ij},$$

deforms the otherwise spherical, static horizon. Because $\mathcal{E}^{\text{ext},20}_{ij}$ is static and axisymmetric, it cannot contribute to the phase shift. For the remaining tidal fields, $\mathcal{E}^{\text{ext},2\pm2}_{ij}$, we shall consider only the $(2, 2)$ mode in detail and the result for the $(2, -2)$ mode follows immediately.

On the horizon, it is the tangential-tangential components of the perturbing tidal field that drive the deformation (see, e.g., Eq. (6.80) of Ref. [21]); knowledge of these components is physically equivalent to knowledge of the Teukolsky function Ψ_0 [15] (see, e.g., Eq. (A7) of Ref. [33]). The Teukolsky function is a particular component of the Weyl tensor [Eq. (2.87a)].

The horizon deformation is governed by the Newman-Penrose equation (Eq. (2.11) of Ref. [14])

$$(\partial_{\tilde{V}} - 2\epsilon)\sigma^{(1)} = -2(i\Omega + \epsilon)\sigma^{(1)} = \Psi_0^{(1)}. \tag{2.47}$$

This is also the "tidal force equation" (equation (6.80) of Ref. [21]). Here $\sigma = -\Sigma^{(1)}$ is a Newman-Penrose spin coefficient [Eq. (2.85)] and $\Sigma^{(1)}$ is the shear (i.e., the rate of change of the shape[5]) of the instantaneous horizon. Note that because Σ and Ψ_0 vanish on the unperturbed instantaneous horizon, the spin coefficient ϵ takes its Schwarzschild value, which (in our tetrad) is the surface gravity of the instantaneous horizon $g_H = (4M)^{-1}$.

Knowing $\Psi_0^{(1)}$, we can evaluate the horizon shear. Because $\Psi_0^{(1)}$ is first order in the perturbation, it may be evaluated on the horizon simply by letting r go to $2M$.

Beginning with the $(\ell, m) = (2, 2)$ metric perturbation [Eq. (2.12), except we now choose the metric signature to be $(+ \; - \; - \; -)$], we compute the perturbed Riemann tensor near the horizon and read off the component $\Psi_0^{(1)}$. The result is

$$\begin{aligned} \Psi_0^{(1)} &= -i\sqrt{\frac{\pi}{5}}\frac{\mu M\Omega}{b^3}\,{}_2Y^{22}e^{-2i\Omega\tilde{V}+(8/3)M\Omega} + O(M^2\Omega^2) \\ &= \left|\Psi_0^{(1)}\right| \exp\left[2i\left(\phi - \Omega\tilde{V} + \frac{4}{3}M\Omega - \frac{\pi}{4}\right)\right] + O(M^2\Omega^2)\,. \end{aligned} \tag{2.48}$$

Here ${}_2Y^{22}$ is the spin-weighted spherical harmonic

$${}_2Y^{22} = \frac{1}{2}\sqrt{\frac{5}{\pi}}\sin^4\left(\frac{\theta}{2}\right)e^{2i\phi}.$$

With $\Psi_0^{(1)}$ in hand, we can calculate $\Sigma^{(1)}$ via Eq. (2.47). Inserting $\epsilon = 2g_H$ and $\omega = 2\Omega$ into Eq. (2.47) yields

$$\begin{aligned} \Sigma^{(1)} &= \frac{\Psi_0^{(1)}}{i\omega + 2\epsilon} = 4M\Psi_0^{(1)}e^{-2i\Omega/g_H} + O(M^2\Omega^2) \\ &= \left|\Sigma^{(1)}\right| \exp\left[2i\left(\phi - \Omega\tilde{V} + \frac{4}{3}M\Omega - \frac{\pi}{4} - \delta_{\text{Horizon}}\right)\right] + O(M^2\Omega^2)\,, \end{aligned} \tag{2.49}$$

where

$$\delta_{\text{Horizon}} \equiv \Omega/g_H = 4M\Omega. \tag{2.50}$$

The shear $\Sigma^{(1)}$ *leads* $\Psi_0^{(1)}$ (or equivalently, the perturbing tidal field at the horizon) *by an angle* δ_{Horizon}. Note that the first equality in Eq. (2.49) appears in Ref. [14] as Eq. (2.12).

---

[5] Recall that the shape of the instantaneous horizon (a two-dimensional surface) is completely specified by its intrinsic scalar curvature $\mathscr{R}$.

The shear is the time derivative of the shape. Therefore, the shape has a phase

$$\mathscr{R}^{(1)} = |\mathscr{R}^{(1)}| \exp\left[2i\left(\phi - \Omega\tilde{V} - \frac{8}{3}M\Omega\right)\right]. \tag{2.51}$$

In other words, *the shear leads the shape by* $\pi/4$.

The horizon phase shift in Eq. (2.50) follows directly from the tidal force equation (2.47). It is gauge-invariant since it only makes reference to gauge-invariant quantities measured on the instantaneous horizon. In Ref. [21] [Eq. (7.45), Fig. 57, and the surrounding discussion], an analogous horizon phase shift $\delta^{\mathrm{H}}_{\mathrm{Horizon}}$ was deduced from the tidal force equation for a slowly rotating black hole perturbed by a stationary, axisymmetric tidal field—physically the same problem as Hartle studied [14]:

$$\delta^{\mathrm{H}}_{\mathrm{Horizon}} = \Omega_H/g_H = 4M\Omega_H = \delta_{\mathrm{Horzion}}\,|_{\Omega\to\Omega_H}\,. \tag{2.52}$$

Here Ω_H is the horizon angular velocity.

Although Hartle also used the tidal force equation in his calculations, he chose to define the tidal phase shift in a different way and made his result gauge-invariant by making a connection between the angular positions on the horizon and angular positions at infinity through a null ray—a choice we will consider in detail in Sec. 2.5.2.1 and apply to our problem in Sec. 2.5.2.2.

The phase lead $\delta_{\mathrm{Horizon}}$ is, in some ways, analogous to the phase shift of a tide raised on a non-rotating fluid planet. In the latter case, viscous dissipation causes the shape of the planet's surface to lag the normal-normal component of the perturbing tidal field by a small angle δ_{visc}; somewhat analogously, the horizon shear leads the tangential-tangential component of the perturbing tidal field. Both phase shifts are small angles associated with dissipation (which manifests itself as a secular evolution of the energy and angular momentum of the moon's orbit). In the absence of dissipation, there is no phase shift. On the other hand, the phase shift $\delta_{\mathrm{Horizon}}$ is a *lead* angle while δ_{visc} is a *lag* angle. Hartle explains this difference as a consequence of the teleological nature of the horizon [14]. Also as Hartle observed, when the angular velocity Ω is not small compared with $1/M$, the deformation of the horizon cannot be described in terms of a phase shift [14].

2.5.2 Phase shift between the tidal bulge and the moon

As an alternative to the above way of defining the tidal phase shift, one can define it as the angle between the tidal bulge on the horizon and the location of the moon in its orbit. Hartle used this approach when he computed the tidal lead on a rotating hole perturbed by a stationary moon [14]. First, we will briefly summarize the aspects of Hartle's analysis which are relevant to our purpose. Then, we will apply his method to a slowly rotating moon around an otherwise Schwarzschild black hole.

2.5.2.1 Tidal phase shift between a rotating horizon and stationary moon

In Ref. [14], Hartle considers the problem of a distant, stationary moon perturbing a slowly rotating black hole. The Kerr metric can be written as

$$\begin{aligned} ds^2 &= \left(1-\frac{2Mr}{\Sigma}\right)d\tilde{V}^2 - 2d\tilde{V}dr + \frac{4aMr\sin^2\theta}{\Sigma}d\tilde{V}d\tilde{\phi} \\ &\quad + 2a\sin^2\theta dr d\tilde{\phi} - \Sigma d\theta^2 - \sin^2\theta\left(a^2+r^2+\frac{2a^2Mr\sin^2\theta}{\Sigma}\right)d\tilde{\phi}^2\ . \end{aligned} \tag{2.53}$$

Here $\Sigma \equiv r^2 + a^2\cos^2\theta$. The coordinates $\tilde{V}$ and $\tilde{\phi}$ are related to the usual Boyer-Lindquist coordinates t and ϕ by

$$dt = d\tilde{V} - \frac{r^2+a^2}{\Delta}dr\ , \tag{2.54a}$$

$$d\phi = d\tilde{\phi} - \frac{a}{\Delta}dr\ , \tag{2.54b}$$

where $\Delta \equiv r^2 - 2Mr + a^2$. When $a = 0$, Eq. (2.53) reduces to the Schwarzschild metric in Eddington-Finkelstein coordinates [Eq. (2.45)].

The event horizon is the surface $r = r_+ \equiv M + \sqrt{M^2-a^2}$. Just as in the Schwarzschild case considered above, the event horizon can be sliced into a single-parameter family of two-dimensional surfaces using the Killing vector $\partial_{\tilde{V}}$ which is timelike at infinity and null on the horizon. This family of surfaces is the instantaneous horizon.

The distant moon raises a tidal bulge on the central hole's instantaneous horizon. In the limit that the moon is far away, the change in the horizon's shape (or equivalently, the change in the scalar curvature $\mathscr{R}$ of the instantaneous horizon), is purely quadrupolar.

The deformation is driven by the transverse-transverse component of the tidal field at the horizon, which is physically equivalent to the Teukolsky function, a particular component of the Riemann tensor Ψ_0 [Eq. (2.87a)]. This component vanishes in the unperturbed Kerr spacetime [Eq. (2.94a)], and the first order correction $\Psi_0^{(1)}$ has the form

$$\Psi_0^{(1)} = S^{\ell m}(r)\,{}_2Y^{\ell m}(\theta,\tilde{\phi})\ , \tag{2.55}$$

where ${}_2Y^{\ell m}$ is a spin-weight-2 spherical harmonic. Because the perturbation is purely quadrupolar, we need only consider the case $\ell = 2, m = 2$ here, although Hartle considers the generic case. Hartle uses Teukolsky's solution [34] for the stationary radial functions $S^{\ell m}$ due to the ℓ-pole perturbation caused by a distant, stationary point particle with mass μ. Furthermore, while Hartle treats the case of a moon at any location $(\theta,\tilde{\phi})$, for concreteness we specify the moon's position as $(\theta,\tilde{\phi}) = (\pi/2, 0)$. On the horizon, the Teukolsky function turns out to have the value (combining Eqs. (4.30), (4.31), (4.15), and (4.18) of Ref. [14])

$$\Psi_0^{(1),\mathrm{H}} = \frac{i\mu M\Omega_H}{2\sqrt{6}b^3}\sin^4\left(\frac{\theta}{2}\right)\exp\left[2i\left(\tilde{\phi}+2M\Omega_H\right)\right] + O\left(\frac{M^4}{b^4}\right) + O\left(M^2\Omega_H^2\right). \tag{2.56}$$

The tidal field deforms the instantaneous horizon, changing its shape and thus its two-dimensional scalar curvature $\mathscr{R}$. Hartle computes the quadrupolar correction to the scalar curvature, $\mathscr{R}^{(1),\ell=2,\mathrm{H}}$, of the instantaneous horizon [Eq. (2.91)]. His result is (Eqs. (4.26)–(4.27) of Ref. [14])

$$\mathscr{R}^{(1),\ell=2,\mathrm{H}} \quad \propto \quad \cos\left[2\left(\tilde{\phi}+\frac{14}{3}M\Omega_H\right)\right]+O\left(\frac{M^4}{b^4}\right)+O\left(M^2\Omega_H^2\right) . \tag{2.57}$$

Instead of measuring the angle between the shear σ and the tidal field Ψ_0 on the horizon, Hartle defines his phase lead as the angle between the shape and the moon's angular position. To make this definition gauge-invariant, Hartle chooses ingoing, zero-angular-monentum, null geodesics to be "lines of constant angle." He then compares the angular position of the horizon tidal bulge,

$$\tilde{\phi}^{\mathrm{H}}_{\mathrm{bulge}} = -\frac{14}{3}M\Omega_H, \tag{2.58}$$

to the angular position of the moon on the horizon.

Consider stationary moon in the equatorial plane at (large) radius $r = b$ and at angular position $\phi = 0$. An ingoing null ray, originating from the moon, intersects the instantaneous horizon at angular position[6]

$$\tilde{\phi}^{\mathrm{H}}_{\mathrm{moon}} = a/b - a/2M. \tag{2.59}$$

The tidal bulge therefore *leads* the moon's position by an amount

$$\delta^{\mathrm{H}}_{\mathrm{null\ map}} \quad = \quad \tilde{\phi}^{\mathrm{H}}_{\mathrm{moon}} - \tilde{\phi}^{\mathrm{H}}_{\mathrm{bulge}} = \frac{8}{3}M\Omega_H + 4\frac{M^2\Omega_H}{b} . \tag{2.60}$$

Here we have used the relation (valid for small a/M) that $a = 4M^2\Omega_H$, with Ω_H being the angular velocity of the hole. For simplicity, one can then take the limit $b \to \infty$.

Before continuing, we should remark that Hartle's prescription for constructing $\delta^{\mathrm{H}}_{\mathrm{null\ map}}$ can be described without reference to the moon's position. Begin by computing the angular location of the tidal bulge on the horizon. Next, ingoing, zero-angular-momentum null rays from infinity define lines of constant angle, so that there is a one-to-one correspondence between angular positions on the horizon and angular positions at infinity. The angular position at infinity of the tidal bulge can thus be computed. Finally, perform the calculation again, but this time perturb a *non-rotating spacetime*; in this case, there will be no tidal friction. Because the Kerr and Schwarzschild spacetimes are asymptotically identical, one can unambiguously compare the angular position of the tidal bulge in the presence and in the absence of tidal friction: $\delta^{\mathrm{H}}_{\mathrm{Null\ Map}} = \phi^{\mathrm{H}}_{\mathrm{bulge}} - \phi^{\mathrm{H}}_{\mathrm{bulge,\ no\ friction}}$. This is equivalent to the previous definition of $\delta^{\mathrm{H}}_{\mathrm{null\ map}}$ provided that $b \to \infty$.

However, this alternative formulation of $\delta^{\mathrm{H}}_{\mathrm{null\ map}}$ breaks down when the moon, not the horizon, rotates. The rotation is then described by Ω, which is a parameter of the perturbation, not of the background space-

---

[6] Note that there is a sign error in Hartle's analysis. Hartle incorrectly states that the ingoing null ray intersects the horizon at $+a/2M + O(a/b)$, not $-a/2M + O(a/b)$. Had we also made this error, there would be a coefficient of 20/3 instead of 8/3 in Eq. (2.60).

time. To eliminate tidal friction, one must let $\Omega \to 0$, which eliminates the perturbation.[7] Because of this failure, we prefer to consider Hartle's phase shift as a comparison of the position of the tidal bulge with the position of the moon.

2.5.2.2 Tidal phase shift between a non-rotating horizon and rotating moon

A similar analysis can be applied to our system, in which a distant moon in a slow, circular orbit raises a tide on a non-rotating black hole. The moon orbits the central black hole along the world line specified by Eq. (2.8). In other words, the moon has a phase given by

$$\phi_{\text{moon}}(\tilde{V}) \equiv \Omega t = \Omega(\tilde{V} - b^*)\,. \tag{2.61}$$

This must be compared with the location of the bulge on the hole's future horizon. Equation (2.51) for $\mathscr{R}^{(1)}$ [or, alternatively, inserting Eq. (2.48) into Eq. (2.91)] shows that the tip of the tidal bulge has a phase given by

$$\phi_{\text{bulge}} = \Omega\tilde{V} + \frac{8}{3}M\Omega\,. \tag{2.62}$$

As time $\tilde{V}$ passes, this bulge rotates around and around the horizon, with the same angular velocity Ω as the moon that raises the tide.

Following Hartle, we compare the angular location of the tidal bulge, $\phi_{\text{bulge}}(\tilde{V})$, with the angular location of the moon, $\phi_{\text{moon}}(\tilde{V})$, using ingoing, zero angular momentum (ZAM) null rays to provide the connection between ϕ at the moon's orbit and ϕ on the horizon. In the ingoing Eddington-Finkelstein coordinates that we are using, these ZAM rays have a very simple form:

$$\{\tilde{V}, \theta, \phi\} = \text{constant}, \;\; r \text{ decreases from } b \text{ to } 2M. \tag{2.63}$$

Since $\tilde{V}$, θ and ϕ are all constant along these rays, they give us a one-to-one map of events $\{\tilde{V}, r = b, \theta, \phi\}$ at the moon's orbital radius to events $\{\tilde{V}, r = 2M, \theta, \phi\}$ on the horizon that have identically the same $\tilde{V}$, θ, and ϕ. With the aid of this map, we conclude that the angle by which the horizon bulge lags the moon's position is

$$\delta_{\text{null map}} \equiv \phi_{\text{bulge}}(\tilde{V}) - \phi_{\text{moon}}(\tilde{V}) = \frac{8}{3}M\Omega + \Omega b^*. \tag{2.64}$$

[Eqs. (2.61) and (2.62)]. Again, the phase shift is a phase lead, not a phase lag, due to the teleological nature of the horizon.

In addition to the teleological phase shift of order $M\Omega$, $\delta_{\text{null map}}$ contains a much larger term of magnitude Ωb^*; this term reflects the choice to use an ingoing-null-ray mapping between the moon and the horizon. A similar term appears in Hartle's calculation [Eq. (2.60)], but in Hartle's system the term is much *smaller* than

---

[7] Even if $\Omega \to 0$ resulted in a non-zero perturbation, it is unclear how to distinguish such a perturbation from a small change in the coordinates of the background spacetime.

the teleological phase shift size (specifically, smaller by a factor of M/b), whereas $\Omega b^* \gg M\Omega$.

One could avoid this problem by *defining* the phase shift to include only terms of order $M\Omega$ and $M\Omega_H$. With this definition, the remaining tidal phase leads are the same: $(8/3)M\Omega$, as one would expect, given that a there should be no tidal shift at all if the moon were to rotate at the hole's angular velocity, i.e., if $\Omega = \Omega_H$.

We prefer, however, to define the tidal lead angle in as the angle $\delta_{\rm Horizon} = 4M\Omega$ by which the horizon shear leads the horizon tidal field. This angle, in contrast to $\delta_{\rm null\ map}$, is defined in terms of an "instantaneous" (spacelike) connection between the moon and the horizon, i.e., by the near zone mapping of the moon's position to the horizon tidal field's [$\Psi_0^{(1)}$'s] maximum. [Had the moon been in the radiation zone ($b \gg \lambda/2\pi$), one would have expected the connection to be lightlike.]

2.6 Concluding discussion

For our simple system of a Schwarzschild black hole and circularly orbiting moon, we have found that the time-dependent part of the moon's tidal field induces a quadrupole moment that is unambiguous. The static induced quadrupole moment was found to be zero in the Regge-Wheeler gauge, but it is ambiguous in general. The ambiguity of the static induced quadrupole moment leads to an ambiguity in the phase of the induced quadrupole moment in the LARF; however, the tidal bulge on the horizon still has a well defined phase shift with respect to the orbiting moon. Because of the ambiguity of the induced quadrupole moment and the LARF phase shift, we conclude that the polarizability and phase shift are not suitable for constructing a body-independent description of tidal coupling in EMRIs.

However, this conclusion does not eliminate the possibility of developing a body-independent language to describe tidal coupling, including cases where the central body is a black hole. It might be possible, for instance, to define a new set of induced "dissipative multipole moments" for the central body—i.e., moments that vanish in the absence of tidal friction. Such dissipative moments would still be linear in the perturbing tidal field, so one could still define a polarizability. Also, by ignoring any non-dissipative tidal coupling, the phase shift might no longer contain additional information. Even if such an extension does not prove feasible, tidal coupling can still be described in the more conventional (but still body-independent) language of energy and angular momentum transfer between the moon and the central body.

Other future work could include generalizing our analysis to spinning black holes, treating noncircular, non-equatorial orbits, and (most importantly) studying how information about tidal coupling in EMRIs can be extracted from the gravitational waves detected by LISA.

Appendices

2.A Symmetric trace-free tensor notation for spherical harmonics

The scalar spherical harmonics $Y^{\ell m}(\theta,\phi)$ can be written in terms of of rank-ℓ symmetric trace-free (STF) tensors [22]. The spherical harmonics $Y^{2m}(\theta,\phi)$ that have been used in this paper are

$$Y^{2\pm2}(\theta,\phi)=\frac{1}{4}\sqrt{\frac{15}{2\pi}}\sin^2\theta e^{\pm 2i\phi}\ , \tag{2.65a}$$

$$Y^{20}(\theta,\phi)=\frac{1}{8}\sqrt{\frac{5}{\pi}}\left(1+3\cos 2\theta\right)\ . \tag{2.65b}$$

They can be written in terms of rank-2 STF tensors as (Eq. (2.11) of Ref. [22])

$$Y^{2m}(\theta,\phi)=\mathscr{Y}^{2m}_{ij}n^i n^j\ , \tag{2.66}$$

where $n^i\equiv x^i/r$ and $\mathscr{Y}^{2m}_{ij}$ are the STF tensors given by (Eq. (2.12) of Ref. [22]):

$$\mathscr{Y}^{20}_{ij} = -\frac{1}{4}\sqrt{\frac{5}{\pi}}\begin{pmatrix}1&0&0\\0&1&0\\0&0&-2\end{pmatrix}, \tag{2.67}$$

$$\mathscr{Y}^{2\pm2}_{ij} = \frac{1}{4}\sqrt{\frac{15}{2\pi}}\begin{pmatrix}1&\pm i&0\\\pm i&-1&0\\0&0&0\end{pmatrix}. \tag{2.68}$$

2.B Time-dependent perturbation equations

In Regge-Wheeler gauge, the metric perturbation for a given even-parity (ℓ,m,ω) mode depends on the three radial functions H, H_1, and K. In this appendix, we introduce the Zerilli function $\mathbb{Z}$ and the Regge-Wheeler function $\mathbb{X}$ and describe how we obtain the radial functions from them. The description here will hold for a general (ℓ,m,ω), while the results derived in Sec. (2.3) rely on the special case when $(\ell,m,\omega)=(2,2,2\Omega)$.

The original Zerilli's master function is defined implicitly through its relation with the two radial functions

H_1 and K [Eqs. (13) and (14) of Ref. [24] with ${R_{LM}}^{(e)}$ replaced by $\mathbb{Z}$]:

$$\begin{aligned} H_1 &= -i\omega\frac{\lambda r^2 - 3\lambda M r - 3M^2}{(r-2M)(\lambda r + 3M)}\mathbb{Z} - i\omega r\frac{d\mathbb{Z}}{dr}, && (2.69)\\ K &= \frac{\lambda(\lambda+1)r^2 + 3\lambda M r + 6M^2}{r^2(\lambda r + 3M)}\mathbb{Z} + \frac{d\mathbb{Z}}{dr^*}, && (2.70)\end{aligned}$$

where

$$\lambda \equiv \frac{1}{2}(\ell-1)(\ell+2).$$

Using the algebraic relationship (Eq. (10) of Ref. [25])

$$\left(\frac{3M}{r}+\lambda\right)H = \left[i\omega r - \frac{i(\lambda+1)M}{\omega r^2}\right]H_1 + \left(\lambda + \frac{M}{r} - \frac{M^2/r^2 + \omega^2 r^2}{1-2M/r}\right)K\,, \tag{2.71}$$

one can obtain H in terms of the Zerilli function,

$$H = \left[\frac{\omega^2 r^2}{2M-r} + \frac{s_1}{r^2(3M+\lambda r)^2}\right]\mathbb{Z} + s_2\frac{d\mathbb{Z}}{dr}\ , \tag{2.72a}$$

in which

$$\begin{aligned} s_1 &= 9M^2(M+\lambda r) + \lambda^2 r^2\Big[3M + (\lambda+1)r\Big]\,, && (2.72b)\\ s_2 &= \frac{-3M^2 - 3\lambda M r + \lambda r^2}{r(3M+\lambda r)}\ . && (2.72c)\end{aligned}$$

The Zerilli function obeys the wave equation (Eqs. (18) and (19) of Ref. [24]):

$$\left[\frac{d^2}{dr^{*2}} + \omega^2 - V(r)\right]\mathbb{Z} = 0\,, \tag{2.73}$$

in which the potential term is given by

$$V(r) = \frac{2(r-2M)}{r^4(\lambda r + 3M)^2}\Big[\lambda^2(\lambda+1)r^3 + 3\lambda^2 M r^2 + 9\lambda M^2 r + 9M^3\Big]\,. \tag{2.74}$$

The odd-parity master function, the Regge-Wheeler function, is defined in Eq. (23) of Ref. [23] (and is called Q in Regge and Wheeler's notation). It obeys the differential equation (Eq. (7) and of Ref. [25]):

$$\left[\frac{d^2}{dr^{*2}} + \omega^2 - \Big(1-\frac{2M}{r}\Big)\Big(\frac{\ell(\ell+1)}{r^2} - \frac{6M}{r^3}\Big)\right]\mathbb{X} = 0. \tag{2.75}$$

The connection between the Regge-Wheeler and Zerilli functions was first found by Chandrasekhar and is listed, e.g., in Eq. (152) of Ch. 4 of Ref. [32]:

$$\Big[\lambda(\lambda+1) - 3iM\omega\Big]\mathbb{Z} = \left[\lambda(\lambda+1) + \frac{9M^2(r-2M)}{r^2(\lambda r+3M)}\right]\mathbb{X} + 3M\left(1-\frac{2M}{r}\right)\frac{d\mathbb{X}}{dr}\ . \tag{2.76}$$

This completes our metric reconstruction scheme from the Regge-Wheeler function. We are now ready to evaluate the radial metric perturbation functions H, H_1, and K for the $(\ell, m) = (2, 2)$ mode of the perturbations. Expanding X^H [given in Eq. (2.15) in powers of $\tilde{r} \equiv r/2M$ to first order in $\varepsilon \equiv 2M\omega$, we obtain

$$X^H = \mathcal{A}\left[\Big(1 + \frac{13}{12} i\varepsilon\Big)\tilde{r}^3 + \sum_{n=5}^{\infty} \frac{i\varepsilon}{n\tilde{r}^{n-3}} + O(\varepsilon^2)\right]. \tag{2.77}$$

Here $\mathcal{A}$ is an overall scaling factor (Eq. (2.19) in Sec. 2.3.1). While the summation can be rewritten as a closed-form expression, we prefer to stay in the series notation, since our interest is in reading various powers of r in the resulting first-order tidal field. Equation (2.77) is the value of the Regge-Wheeler function in the LARF; inserting it into Eq. (2.76) yields the expression for $\mathbb{Z}$ in the LARF [we shall suppress "$O(\varepsilon^2)$" hereafter]:

$$\mathbb{Z} \;=\; \mathcal{A}\Big(1 + \frac{4i\varepsilon}{3}\Big)\Big[\tilde{r}^3 + \frac{3\tilde{r}^2}{4} - \frac{9\tilde{r}}{16} - \frac{21}{64} + \frac{63}{256\tilde{r}}\Big] + \mathcal{A}\Big[\frac{-945 - 236i\varepsilon}{5120\tilde{r}^2} + \frac{8505 + 15436i\varepsilon}{61440\tilde{r}^3} + O\Big(\frac{1}{\tilde{r}^4}\Big)\Big]\,.$$

Inserting $\mathbb{Z}$ into Eqs. (2.69), (2.70) and (2.72) yields H_1, K and H. Expanded in powers of $\tilde{r}$ and to first order in ε, these radial functions are given by

$$H \;=\; \frac{\mathcal{A}}{M}\Big[(3 + 4i\varepsilon)(\tilde{r}^2 - \tilde{r}) + \frac{i\varepsilon}{10\tilde{r}^3} + \frac{3i\varepsilon}{20\tilde{r}^4}\Big] + O(\tilde{r}^{-5})\,, \tag{2.78a}$$

$$H_1 \;=\; \frac{i\mathcal{A}\varepsilon}{4M}\Big[- 8\tilde{r}^3 - 2\tilde{r}^2 + 4\tilde{r} + 1 + \tilde{r}^{-1} + \tilde{r}^{-2} + \tilde{r}^{-3} + \tilde{r}^{-4}\Big] + O(\tilde{r}^{-5})\,, \tag{2.78b}$$

$$K \;=\; \frac{\mathcal{A}}{M}\Big[(3 + 4i\varepsilon)\Big(\tilde{r}^2 - \frac{1}{2}\Big) + \frac{i\varepsilon}{10\tilde{r}^3} + \frac{i\varepsilon}{8\tilde{r}^4} + \frac{9i\varepsilon}{70\tilde{r}^5} + \frac{i\varepsilon}{8\tilde{r}^6}\Big] + O(\tilde{r}^{-7})\,. \tag{2.78c}$$

2.C Time-independent perturbation equations

As is evident from the time-dependent perturbation theory, as $\omega \to 0$, H_1 goes to zero. In the static case, then, there are only two radial functions, $\hat{H}$ and $\hat{K}$ (where the hats signify that they represent the time-independent perturbations). Specializing to the axisymmetric case, the metric perturbation is

$$h_{ab}^{(\ell 0)} = \mathrm{Diag}\Big[\,(1 - 2M/r)\,\hat{H},\; \frac{\hat{H}}{1 - 2M/r}\,,\; r^2\hat{K},\; r^2\hat{K}\sin^2\theta\Big] \times Y^{\ell 0}(\theta, \phi)\,.$$

The linearized Einstein equations governing $\hat{H}$ and $\hat{K}$ are given in Eqs. (9d) and (9e) of Ref. [25] with $H_1 = 0$ and $\omega = 0$ ($k = 0$ in Edelstein and Vishveshwara's notation):

$$\frac{d\hat{K}}{dr} \;=\; \frac{d\hat{H}}{dr} + \frac{2M}{r^2}\left(1 - \frac{2M}{r}\right)^{-1}\hat{H}, \tag{2.79}$$

$$\frac{2M}{r^2}\frac{d\hat{K}}{dr} \;=\; \left(1 - \frac{2M}{r}\right)\frac{d^2\hat{H}}{dr^2} + \frac{2}{r}\frac{d\hat{H}}{dr} - \frac{\ell(\ell+1)}{r^2}\hat{H}. \tag{2.80}$$

Eliminating $d\hat{K}/dr$ from these two equations, we can then write a single second-order differential equation for H in terms of the variable $z \equiv r/M - 1$ (same as Eq. (4.9) of Ref. [13]):

$$(1-z^2)\frac{d^2\hat{H}}{dz^2} - 2z\frac{d\hat{H}}{dz} + \left[\ell(\ell+1) - \frac{4}{1-z^2}\right]\hat{H} = 0.$$

This takes a form of the associated Legendre differential equation. The general solution for $\hat{H}$ is therefore

$$\hat{H} = \alpha_\ell P_\ell^2(r/M-1) + \beta_\ell Q_\ell^2(r/M-1). \tag{2.81}$$

With the general solution for $\hat{H}$, we can integrate Eq. (2.79) or (2.80) to find $\hat{K}$. For $\ell = 2$, we have

$$\hat{K}_2(r) \;=\; \left[\alpha_2 P_2^1\,(r/M-1) + \beta_2 Q_2^1\,(r/M-1)\right] \times \frac{2M}{\sqrt{r(r-2M)}} + \hat{H}_2(r). \tag{2.82}$$

2.D Newman-Penrose formalism

In this appendix, we summarize some equations of the Newman-Penrose formalism for our choice of tetrad. *In this Appendix and in Sec. 2.5 only*, we use ingoing Eddington-Finkelstein coordinates $(\tilde{V}, r, \theta, \phi)$ and a $(+\ -\ -\ -)$ signature of the metric.

2.D.1 Newman-Penrose quantities for Schwarzschild spacetimes

We adopt the Hartle-Hawking null tetrad, which is given by Eqs. (4.2) of Ref. [14], together with the normalization conditions $\ell^\mu n_\mu = 1$ and $m^\mu \bar{m}_\mu = -1$. The tetrad vectors have components [using the notation $e^\mu = (e^{\tilde{V}}, e^r, e^\theta, e^\phi)$]

$$\ell^\mu = \left(1, \frac{1}{2} - \frac{M}{r}, 0, 0\right), \tag{2.83a}$$

$$n^\mu = (0, -1, 0, 0), \tag{2.83b}$$

$$m^\mu = \left(0, 0, \frac{1}{\sqrt{2}r}, \frac{i}{\sqrt{2}r\sin\theta}\right), \tag{2.83c}$$

$$\bar{m}^\mu = \left(0, 0, \frac{1}{\sqrt{2}r}, -\frac{i}{\sqrt{2}r\sin\theta}\right). \tag{2.83d}$$

Note that throughout this Appendix, an overbar denotes complex conjugation. From these basis vectors, we define the direction derivatives

$$D = \ell^\mu\partial_\mu,\ \Delta = n^\mu\partial_\mu,\ \delta = m^\mu\partial_\mu \text{ and } \bar{\delta} = \bar{m}^\mu\partial_\mu. \tag{2.84}$$

Our conventions for the spin coefficients follow Ref. [14] [specifically, Eqs. (2.2) and (2.3)]. The spin coefficients are defined by

$$\kappa = \ell_{\mu;\nu} m^\mu \ell^\nu \,, \qquad \pi = -n_{\mu;\nu}\bar{m}^\mu \ell^\nu \,, \tag{2.85a}$$

$$\rho = \ell_{\mu;\nu} m^\mu \bar{m}^\nu \,, \qquad \mu = -n_{\mu;\nu}\bar{m}^\mu m^\nu \,, \tag{2.85b}$$

$$\sigma = \ell_{\mu;\nu} m^\mu m^\nu \,, \qquad \lambda = -n_{\mu;\nu}\bar{m}^\mu \bar{m}^\nu \,, \tag{2.85c}$$

$$\epsilon = \frac{1}{2}\left(\ell_{\mu;\nu} n^\mu \ell^\nu - m_{\mu;\nu}\bar{m}^\mu \ell^\nu\right) \,, \tag{2.85d}$$

$$\alpha = \frac{1}{2}\left(\ell_{\mu;\nu} n^\mu \bar{m}^\nu - m_{\mu;\nu}\bar{m}^\mu \bar{m}^\nu\right) \,, \tag{2.85e}$$

$$\beta = \frac{1}{2}\left(\ell_{\mu;\nu} n^\mu m^\nu - m_{\mu;\nu}\bar{m}^\mu m^\nu\right) \,. \tag{2.85f}$$

The spin coefficients for the Schwarzschild spacetime are

$$\kappa = \sigma = \lambda = \nu = \tau = \pi = \gamma = 0 \,, \tag{2.86a}$$

$$\epsilon = \frac{M}{2r^2} \,, \qquad \rho = -\frac{r-2M}{2r^2} \,, \tag{2.86b}$$

$$\mu = -\frac{1}{r} \,, \qquad \alpha = -\beta = -\frac{1}{2\sqrt{2}r\tan\theta} \,. \tag{2.86c}$$

Because we are only interested in vacuum regions of spacetime, the Riemann and Weyl tensors are interchangeable. The Weyl components are defined in vacuum by

$$\Psi_0 = -R_{\alpha\beta\gamma\delta}\ell^\alpha m^\beta \ell^\gamma m^\delta \,, \tag{2.87a}$$

$$\Psi_1 = -R_{\alpha\beta\gamma\delta}\ell^\alpha n^\beta \ell^\gamma m^\delta \,, \tag{2.87b}$$

$$\Psi_2 = -\frac{1}{2}R_{\alpha\beta\gamma\delta}\left(\ell^\alpha n^\beta \ell^\gamma n^\delta + \ell^\alpha n^\beta m^\gamma \bar{m}^\delta\right) \,, \tag{2.87c}$$

$$\Psi_3 = -R_{\alpha\beta\gamma\delta}\ell^\alpha n^\beta \bar{m}^\gamma n^\delta \,, \tag{2.87d}$$

$$\Psi_4 = -R_{\alpha\beta\gamma\delta}n^\alpha \bar{m}^\beta n^\gamma \bar{m}^\delta \,. \tag{2.87e}$$

Their values for the Schwarzschild spacetime are

$$\Psi_0 = \Psi_1 = \Psi_3 = \Psi_4 = 0, \qquad \Psi_2 = -\frac{M}{r^3} \,. \tag{2.88}$$

The Ricci identities are

$$\left(\nabla_\mu \nabla_\nu - \nabla_\nu \nabla_\mu\right) e_\gamma = R_{\sigma\gamma\mu\nu} e^\sigma. \tag{2.89}$$

Inserting the null tetrad vectors for e^σ and projecting along the tetrad yields the Ricci identities in Newman-Penrose notation. One of these equations is, in our tetrad and evaluated on the horizon,

$$D\sigma^{(1)} - 2\epsilon\sigma^{(1)} = \partial_{\tilde{V}}\sigma^{(1)} - 2\epsilon\sigma^{(1)} = \Psi_0^{(1)}. \tag{2.90}$$

(Note that we have used the fact that σ and Ψ_0 vanish for Schwarzschild.) This is the *tidal force equation*; it relates $\Psi_0^{(1)}$, which is physically equivalent to the tangential-tangentail component of the perturbing tidal field on the horizon, to σ, which is physically equivalent to the shear of the instantaneous horizon.

The shape of the perturbed instantaneous horizon is determined by its two-dimensional scalar curvature $\mathscr{R} + \mathscr{R}^{(1)}$ where $\mathscr{R}$ is the curvature of the unperturbed horizon. According to the tidal force equation (2.90), $\Psi_0^{(1)}$ drives the shear, which is the "rate of change of the shape" of the horizon as measured by fiducial observers on the horizon [21]. Thus, it is not surprising that $\mathscr{R}^{(1)}$ can be computed directly from $\Psi_0^{(1)}$. Hartle [14] has derived the explicit formula, a consequence of Gauss' relation [35], in the Newman-Penrose formalism with the present choice of coordinates and tetrad:

$$\mathscr{R}^{(1)} = -4\mathrm{Im}\left[\frac{(\bar{\delta} + 2\pi - 2\alpha)(\bar{\delta} + \pi - 4\alpha) + 2\epsilon\lambda}{\omega(i\omega + 2\epsilon)}\right]\Psi_0^{(1)}, \tag{2.91}$$

where ω is the frequency of the perturbation. When a Schwarzschild black hole is perturbed by a distant moon in a slow, circular, orbit with angular velocity Ω, then $\omega = 2\Omega$.

2.D.2 Newman-Penrose quantities for Kerr spacetimes

Finally, to facilitate our comparison to Hartle's results, we here list the relevant Newman-Penrose quantities for the Kerr spacetime [Eq. (2.53)] using Hartle's choice [14] of coordinates and tetrad. In the limit $a = 0$, Hartle's tetrad and spin coefficients reduce to those listed in the previous subsection.

The null tetrad vectors [using the notation $e^\mu = (e^{\tilde{V}}, e^r, e^\theta, e^{\tilde{\phi}})$] are

$$\ell^\mu = \left(1, \frac{r^2 - 2Mr + a^2}{2\,(r^2 + a^2)}, 0, \frac{a}{r^2 + a^2}\right), \tag{2.92a}$$

$$\begin{aligned} n^\mu = {}& \left(0, -\frac{2(a^2 + r^2)}{2r^2 + a^2 + a^2\cos 2\theta}, 0, 0\right) + \frac{-a^2 + a^2\cos 2\theta}{2\,(a^2 + 2r^2 + a^2\cos 2\theta)}\ell^\mu \\ & + \frac{-a\sin\theta}{\sqrt{2}\,(ir + a\cos\theta)} m^\mu + \frac{-a\sin\theta}{\sqrt{2}\,(-ir + a\cos\theta)}\bar{m}^\mu\,, \end{aligned} \tag{2.92b}$$

$$m^\mu = \left(0, -\frac{a\sin\theta\left(r^2 - 2Mr + a^2\right)}{2\sqrt{2}\,(r^2 + a^2)\,(-ir + a\cos\theta)}, \frac{1}{\sqrt{2}\,(r + ia\cos\theta)}, \frac{(ir + a\cos\theta)\csc\theta}{\sqrt{2}\,(r^2 + a^2)}\right), \tag{2.92c}$$

$$\bar{m}^\mu = \left(0, -\frac{a\sin\theta\left(r^2 - 2Mr + a^2\right)}{2\sqrt{2}\,(r^2 + a^2)\,(ir + a\cos\theta)}, \frac{1}{\sqrt{2}\,(r - ia\cos\theta)}, \frac{(-ir + a\cos\theta)\csc\theta}{\sqrt{2}\,(r^2 + a^2)}\right). \tag{2.92d}$$

Then, one can compute the spin coefficients for this tetrad from Eqs. (2.85a)–(2.85f):

$$\kappa = \sigma = 0, \qquad \lambda = O(a^2), \qquad \nu = O(a^2), \tag{2.93a}$$

$$\tau = \frac{-i(2M+r)\sin\theta a}{2\sqrt{2}r^3}\,, \qquad \pi = \frac{i(4M+r)\sin\theta a}{2\sqrt{2}r^3}\,, \tag{2.93b}$$

$$\gamma = \frac{-i\cos\theta a}{2r^2} + O(a^2)\,, \qquad \epsilon = \frac{M}{2}\frac{r^2-a^2}{(r^2+a^2)^2} = \frac{M}{2r^2} + O(a^2)\,, \tag{2.93c}$$

and

$$\rho = -\frac{r-2M}{2r^2} - \frac{i(r-2M)\cos\theta a}{2r^3} + O(a^2)\,, \tag{2.93d}$$

$$\mu = -\frac{1}{r} + O(a^2)\,, \tag{2.93e}$$

$$\alpha = \frac{-\cot\theta}{2\sqrt{2}r} - \frac{i[-3M+(2M+2r)\cos 2\theta]a}{4\sqrt{2}r^3\sin\theta} + O(a^2)\,, \tag{2.93f}$$

$$\beta = \frac{\cot\theta}{2\sqrt{2}r} - \frac{i[M+r+(r-M)\cos 2\theta]a}{4\sqrt{2}r^3\sin\theta} + O(a^2)\,. \tag{2.93g}$$

The directional derivatives are then given by Eq. (2.84).

Using the Kerr metric [Eq. (2.53)] and Hartle's choice for the tetrad [Eqs. (2.92a)–(2.92d)], one can compute the curvature for Kerr and read off the curvature scalars via Eqs. (2.87a)–(2.87e):

$$\Psi_0 = \Psi_1 = 0\,, \qquad \Psi_2 = -\frac{M}{(r-ia\cos\theta)^3}\,, \tag{2.94a}$$

$$\Psi_3 = -\frac{3iaM\sin\theta}{\sqrt{2}\,(r-ia\cos\theta)^4}\,, \qquad \Psi_4 = \frac{3ia^2M\sin^2\theta}{(ir+a\cos\theta)^5}\,. \tag{2.94b}$$

The tidal force equation (2.90) relates $\Psi_0^{(1)}$ to $\sigma^{(1)}$. The correction to the scalar curvature of the horizon, $\mathscr{R}^{(1)}$, is given by Eq. (2.91). For a stationary moon perturbing a slowly rotating Kerr black hole, the frequency of the perturbation is $\omega = -2\Omega_H = -8M^2\Omega_H$.

Bibliography

[1] A. Abramovici, K. S. Thorne, et. al., LIGO: The Laser Interferometer Gravitational Wave Observatory. Science, 256, 325–333 (1992).

[2] K. S. Thorne, in *Proceedings of the Snowmass 94 Summer Study on Particle and Nuclear Astrophysics and Cosmology*, edited by E. W. Kolb and R. Peccei (World Scientific, Singapore, 1995), p. 398, gr-qc/9506086.

[3] F. D. Ryan, Phys. Rev. D **52**, 5707 (1995).

[4] The word "bothrodesy" was coined by Sterl Phinney, and he first used it in a seminar at Caltech on June 8, 2001.

[5] E. S. Phinney, *LISA Science Requirements*, Presentation to the LISA International Science Team [LIST] (December 12, 2001), available at the website of LIST Working Group 1: `http://www.tapir.caltech.edu/~listwg1`.

[6] J. R. Gair, L. Barack, T. Creighton, C. Cutler, S. L. Larson, E. S. Phinney, and M. Vallisneri, Class. Quant. Grav. **21**, S1595 (2004), gr-qc/0405137.

[7] L. S. Finn and K. S. Thorne, Phys. Rev. D **62**, 124021 (2000).

[8] K. S. Thorne, in *The Future of Theoretical Physics and Cosmology*, edited by G. Gibbons, E. P. Shellard, and S. J. Rankin (Cambridge University Press, 2003), Chap. 5.

[9] K. S. Thorne, private communication.

[10] M. Colpi, S. L. Shapiro, and I. Wasserman, Phys. Rev. Lett. **57**, 2485 (1986).

[11] F. D. Ryan, Phys. Rev. D **55**, 6081 (1996).

[12] T. D. Lee, Phys. Rev. D **35**, 3637 (1987).

[13] J. B. Hartle, Phys. Rev. D **8**, 1010 (1973).

[14] J. B. Hartle, Phys. Rev. D **9**, 2749 (1974).

[15] S. A. Teukolsky, Phys. Rev. Lett. **29**, 1114 (1972).

[16] G. H. Darwin, Philos. Trans. R. Soc. (Pt. I) **170**, 1 (1879).

[17] K. S. Thorne and J. B. Hartle, Phys. Rev. D **31**, 1815 (1985).

[18] W. M. Suen, Phys. Rev. D **34**, 3633 (1986).

[19] We follow the same notation as in Ref. [22].

[20] E. Poisson, Phys. Rev. D **70**, 084044 (2004).

[21] K. S. Thorne, R. Price, and D. MacDonald, *Black Holes: The Membrane Paradigm* (Yale University Press, New Haven, 1986).

[22] K. S. Thorne, Rev. Mod. Phys. **52**, 299 (1980).

[23] T. Regge and J. A. Wheeler, Phys. Rev. **108**, 1063 (1957).

[24] F. J. Zerilli, Phys. Rev. D **2**, 2141 (1970).

[25] L. Edelstein and C.V. Vishveshwara, Phys. Rev. D **1**, 3514 (1970).

[26] E. Poisson and M. Sasaki, Phys. Rev. D **51**, 5753 (1995).

[27] Erdélyi et al., *Higher Transcendental Functions*, vol. I (McGraw-Hill, New York, 1953).

[28] X.-H. Zhang, Phys. Rev. D **31**, 3130 (1985).

[29] C. Misner, K. S. Thorne, and J. A. Wheeler, *Gravitation* (W. H. Freeman and Company, New York, 1973).

[30] W. M. Suen, Phys. Rev. D **34**, 3617 (1986).

[31] E. Newman and R. Penrose, J. Math. Phys. **3**, 566 (1962).

[32] S. Chandrasekhar, *The Mathematical Theory of Black Holes* (Oxford University Press, Oxford, 1985).

[33] R. H. Price and K. S. Thorne, Phys. Rev. D **33**, 915 (1986).

[34] S. Teukolsky, PhD Thesis, Caltech, 1973.

[35] S. Kobayashi and K. Nomizu, *Foundation of Differential Geometry*, vol. II (Interscience, New York, 1963).

Chapter 3

Gravitational Waves from Intermediate-mass-ratio Inspirals for Ground-based Detectors

Early in the next decade, Advanced LIGO and its international partners are anticipated to achieve a much higher detection sensitivity and broader sensitivity band than their first-generation counterparts have today, and thereby should increase the volume of the universe searched a thousand-fold or more. These improvements will make it possible for the ground-based detectors to search for new sources of gravitational waves, including those from neutron stars and stellar mass black holes spiraling into intermediate-mass ($M \sim 50 M_\odot$ to $350 M_\odot$) black holes. The event rate for such *intermediate-mass-ratio inspirals* (IMRIs) is estimated to be $\sim$ 10–30 per year. It is conceivable that the central body of an IMRI can be some other type of general relativistic object (e.g. a boson star or a naked singularity). In this chapter we give an overview of the prospects for using Advanced LIGO to detect IMRI waves, and the possibility to use IMRI waves to probe the properties of the IMRIs' central bodies — e.g., $\dot{E}_{\rm body}$ and $\dot{L}_{\rm body}$, the tide-induced energy and angular momentum transfer (*tidal coupling*) from the orbit to the central body. To estimate Advanced LIGO's measurement accuracy for tidal coupling, we construct 3.5PN-Teukolsky waveforms for circular inclined orbits. Our study shows that at signal-to-noise ratio 10, the accuracy of measuring tidal coupling $\Delta\dot{E}_{\rm body}$ is roughly a few percent of the gravitational energy flux to infinity. This suggests that Advanced LIGO will be able to determine with modest but interesting accuracy whether a source's tidal response is in accord with that of a Kerr black hole, and perform interesting searches for non-Kerr central bodies.

Much of the research described in this chapter underlies portions of the manuscript [1] by D.A. Brown, H. Fang, J.R. Gair, C. Li, G. Lovelace, I. Mandel , and K.S. Thorne, Gravitational waves from intermediate-mass-ratio inspiral for ground based detectors, gr-qc/0612060, submitted to Phys. Rev. Lett. This chapter's implementation of the Manko-Novikov metric and its study of orbital periapse precession in that metric (Appendix A) underlies portions of a manuscript [2] by J.R. Gair, C. Li, G. Lovelace, I. Mandel, and H. Fang, in preparation. Some of the prose in this chapter is adapted from these two papers.

3.1 Introduction and overview

3.1.1 Advanced LIGO and IMRIs

After decades of development, first-generation interferometric gravitational-wave detectors, such as the American LIGO detectors and the French-Italian VIRGO detector, are now carrying out wave searches at or near their design sensitivities. The most promising sources of gravitational waves for this network are the late stages of inspiral and coalescence of binaries composed of black holes (BHs) and/or neutron stars (NSs). Current searches are targeting objects with masses no larger than $40M_\odot$—specifically: NS binaries with masses ~ 1–$3\,M_\odot$, BH binaries with masses ~ 3–$40\,M_\odot$, and NS-BH binaries with components in these mass ranges [3, 4]. The proposed Advanced LIGO interferometers [5, 6, 7] are scheduled for construction in the near future and by $\sim$ 2014 will further improve the detection sensitivity by more than a factor 10 over the entire initial LIGO frequency band, thereby enlarging the observable distance by a factor $\gtrsim 10^3$. Advanced LIGO will also widen the initial sensitivity band by pushing the low frequency end to $\sim$ 10Hz and high frequency limit to $\sim$ 1000Hz, opening up possibilities for observations of new gravitational wave sources.

Evidence from ultra-luminous X-ray sources and from the dynamics of globular clusters suggests that there exists a population of intermediate mass black holes (IMBHs) with masses in the range $\sim 10^2$–$10^4\,M_\odot$ [8]. Gravitational waves from the inspiral and coalescence of a NS or small BH into an IMBH with mass ~ 50–$350M_\odot$[1] will lie in the frequency band of Advanced LIGO and its partners. These *intermediate-mass-ratio inspirals* (IMRIs) are analogous to the extreme-mass-ratio inspirals (EMRIs)[2] targeted by LISA, the planned space-based gravitational wave observatory [9].

Core-collapsed globular clusters are the most likely locations for IMRI sources, since they may contain IMBHs and a significant number of stellar mass BHs and NSs [8]. Numerical simulations show that it is plausible to grow IMBHs with masses up to $M_{\rm max} \sim 350\,M_\odot$ through a series of mergers in the core of a cluster [10]. Phinney has suggested the following estimation for an upper limit on the rate of IMRIs in globular clusters [11]: assume that each cluster has a black hole that grows from $\sim 50M_\odot$ to $\sim 350M_\odot$ by capturing objects of mass m in 10^{10} years; core-collapsed clusters have a space density of 0.7 Mpc^{-3}, which gives an estimated IMRI rate of $\sim 0.7\times(300M_\odot/m)\times 10^{-10}\,\mathrm{Mpc}^{-3}\mathrm{yr}^{-1}$. Based on this rate, Mandel et al. [12] estimate that Advanced LIGO can have as much as $\sim$ 10–30 IMRI detections per year—although the number may be a factor of 10 smaller, if one includes a more realistic model of cluster dynamics [8].

With an open mind, it is both reasonable and instructive to consider the possibility that the central body of an IMRI (or EMRI) is not a black hole, but some other type of general relativistic object, e.g. a boson star or a naked singularity [13]. This possibility raises the question of whether the emitted IMRI (EMRI) waves will be informative enough to tell different objects apart. In the early 1990s, Thorne [14, 15] speculated that when a small object spirals into a massive, compact central body, the emitted gravitational waves will carry

---

[1] $M_{\rm max} \sim 350M_\odot$ is set by requiring that we see at least 30 wave cycles above the 10 Hz low frequency cutoff of Advanced LIGO.

[2] The extreme-mass-ratio inspiral (EMRI) targeted by LISA typically consists of a (super)massive black hole with mass ranging between 10^6–$10^9M_\odot$ and a stellar-mass compact object, such as a neutron star.

encoded in themselves the details of the massive body's metric. In 1995, Ryan [16] carried out a partial proof of Thorne's conjecture, showing that if the energy and momentum exchange (*tidal coupling*) between the central body and the orbit is negligible, then the EMRI waves from a nearly circular and nearly equatorial orbit contain (in principle) full details of the metric of *any* stationary, axisymmetric and reflection-symmetric object, including a Kerr black hole. Recently, Li and Lovelace [17, 18] have made generalizations to Ryan's theorem. They *argue* that as long as the central body of the IMRI/EMRI has an exterior spacetime that is stationary, axisymmetric, reflection-symmetric and asymptotically flat (SARSAF), and if the IMRI/EMRI waves remain tri-periodic [19, 20], the evolution of the waves' three fundamental frequencies and of the complex amplitudes of their spectral components will encode (in principle), (i) a full map of the central body's metric, (ii) full details of tidal coupling between the central body and the orbits, and (iii) the time-evolving orbital elements—and Li and Lovelace *prove* this is so for nearly circular, nearly equatorial orbits.

In a recent letter [1], my coauthors and I report on initial explorations of the prospects for Advanced LIGO to detect IMRI waves, and on initial study of using IMRI waves to probe the properties of the massive central body. Here in this introductory section, I shall highlight two aspects of that work. The first concerns explorations of the character of the IMRI/EMRI waves when the central body is not a black hole—more specifically when the central body deviates from a black hole by an anomalous *quadrupole moment*. The second concerns estimates of measurement accuracies with which information encoded in IMRI waves—e.g., the quadrupole moment and tidal coupling—can be extracted by Advanced LIGO. (We will describe the parameter estimation in more detail in Sec. 3.3.) Both studies serve as valuable tools to quantify the accuracy with which any observed central body has the properties predicted for a black hole, in particular: (i) the accuracies with which it obeys the black-hole no-hair theorem (its spacetime geometry is fully determined by its mass and spin and has the Kerr-metric form), and (ii) the accuracies with which its tidal coupling agrees with black-hole predictions. We can also use results from these studies to estimate the accuracy of searches for other types of central bodies—searches that could lead to a very unexpected discovery.

3.1.2 IMRI and EMRI orbital dynamics in "SARSAF" spacetimes

The spacetime metric around a Kerr black hole belongs to a larger classification of geometries that are Stationary, Axially symmetric, Reflection Symmetric about an equatorial plane, and Asymptotically Flat (SARSAF). In realistic astrophysical situations, it is reasonable to assume that the external spacetime geometry of any massive central object is SARSAF. If initially the spacetime is not axisymmetric then rotation will make it nonstationary, and gravitational-wave emission presumably will then drive it to stationarity and axisymmetry on an astrophysically small timescale; and almost all stationary, axisymmetric, self-gravitating objects that have been studied theoretically or observed in nature are reflection symmetric.

One powerful tool to characterize spacetime geometry is relativistic gravitational multipole moments. These moments are analogous of Newtonian multipole moments in Euclidean space, but differ from them because of the curvature of spacetime. Historically, Geroch [21] first developed the idea of how to define multipole moments in curved, static, asymptotically flat and empty spacetimes. Later Hansen [22], Thorne [23], and Simon and Beig [24] generalized Geroch's moments to asymptically flat, stationary spacetimes. Their definitions were equivalent to each other despite the different mathematical approaches they took. Geroch also conjectured that there is a unique correspondence between a given (stationary) spacetime and its moments, which has been supported by later studies [24, 25]. In the case of stationary, axisymmetric and asymptotically flat (SAAF) spacetimes, this unique connection has been found [26] and is intimately tied to the generation of exact solutions to the vacuum field equations.

In SARSAF spacetimes, the relativistic multipole moments reduce to two families of scalars: the "mass moments" $\{M_0, M_2, M_4, \ldots\}$ and the "current moments" $\{S_1, S_3, S_5, \ldots\}$.[3] The black-hole no-hair theorem states that the entire multipole-moment structure of a black hole spactime is determined solely by the mass and spin of the black hole (i.e., by the mass monopole $M_o \equiv M$ and current dipole $S_1 = aM$, where a is the hole's spin parameter); specifically, M_ℓ and S_ℓ are given by

$$M_\ell + i S_\ell = M(ia)^\ell, \qquad \ell = 0, 1, 2, \ldots. \tag{3.1}$$

LISA seeks to measure as many moments as possible, via EMRI waves, and determine the accuracy with which each moment satisfies this relation [27]; Advanced LIGO will do the same for IMRIs.

For IMRIs and EMRIs, the orbiting object moves along an orbit that is nearly a geodesic; gravitational radiation reaction drives it slowly from one geodesic to another. If the central body is a Kerr black hole, then: (i) each geodesic has three isolating integrals of the motion: energy E, axial component of angular momentum L_z, and Carter constant Q (and also a fourth, "trivial" isolating integral, the length of the orbit's tangent vector, which we shall not include in the counting); (ii) the emitted gravitational waves are tri-periodic [19, 20] with $h^{\mu\nu} = \mathrm{Re} \sum_{Pkmn} h^{\mu\nu}_{Pkmn} e^{i(k\Omega_\theta + m\Omega_\phi + n\Omega_r)t}$. Here the $P = +, \times$ is the polarization, and the three *principal frequencies* Ω_θ, Ω_ϕ, Ω_r, in a precise but subtle sense, are associated with the orbital motion in the polar (θ), azimuthal (ϕ) and radial (r) directions. The fundamental frequencies (Ω_θ, Ω_ϕ, Ω_r) and complex amplitudes $h^{\mu\nu}_{Pkmn}$ evolve with time as radiation reaction drives the orbit through a sequence of geodesics.

From Eq. (3.1), we expect that the leading order deviation from a black hole in an arbitrary SARSAF spacetime will be an anomalous mass quadrupole moment M_2—one that violates $M_2 = -Ma^2$. The imprints of an anomalous quadrupole moment on orbital dynamics and on the observational features of gravitational waves have therefore become an active area of study. In [28], Collins and Hughes constructed a non-spinning "bumpy black hole" metric with a small excess mass quadrupole moment (bump) and examined the properties of the corresponding equatorial geodesics. Collins and Hughes' metric construction approach was to expand the static ($S_\ell = 0$) Weyl solutions to the vacuum Einstein equations in "multipoles" of the Weyl metric function ψ (which satisfies a flat-space Laplace equation), and keep only the leading order, quadrupolar "bumpiness". Other perturbative solutions that incorporate a small anomalous quadrupole moment include:

---

[3] The odd mass moments and even current moments vanish because of the reflection-symmetry.

(i) the quasi-Kerr spacetime [29] derived by Glampedakis and Babak through a transformation of the exterior Hartle-Thorne metric [30] , (ii) the metric of a tidally perturbed spinning black hole [31] derived by Yunes and Gonzáles via the Chrzanowski procedure, and (iii) a similar family of perturbative solutions obtained by the same procedure by Lovelace and Li [2].

To survey a larger domain of SARSAF geometries (beyond small deviations from Kerr), it is necessary to find and work with families of exact solutions for SARSAF spacetimes that contain a tunable, arbitrary quadrupole moment. In Appendix 3.A, we shall delineate and implement a solution generation scheme due to Manko and Novikov [32], and use it to give the explicit form of metric functions that possess an arbitrary mass quadrupole moment.[4] We shall also explore the effect of this quadrupole moment on the periapsis precession of equatorial orbits and compare it with results from [28].

Given an exact solution for a SARSAF spacetime, it is most interesting to ask whether the third integral of motion (the Carter constant) still exists, as in a Kerr spacetime. If the third integral is lost, orbital motion may become ergodic rather than multi-periodic, which would make detection of the gravitational waves difficult. Numerical explorations show that in some cases, geodesics appear ergodic, i.e., lack a third integral. In particular, Guéron and Letelier [33] have used Poincare maps to search for ergodic geodesics in the static Erez-Rosen metric and a stationary metric representing the nonlinear superposition of a Kerr solution with a quadrupole field; Gair et al. [2] have carried out similar studies for a variant of the stationary Manko-Novikov metric [32]. These metrics all have an arbitrary mass quadrupole moment M_2, and higher moments fixed by M_2, M_o and S_1 (which is zero for Erez-Rosen). The Poincare maps in these spacetimes reveal no sign of ergodic geodesics when $M_2 < 0$ (oblate spacetimes). In some set of prolate spacetimes ($M_2 > 0$) both with spin (Manko-Novikov) and without (Erez-Rosen), there are ergodic geodesics at very small radii $r \sim$ a few M, but none at large radii. It has been found, however, that radiation reaction from gravitational wave emission drives the evolution of energy and angular momentum in a way that makes it unlikely that the ergodic geodesics could be encountered in the course of an inspiral [2]. For the non-ergodic geodesics, the spatial coordinates are multi-periodic functions of Killing time t to a numerical accuracy of 10^{-7}, and a general argument [17] based on the structure of the gravitational propagator shows that their gravitational waves will have the same kind of tri-periodic form as for Kerr black holes.

3.1.3 Overview of estimates on measurement accuracies for Advanced LIGO

Estimates have been made of the accuracy with which Advanced LIGO, via IMRI waves, can constrain deviations of the central body's quadrupole moment M_2 (Brown [34]) and its tidal coupling $\dot{E}_{\text{body}}$ (Sec. 3.3 in this chapter) from those of a Kerr black hole. In the absence of accurate waveforms (see discussions of the choice of waveform templates in Sec. 3.2.2), such estimations are done by using post-Newtonian waveforms as both signals and templates. This may introduce systematic error, but the results are expected

---

[4] There exist other types of solution generation methods and their applications. We choose to work with Manko and Novikov's formulation because of its relatively compact analytic form.

to be indicative of the accuracies Advanced LIGO can achieve.

To investigate the measurement accuracy of tidal coupling, in Sec. 3.3 we model the tidal energy transfer as $\dot{E}_{\rm body} \equiv \epsilon \dot{E}_H$. Here $\dot{E}_H$ is the energy flow into a Kerr black hole [35], and we seek to measure deviations from it parametrized by ϵ. Our source is the circular inspiral of a neutron star into a $100 M_\odot$ IMBH (under the assumption that radiation reaction has circularized the orbit [12]). The orbit is inclined to the black-hole's equatorial plane, to produce modulation that is crucial for breaking degeneracy between the IMBH spin and the parameters $\dot{E}_{\rm body}$.

We construct precessional waveforms according to Apostolatos et al. [36], using the 3.5PN orbital energy loss $\dot{E}_\infty$ (to infinity) and $\dot{E}_H$ (to the horizon) for circular equatorial orbits from [37] with corrections for small inclination angles from [38]. We restrict the orbital inclination angles to be $\lambda_L \lesssim \pi/4$, fix the central body's spin orientation, and use the Fisher matrix to estimate parameter measurement accuracies. If the central body is a black hole, then at signal-to-noise ratio (SNR) 10 and spin $q = a/M = 0.9$, we find that Advanced LIGO can typically measure ϵ to $\Delta \ln \epsilon \sim 1$ to 6 for $\lambda_L = \pi/6$. For spin $q = 0.3$, the error increases to $\Delta \ln \epsilon \sim 50$. While this error for $q = 0.3$ may seem much larger than we would like, we note that at leading order in the orbital velocity v and spin q, the black-hole energy absorption is $\dot{E}_H \simeq -\frac{1}{4} q v^5 \dot{E}_\infty$ [see Eq. (3.36b)], which predicts that $\dot{E}_H \sim 0.08\% \dot{E}_\infty$ for a $1.4 M_\odot + 100 M_\odot$ IMRI system in the Advanced LIGO band. Hence for $q = 0.3$ and $\lambda = \pi/6$, the accuracy of measuring tidal coupling is $\Delta \dot{E}_{\rm body} = \Delta \varepsilon \times \dot{E}_H \sim 50 \times 0.08\% \dot{E}_\infty$, i.e., 4% of the power radiated to infinity, an interesting accuracy for central bodies with anomalously large $\dot{E}_{\rm body}$.

These results suggest that Advanced LIGO will be able to verify with interesting accuracy that a source's properties are in accord with those of a Kerr black hole, and perform interesting searches for non-Kerr central bodies. Although Advanced LIGO's accuracies for probing the central body are far worse than LISA's (as expected, since there are a thousand fold fewer wave cycles), Advanced LIGO is likely to be operational some years before LISA. Its studies of central bodies will be a valuable precursor to LISA's EMRI science, and might possibly yield a big surprise.

3.1.4 Outline of this chapter

This chapter is organized as follows. In Sec. 3.2, we shall give initial estimates of the prospects of using LIGO to detect IMRI waves. This includes estimates of the detection range and number of wave cycles in the Advanced LIGO band. We shall also discuss the choice of available waveform templates. In Sec 3.3, we shall present detailed calculations of measurement accuracies for tidal coupling. This involves constructing restricted post-Newtonian waveforms for both circular equatorial and circular inclined orbits. The results for the parameter estimation accuracies are listed in Tables 3.2-3.4.

The main notations used in this chapter are summarized as follows. In a binary we shall use M to denote the mass of the more massive object, $q \equiv a/M = S_1/M^2$ for its dimensionless spin, μ for the mass of its compact companion, and $\nu \equiv \mu/M$ for the mass ratio. We also use $\tilde{r} \equiv r/M$ for the dimensionless orbital radius. As in the standard post-Newtonian formalism, we define the total mass $\mathscr{M} = \mu + M$, the reduced mass

$\mathfrak{m} = \mu M/(\mu + M)$, and the symmetric mass ratio $\eta = \mathfrak{m}/\mathscr{M}$. We will restrict our attention to circular orbits in this chapter, and will use F to denote the primary wave frequency: $F = \Omega_\phi/\pi$, where Ω_ϕ is the orbital angular velocity. We shall use $f_{\rm lower}$ and $f_{\rm upper}$ to indicate the lower and upper frequency limit to observe IMRI waves in the Advanced LIGO band. The lower frequency limit is taken to be $f_{\rm lower} = F_{\rm lower} = 10{\rm Hz}$; and the upper frequency is taken to be the ISCO (inner most stable circular orbit) frequency of the IMBH: $f_{\rm upper} = F_{\rm isco}$ (see Fig. 3.2 and surrounding discussions).

3.2 Initial estimates

3.2.1 Detection range

In this section, we shall estimate the detection range of Advance LIGO detectors for "canonical" IMRI sources at a prescribed signal-to-nosie ratio (SNR) by assuming the binaries move along circular equatorial orbits. Under the same assumption, we shall also estimate on the number of wave cycles that sweep through the advanced LIGO band.

The detector output, i.e., the measured gravitational-wave strain, can be written as

$$s(t) \quad = \quad h(t) + n(t)\ , \tag{3.2}$$

where $h(t)$ is the (possibly present) gravitational-wave signal and $n(t)$ the detector noise. The detector output of the gravitational-wave signal $h(t)$ is a linear combination of the waveform from the source (h_+ and $h_\times$ in TT gauge) multiplied by the detector beam-pattern functions (F_+ and $F_\times$). It can be written as (see, e.g., Eq. (103) in Ref. [39])

$$h(t) = F_+(\theta_N, \phi_N, \psi_N)\, h_+(t\,; \iota, \beta) + F_\times(\theta_N, \phi_N, \psi_N)\, h_\times(t\,; \iota, \beta)\,, \tag{3.3}$$

where the angles ι and β describe the direction towards the detector in the source's preferred local axes (see Figs. 9.2 and 9.9 in Ref. [39] for illustrations); the beam-pattern functions are given by

$$F_+(\theta_N, \phi_N, \psi_N) \quad = \quad \frac{1}{2}(1 + \cos^2\theta_N)\cos 2\phi_N \cos 2\psi_N - \cos\theta_N \sin 2\phi_N \sin 2\psi_N\ , \tag{3.4a}$$

$$F_\times(\theta_N, \phi_N, \psi_N) \quad = \quad \frac{1}{2}(1 + \cos^2\theta_N)\cos 2\phi_N \sin 2\psi_N + \cos\theta_N \sin 2\phi_N \cos 2\psi_N\ . \tag{3.4b}$$

Here the angles θ_N and ϕ_N describe the direction of the source with respect to the detector; and ψ_N characterizes the orientation of the polarization axes (see Fig. 3.7 in Appendix B).

We shall assume that the detector noise $n(t)$ follows a Gaussian distribution, and is statistically characterized by the autocorrelation function $C_n(\tau) = \langle n(t)n(t + \tau)\rangle$, where angular brackets denote a time average.

The one-sided noise spectral density is the Fourier transform of the autocorrelation function

$$S_n(f) \quad = \quad 2\int_{-\infty}^{\infty} C_n(\tau)\, e^{2\pi i f \tau} d\tau\,, \qquad f > 0\,. \tag{3.5}$$

In this chapter, we shall adopt the numerical Advanced LIGO strain noise spectrum from [40], and simplify it by means of an analytic fit.[5] Our fit to the one-sided spectral density function $S_n(f)$ is given by [34]

$$\begin{aligned} S_n(f) \quad = \quad & 1.6\times 10^{-49}\Big[300\,(f/15)^{-17} + 7\,(f/50)^{-6} + 24\,(f/90)^{-3.45} - 3.5\,(f/300)^{-2} \\ & + \Big(561/5 - (33/10)(f/50)^2 + (22/30)(f/100)^4\Big)\Big(1 + (7/3)(f/1000)^2\Big)^{-1}\Big]\,\mathrm{Hz}^{-1}. \end{aligned} \tag{3.6}$$

Figure 3.1 shows the fitted noise strain $\sqrt{S_n(f)}$ as well as the simulation data: the two match each other well.

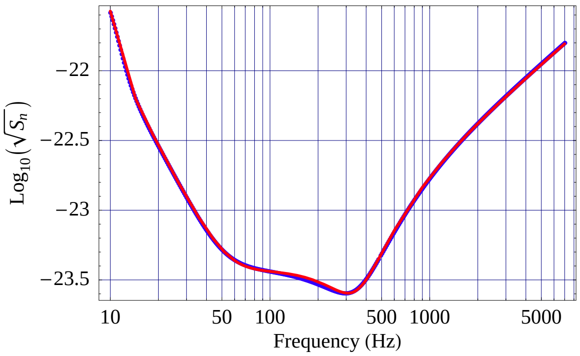

Figure 3.1: Equivalent strain noise versus frequency for the nominal Advanced LIGO interferometer, using fused silica test masses; the signal recyling parameters are tuned to optimize the NS-NS inspiral range. Blue dots are drawn according to numeric data from [40]. The red curve represents the analytic fit defined in Eq. (3.6).

For ground-based interferometers, the amplitude of the expected IMRI gravitational wave signals will be close to, or more likely, below the instrumental noise level in the detector output data. To distinguish the signal contribution from the noise background, a pattern recognition technique of matched filtering is widely used in LIGO data analysis. To perform matched filtering, the detector output $s(t)$ is first convolved against a Wiener optimal filter $w(t)$ whose Fourier transform is proportional to $1/S_n(f)$. This procedure is meant to suppress the those frequency components of the output at which the detector noise is dominant. The filtered data are then matched to a bank of theoretical template waveforms $\{h^T(t;\alpha)\}$, each characterized by a different parameter set α. The SNR for a particular waveform template is defined by (cf. Eq. (1.2) in Ref. [43])

$$\left(\frac{S}{N}\right)_{h^T} \quad = \quad \frac{\int h^T(t)\, w(t-\tau)\, h(\tau)\, d\tau dt}{\mathrm{rms}\int h^T(t)\, w(t-\tau)\, n(\tau)\, d\tau dt}\,, \tag{3.7}$$

---

[5] The LIGO-II noise curve fit in Owen and Sathyaprakash [41], which is often used by theorists, predates the work of Buonanno and Chen [42], which has changed the noise curves significantly. Reference [41] also assumes sapphire mirrors, which are no longer used; and it ignores coating thermal noise—so its thermal noises are incorrect. This has motivated us to construct the new fit, Eq. (3.6).

where "rms" means root-mean-square value of the denominator and the average is taken over an ensemble of realizations of the noise $n(t)$. When the template waveform matches the incoming gravitational-wave signal exactly, the SNR becomes

$$\left(\frac{S}{N}\right)^2 = 4\int_0^\infty \frac{|\tilde{h}(f)|^2}{S_n(f)} df\,. \tag{3.8}$$

In the following discussion of detection ranges at a prescribed SNR, we shall refer to Eq. (3.8) as our definition. It can be shown that the SNR is approximately proportional to the square-root of the number of wave cycles contained in the data, and is inversely proportional to the distance between the source and the detector.

For sources at a fixed distance r from the detector, the squared signal-to-noise ratio [Eq. (3.8)] averaged over sky positions and source orientations is given by[6]

$$\left(\frac{S}{N}\right)^2_{\text{avg}} = 4\langle F_+^2(\theta_s,\phi_s,\psi_s)\rangle \int_0^\infty \frac{\langle|\tilde{h}_+(f)|^2 + |\tilde{h}_\times(f)|^2\rangle}{S_n(f)} df\,, \tag{3.9a}$$

where $\tilde{h}_{+,\times}(f)$ are the Fourier transformation of the time-domain waveform $h_{+,\times}(t)$. The average over the beam-pattern function (i.e., average over sky positions), in the case of LIGO's L-shaped interferometers, is (Eq. (110) in [39])

$$\langle F_+^2\rangle = \langle F_\times^2\rangle = \frac{1}{5}\,. \tag{3.9b}$$

The average over the source orientation can be written as (Eq. (44) in [39])

$$\langle|\tilde{h}_+|^2 + |\tilde{h}_\times|^2\rangle = \frac{\pi}{12}\left(\frac{\mathfrak{m}}{r}\right)^2 \frac{\mathscr{M}^3}{\mathfrak{m}} \frac{1}{(\pi\mathscr{M}f)^{7/3}}\,, \tag{3.9c}$$

where $\mathscr{M} = M+\mu$ is the total mass of the binary and $\mathfrak{m} = M\mu/(M+\mu)$ is the reduced mass. Note that Eq. (3.9c) contains only the leading quadrupole-radiation contribution to the evolution of the waveform strength. In computing the integration in Eq. (3.9a), we shall take the starting frequency to be $f_{\text{lower}} = F_{\text{lower}} = 10$Hz, the lower cut-off frequency of advanced LIGO interferometers; and take the ending frequency to be $f_{\text{upper}} = F_{\text{isco}} = \Omega_{\text{isco}}/\pi$, where Ω_{isco} is the orbital angular frequency at the innermost-stable-circular-orbit (isco) of the central black hole. The formula to compute Ω_{isco} (and hence F_{isco}) can be found from, e.g, Eq. (3.20)-(3.21) in [44]. In Fig. 3.2, we plot F_{isco} as a function of the black-hole spin for three different black-hole masses. It can be seen that F_{isco} increases sharply as the black-hole spin approaches its maximal value 1, which has to do with the fact that the ISCO radius shrinks for rapidly spinning holes, and can get very close to the horizon radius r_H (the two become $r_{\text{isco}} = r_H = M$ when $a/M = 1$).[7]

Using the above formulas we have computed the SNR curves shown in Fig. 3.3—angle-averaged SNR as a function of BH mass M for an inspiraling $\mu = 1.4M_\odot$ NS at a distance $r = 100$Mpc from Earth as observed

---

[6] This is obtained by combining Eq. (26) and (29) in [39]. Note that there is a factor-of-2 error in Eq. (29) in [39].

[7] The proper distance between the isco and horizon approaches infinity as $a \to M$, but radii become the same. See Fig. 2 in Ref. [45].

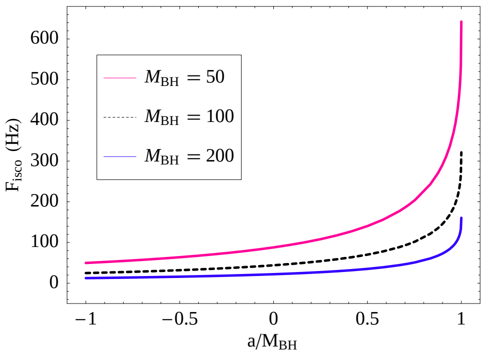

Figure 3.2: The ISCO wave frequency as a function of black-hole spin.

by Advanced LIGO. (Note that core-collapsed globular clusters, which are the most likely location for IMRIs, have a space density of $\sim 0.7{\rm Mpc}^{-3}$.) The four curves shown in Fig. 3.3 correspond to different black hole spin parameters. The figure shows that for rapidly spinning black holes with $q \gtrsim 0.9$, the accumulated SNR can reach ~ 40 to ~ 50 at 100Mpc; even for slowly rotating holes $q \lesssim 0.3$, the accumulated SNR can be ~ 20 to ~ 30.

3.2.2 Choice of IMRI waveform templates

To search for IMRI signals with matched filtering requires (detection) templates of sufficient accuracy that the mismatch between the template and signal does not cause a large loss in event rate. We will also need sufficiently good (physical) templates to estimate the number of wave cycles in the Advanced LIGO band (Sec. 3.2.3 and Sec. 3.2.4) and to estimate the measurement accuracy of the IMRI parameters (Sec. 3.3). Here we shall discuss the choice of IMRI waveform templates.

IMRIs, as their name suggests, fall in the interesting (yet less well-known) intermediate domain between EMRIs and comparable-mass inspirals. The canonical tool for studying EMRI waveforms is the Teukolsky formalism for the black hole perturbation theory, which treats the full spacetime as being almost identical to the background black hole spacetime, except for small perturbations from the presence of the compact object. The perturbations are proportional to the mass ratio $\nu = \mu/M \ll 1$ and are determined by the energy-momentum tensor of the compact object via the Einstein field equations. If we idealize the compact object as a non-spinning test particle, then its energy-momentum tensor is solely determined by μ and its trajectory. Driven by the emission of gravitational radiations [leading-order $\mathcal{O}(\nu^2)$], the trajectory of the test particle is a gradual migration from one (nearly) geodesic orbit—characterized by some orbital parameters—to another one with a different set of parameters. For EMRIs and IMRIs, the orbital evolution happens on a radiation reaction time scale $T_{\rm RR} \sim r^4/\mu M^2$, whereas the characteristic time scale of orbital motion is $T_{\rm orb} \sim r^{3/2}/M^{1/2}$ (r is the orbital radius). The small mass ratio of therefore implies that the orbital parameters evolve on a much longer time scale than the orbital period: $T_{\rm orb}/T_{\rm RR} \sim \mu M^{3/2}/r^{5/2} < \mu/M \ll 1$ (adiabaticity condition),

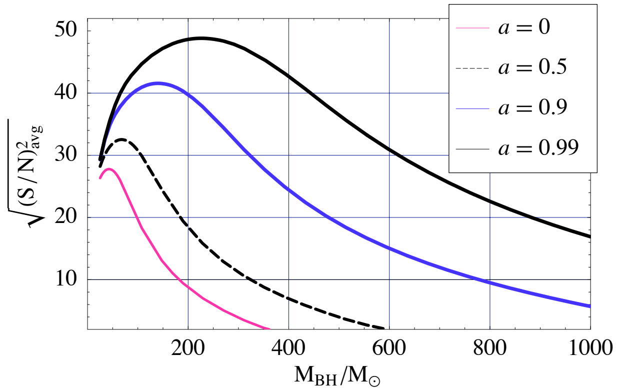

Figure 3.3: Square-root of $\langle (S/N)^2 \rangle$ for IMRI waves from an inspirling $1.4M_\odot$ NS at a distance of 100Mpc as a function of the central black hole's mass. In computing the integral Eq. (3.9a), we take the starting frequency to be 10Hz (the lower cut-off frequency of the Advanced LIGO interferometers), and the ending frequency to be the wave frequency ($F_{\rm isco}$) corresponding to the innermost-stable-circular-orbit (isco) of the central black hole. The formula to compute $F_{\rm isco}$ can be inferred from, e.g, Eq. (3.20)-(3.21) in [44]. The ISCO wave frequency as a function of spin is shown in Fig. 3.2 for three different masses. The estimated square-root of $\langle (S/N)^2 \rangle$ is inversely proportional to the IMRI distance r, and scales approximately proportional to the mass μ of the small object.

and that the full inspiral can be approximated as a flow through a sequence of geodesic orbits.

To date, the leading-order adiabatic EMRI waveforms are computed via the so-called ”Radiation Reaction without Radiation Reaction Forces” program [46, 47] for special classes of orbits. It involves computing the time-averaged rates of the change of the constants of motion (E, L_z) from the leading-order $\mathcal{O}(\nu^2)$ graviational-wave fluxes. When augmented with Mino's [48] adiabatic self-force rule to evaluate the (time-averaged) rate of change of the Carter constant, this program can be used to evolve generic orbits [49]. However, it is also important to determine the effect of conservative finite mass ratio corrections $\mathcal{O}(\nu^2)$ (sometimes called “non-dissipative self-force effects”), which contribute to the secular change in orbital (and waveform) phase but do not change the constants of motion. The self-force issue is more pronounced for the IMRIs , whose mass ratio lies in the range $\sim 10^{-3}$ to $\sim 10^{-2}$, than for LISA's EMRIs with $\mu/M \sim 10^{-6}$. This is because, if we ignore the $\mathcal{O}(\nu^2)$ conservative self-force, we can only accurately track the phase of the waveform up to $O(M/\mu)$ cycles [50].

By constrast, the standard post-Newtonian (PN) formulation, the tool for studying comparable-mass inspirals, has built-in self-force ingredients. It is based on the expansion in the parameter $\mathscr{M}/r$ $(\ll 1)$ and the symmetric mass ratio $\eta = \mathfrak{m}/\mathscr{M}$ $(0 < \eta \leq 1/4)$. For circular equatorial orbits and nonspinning bodies, the orbital energy and the energy flux have been determined by PN-expansion techniques up to 3.5PN order [51], and the spin effects have been calculated up to 2.5PN order [16, 52, 53, 54]. To assess the importance of the $\mathcal{O}(\nu^2)$ conservative self-force and the efficiency of adiabatic Teukolsky waveforms as search templates for IMRI waves, Brown [34] has computed the mismatch between restricted PN stationary phase teimplates that contain all known η terms (contributed by the leading-order radiation reaction as well as conservative self-force), and the same templates containing only the $\mathcal{O}(\eta^{-1})$ terms (i.e. the terms of leading order in the waves' phase evolution; contributed only by the leading-order radiation reaction). He finds that the mismatch falls to less than 10% in all except the most rapid spinning cases. Therefore it is reasonable to believe that the adiabatic Teukolsky waveforms will lose no more than $\sim$ 10% of the SNR due to the absence of $\mathcal{O}(v^2)$ conservative self-force terms (corresponding to no more than $\sim$ 30% loss of event rate).

Although the PN formulation is capable of including higher-order contributions from the self-force, it can become inaccurate at a rather early stage after the IMRI wave enters the Advanced LIGO band at $f_{\rm lower} =$ 10Hz. In [55], Brady et al. analyzed the failure point of the PN expansion (defined as the stage when the PN series carried to 3PN makes a 2% error in the energy loss rate) during the binary inspiral phase. They estimated that the PN failure point is at the orbital speed $v \equiv (\pi \mathscr{M} F)^{1/3} \simeq 0.3$, corresponding to separation distance $r \simeq 10\mathscr{M}$. This failure causes problem for IMRIs in the Advanced LIGO band.

Table 3.1 lists the basic profile for three canonical IMRIs, assuming the system evolves along circular equatorial orbits. This includes: (i) the separation of the neutron star and the central black hole when the wave frequency reaches 10Hz; (ii) the wave frequency F_{10M} when their separation is $10M$; (iii) the ISCO frequency of the central black hole; (iv) the ratio ($\Delta N_{>10M}\%$) of the wave cycles spent between 10Hz and $10M$, to the total wave cycles spent in the advanced LIGO band (i.e., from $f_{\rm lower} = 10$Hz to $f_{\rm upper} = F_{\rm isco}$) [The calculation of (iv) is based on Eq. (3.14)]. Table 3.1 shows that for central black holes with masses $M \gtrsim 200 M_\odot$, very few wave cycles (if any) are spent at $r > 10M$ in the Advanced LIGO band. By contrast, for black holes with masses $M \sim$ 50-100$M_\odot$, a sizable portion of the wave cycles is spent at $r > 10M$. However, this will not bring a proportional increase in the accumulated SNR in the corresponding frequency band (i.e., from $f_{\rm lower}$ to F_{10M}). Because the noise spectrum is steep at low frequencies (~10Hz).

a/M	$M(M_\odot)$	$r_{\rm 10Hz}$ (M)	$F_{\rm 10M}$ (Hz)	$F_{\rm isco}$ (Hz)	$\Delta N_{>10M}\%$
0	50	25.6	40.9	87.9	92.6%
	100	16.1	20.4	44.0	75.5%
	200	10.1	10.2	22.0	4.8%
0.9	50	25.4	39.7	291.4	90.0%
	100	16.0	19.9	145.7	68.6%
	200	10.0	9.9	72.8	–

Table 3.1: Profile of IMRIs in advanced LIGO band. The column "$\Delta N_{>10M}\%$" lists the ratio of the wave cycles spent between 10Hz and $10M$, to the total wave cycles spent in the advanced LIGO band (i.e., from 10Hz to $F_{\rm isco}$) [The calculation of is based on Eq. (3.14)]. For descriptions of other columns, see text above.

The above argument suggests that both the (adiabatic) Teukolsky waveforms and the standard PN waveforms have their limitations. By comparison, the Teukolsky waveforms should by far the most accurate templates available for IMRIs. In the following two subsections, we shall mainly use results from the Teukolsky formalism (in conjunction with 2PN formulas) to estimate the number of IMRI wave cycles in the Advanced LIGO band.

3.2.3 Number of wave cycles in the Advanced LIGO band

In this section we shall estimate the number of wave cycles of typical NS-IMBH binaries in the Advanced LIGO band. We shall use both the post-Newtonian and black hole perturbation formalisms to make the assessment. Of course, the perturbation results will be more accurate than the PN results.

According to standard post-Newtonian calculations, the evolution of the orbital frequency Ω can be written up to 2PN order as [53]

$$\begin{aligned}\left(\frac{d\Omega}{dt}\right)_{\rm 2PN} &= \frac{96}{5}\eta\,\Omega^2(\mathscr{M}\Omega)^{5/3}\left[1-\left(\frac{743}{336}+\frac{11}{4}\eta\right)(\mathscr{M}\Omega)^{2/3}+(4\pi-\beta)(\mathscr{M}\Omega)\right.\\ &\left.\quad+\left(\frac{34103}{18144}+\frac{13661}{2016}\eta+\frac{59}{18}\eta^2+\sigma_{\rm ss}+\sigma_{\rm qm}+\frac{1}{16}q^2\right)(\mathscr{M}\Omega)^{4/3}\right], \qquad (3.10a)\end{aligned}$$

where $q = a/M$ is the dimensionless spin parameter for the central black hole (the q^2-term in Eq. (3.10a) was derived in [16]). The quantites β and $\sigma_{\rm ss}$ characterize the “spin-orbit” and “spin-spin” coupling (see Eq. (2)-(3) in [53]; Blanchet et al. have recently computed the spin-orbit coupling effect to 2.5PN order [54]). The quantity $\sigma_{\rm qm}$ represents the influence from the quadrupole moment. For the IMRI problem that interests us, we shall make the simplification of ignoring the internal structure of the compact object—we shall treat it as a point particle with no spin ($\sigma_{\rm ss} = 0$). Further, when evaluating β and $\sigma_{\rm qm}$, we shall take the limit $\eta \to 0$ and thus obtain

$$\beta = \frac{113}{12}\,q\,, \qquad \sigma_{\rm qm} = -5M_2/M^3 = 5q^2. \qquad (3.10b)$$

For circular equatorial orbits, the frequencies of emitted gravitational waves are various harmonics of the orbital frequency. The dominant wave frequency F is due to the quadrupole radiation and is related to the orbital frequency by $F = \Omega/\pi$. Its contribution to the phase evolution of the gravitational wave is

$$\begin{aligned}\Phi_{\rm 2PN}(F) &= \phi_o-\frac{1}{16}(\pi\mathscr{M}_{\rm chirp}F)^{-5/3}\left[1+\frac{5}{3}\left(\frac{743}{336}+\frac{11}{4}\eta\right)(\pi\mathscr{M}F)^{2/3}-\frac{5}{2}\left(4\pi-\frac{113}{12}q\right)(\pi\mathscr{M}F)\right.\\ &\left.\quad+5\left[\frac{3058673}{1016064}+\frac{5429}{1008}\eta+\frac{617}{144}\eta^2-\left(\frac{1}{16}q^2+5q^2\right)\right](\pi\mathscr{M}F)^{4/3}\right], \qquad (3.11a)\end{aligned}$$

where the chirp mass is defined as

$$\mathscr{M}_{\rm chirp} \equiv \eta^{3/5}\mathscr{M}\ . \qquad (3.11b)$$

Hence the 2PN prescription for the number of wave cycles between $F_{\rm lower} = 10$Hz and the ISCO is

$$N_{\rm 2PN} = \frac{1}{2\pi}\left[\Phi_{\rm 2PN}(F_{\rm isco})-\Phi_{\rm 2PN}(F_{\rm lower})\right]. \qquad (3.12)$$

Next we shall use results from numerically integrating the Teukolsky equation to compute the number of wave cycles, which should be more accurately than the PN formula (3.12). In [44], Finn and Thorne studied the gravitational emission from EMRIs on circular equatorial orbit. Their calculations were based on the Teukolsky-Sasaki-Nakamura (TSN) formalism, and the results were tabulated as a set of functions representing relativistic corrections to the lowest order Newtonian formulas. For example, the number of orbits remaining until the ISCO is written as[8]

$$N_{\rm orb}(F) = \frac{1}{2\pi}\int_{\ln\Omega}^{\ln\Omega_{\rm isco}} \frac{d\Phi}{d\ln\Omega}\, d\ln\Omega = \frac{5}{192\pi}\left(\frac{M}{\mu}\right)\int_{\ln\Omega}^{\ln\Omega_{\rm isco}} (M\Omega)^{-5/3}\mathcal{N}\, d\ln\Omega\,. \tag{3.13}$$

Here $\mathcal{N}$ is the relativistic correction to $\Omega^2/\dot{\Omega} = d\Phi/d\ln\Omega$ (see Eq. (3.2) in [44]). When $\mathcal{N}$ is set to unity, equation (3.13) reduces to the familiar low-orbital-velocity result contributed solely by the quadrupole radiation. Since we only consider the harmonic $m = 2$ component of the gravitational wave, the number of wave cycles until the isco is

$$N_{\rm TSN}(F) = 2\times N_{\rm orb}(F)\,. \tag{3.14}$$

In Table VIII of Ref. [44], numerical values of $\mathcal{N}$ are listed as a function of the ratio $r/r_{\rm isco}$ for different BH spin parameters. To evaluate Eq. (3.13), we must transform the dependent variable of $\mathcal{N}$ from $r/r_{\rm isco}$ into gravitional wave frequency. This can be done by using Eq. (3.18), (3.20) and (3.21) in [44].

Evaluating Eq. (3.13) in this manner, we obtain the Teukolsky-Sasaki-Nakamura formalism's results $N_{\rm TSN}(F_{\rm lower})$ shown in Fig. 3.4(a). Here $F_{\rm lower} = 10$Hz, is the lower cutoff frequency of advanced LIGO, and $N_{\rm TSN}(F_{\rm lower})$ is shown as a function of the central black hole's mass, and for various spins. As expected, a larger spin parameter corresponds to an increased number of wave cycles, since the isco is being pushed deeper into the vicinity of the central black hole. Also as expected, a smaller BH mass corresponds to an increased number of wave cycles. This is because at $F_{\rm lower} = 10$Hz, the orbital speed $v_{\rm lower} = (\pi M F_{\rm lower})^{1/3}$ of the inspiraling object is smaller for a less massive BH, whereas $v_{\rm isco}$ is a fixed quantity for a given BH spin: a longer history of the inspiraling object (more wave cycles) will be recorded in the Advanced LIGO band. In Fig. 3.4(b), we show the number wave cycles predicted by the 2PN formula (3.12). It must be emphasized that this 2PN prediction is *invalid* (see Table 3.1 and surrounding discussions). We plot $N_{\rm 2PN}$ in Fig. 3.4 (b) just for the purpose of seeing its difference from the Teukolsky result [Fig. 3.4(a) for Eq. (3.14)].

Figure 3.4 shows that for a $1.4M_\odot$ NS inspiraling into an IMBH with mass $\sim 50M_\odot$ to $200M_\odot$, the emitted gravitational waves will spend $\sim$ 200 to 1000 cycles in the Advanced LIGO band. Although this number of wave cycles observed by Advanced LIGO is less than that from the canonical NS/BH binaries (a few thousands), and much less than that from EMRIs in the LISA band (hundreds of thousands), it is still large enough to promise accurate parameter extraction. Comparing Fig. 3.4(a) (results from TSN) and Fig. 3.4(b) (results from 2PN), we note that for IMBHs with spin $a \lesssim 0.5M$, 2PN predicts slightly more wave cycles than TSN does. This could be attributed to the fact that the TSN results have included higher and more

---

[8] See Eq. (3.2) and (3.4) of [44], where we have substituted the primary gravitational wave frequency F for twice the orbital frequency.

harmonic modes of radiation, which are not captured by the 2PN formalism in the strong gravity region. Hence TSN prescribes a slightly larger "acceleration" for the IMRI evolution, resulting in fewer wave cycles. By contrast, for rapidly spinning IMBHs ($a = 0.99M$), TSN predicts more wave cycles than 2PN does. This suggests that spin-dependent terms beyond 2PN order may be important [54].

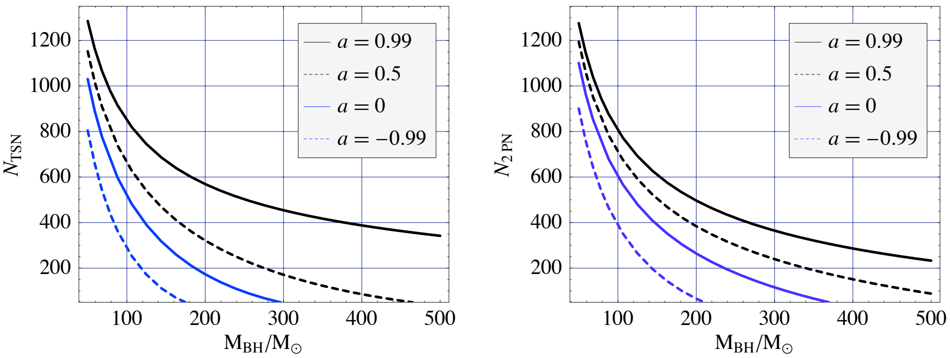

(a)

(b)

Figure 3.4: Number of IMRI wave cycles in the Advanced LIGO band as a function of the central black-hole mass for a $1.4M_\odot$ inspiraling object in a circular equatorial orbit. The entering wave frequency is taken to be the lower cutoff frequency of Advanced LIGO $f_{\rm lower} = 10$Hz; and the ending frequency is taken to be the ISCO frequency of the central black hole. Panel (a) shows the results based on Teukolsky calculations [Eq. (3.14)], which is the best approximation we have at present to realistic IMRI waves. Panel (b) shows the results based on PN calculations [Eq. (3.12)]. It must be emphasized that PN results shown in (b) are *invalid* (see Table 3.1 and surrounding discussions). We plot them here just to see their difference from the Teukolsky results. It can be seen from Eq. (3.11) and (3.13) that the number of wave cycles in inversely proportional to the small mass (approximately so for PN results in the limit of small mass ratios μ/M).

3.2.4 Number of wave cycles contributed by tidal coupling

In Ryan's proof that the EMRI waves carry a map of the central body's metric [16], he made several idealizing assumptions including ignoring the tidal coupling (TC) between the central body and the orbiting object. However, as has been shown by Finn and Thorne [44], for values of the central black hole and orbiting object with masses in the range relevant to LISA, tidal coupling can have an influence as large as a few percent on the evolution of the waves' inspiral phase. This suggests that the EMRI waveforms as seen by LISA will also carry high-precision information about the tidal coupling. As a first step to quantify the tidal coupling effect for the IMRI systems relevant to Advanced LIGO detectors, we perform a similar analysis: we estimate TC's contribution to the IMRI's number of wave cycles in the Advanced LIGO band. We again adopt the Teukolsky formulas from [44].

Equations (3.13) and (3.14) in Sec. 3.2.3 pose a good starting point for the analysis. By combining the two equations we can rewrite the total number of wave cycles as

$$N_{\rm TSN} = \frac{1}{\pi}\int \frac{\Omega}{\dot{\Omega}}\,d\Omega = \frac{5}{96\pi}\left(\frac{M}{\mu}\right)\int_{\Omega}^{\Omega_{\rm isco}} M^{-5/3}\Omega^{-8/3}\;\mathcal{N}\,d\Omega. \tag{3.15}$$

The influence of the tidal coupling is contained in the correction term $\mathcal{N}$. In [44], the relativistic correction $\dot{\mathcal{E}}$ to the total energy loss rate is introduced (Eq. (3.7) in [44]):

$$\dot{E}_{\rm GW} = \dot{E}_{\infty} + \dot{E}_{H} = \frac{32}{5}\left(\frac{\mu}{M}\right)^{2}(M\Omega)^{10/3}\dot{\mathcal{E}}\;. \tag{3.16}$$

Here $\dot{E}_{\infty}$ and $\dot{E}_{H}$ denote the energy flux carried by the gravitational waves to infinity and to the black hole horizon, respectively. The correction function $\mathcal{N}$ is inversely proportional to $\dot{\mathcal{E}}$ by the relation (Eq. (3.19) in [44]):

$$\mathcal{N} = \frac{1}{\dot{\mathcal{E}}}\left(1+\frac{a}{\tilde{r}^{3/2}}\right)^{5/3}\left(1-\frac{6}{\tilde{r}}+\frac{8a}{\tilde{r}^{3/2}}-\frac{3a^{2}}{\tilde{r}^{2}}\right)\left(1-\frac{3}{\tilde{r}}+\frac{2a}{\tilde{r}^{3/2}}\right)^{-3/2}\;, \tag{3.17}$$

where $\tilde{r} \equiv r/M$ is the dimensionless orbital radius. To single out the contribution of tidal coupling, we deduct $\dot{E}_{H}$ from the total energy flux $\dot{E}_{\rm GW}$, so that the inspiral evolves under a slightly different radiation rate at each orbit. This effectively changes the quantity $\dot{\mathcal{E}}$ in Eq. (3.16) by a factor of $(1-\dot{E}_{H}/\dot{E}_{\rm GW})$, which can be greater or less than 1; and the relativistic correction term in Eq. (3.15) is reduced by the same factor:

$$\mathcal{N}' = \mathcal{N}/(1-\dot{E}_{H}/\dot{E}_{\rm GW})\,. \tag{3.18}$$

Numerical data are tabulated for function $\mathcal{N}$ and $\dot{E}_{\rm H}/\dot{E}_{\rm GW}$ at different radii in [44]. They enable us to perform numerical integration of Eq. (3.15) with $\mathcal{N}$, and also with $\mathcal{N}'$ defined in Eq. (3.18). The wave cycles contributed by tidal coupling can be deduced from the difference:

$$\Delta N_{\rm TC} \equiv N_{\rm TSN}(\mathcal{N}) - N'_{\rm TSN}(\mathcal{N}')\;. \tag{3.19}$$

Figure 3.5 shows $\Delta N_{\rm TC}$ as a function of the central BH's mass for various spin parameters, when the inspirling object has mass $\mu = 1.4M_{\odot}$. For example, for a $200M_{\odot}$ IMBH with large spin $0.9 \lesssim a/M \lesssim 0.99$, there are about 500 wave cycles in the Advanced LIGO band (Fig. 3.4), among which tidal coupling contributes $\sim$ 3 to 7 cycles.[9] This appreciable amount of TC's influence on the phasing evolution leaves us the possibility to measure it to some accuracy.

---

[9] This suggests that about 1% of the wave cycles are contributed by tidal coupling for rapidly spinning holes, and that the black hole absorption is about 1% of the total orbital energy being radiated in the advanced LIGO band. The finite mass ratio between the NS and IMBH (a typical IMRI) will give a higher order correction to TC's phasing contribution; this correction should be small enough that its accumulative influence on $\Delta N_{\rm TC}$ is negligible. To see why, note that the leading order mass-ratio term corrects the horizon energy absorption into a form $(dE/dt)_{H}(1+\mu/M)$, i.e., the black hole absorption will be changed fractionally by μ/M at the lowest order. Thus $\Delta N_{\rm TC}$ will be corrected accordingly by the same fraction. The correction will have a negligible observational effect. For example, take $\Delta N_{\rm TC} \simeq 5$ and $\mu/M \simeq 1.4/100$ for the case when $a = 0.99$; then the correction to $\Delta N_{\rm TC}$ is ~ 0.07—quite negligible.

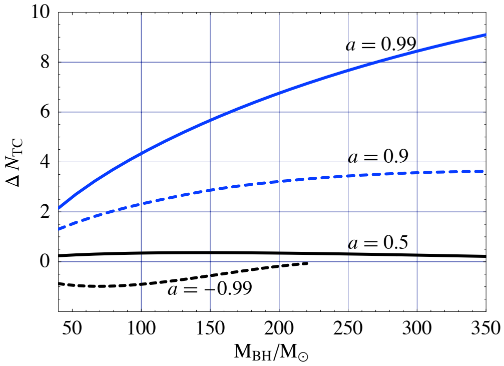

Figure 3.5: Number of wave cycles contributed by tidal coupling, ΔN_{TC} in Eq. (3.19), as a function of the central black-hole mass, for a $1.4M_{\odot}$ object inspirling inward in a circular equatorial orbit. The function ΔN_{TC} scales as $1/\mu$ [see Eq. (3.15)].

3.3 Advanced LIGO's accuracy for measuring tidal coupling

In this section, we shall carry out a semi-quantitative analysis of how accurately Advanced LIGO can measure TC in an IMRI. We model the tide-induced energy flow into the central body as

$$\dot{E}_{\rm body} \equiv \varepsilon \dot{E}_H \,. \tag{3.20}$$

Here $\dot{E}_H$ is the energy flow into a Kerr black hole, and we seek to measure deviations from it parameterized by ε. When $\varepsilon = 1$, the total energy flux takes its "true" theoretical value; when $|\varepsilon - 1| \gtrsim 1$, ε represents a strong deviation from black-hole predictions due to the "wrong" horizon flux. The total energy loss from the orbit is then

$$\dot{E}_{\rm GW} = \dot{E}_\infty + \varepsilon \dot{E}_H \,. \tag{3.21}$$

We shall use this $\dot{E}_{\rm GW}$ to construct theoretical waveforms[10] for circular orbits, both equatorial and inclined. Given the waveforms, we shall perform parameter estimation based on the Fisher information matrix to investigate how accurately we can extract the tidal coupling parameter ε (along with the IMRI's other unknown parameters). If the parameter-estimation error of ε is sufficiently small, then it suggests that we can achieve a high-precision test of tidal coupling and constrain its deviation from theoretical predictions to a great accuracy.

Within the Teukolsky formalism, the calculation of the energy flux $\dot{E}_H$ and $\dot{E}_\infty$ involves summing over radiation components for an (infinite) array of frequency harmonics [56]. The result for $\dot{E}_H$ and $\dot{E}_\infty$ only contains the leading $\mathcal{O}(v^2)$ radiation. Using Eq. (3.21) to construct IMRI waveforms, we also neglect the influence of the $\mathcal{O}(v^2)$ conservative self-force. However, as discussed in Sec. 3.2.2, the Teukolsky waveforms present the closest approximation available today to realistic IMRI waves. So we shall base our parameter

---

[10] We shall focus on the waveforms' evolving phase.

estimation on the Teukolsky waveforms and expect that the result, while not fully reliable, is at least indicative of the accuracies that Advanced LIGO can achieve.

Numerical data for $\dot{E}_\infty$ and $\dot{E}_H$ can be found, e.g., in Refs. [44, 57], and can be used to construct numerical inspiral waveforms. To ease the calculation, we adopt the analytical 3.5 post-Newtonian expansions of the Teukolsky function and $\dot{E}_\infty$ and $\dot{E}_H$ from Tagoshi et al. [37, 35], so that the inspiral waveforms can be computed analytically. Although this PN expansion “downgrades” the applicability of the full Teukolsky formalism (i.e., as discussed in Sec. 3.2.2, it fails to produce the correct energy loss rate when the separation of the binary is $\sim 10M$), the main advantage of using PN-Teukolsky rather than the standard PN results is that PN-Teukolsky consistently gives both $\dot{E}_\infty$ and $\dot{E}_H$ (whereas the standard PN only concerns with radiation at infinity), and at each PN order gives all spin terms from the leading $\mathcal{O}(v^2)$ radiation reaction (whereas the standard PN currently only contains spin terms, i.e. spin-orbit coupling, up to 2.5PN [54]).

To assess the deviation of 3.5PN $\dot{E}_\infty$ and $\dot{E}_H$ from the full Teukolsky results (i.e., numerical data from [44]), we plot their fractional difference as a function of $r/r_{\rm isco}$ in Fig. 3.6 for variousl different black-hole spins. Figure 3.6 shows that for $r \gtrsim 2r_{\rm isco}$ and $a/M \lesssim 0.9$, the total PN energy fluxes are accurate to within 10%. In the ultra-strong field region $r_{\rm isco} \lesssim r \lesssim 2r_{\rm isco}$, the fractional difference is as large as $\sim 50\%$ for the total energy flux and is a fractor 4 for the horizon energy flux, which can have a large impact on the IMRI waveforms. Moreover, the difference at the horizon is always positive, which indicates that 3.5PN $\dot{E}_H$ is an overestimate of the energy flow into the black-hole horizon.[11]

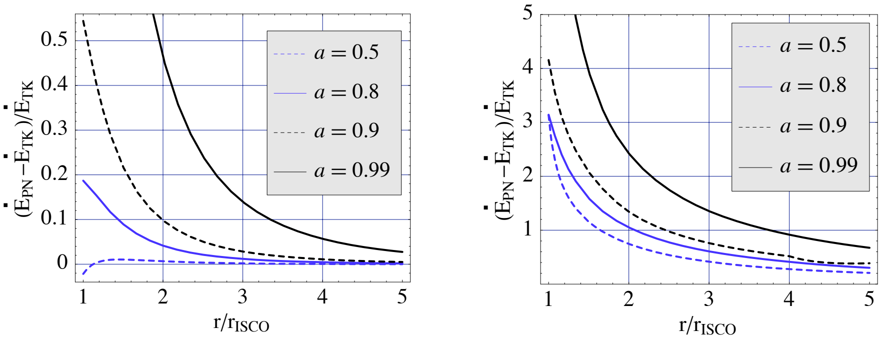

(a) Fractional difference in total energy flux.

(b) Fractional difference in horizon energy flux.

Figure 3.6: Fractional difference of 3.5PN energy fluxes [Eq. (3.36)] with full Teukolsky results (using data from [44]) as a function of $r/r_{\rm isco}$. Panel (a) shows the comparison of the total energy flux ($\dot{E}_{\rm GW} = \dot{E}_\infty + \dot{E}_H$); Panel (b) shows the comparison of horizon energy flux ($\dot{E}_H$).

Despite these limitations of the post-Newtonian expansions, we believe that 3.5PN-Teukolsky waveforms contain enough information (i.e., interrelation among different physical paramters) to be a useful family of model templates. When we perform parameter estimation based on them, we expect that the results should be indicative of the accuracies Advanced LIGO can achieve.

---

[11] While plotting Fig 3.6, we have also examined the adjacent-order PN expressions (i.e., 3PN and 4PN) for the energy flux functions. It turns out 3.5PN fluxes give the closest approximation to Teukolsky results among the three.

3.3.1 Review of parameter estimation

The problem of how to estimate the accuracy of parameter measurements is discussed thoroughly by Finn [58], and by Cutler and Flannagan [43], both from a *Frequentist's* viewpoint. Here we adopt the same standpoint and summarize the basic principles when the noise follows a Gaussian distribution. We shall describe how to compute the root-mean-square errors of the parameter estimation via the so-called Fisher information matrix, from which our results in Sec 3.3.4 below are obtained.

The data stream $s(t)$ collected from the detector output consists of a gravitational-wave signal (if it exists) and instrumental noise: $s(t) = h(t;\boldsymbol{\alpha}) + n(t)$, where $\boldsymbol{\alpha}$ is a set of parameters that characterize the signal. We define the likelihood ratio (Eq. (2.22) in [58])

$$\Lambda(\boldsymbol{\alpha}; s) \equiv p(\boldsymbol{\alpha})\,\frac{p(s|\boldsymbol{\alpha})}{p(s|0)}\,, \tag{3.22}$$

where

- $p(\boldsymbol{\alpha})$ is the *a priori* probability density that $h(t)$ is characterized by $\boldsymbol{\alpha}$. [In this section, we shall assume that we do *not* have any *a prior* knowledge of parameter distributions and so will ignore $p(\boldsymbol{\alpha})$ in later calculations.]
- $p(s|\boldsymbol{\alpha})$ is the conditional probability density of observing $s(t)$ if $h(t;\boldsymbol{\alpha})$ is present in the data;
- $p(s|0)$ is the conditional probability density of observing $s(t)$ when no signal is present.

It can be shown that [58], *the conditional probability density that the particular signal $h(t;\boldsymbol{\alpha})$ is present in the data stream $s(t)$*, i.e. $p(\boldsymbol{\alpha}|s)$, is directly proportional to the likelihood ratio $\Lambda(\boldsymbol{\alpha}; s)$.[12]

$$p(\boldsymbol{\alpha}|s) \propto \Lambda(\boldsymbol{\alpha}; s)\,. \tag{3.23}$$

We define an *unbiased estimator* $\hat{\boldsymbol{\alpha}}$ of the parameter set as the one that maximizes the probability density $p(\boldsymbol{\alpha}|s)$. It can be computed from

$$\frac{\partial}{\partial\alpha^i}\Lambda(\hat{\boldsymbol{\alpha}}; s) \;=\; 0\,. \tag{3.24}$$

Note that the values of the estimator $\hat{\boldsymbol{\alpha}}$ vary for different realizations of the noise, and generally deviate from the "true" parameters $\tilde{\boldsymbol{\alpha}}$ that are encoded in the incoming gravitational-wave signal.

When the instrumental noise $n(t)$ follows a Gaussian distribution and is characterized by a spectral density $S_n(f)$, the likelihood ratio (3.22) can be written as (Eq. (2.26) in [58] with the *a prior* probability density ignored)

$$\ln\Lambda(\boldsymbol{\alpha}, s) \;=\; 2[h(\boldsymbol{\alpha})\,, s(t)] - [h(\boldsymbol{\alpha})\,, h(\boldsymbol{\alpha})]\,. \tag{3.25}$$

---

[12] The likelihood ratio $\Lambda(\boldsymbol{\alpha}; s)$ (its integration over $\boldsymbol{\alpha}$ to be more exact) also determines $P(h|d)$, the conditional probability that a signal $h(t;\boldsymbol{\alpha})$, for unknown $\boldsymbol{\alpha}$, is present given the observed data stream $s(t)$. A detection of the gravitational wave signal is announced if $P(h|d)$ exceed a prescribed threshold. See Eq. (2.7)-(2.9) and (2.22) in [58] for details.

Here the inner product [... , ...] is defined as

$$[h_1\,,h_2] \;=\; 2\int_0^\infty \frac{\tilde{h}_1(f)\tilde{h}_2^*(f)+\tilde{h}_1^*(f)\tilde{h}_2(f)}{S_n(f)}\,df\;, \tag{3.26}$$

where $\tilde{h}_1$ and $\tilde{h}_2$ are the Fourier transforms of h_1 and h_2. When the SNR is large,[13] it can be shown that the distribution of the measurement error $\delta\boldsymbol{\alpha} \equiv \tilde{\boldsymbol{\alpha}} - \hat{\boldsymbol{\alpha}}$ follows a multivariate Gaussian distribution (Eq. (2.6) in [43] and Eq. (3.19) in [58]):

$$p(\delta\boldsymbol{\alpha}|\hat{\boldsymbol{\alpha}}) \;\;\propto\;\; \exp\left(-\frac{1}{2}\mathscr{F}_{ij}\,\delta\alpha^i\delta\alpha^j\right), \tag{3.27}$$

where $\mathscr{F}_{ij}$ is the Fisher information matrix given by

$$\mathscr{F}_{ij} \;\;\equiv\;\; \left[\frac{\partial h}{\partial\alpha^i}\,,\,\frac{\partial h}{\partial\alpha^j}\right]_{\alpha=\hat{\alpha}}\,. \tag{3.28}$$

The variance-covariance matrix can be identified as the inverse of the Fisher matrix

$$\Sigma^{ij} \equiv \langle\delta\alpha^i\delta\alpha^j\rangle = (\mathscr{F}^{-1})^{ij}\,. \tag{3.29}$$

Here the angular bracket denote an average over many noise realizations. The diagonal elements of Σ represent the expected mean-square errors:

$$\langle(\delta\alpha^i)^2\rangle = \Sigma^{ii}\;, \tag{3.30}$$

and its off-diagonal elements contain information on the correlation among different parameters. The correlation coefficient for α^i and α^j is given by

$$c^{ij} \equiv \frac{\langle\delta\alpha^i\delta\alpha^j\rangle}{\langle\delta\alpha^i\delta\alpha^i\rangle^{1/2}\langle\delta\alpha^j\delta\alpha^j\rangle^{1/2}} = \frac{\Sigma^{ij}}{\sqrt{\Sigma^{ii}\Sigma^{jj}}}\,. \tag{3.31}$$

We shall close this brief review of parameter estimation with a cautionary note. The variance-covariance matrix Σ, defined as the inverse of the Fisher matrix, in fact provides a lower bound (the so-called Cramér-Rao bound) to the *minimum* mean-square error (see, e.g. [59] and references therein). In our problem, only in the limit of large signal-to-noise ratio, i.e. when the distribution of the estimator is close to Gaussian, does Σ^{ii} approaches the exact mean-square error.

---

[13] For large SNR, the difference $h(\tilde{\alpha}) - h(\hat{\alpha})$ can be linearized in $\delta\alpha \equiv \tilde{\alpha} - \hat{\alpha}$, and the quadratic and higher-order correction can be ignored.

3.3.2 Gravitational waveforms for circular equatorial orbits

For circular equatorial orbits, the gravitational-wave strain at the detector output [Eq. (3.3)] can be modeled as (cf. Eq. (2.12) in [43]):[14]

$$h(t) \quad = \quad \left(\frac{384}{5}\right)^{1/2} \frac{\pi^{2/3} Q(\theta_N, \varphi_N, \psi_N, \iota)\, \mu M}{D\, r(t)} \cos\Phi(t)\,. \tag{3.32a}$$

Here D is the distance between the detector and source, and$r(t)$ is the radius of the orbit. The function Q incorporates all the angular factors that contribute to the amplitude of the strain [cf. Eq. (3.3)]. The accumulative phase of the strain is defined as

$$\Phi(t) \quad \equiv \quad \int 2\pi\, F(t)\, dt\,. \tag{3.32b}$$

Here again we take the frequency F in the integrand to be the dominant gravitational wave frequency, i.e., twice the orbital frequency: $F = 2(\Omega/2\pi)$. Equations (3.32) describe the so-called *restricted waveform*, which includes only the quadrupolar component and disregards all higher moments. The Fourier transform of the gravitational-wave strain (3.32) can be computed by applying the stationary phase approximation (SPA) [60]. The result is (Eq. (2.20) in [43]):

$$\tilde{h}(f) \quad = \quad \int_{-\infty}^{\infty} h(t)\, e^{2\pi i f t} dt = \mathcal{A} f^{-7/6} \exp\left[i\,\Psi(f)\right], \tag{3.33a}$$

where $\mathcal{A} = (Q/D)\,\mu^{1/2} M^{1/3}$ is the geometric factor. In terms of the primary wave frequency, the phase Ψ is given by

$$\Psi(F) \quad = \quad 2\pi F\, t(F) - \Phi(F) - \pi/4\,. \tag{3.33b}$$

Here the function $t(F)$ is defined as the time when $\dot{\Phi}(t) = 2\pi F$; and $\Phi(F)$ means $\Phi[t(F)]$.

The functions $t(F)$ and $\phi(F)$ depend on the evolution of the wave frequency, which in turn depends on the orbital energy function $E_{\rm orb}$ and the gravitational energy flux function $\dot{E}_{\rm GW}$ via the energy-balance equation $\dot{E}_{\rm orb} = -\dot{E}_{\rm GW} = -(\dot{E}_\infty + \varepsilon \dot{E}_H)$. In terms of the orbital velocity $v \equiv (\pi M F)^{1/3}$, these two functions can be written as

$$t(v) \quad = \quad t_o + \int_v^{v_o} \frac{dE_{\rm orb}(v')/dv'}{\dot{E}_\infty + \varepsilon \dot{E}_H} dv', \tag{3.34a}$$

$$\Phi(v) \quad = \quad \Phi_o + \int_v^{v_o} \left(\frac{2v'^3}{M}\right) \frac{dE_{\rm orb}(v')/dv'}{\dot{E}_\infty + \varepsilon \dot{E}_H} dv'. \tag{3.34b}$$

---

[14] By contrast with [43], we have taken the test-particle limit; so μ and M denote the small mass and black-hole mass in our equation.

In the test-particle limit, the total orbital energy is related to the wave frequency by the following equations

$$
\begin{aligned}
E_{\rm orb} &= -\mu \frac{1 - 2/\tilde{r} + q/\tilde{r}^{3/2}}{\sqrt{1 - 3/\tilde{r} + 2q/\tilde{r}^{3/2}}} \,, && (3.35a) \\
\tilde{r} &= \left(v^{-3} - q\right)^{2/3} \,. && (3.35b)
\end{aligned}
$$

For the energy flux function $\dot{E}_\infty$ and $\dot{E}_H$, we adopt the PN expansions of the Teukolsky equation from Tagoshi et al. [37, 35]. The results are (up to 3.5PN order)

$$
\begin{aligned}
\dot{E}_\infty &= \dot{E}_N \Bigg[1 - \frac{1247}{336} s^2 + \left(4\pi - \frac{73q}{12}\right) s^3 + \left(\frac{-44711}{9072} + \frac{33q^2}{16}\right) s^4 + \left(\frac{-8191\pi}{672} + \frac{3749q}{336}\right) s^5 \\
&\quad + \left(\frac{6643739519}{69854400} + \frac{16\pi^2}{3} - \frac{1712\gamma}{105} - \frac{169\pi q}{6} + \frac{3419q^2}{168} - \frac{1712}{105}\log(4\,s)\right) s^6 \\
&\quad + \left(\frac{-16285\pi}{504} + \frac{83819q}{1296} + \frac{65\pi q^2}{8} - \frac{151q^3}{12}\right) s^7 + \mathcal{O}(s^8) \Bigg] , && (3.36a) \\
\dot{E}_H &= \dot{E}_N v^5 \left[\left(-\frac{1}{4}q - \frac{3}{4}q^3\right) + \left(-q - \frac{33}{16}q^3\right) v^2 + \mathcal{O}(v^3) \right] . && (3.36b)
\end{aligned}
$$

Here in Eq. (3.36a), the parameter s is related to the dimensionless orbital radius $\tilde{r}$ by $s = 1/\tilde{r}^{1/2}$ (this is the parameter that Tagoshi et al. have used to calculate the expansion of $\dot{E}_\infty$). The function $\dot{E}_N$ is the lowest order Newtonian energy flux (quadrupole radiation) given by

$$
\dot{E}_N = \frac{32}{5}\left(\frac{\mu}{M}\right)^2 v^{10} \,. \qquad (3.36c)
$$

So for a rotating black hole, the influence of black hole absorption on the SPA phasing starts at the 2.5PN order (and also appears at 3.5PN and higher). This agrees with Gal'tsov's slow-motion calculation [61].

Inserting Eq. (3.35)-(3.36) into (3.34) and combining the results with Eq. (3.33b), we obtain the phase of the frequency-domain waveform

$$
\Psi(F) = 2\pi f t_o - \Phi_o - \frac{\pi}{4} + \frac{3M}{128\mu v^5} \sum_{k=0}^{N} \Gamma_k v^k , \qquad (3.37a)
$$

where the coefficients are

$$
\begin{aligned}
\Gamma_0 &= 1 \,, && (3.37b) \\
\Gamma_1 &= 0 \,, && (3.37c) \\
\Gamma_2 &= \frac{3715}{756} \,, && (3.37d) \\
\Gamma_3 &= -16\pi + \frac{113}{3} q \,, && (3.37e) \\
\Gamma_4 &= \frac{15293365}{508032} - \frac{405}{8} q^2 \,, && (3.37f)
\end{aligned}
$$

and

$$\Gamma_5 = \frac{38645\,\pi}{756}\left[1+3\log\left(\frac{v}{v_{\rm lso}}\right)\right] - \frac{732985}{756} q \log\left(\frac{v}{v_{\rm lso}}\right) - \frac{10}{3}\varepsilon\, q\left(1+3q^2\right)\log\left(\frac{v}{v_{\rm lso}}\right), \tag{3.37g}$$

$$\Gamma_6 = \left(\frac{11583231236531}{4694215680} - \frac{640\,\pi^2}{3} - \frac{6848\,\gamma}{21}\right) + \frac{2270\pi}{3} q + \frac{75515}{288} q^2 - \frac{6848}{21}\log(4\,v), \tag{3.37h}$$

$$\Gamma_7 = \frac{77096675\pi}{254016} - \frac{25150083775}{3048192} q - \frac{815\pi}{2} q^2 + \frac{14585}{24} q^3 - \varepsilon\left(\frac{8335}{168} q + \frac{7285}{56} q^3\right). \tag{3.37i}$$

Equations (3.33) and (3.37) now completely specify the 3.5PN-Teukolsky waveforms for circular equatorial orbits. Note that the amplitude $|\tilde{h}(f)| = \mathcal{A} f^{-7/6}$ only reflects the Newtonian, quadrupole-radiation contribution. This limitation does not concern us since most of the "information" is contained in the phase of the waveform [i.e., in Eq. (3.37)]. Further, we shall not be concerned with the explicit form of the geometric factor $\mathcal{A}$, which can be specified implicitly via the SNR, i.e., via

$$\left(\frac{S}{N}\right)^2 = \mathcal{A}^2 \int_0^\infty \frac{f^{-7/3}}{S_n(f)}\, df \equiv \mathcal{A}^2 I_o\,, \tag{3.38}$$

where we have defined I_o to be the integral in the second equation. From the definition of the Fisher matrix (3.28), it is a simple exercise to show that $\mathscr{F}_{\mathcal{A}j} = 0$, where j is any other parameter. Hence $\mathcal{A}$ is uncorrelated with the rest of the parameters. Its measurement error is given by

$$\Delta\mathcal{A} = (\mathscr{F}_{\mathcal{A}\mathcal{A}})^{-1/2} = \frac{\mathcal{A}}{(S/N)}\,. \tag{3.39}$$

For the other six parameters

$$\boldsymbol{\alpha} = (\ln\mu,\ \ln M,\ q,\ \varepsilon,\ f_s t_o,\ \Phi_o)\,, \tag{3.40}$$

the components of their Fisher matrix are

$$\mathscr{F}_{ij} = \left(\frac{S}{N}\right)^2 I_o^{-1} \int_0^\infty \frac{f^{-7/3}\Psi_{,\alpha_i}\Psi_{,\alpha_j}}{S_n(f)}\, df\,. \tag{3.41}$$

3.3.3 Approximate waveforms for circular inclined orbits

We now turn to circular inclined orbits. The general relativistic spin-orbit coupling in this case will cause the orbital plane to precess (Lense-Thirring precession is the leading order effect). The resulting precession-modulated waveforms will then contain "extra" information about the black-hole spin. We expect that when such waveforms are being used to perform parameter estimations, the degeneracy (correlation) between the spin and other parameters will be greatly reduced (this is verified by the results shown in Sec. 3.3.4).

In [36], Apostolatos et al. (ACST) analyzed the binary system with two spinning bodies, using post^2-Newtonian equations to describe the precession of the orbital plane and of the two spins (Eq. (11) in [36]).

They then computed the resulting modulation of the inspiral gravitational waveforms, but used only the leading-order, quadrupole moment approximation to describe the orbital evolution and wave generation. A key to the construction of ACST waveforms (and other similar precessional-waveform construction schemes) is the separation of motion in the instantaneous orbital plane and the motion of the orbital plane itself, which is made possible by the different time scales associated with the two. As ACST have shown, the frequency-domain waveform can be written in the following form (we shall ignore the so-called "polarization amplitude" in $\tilde{h}(f)$ when computing the Fisher matrix; see Eq. (3.83) in Appendix 3.B):

$$\tilde{h}(f) \propto f^{-7/6} \exp\Big[i \Big(\underbrace{\Psi_c(f) - 2\delta\Phi(t_f) - \varphi(t_f)}_{\Psi_{\rm prec}} \Big) \Big] \, . \tag{3.42}$$

Here $\Psi_{\rm prec}$ is the combined precessional phase, in which $\Psi_c \equiv 2\pi f t - \Phi_c(f) - \pi/4$ [cf. Eq. (3.33b)] and Φ_c is the *carrier* phase of the waveform which describes the azimuthal accumulation in the orbital plane [as in Eq. (3.32b)]. Regardless of the presence of precession, Ψ_c contains the same information as the Ψ in Eq. (3.33). The piece $\delta\Phi$ is the precessional correction to Φ_c; it arises from the changing orientation of the orbital plane. Lastly the piece φ is the polarization phase, which is due to the changing projection of the orbital plane onto the detector's frame.

In Appendix B, we construct ACST waveforms [Eq. (3.42)] for IMRIs by specializing to the case when the spin of the small-mass companion can be ignored. In this case the equation of motion for the orbital angular momentum simplifies greatly and one can show that the direction of orbital angular momentum $\hat{\boldsymbol{L}}$ remains unchanged during the inspiral up to 2PN order.

By contrast with ACST's simplified, leading-order quadrupole radiation approximation, here again we adopt the PN-Teukolsky energy flux to evolve the orbits. Specifically, we use the 3.5PN-Teukolsky $\dot{E}_\infty$ for circular equatorial orbits, augmented by corrections from small inclination angles.

Shibata et al. [38] studied circular inclined orbits for a test particle moving around a massive Kerr black hole. They defined an orbital inclination parameter by

$$y \equiv \frac{Q}{L_z^2 + a^2(1-E^2)^2} \, . \tag{3.43}$$

[Equation (2.64) in [38]; notice that Shibata et al. use the symbol "C" to denote the Carter constant Q.] In the Newtonian limit, this parameter can be identified as $y = \lambda_L^2$ [47], where λ_L is the opening angle between the orbital angular momentum and the black-hole spin, i.e. the orbital inclination angle (see Fig. 3.7 in Appendix B). Adding corrections from Shibata et al. (Eq. (3.13) in [38]) to Eq. (3.36a) above, we obtain

$$\begin{aligned} \dot{E}_\infty \;\; = \;\; & \dot{E}_N \Big[1 - \frac{1247}{336} s^2 + \Big(4\pi - \frac{73}{12} q\,(1 - y/2) \Big) s^3 + \Big(\frac{-44711}{9072} + \frac{33}{16} q^2 - \frac{527}{96} q^2 y \Big) s^4 \\ & + \Big(\frac{-8191}{672}\pi + \frac{3749}{336} q\,(1 - y/2) \Big) s^5 + \; \mathcal{O}(s^6) \;\&\; \mathcal{O}(s^7) \text{ terms in Eq. (3.36a)} \; + \; \mathcal{O}(s^8) \Big] . \end{aligned} \tag{3.44}$$

In the case of circular inclined orbits, the total conserved orbital energy now depends on the inclination angle [cf. Eq. (3.35)]. The relation between the orbital angular frequency and the radius also changes. By solving the geodesic equations under the assumption of small inclination angle, we obtain (see Appendix B; cf. Eq. (2.65) and (4.6) in [38])

$$\begin{aligned}
E/\mu &= 1 - \frac{s^2}{2} + \frac{3s^4}{8} - \left(1 - \frac{y}{2}\right) q s^5 + \left[\frac{27}{16} + \frac{q^2}{2}(1-y)\right] s^6 - \frac{9}{2}\left(1 - \frac{y}{2}\right) q s^7 \\
&\quad + \left[\frac{675}{128} + \frac{q^2}{4}(15 - 23y)\right] s^8 - \left[\frac{135}{16}(2-y) + q^2(1-5y)\right] q s^9 + \mathcal{O}(s^{10}) \qquad (3.45) \\
M\Omega &= s^3\left[1 + \frac{1}{2} q(-2+y) s^3 - \frac{3}{4} q^2 y s^4 + q^2(1-2y) s^6 + \frac{9}{4} q^3 y s^7 + \mathcal{O}(s^9)\right] \qquad (3.46)
\end{aligned}$$

Inverting Eq. (3.46), we obtain s as a function of the dimensionless orbital angular velocity $\tilde{\Omega} \equiv M\Omega$:

$$\begin{aligned}
s &= \tilde{\Omega}^{1/3}\Big[1 + \frac{1}{6} q(2-y)\tilde{\Omega} + \frac{1}{4} q^2 y \tilde{\Omega}^{4/3} + \frac{1}{9} q^2 (2+y)\tilde{\Omega}^2 + \frac{1}{6} q^3 y \tilde{\Omega}^{7/3} + \frac{14}{81} q^3 (1+3y)\tilde{\Omega}^3 \\
&\quad - \frac{1}{9} q^4 y \tilde{\Omega}^{10/3} + \frac{35}{243} q^4 (1+7y)\tilde{\Omega}^4 - \frac{44}{81} q^5 y \tilde{\Omega}^{13/3} + \mathcal{O}(\tilde{\Omega}^5)\Big]. \qquad (3.47)
\end{aligned}$$

Equation (3.47) is the equivalent of Eq. (3.35b) for the case of circular inclined orbits. Equations (3.45)-(3.47), together with $\dot{E}_H$ given by Eq. (3.36b), are sufficient to deduce Ψ_c. The result is

$$\Psi_c(F) = 2\pi f t_o - \Phi_o - \frac{\pi}{4} + \frac{3M}{128\mu v^5} \sum_{k=0}^{N} \Gamma_k^{(c)} v^k, \qquad (3.48a)$$

where the coefficients are

$$\begin{aligned}
\Gamma_j^{(c)} &= \Gamma_j, \qquad j = 0, 1, 4 \qquad (3.48b) \\
\Gamma_2^{(c)} &= \Gamma_2 - \frac{113}{6} q y, \qquad (3.48c) \\
\Gamma_3^{(c)} &= \Gamma_3 + \frac{3595}{48} q^2 y, \qquad (3.48d) \\
\Gamma_5^{(c)} &= \Gamma_5 + \frac{732985}{1512} q y \log\left(\frac{v}{v_{\rm lso}}\right), \qquad (3.48e) \\
\Gamma_6^{(c)} &= \Gamma_6 - \left(660\pi q + \frac{244465}{448} q^2\right) y, \qquad (3.48f) \\
\Gamma_7^{(c)} &= \Gamma_7 + \left(\frac{29092929535}{6096384} q + \frac{3295\pi}{3} q^2 - \frac{127375}{72} q^3\right) y. \qquad (3.48g)
\end{aligned}$$

In Appendix B, we complete our description of circular inclined precessional waveforms by giving explicit expressions for $\delta\Phi$ (the precessional correction) and φ (the polarization phase). The parameter set on which these waveforms depend is 12 dimensional:

$$\alpha = (\ln\mu,\ \ln M,\ q,\ \lambda_L \equiv y^{1/2},\ \xi_o,\ \varepsilon,\ t_o,\ \Phi_o,\ \theta_N,\ \phi_N,\ \theta_S,\ \phi_S)\,, \qquad (3.49)$$

	Δt_o	$\Delta\Phi_o$	$\Delta\mu/\mu$	$\Delta M/M$	Δq	$\Delta\varepsilon$	$c^{\varepsilon\mu}$	$c^{\varepsilon M}$	$c^{\varepsilon q}$
$1.4M_\odot$+$50M_\odot$									
	0.086	222.48	7.51%	13.3%	0.129	14.34	0.984	−0.993	−0.993
$1.4M_\odot$+$100M_\odot$									
	0.433	756.39	8.07%	17.9%	0.279	24.63	0.972	−0.995	−0.997
$1.4M_\odot$+$200M_\odot$									
	2.98	3415.3	7.14%	31.9%	0.767	56.00	0.847	−0.997	−0.998

Table 3.2: Measurement errors and correlations for circular equatorial orbits with BH spin $a = 0.9M$ and SNR = 10.

where ξ_o describes the initial orientation of the orbital plane [cf. Eq. (3.89) in Appendix B], the angles (θ_N, ϕ_N) describe the sky location of the source, and (θ_S, ϕ_S) describe the black-hole spin orientation. These are the parameters that we seek to measure in the data analysis. Similar to Eq. (3.41), the components of their Fisher matrix are

$$\mathscr{F}_{ij} = \left(\frac{S}{N}\right)^2 I_o^{-1} \int_0^\infty \frac{f^{-7/3}\Psi_{\mathrm{prec},\alpha_i}\Psi_{\mathrm{prec},\alpha_j}}{S_n(f)}\, df \,, \tag{3.50}$$

where the constant I_o is defined in the second equation of (3.38).

3.3.4 Results and comparison

Having obtained the waveforms for circular equatorial orbits (3.33) and for circular inclined orbits (3.42), we proceed to compute the Fisher matrix components according to Eq. (3.41) and Eq. (3.50), respectively. We then calculate the variance-covariance matrix Σ^{jk} by inverting the Fisher matrix, and estimate the root-mean-square (rms) error of each parameter as $\Delta\alpha_j = (\Sigma^{jj})^{1/2}$ [cf. Eq. (3.30)].

In Table 3.2, we list the results of these parameter estimation computations for circular equatorial orbits at SNR = 10. The three IMRI systems being considered have IMBH with masses $M = 50M_\odot$, $100M_\odot$ and $200M_\odot$, and an inspiraling NS with mass $\mu = 1.4M_\odot$. The spin of the IMBH is $a = 0.9M$. Table 3.2 shows that the measurement errors increase for a larger black-hole mass; this is because the IMRI spends fewer wave cycles in the Advanced LIGO band. The measurement error for the tidal coupling parameter is $\Delta\varepsilon \gtrsim 14$, which is much greater than its true value of unity. The correlations between ε and other parameters (μ, M, q) are also very large (close to one). These results suggest that it may be impossible to measure the effect of tidal coupling within any interesting accuracy using circular equatorial orbits. We must add precession to break the degeneracy between ε and the other physical parameters.

Before we discuss the results of our parameter estimation for circular inclined orbits, we point out that for their corresponding 12-dimensional parameter space (3.49), the resulting Fisher matrix (3.50) is ill-conditioned—usually with a large condition number $\gtrsim 33$. This degeneracy largely comes between the source location (θ_N, ϕ_N) and the spin orientation (θ_S, ϕ_S), since they enter the precession correction term $\delta\Phi$

simultaneously and play similar roles in producing the modulation effects [see Eq. (3.96a)]. Their degeneracy has made the full, 12-dimensional Fisher matrix become non-invertible. Because it is important to the interpretation of our parameter estimation results, we shall briefly explain the subtleties in the inversion of an ill-conditioned Fisher matrix—subtleties previously discussed in the context of gravitational wave data analysis by Berti et al. [62] and by Barack and Cutler [63]. In [62], Berti et al. used a principal component analysis of singular-value-decomposition, to decompose the Fisher matrix **F** as (Eq. (B2) in [62])

$$\mathbf{F} = \mathbf{U}\mathbf{W}\mathbf{V}^T \,. \tag{3.51}$$

Here **U** and **V** are orthogonal matrices, the superscript "T" denotes transpose, and **W** is a diagonal matrix with components $w_j \geq 0$ (the singular values). The inverse of the Fisher matrix is then given by

$$\mathbf{F}^{-1} = \mathbf{V}\mathbf{W}^{-1}\mathbf{U}^T \,, \tag{3.52}$$

where $\mathbf{W}^{-1}$ is the inverse of **W** with diagonal elements $1/w_j$. A matrix becomes ill-conditioned when one or more of its singular values approach zero, in which case the reciprocal of the singular value becomes extremely sensitive to the precise value of itself. The matrix hence becomes numerically non-invertible in this sense. In our calculation, we find there are two vanishing singular values of the Fisher matrix, which can be removed either by eliminating the source location (θ_N, ϕ_N) or the spin orientation (θ_S, ϕ_S) from the parameter space (3.49). As Berti et al. has suggested, this is equivalent to obtaining a "pseudoinverse", which is closest to the "real" inverse of the Fisher Matrix in a least-square sense. So in order to get robust and sensible results from the inversion of the Fisher matrix, we perform estimation on a reduced, 10-dimensional parameter set by fixing the spin orientations (θ_S, ϕ_S):[15]

$$\boldsymbol{\alpha}^{(10)} = (\ln\mu,\ \ln M,\ q,\ \lambda_L,\ \xi_o,\ \varepsilon,\ t_o,\ \Phi_o,\ \theta_N,\ \phi_N) \,. \tag{3.53}$$

In what follows, we shall first give the results of our estimation of the above 10 parameters. Then we shall explain why we expect the measurement error $\Delta\varepsilon$ for tidal coupling would remain roughly the same (i.e., within the same order of magnitude) even if we could include the spin orientation in our estimation.

In Table 3.3, we list the results of our parameter estimation computations for circular inclined orbits at SNR = 10. We have chosen the black-hole spin to be $a = 0.9M$ and along the direction $\theta_S = \pi/3$, $\phi_S = \pi/4$; we have chosen the source direction to be $\theta_N = 3\pi/5$, $\phi_N = \pi/3$. We have examined other choices of the source location and spin orientation, and find that these values give typical results for $\Delta\varepsilon$ (see examples in Table 3.4). Compared with non-precessing circular equatorial orbits, Table 3.3 shows that the correlation between ε and other parameters (μ, M, q) has decreased and the measurement error for various parameters

---

[15] Or we can choose to fix the source locations (θ_N, ϕ_N), in which case we find similar results for the measurement errors.

λ_L	$\Delta\lambda_L$	Δt_o	$\Delta\mu/\mu$	$\Delta M/M$	Δq	$\Delta\varepsilon$	$c^{\varepsilon\mu}$	$c^{\varepsilon M}$	$c^{\varepsilon q}$
$1.4M_\odot$+$50M_\odot$									
$\pi/8$	0.053	0.014	0.98%	1.76%	0.016	1.87	0.352	−0.916	−0.792
$\pi/6$	0.035	0.010	0.74%	1.27%	0.011	1.38	0.085	−0.917	−0.764
$1.4M_\odot$+$100M_\odot$									
$\pi/8$	0.068	0.069	1.22%	2.08%	0.014	2.09	0.155	−0.987	−0.905
$\pi/6$	0.043	0.052	0.93%	1.59%	0.009	1.56	-0.117	−0.985	−0.888
$1.4M_\odot$+$200M_\odot$									
$\pi/8$	0.068	0.286	1.51%	2.37%	0.014	2.34	0.399	−0.988	−0.946
$\pi/6$	0.044	0.221	1.07%	1.90%	0.010	1.78	0.131	−0.982	−0.936

Table 3.3: Measurement errors and correlations for circular inclined orbits with BH spin $a = 0.9M$ and SNR = 10. For the three IMRI systems considered, we consider two orbital inclination angles $\lambda_L = \pi/8, \pi/6$. We have fixed the black-hole spin along the typical direction $\theta_S = \pi/3$, $\phi_S = \pi/4$ and the source direction to be $\theta_N = 3\pi/5$, $\phi_N = \pi/3$; inn this case the angle between the source direction and the spin is about 0.28π.

has decreased significantly. The error for the tidal coupling parameter has dropped to $\Delta\epsilon \sim 1$ to 2,[16] which suggests that Advanced LIGO may measure the deviation of tidal coupling from its Kerr value with modest yet interesting accuracy. For favorable configurations, i.e. a bright source (large SNR) and a favorable choice of source location and spin orientation, the measurement error can be further reduced.

Table 3.4 shows the results for $\Delta\epsilon$ for various choices of source location, spin orientation, and other parameters. The IMRI system being considered consists of an inspiraling $\mu = 1.4M_\odot$ NS and a BH with $M = 100M_\odot$. We mainly look at two different orbital inclination angles: $\lambda_L = \pi/8$ and $\pi/6$, and two black-hole spins: $a = 0.9M$ and $a = 0.3M$. The results show that the measurement error $\Delta\varepsilon$ depends rather sensitively on the source location and spin orientation, but it roughly remains the same to within an order of magnitude for a fixed inclination angle λ_L and black-hole spin a. We note that $\Delta\varepsilon$ becomes quite large for the smaller black-hole spin $a = 0.3M$. A typical number may be $\Delta\varepsilon \sim 50$ for inclination angle $\lambda_L \simeq \pi/6$, and $\Delta\varepsilon \sim 30$ for $\lambda_L \simeq \pi/4$.[17] This is not surprising. For smaller spins, the black-hole energy absorption and its contribution to the wave cycles are much reduced (see Fig. 3.5). At leading order in spin, $\dot{E}_H \simeq (-a/4M)\, v^5 \dot{E}_\infty$ [see Eq. (3.36b)]. For $a = 0.3M$, this predicts that $\dot{E}_H \sim 0.08\% \dot{E}_\infty$ for a $1.4M_\odot + 100M_\odot$ IMRI system in the Advanced LIGO band; hence at $\lambda_L = \pi/6$ the accuracy of measuring the tide-induced energy transfer is approximately $\Delta\dot{E}_H \sim 50 \times 0.08\% \dot{E}_\infty$, i.e. 4% of the power radiated to infinity—still an interesting accuracy for central bodies with anomalously large $\dot{E}_{\rm body}$.

To justify the statement that the above results for $\Delta\varepsilon$ represent Advanced LIGO's accuracy for measuring tidal coupling, we must assess the outcome when we include the "degenerate" directions, i.e. the spin orientation (θ_S, ϕ_S), into our parameter space. We regard this not as a numerical problem of correctly inverting ill-conditioned Fisher matrices; rather, the vanishing singular values of the Fisher matrices indicate a lack of

---

[16] If we consider all the samples in Table 3.4, the error $\Delta\varepsilon$ acutally ranges from ~ 1 to 6 for configurations with $a = 0.9$ and $\lambda_L = \pi/6$.

[17] For $\lambda_L = \pi/4$, the inclination angle significantly violates the $\lambda_L \ll 1$ assumption underlying our computations. Nevertheless we extrapolate our results to $\lambda_L = \pi/4$ to get a rough estimate of what the typical parameter extraction accuracies might be.

Source direction and spin orientation					$a = 0.9M$		$a = 0.3M$		
θ_N	ϕ_N	θ_S	ϕ_S	φ_{NS}	$\Delta\varepsilon_{\ \lambda_L=\pi/8}$	$\Delta\varepsilon_{\ \lambda_L=\pi/6}$	$\Delta\varepsilon_{\ \lambda_L=\pi/8}$	$\Delta\varepsilon_{\ \lambda_L=\pi/6}$	$\Delta\varepsilon_{\ \lambda_L=\pi/4}$
$\pi/10$	$\pi/6$	$\pi/6$	$\pi/4$	0.07π	7.20	5.99	61.4	79.6	116.
$\pi/4$	$\pi/6$	$\pi/12$	$\pi/4$	0.17π	5.56	–	74.0	67.9	39.4
$3\pi/5$	$\pi/3$	$\pi/4$	$\pi/4$	0.18π	1.83	1.36	59.4	32.2	34.7
$\pi/4$	$\pi/6$	$5\pi/12$	$\pi/4$	0.18π	5.11	4.34	30.6	22.4	28.4
$\pi/10$	$\pi/6$	$\pi/3$	$\pi/4$	0.24π	2.81	2.37	49.0	26.9	9.48
$3\pi/5$	$\pi/3$	$\pi/3$	$\pi/4$	0.28π	2.09	1.56	97.2	59.8	22.1
$\pi/20$	$\pi/6$	$8\pi/20$	$\pi/4$	0.35π	1.62	1.47	38.1	28.1	41.6
$3\pi/5$	$\pi/6$	$\pi/4$	$\pi/4$	0.36π	1.76	1.34	77.7	32.3	34.5
$3\pi/5$	$2\pi/3$	$\pi/3$	$\pi/4$	0.48π	4.88	4.26	182.	101.	58.3
$\pi/20$	$\pi/6$	$11\pi/20$	$\pi/4$	0.50π	7.05	4.51	94.8	66.1	32.6
$\pi/10$	$\pi/6$	$3\pi/5$	$\pi/4$	0.50π	7.07	4.54	91.6	66.0	32.8
$3\pi/5$	$4\pi/5$	$\pi/4$	$\pi/4$	0.60π	2.77	1.90	82.2	42.3	21.4
$3\pi/5$	$8\pi/5$	$\pi/4$	$\pi/4$	0.68π	2.01	1.34	75.2	44.1	40.8

Table 3.4: Samples of measurement error $\Delta\varepsilon$ for various source directions, spin orientations and spin magnitudes, and orbital inclination angles. The IMRI system consists of an inspiraling $\mu = 1.4M_\odot$ NS and BH with $M = 100M_\odot$.

information. Our precessional waveform is constructed based on the output of a *single* detector. Although the waveform modulation carries extra information of the central body's spin, it also introduces unknown *geometric factors* (the source location and spin orientation), whose information cannot be extracted effectively from a single detector's output. For our problem, the degeneracy between the source location and spin orientation could be overcome by, e.g., using a network of ground-based detectors to enhance the resolution of the geometric factors. Such enhancement will lead to a "recovery" of the spin orientation into our parameter space—i.e., the full Fisher matrix should be well-behaved. The inclusion of the spin orientation should not, at least not significantly, "dilute" the information from tidal coupling and deteriorate the measurement error of ε. This is because the geometric factors only correlate weakly with ε—this is supported by our results for the 10-dimensional parameter set $\alpha^{(10)}$, where the correlation between ε and (θ_N, ϕ_N) is typically $\lesssim 0.2 \sim 0.5$.

Appendices

3.A SARSAF spacetimes that differ from Kerr

This appendix presents results of the author's work on SARSAF spacetimes—results that underlie portions of the forthcoming paper [1] and [2]. In particular, in this appendix we first introduce the Ernst formalism and describe how the familiar Schwarzschild and Kerr solutions can be derived from it. We then introduce Manko and Novikov's [32] application of the HKX (Hoenselaers-Kinnersley-Xanthopoulos) transform [64], a solution generation technique, and use their prescription to construct a family of metrics parametrized by the mass quadrupole moment, which are used in papers [1] and [2]. Higher moments of these metrics are calculated and compared with those of the Kerr solution. Next we review previous and ongoing studies on the effects of the quadrupole moment that might be useful in testing the black-hole no-hair theorem. Specializing to the Manko-Novikov spacetime, we calculate the periapsis precession rate for equatorial orbits as a function of the semi-latus rectum (p). Our results, which are summarized in [2], show that moments of different order appear first at different powers of p, in agreement with Collins and Hughes' study [28] for static bumpy black-holes and with Ryan's study [16] of nearly-circular orbits in general SARSAF spacetimes.

3.A.1 Exact vacuum solutions: The Manko-Novikov Spacetime

Stationary, axisymmetric gravitational fields can be described by the Papapertrou line element, which is given in prolate spheroidal coordinates by

$$ds^2 = -f(dt-\omega d\phi)^2 + k^2 f^{-1} e^{2\gamma}(x^2-y^2)\left(\frac{dx^2}{x^2-1}+\frac{dy^2}{1-y^2}\right) + k^2 f^{-1}(x^2-1)(1-y^2)d\phi^2. \quad (3.54)$$

Here k is a real constant; f, ω and γ are functions of x and y only, and prolate spheroidal coordinates are related to familiar cylindrical coordinates of an auxiliary, unphysical flat space, by

$$\rho = k(x^2-1)^{1/2}(1-y^2)^{1/2}, \qquad z = kxy. \quad (3.55)$$

The metric functions f and ω are governed by a set of equations that can be obtained by performing functional derivatives on the Lagrangian density of the gravitational field [65]. These quantities are often written in terms of the complex Ernst potential

$$\mathscr{E} \equiv f + i\varphi. \tag{3.56}$$

Here the auxiliary function φ is independent of azimuth and satisfies

$$f^{-2}\nabla\varphi = -\rho^{-1}\vec{n}_\phi \times \nabla\omega\,, \tag{3.57}$$

in which $\vec{n}_\phi$ is a unit vector in the azimuthal direction of the auxiliary flat space and ∇ is the (flat-space) three-dimensional divergence operator.[18] The field equations governing function f and ω can then be written in terms of the Ernst potential as

$$(\mathrm{Re}\,\mathscr{E})\,\nabla^2\mathscr{E} = \nabla\mathscr{E}\cdot\nabla\mathscr{E}. \tag{3.58}$$

Given f and ω, the function γ can then be computed from a set of first-order differential equations (see, e.g. Eq. (4) in [32]). In the static limit when $\omega = 0$, the Ernst potential becomes real, $\mathscr{E} = f$, and the metric (3.54) takes the familiar Weyl form in cylindrical coordinates

$$ds^2 = -e^{2\psi}dt^2 + e^{2(\gamma-\psi)}(d\rho^2 + dz^2) + e^{-2\psi}\rho^2 d\phi^2. \tag{3.59}$$

Here we have set $f = e^{2\psi}$, where ψ is the so-called static Weyl function, satisfying the simple Laplace equation $\nabla^2\psi = 0$ [a result from Eq. (3.58)]. The Schwarzschild solution is obtained by taking ψ to be the Newtonian gravitational field of a line mass in the auxiliary space (see, e.g., Ref. [66])

$$\psi_S = \frac{1}{2}\log\frac{x-1}{x+1} = \frac{1}{2}\log\frac{\sqrt{\rho^2+(k-z)^2}-(k-z)}{\sqrt{\rho^2+(k+z)^2}+(k+z)}, \tag{3.60a}$$

$$\gamma_S = \frac{1}{2}\log\frac{x^2-1}{x^2-y^2} = \frac{1}{2}\log\frac{\left(\sqrt{\rho^2+(z-k)^2}+\sqrt{\rho^2+(z+k)^2}\right)^2-4k^2}{4\sqrt{\rho^2+(z-k)^2}\,\sqrt{\rho^2+(z+k)^2}}. \tag{3.60b}$$

For the solution (3.60), the metric (3.59) can be brought into the usual Schwarzschild form by a further transformation into the Schwarzschild coordinates (r_S, θ_S) defined by $\rho = \sqrt{r_S(r_S-2k)}\sin\theta$ and $z = (r_S - k)\cos\theta_S$.

In Ernst's original paper [65], an exact solution of (3.58) was found and was manifestly shown to be equivalent to the Kerr solution. The solution is

$$\mathscr{E}_K = f_K + i\varphi_K = \frac{x\cos\lambda + iy\sin\lambda - 1}{x\cos\lambda + iy\sin\lambda + 1}, \tag{3.61}$$

---

[18] It can be reduced to two dimensions, since the metric functions only depend on x and y. The explicit form of ∇ in terms of x and y can be found in [32].

where the parameter λ is a real number and is related to the Kerr mass and spin by

$$\sec\lambda = M/k\,, \quad \tan\lambda = a/k\,. \tag{3.62}$$

To transform into the Boyer-Lindquist coordinates (r, θ), we identify

$$r = kx + M\,, \quad \cos\theta = y\,, \tag{3.63}$$

together with $k = (M^2 - a^2)^{1/2}$. In [65], Ernst also considered a perturbation treatment to solve for Eq. (3.58), and speculated that the perturbation theory could be a guide to discover a class of more complicated solutions in which the Kerr solution (3.61) is only a special case. While today we know that there indeed exist large families of exact solutions for stationary, axisymmetric and asymptotically flat spacetimes, the various solution techniques developed in the 1970s largely arise from the existence of symmetry group of transformations that preserve the field equations [26].

One of the solution generation techniques is the HKX transformation, which provides a way to generate new stationary, axisymmetric solutions from the static Weyl solutions.[19] Manko and Novikov's solution generation scheme [32], which can be derived from the HKX transformation, gives the following formulas to describes the non-linear superposition of the Kerr spacetime with arbitrary static vacuum Weyl fields:

$$\mathscr{E} = e^{2\psi} A_-/A_+\,, \tag{3.64a}$$

$$A_\mp = x(1+ab) + iy(b-a) \mp (1-ia)(1-ib). \tag{3.64b}$$

Here ψ is any solution of the flat-space Laplace equation and is chosen to be a set of ordinary Weyl multipoles

$$\psi = \sum_{n=1}^{\infty} \beta_n \psi_n = \sum_{n=1}^{\infty} \beta_n R^{-n-1} P_n(xy/R), \qquad \text{with } R \equiv (x^2 + y^2 - 1)^{1/2},\ \beta_n = \text{constant}. \tag{3.65}$$

The function a [not to be confused with the spin parameter in the Kerr metric!] and b depend on (x, y) and satisfy a set of first-order differential equations that guarantee the original Ernst equation (3.58) is satisfied by the right hand side of (3.64a). It is worthwhile to note that: (i) ψ does not contain the Schwarzschild solution ψ_S and it only represents the static Weyl fields with mass multipoles $\ell \geq 1$. (ii) Nonzero a and b indicate the presence of rotation. (iii) The Schwarzschild solution corresponds to the case $\psi = a = b = 0$ and the Kerr solution corresponds to $\psi = 0$, $a = -b =$ constant.

---

[19] See [67, 68] for a brief introduction; also see [64, 69] for the original development of the subject. To give a brief summary, (i) Geroch [70] first showed how to generate infinite parameter families of stationary, axisymmetric solutions of the Einstein's equation (Group "G"). (ii) Kinnersley and Chitre examined different symmetry groups of the field equations and their relation to each other in their paper I [69]. In paper II, they identified four one-index potentials that reduce the field equations to a linear problem. Based on those four potentials, they constructed an infinite *hierarchy* of two-index potentials and found the symmetry group K ($G \subset K$) that characterize their transformation. New solutions can be obtained once the hierarchy of potentials is known. (iii) In paper III they introduce a generating function $F(t)$ to calculate the one-index potential (the two-index potential can be eliminated). The linear function that governs $F(t)$ was identified. (iv) Finally, they showed that the generating function $F(t)$ (and $G(t)$ defined in [64]) describe the "motion" in solution space from knowledge of symmetry groups.

In connection with the research that I report in [1, 2] with my coauthors, I have computed the relativistic multipole moments for the Manko-Novikov solution (3.64). To do so, I adopt the recurrence formula derived by Quevedo (see Appendix of [71]). Quevedo's formula presents the relation between the Ernst potential of a given metric and its multipole moment, which was originally found by Hoenselaers. Following his procedure, the multipole moments of solution (3.64) are found to be[20]

$$\begin{array}{rlrl}
M_0 = & k(1+\alpha^2)/(1-\alpha^2), & J_0 = & 0, \\
M_1 = & -k^2\beta_1, & J_1 = & -2\alpha k^2(1+\alpha^2)/(1-\alpha^2)^2, \\
M_2 = & -k^3[\beta_2 + 4\alpha^2(1+\alpha^2)(1-\alpha^2)^{-3}], & J_2 = & 4\alpha\beta_1 k^3/(1-\alpha^2), \\
M_3 = & k^4[-\beta_3 + \beta_1(\alpha^4+10\alpha^2+1)(1-\alpha^2)^{-2}], & J_3 = & 4\alpha k^4[\beta_2 + 2\alpha^2(1+\alpha^2)(1-\alpha^2)^{-3}]/(1-\alpha^2), \\
M_4 = & \ldots\,, & J_4 = & \ldots\,.
\end{array} \tag{3.66}$$

Here α is the asymptotic value of $-a(x,y)$ and $b(x,y)$ when x is large. The two parameters, α and k, which can be mapped into M and a (black hole spin parameter), determine the full set of Kerr multipole moments. The β_n terms add anomalousness to the Kerr moments. It can be seen from Eq. (3.66) that, to obtain an extra piece of the mass quadrupole moment M_2, we need to choose a nonzero "anomalous" β_2.

Let ψ_2 be the Weyl quadrupole field associated with this β_2:

$$\psi_2 = \beta_2 R^{-3} P_2\left(xy/R\right). \tag{3.67}$$

Then the auxiliary potentials defined in Eq. (11) and (12) of [32] are found to be

$$\psi' \;=\; \psi_S + \psi_2 = \frac{1}{2}\ln\frac{x-1}{x+1} + \frac{\beta_2(3x^2y^2 - x^2 - y^2 + 1)}{2(x^2+y^2-1)^{5/2}}, \tag{3.68a}$$

$$\begin{aligned}\gamma' \;=\; & \frac{1}{2}\log\frac{x^2-1}{x^2-y^2} + \frac{\beta_2 x}{R^5}\left(2x^4 - 5x^2 + 5x^2y^2 + 3 - 3y^2\right) - 2\beta_2 \\ & + \frac{3\,\beta_2^2}{8R^{10}}\left[\frac{x^2y^2(5x^2y^2 - 3R^2)^2}{R^2} - \left(3x^2y^2 - R^2\right)^2\right],\end{aligned} \tag{3.68b}$$

and functions $a(x,y)$ and $b(x,y)$ can be computed according to Eq (13) of Ref. [32]:

$$a(x,y) \;=\; -\alpha\exp\left(-2\beta_2\left(-1 + \sum_{\ell=0}^{2}\frac{(x-y)P_\ell}{R^{\ell+1}}\right)\right) \sim\; -\alpha + \mathcal{O}\left(1/x^3\right), \tag{3.69}$$

$$b(x,y) \;=\; \alpha\exp\left(2\beta_2\left(1 + \sum_{\ell=0}^{2}\frac{(-1)^{1-\ell}(x+y)P_\ell}{R^{\ell+1}}\right)\right) \sim\; \alpha + \mathcal{O}\left(1/x^3\right). \tag{3.70}$$

Equations (3.68b), (3.69) and (3.70) can then be inserted into expression (9) of [32], and finally the metric functions are obtained. With a furhter transformation into Boyer-Linquist coordinates, the metric functions

---

[20] There seems to be a typo in the expression for M_2 in Ref. [32]: the last α_2 should be α^2.

can be written as

$$\begin{aligned}
f &= f_K + \frac{\beta_2}{r^3}\left(1+\frac{M}{r}\right)\left(M^2-a^2\right)^{3/2}(3\cos^2\theta-1) + \frac{\beta_2}{2r^5}\left(M^2-a^2\right)^{3/2}\Big[4a^2\cos^2\theta\,(3-5\cos^2\theta) \\
&\qquad -3M^2(1-6\cos^2\theta+5\cos^4\theta)\Big] + O\left(r^{-6}\right), \qquad (3.71a) \\
\omega &= \omega_K\left[1-\frac{\beta_2\left(M^2-a^2\right)^{3/2}(5\cos^2\theta-1)}{Mr^2} - \frac{\beta_2\left(M^2-a^2\right)^{3/2}(47\cos^2\theta-11)}{4r^3} + O\left(r^{-4}\right)\right], \qquad (3.71b) \\
e^{2\gamma} &= e^{2\gamma_K}\left[1+\frac{\beta_2}{r^4}\left(\frac{3}{2}+\frac{6M}{r}\right)M(M^2-a^2)^{3/2}(5\cos\theta^2-1)\sin\theta^2 + O\left(r^{-6}\right)\right]. \qquad (3.71c)
\end{aligned}$$

Here f_K, ω_K and γ_K denote the original Kerr functions

$$\begin{aligned}
f_K &= 1-\frac{2Mr}{r^2+a^2\cos^2\theta}, \qquad (3.72a) \\
\omega_K &= \frac{2aMr\sin^2\theta}{r^2-2Mr+a^2\cos^2\theta}, \qquad (3.72b) \\
e^{2\gamma_K} &= 1-\frac{M^2\sin^2\theta}{(M-r)^2-(M^2-a^2)\cos^2\theta}. \qquad (3.72c)
\end{aligned}$$

It can be deduced from Eq. (3.66) that the deviation of the mass quadrupole moment from the Kerr value is

$$\Delta M_2 = \beta_2(M^2-a^2)^{3/2}, \qquad (3.73)$$

and that higher moments (J_3, M_4, ...) also depart from the "Kerr value". It is interesting to note that regardless of the magnitude of β_2, the deviation always goes to zero for the extreme Kerr case ($a = M$). The ratio of the deviation to the Kerr quadrupole moment is

$$\frac{\Delta M_2}{M_{2,K}} = \beta_2\,\frac{(M^2-a^2)^{3/2}}{Ma^2}. \qquad (3.74)$$

This is a decreasing function of a. Note that the next multipole that differs from Kerr's is J_3 [J_2 and M_3 retain vanishing Kerr values because the spacetime remains reflection symmetric; see Eq. (3.66)] the factional difference for J_3 is

$$\frac{\Delta J_3}{J_{3,K}} = 2\beta_2\,\frac{(M^2-a^2)^{3/2}}{Ma^2}, \qquad (3.75)$$

which is twice that for the mass quadrupole moment.

3.A.2 Effects of the anomalous mass quadrupole moment

In many ways, the Kerr spacetime is a "neat" geometric entity. It is of Petrov type D and admits three isolating integrals of motion for the geodesic equation. In the Kerr background, the first order perturbation equation (the Teukolsky equation) decouples into four ordinary differential equations. However, these miracles are likely to disappear when we introduce an anomalous mass quadrupole moment. If the third integral of motion is lost, the geodesic motion may become ergodic. Guéron and Letelier [33] have shown that in somewhat similar, static and stationary spacetimes with adjustable mass quadrupole M_2, chaos occurs on some bound geodesics. Such an onset of chaos could have a great impact on gravitational wave data analysis. Numerical studies of the influence of M_2 on geodesic orbits and gravitational waveforms are under way [2, 34, 63]

Past analytic studies of the influence of the mass quadrupole have largely focused on geodesic motion in the equatorial plane, in which case the possible loss of the third integrals does not matter. In [28], Collins and Hughes constructed a bumpy black hole spacetime via the Weyl formalism. The procedure involves superimposing an extra perturbative mass distribution—a pair of points each with positive mass $\mu/2$ at the poles and a ring of negative mass $-\mu$ around the equator—onto the Schwarzschild solution. The pair of point mass and ring of mass are all at distance b away from the origin of the Weyl coordinates. The net result is a spacetime that is a almost Schwarzschild, but with a nonzero quadrupole and higher mass moments. However, this bumpy solution is not an exact solution to the vacuum field equations. Collins and Hughes assumed that the Weyl potential ψ_μ due to the mass distribution is small compared to ψ_M of the Schwarzschild solution; after linearizing the Einstein equations for the other metric function γ, they were able to obtain γ in compact analytic form. Although the γ function in the Collins-Hughes metric is not an exact solution, the Ernst potential is solely determined by ψ, the exact Weyl potential. From ψ we can compute the relativistic multipole moments of the Collins-Hughes spacetime by treating it as an exact solution:

$$M_o^{\mathrm{CH}} = M, \quad M_2^{\mathrm{CH}} = \frac{3}{2}\,\mu b^2, \quad M_4^{\mathrm{CH}} = \frac{1}{8}\,ub^2(5b^2 - 12M^2), \quad \ldots, \quad J_i = 0\,. \tag{3.76}$$

For equatorial orbits in the weak-field limit, Collins and Hughes found that the periapse phase shift due to the mass quadrupole moment is (Eq. (7.2) in [28])

$$\Delta\phi^{\mathrm{CH}}_{\mathrm{quad}} = \frac{9\pi\mu b^2}{2Mp^2} = \frac{3\pi M_2^{\mathrm{CH}}}{Mp^2}. \tag{3.77}$$

We have performed the same weak-field analysis for Manko-Novikov spacetime, and found the total periapse phase shift to be

$$\Delta\phi^{MN} \quad = \quad \frac{6\pi M_o}{p} + \frac{8\pi J_1}{M_o^{1/2}p^{3/2}} + \frac{3\pi M_o^2}{2p^2}(18+\epsilon^2) + \frac{3\pi M_2}{M_o p^2} + \mathcal{O}\left(M_o^3/p^3\right). \tag{3.78}$$

This result is consistent with the CH shift (3.77). Notice that the mass monopole, current dipole, and mass quadrupole moments first appear at orders p^{-1}, $p^{3/2}$, and p^{-2}.

3.B ACST waveforms

In this appendix, we shall summarize the analysis of spin-induced orbital precession and its modulation of gravitational waveforms, by Apostolatos et al. (ACST) [36]. We then apply their analysis to IMRIs, in which case the spin of the companion mass can be ignored (ACST call this "*simple precession*"), and give analytical solutions for the precessional phase correction $\delta\Phi$ and the polarization phase φ that are needed in the body of this chapter [see expression (3.42) in Sec. 3.3.3 and Eq. (3.86) below].

3.B.1 Construction of ACST waveforms

The general procedure to compute the gravitational-wave strain from a binary at the detector output involves identifying three interrelated frames (see, e.g., discussions in [48]): (i) the *source frame* attached to the binary; (ii) the *radiation frame* attached to the direction from the source to the detector; and (iii) the *detector frame* attached to the detector itself. Figure 3.7 gives a schematic illustration of the three.

We set up the detector frame as in Fig. 3.7: the x- and y-axes are along the two detector arms. In the detector frame, the direction of the source $\hat{\boldsymbol{N}}$ is described by two angles: θ_N and ϕ_N; the direction of the black-hole spin $\hat{\boldsymbol{S}}$ is described by angles θ_S and ϕ_S (not shown).

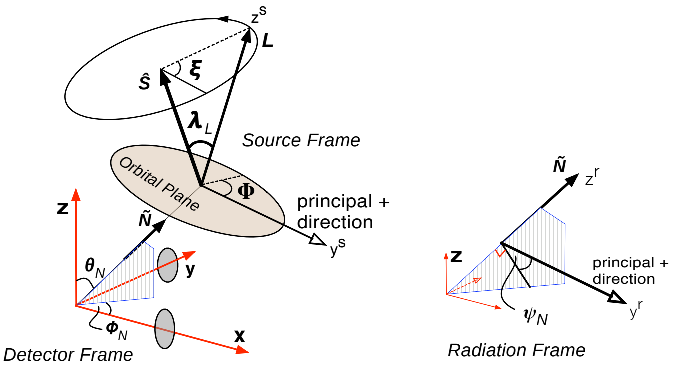

Figure 3.7: Schematic illustration: Precession of the orbital angular momentum $\boldsymbol{L}$ around the spin of the black hole $\boldsymbol{S}$. Here λ_L is the (constant) angle between $\boldsymbol{L}$ and $\boldsymbol{S}$; the angle ξ describes the accumulative rotation of $\boldsymbol{L}$. In the detector's frame, the $\boldsymbol{x}$ and $\boldsymbol{y}$ direction are along the detector's two arms. The vector $\hat{\boldsymbol{N}}$ points to the source, specified by polar angle θ_N and azimuthal angle ϕ_N.

Following ACST, we set up the source frame by (i) identifying the vector $\hat{\boldsymbol{z}}^s$ to be along the direction of the orbital angular momentum $\boldsymbol{L}$ and (ii) setting $\hat{\boldsymbol{y}}^s \propto \pm\hat{\boldsymbol{N}}\times\hat{\boldsymbol{L}}$ (ACST call it the "*principal* +" direction). The radiation frame is chosen such that $\hat{\boldsymbol{z}}^r = \hat{\boldsymbol{N}}$ and $\hat{\boldsymbol{y}}^r = \hat{\boldsymbol{y}}^s$. With these choices, the gravitational fields h_+ and $h_\times$ in the transverse-traceless (TT) gauge will have a relative phase delay of precisely $\pm\pi/2$. Specifically, they take the following form at the leading post-Newtonian order (Eq. (2) in [36])

$$h_+(t) = -\frac{2\mu M}{rD}\left[1+\left(\hat{\boldsymbol{L}}(t)\cdot\hat{\boldsymbol{N}}\right)^2\right]\cos 2\Phi(t)\,, \tag{3.79}$$

$$h_\times(t) = -\frac{2\mu M}{rD}\left[-2\,\hat{\boldsymbol{L}}(t)\cdot\hat{\boldsymbol{N}}\right]\sin 2\Phi(t)\,, \tag{3.80}$$

where D is the distance to the binary [cf. Eq. (3.32a)] and $\Phi(t)$ is the accumulated orbital phase shift. Notice that the amplitude modulation is embodied in the time-varying dot product $\hat{\boldsymbol{L}}\cdot\hat{\boldsymbol{N}}$.

The gravitational-wave strain at the detector output is $h(t) = h_+(t)\,F_+ + h_\times(t)\,F_\times$, where $F_{+,\times}$ are the detector response (beam-pattern) functions introduced earlier in Eq. (3.4). We rewrite them here:

$$F_+(\theta_N,\phi_N,\psi_N) = \frac{1}{2}(1+\cos^2\theta_N)\cos 2\phi_N\cos 2\psi_N - \cos\theta_N\sin 2\phi_N\sin 2\psi_N\,, \tag{3.81a}$$

$$F_\times(\theta_N,\phi_N,\psi_N) = \frac{1}{2}(1+\cos^2\theta_N)\cos 2\phi_N\sin 2\psi_N + \cos\theta_N\sin 2\phi_N\cos 2\psi_N\,. \tag{3.81b}$$

Here ψ_N is the polarization angle, the angle from the principal+ direction, clockwise in the plane of the sky to the direction of constant azimuth (see Fig. 3.7; also see Fig. 1 in Ref. [36])

$$\psi_N = \tan^{-1}\left(\frac{\hat{\boldsymbol{L}}\cdot\hat{\boldsymbol{z}} - (\hat{\boldsymbol{L}}\cdot\hat{\boldsymbol{N}})\,(\hat{\boldsymbol{z}}\cdot\hat{\boldsymbol{N}})}{\hat{\boldsymbol{N}}\cdot(\hat{\boldsymbol{L}}\times\hat{\boldsymbol{z}})}\right)\,. \tag{3.82}$$

As the orbital plane precesses, the principal+ direction varies accordingly; hence the polarization angle ψ_N is also time-varying—contributing to the modulation of the output signal. More explicitly, the combined gravitational strain $h(t) = h_+(t)\,F_+ + h_\times(t)\,F_\times$ can be written as

$$h(t) = -\frac{2\mu M}{rD}A_p(t)\,\cos\left[2\Phi(t) + \varphi(t)\right]\,, \tag{3.83a}$$

where $A_p(t)$ is the polarization amplitude and the angle φ is the signal's polarization phase [Eq. (7b) in [36]]:

$$A_p(t) = \left(\left[1+(\hat{\boldsymbol{L}}(t)\cdot\hat{\boldsymbol{N}})^2\right]^2 F_+^2(\theta_N,\phi_N,\psi_N) + 4\left[\hat{\boldsymbol{L}}(t)\cdot\hat{\boldsymbol{N}}\right]^2 F_\times^2(\theta_N,\phi_N,\psi_N)\right)^{1/2}\,, \tag{3.83b}$$

$$\varphi = \tan^{-1}\left(\frac{2(\hat{\boldsymbol{L}}(t)\cdot\hat{\boldsymbol{N}})\,F_\times(\theta_N,\phi_N,\psi_N)}{[1+(\hat{\boldsymbol{L}}(t)\cdot\hat{\boldsymbol{N}})^2]F_+(\theta_N,\phi_N,\psi_N)}\right)\,. \tag{3.83c}$$

Equations (3.83) contains information about amplitude modulation from $h_+(t)$ and $h_\times(t)$, as well as the change of ψ_N as a function of time.

Besides the modulating polarization phase, Apostolatos et al. show that there is an additional modulation of the waveform phase appearing in the azimuthal angle Φ. Recall that the definition of Φ depends explicitly on the direction $\hat{\boldsymbol{L}}$, which is time varying as the orbital angular momentum precesses around the total angular momentum. Hence we can decompose Φ into two pieces: one whose definition does not depend on the change of $\hat{\boldsymbol{L}}$; the other whose definition reflects the change of orientation of the orbital plane. More explicitly,

$$\Phi(t) \quad = \quad \Phi_c(t) \; + \; \delta\Phi(t) \; . \tag{3.84a}$$

Here Φ_c is the "carrier phase" defined as the integral of the small body's orbital angular velocity Ω in the orbital plane.

$$\Phi_c(t) \quad \equiv \quad \int \Omega(t)\, dt \; . \tag{3.84b}$$

This is the piece that involves *explicitly* the orbital precession (although the time evolution of Ω can depend on spin-orbit coupling via radiation reaction). An additional modulation is embodied in the second term $\delta\Phi$, which is the *precessional correction* to the orbital phase and is given by the integral (Eq. (29) in [36])

$$\delta\Phi(t) \quad = \quad - \int_t^{t_c} \left(\frac{\hat{\boldsymbol{L}} \cdot \hat{\boldsymbol{N}}}{1 - (\hat{\boldsymbol{L}} \cdot \hat{\boldsymbol{N}})^2} \right) \left(\hat{\boldsymbol{L}} \times \hat{\boldsymbol{N}} \right) \cdot \dot{\hat{\boldsymbol{L}}}\, dt' \; . \tag{3.84c}$$

Here the boundary condition that $\delta\Phi = 0$ at the end point of the coalescence (i.e., at time t_c) is used.

ACST approximate the Fourier transformation of the waveform (3.83a) by using the stationary phase approximation (see Eq. (38) in [36]). The resulting frequency-domain waveform contains both phase modulation and amplitude modulation from spin-induced orbital precessions. To simplify our calculations, we shall ignore the amplitude modulation (which is fairly unimportant for gravitational-wave parameter extimation) and write down the waveform as[21]

$$\tilde{h}(f) \propto f^{-7/6} \exp\left[i \left(\Psi_c(f) - 2\delta\Phi(t_f) - \varphi(t_f) \right) \right] . \tag{3.86}$$

Here the carrier phase Ψ_c is computed in Sec. 3.3.3 and is given by Eq. (3.48). We shall now specialize to the IMRI problem and compute the precessional correction $\delta\Phi$ and the polarization phase φ, which are used in the body of this chapter (Sec. 3.3.3).

---

[21] ACST give the frequency-domain waveform as [Eq. (38) in [36]]

$$\tilde{h}(f) \approx \frac{1}{2} \Lambda(t_f) \tilde{h}_c(f) + \frac{1}{4\pi i} \frac{d\Lambda}{dt} \left[\frac{d\tilde{h}_c(f)}{df} - 2\pi\, i\, t\, \tilde{h}_c(f) \right] \qquad \text{for } f > 0 \; . \tag{3.85a}$$

The carrier waveform in the frequency domain $\tilde{h}_c$ is given in Eq. (3.33) [cf. Eq. (35) in [36]]. The complex modulation factor is defined as [Eq. (36) in [36]]

$$\Lambda(t) \equiv A(t) \left[\frac{\mu M}{rD} \right]^{-1} \exp\left[-2i\, \delta\Phi(t) - i\varphi(t) \right] . \tag{3.85b}$$

Equations (3.85) are obtained by applying the stationary phase approximation *twice* to the Fourier transformation of $h(t)$ [Eq. (3.83a)]. Note that the phase of $\tilde{h}(f)$ in Eq. (3.85a) is the same as that in Eq. (3.86).

3.B.2 Expression for the polarization phase and precessional correction

In Sec. 3.3.3, we have used the energy flux of gravitational waves from circular inclined orbits to derive an expression for Ψ_c. To fully describe the phase evolution of the waveform [Eq. (3.86)], we need to obtain the precessional correction $\delta\Phi$ and the polarization phase φ from Eq. (3.84c) and Eq. (3.83c), respectively. The key quantity that determines $\delta\Phi$ and φ is the time-evolving $\hat{\boldsymbol{L}}$, the direction of the orbital angular momentum.

ACST introduced post^2-Newtonian precession equations for the orbital angular momentum $\boldsymbol{L}$ and the spin angular momentum, $\boldsymbol{S}$ and $\boldsymbol{S}'$, of the two bodies in the binary. They showed that when the spin of one body is negligible ($\boldsymbol{S}' \simeq 0$), as in the case for an IMRI, the precessional equations simplify considerably. The result is that both the total spin (i.e., $\boldsymbol{S}$) and its projection on the orbital angular momentum are constants of motion:

$$\dot{\boldsymbol{S}}(t) = 0\,, \tag{3.87a}$$

$$\hat{\boldsymbol{L}}(t)\cdot\boldsymbol{S}(t) = \text{constant}. \tag{3.87b}$$

We shall define the constant angle (i.e. the orbital inclination angle) between $\boldsymbol{L}$ and $\boldsymbol{S}$ to be λ_L: $\hat{\boldsymbol{L}}\cdot\hat{\boldsymbol{S}} \equiv \cos\lambda_L$. Further more $\hat{\boldsymbol{L}}$ can be shown to precess around $\boldsymbol{S}$ at angular velocity $\Omega_p(t) = 2S/r^3(t)$, where $S = |\boldsymbol{S}|$ is the magnitude of the black-hole spin,

$$\frac{d\hat{\boldsymbol{L}}}{dt} = \Omega_p\hat{\boldsymbol{S}}\times\hat{\boldsymbol{L}}\,. \tag{3.88}$$

Note that, not surprisingly, the precession angular velocity Ω_p is the same as the frame dragging rate (i.e., Lense-Thirring precession rate). We define the accumulative rotation angle of $\boldsymbol{L}$ to be (see Fig. 3.7 for illustration)

$$\xi \equiv \Omega_p\, t + \xi_o\,, \tag{3.89}$$

where ξ_o is the initial position of $\hat{\boldsymbol{L}}$ when the IMRI wave enters the Advanced LIGO band. With definition (3.89), the vector $\hat{\boldsymbol{L}}$ takes the following form in the source frame:

$$\hat{\boldsymbol{L}} = \hat{\boldsymbol{S}}\cos\lambda_L + \left(\frac{\hat{\mathfrak{z}} - \hat{\boldsymbol{S}}\cos\theta_S}{\sin\theta_S}\right)\sin\lambda_L\,\cos\xi + \left(\frac{\hat{\boldsymbol{S}}\times\hat{\mathfrak{z}}}{\sin\theta_S}\right)\sin\lambda_L\,\sin\xi\,. \tag{3.90}$$

The total number of precessions that occur after the carrier waves reach frequency f can be estimated by using Eq. (45) from ACST

$$\mathcal{N}_p(f) = \frac{1}{2\pi}\int\Omega_p\,dt \simeq \frac{1.9a}{M}\left(\frac{M}{\mu}\right)\left(\frac{10M_\odot}{M}\frac{10\text{Hz}}{f}\right)^{2/3}\,. \tag{3.91}$$

For a $1.4M_\odot$ NS inspiraling into a $100M_\odot$ IMBH with spin $a = 0.9M$, the number of precessions in the Advanced LIGO frequency band is about 25, as can be seen by setting $f = 10$Hz (Advanced LIGO's lower cut-off frequency).

With $\hat{\boldsymbol{L}}$ specified by Eq. (3.90), it is straightforward to compute the polarization angle ψ_N from Eq. (3.82) and obtain the polarization phase φ according to Eq. (3.83c). To compute the precessional correction $\delta\Phi$, we need to evaluate the integral in Eq. (3.84c). It is useful to note that

$$\left(\frac{\hat{\boldsymbol{L}}\times\hat{\boldsymbol{N}}}{\Omega_p}\right)\cdot\left(\frac{d\hat{\boldsymbol{L}}}{dt}\right) = (\hat{\boldsymbol{L}}\cdot\hat{\boldsymbol{N}})\cos\lambda_L - \hat{\boldsymbol{N}}\cdot\hat{\boldsymbol{S}}\,. \tag{3.92}$$

Hence,

$$\delta\Phi(t) \quad = \quad -\int_t^{t_c}\left(\frac{\hat{\boldsymbol{L}}\cdot\hat{\boldsymbol{N}}}{1-(\hat{\boldsymbol{L}}\cdot\hat{\boldsymbol{N}})^2}\right)\Big[(\hat{\boldsymbol{L}}\cdot\hat{\boldsymbol{N}})\cos\lambda_L - \hat{\boldsymbol{N}}\cdot\hat{\boldsymbol{S}}\Big]\; d(\Omega_p t')\,. \tag{3.93}$$

Notice that when the central IMBH has a non-negligible spin (e.g., $a/M \gtrsim 0.1$), the precessional angular velocity Ω_p changes over a longer time scale than the precession period of $\hat{\boldsymbol{L}}$ precess.[22] Therefore we shall approximate Ω_p as a constant, leaving $\hat{\boldsymbol{L}}\cdot\hat{\boldsymbol{N}}$ as the only time-evolving quantity in the integrand of Eq. (3.93). To facilitate the calculation, we can further decompose the expression for $\hat{\boldsymbol{L}}\cdot\hat{\boldsymbol{N}}$ into

$$\hat{\boldsymbol{L}}\cdot\hat{\boldsymbol{N}} \quad = \quad Q_1\cos\xi + Q_2\sin\xi + Q_3 Q_4\,, \tag{3.94}$$

where the factors Q_i $(i = 1, 2, 3, 4)$ are geometric constants given by

$$Q_1 \quad = \quad \Big[\cos\theta_N - (\hat{\boldsymbol{N}}\cdot\hat{\boldsymbol{S}})\cos\theta_S\Big]\,\frac{\sin\lambda_L}{\sin\theta_S}\,, \tag{3.95a}$$

$$Q_2 \quad = \quad \Big[(\hat{\boldsymbol{S}}\times\hat{z})\cdot\hat{\boldsymbol{N}}\Big]\,\frac{\sin\lambda_L}{\sin\theta_S}\,, \tag{3.95b}$$

$$Q_3 \quad = \quad \cos\lambda_L\,, \tag{3.95c}$$

$$Q_4 \quad = \quad (\hat{\boldsymbol{N}}\cdot\hat{\boldsymbol{S}})\,. \tag{3.95d}$$

With some algebra, the precessional correction can be obtained as

$$\begin{aligned}\delta\Phi(t) \quad &= \quad -\int\frac{Q_1\cos\xi + Q_2\sin\xi + Q_3Q_4}{1-(Q_1\cos\xi + Q_2\sin\xi + Q_3Q_4)^2}\times\Big[Q_3(Q_1\cos\xi + Q_2\sin\xi + Q_3Q_4) - Q_4\Big]\,d\xi \\ &= \quad Q_3\,\xi + (Q_3 - Q_4)\,K_1^{-1}\;\arctan\Big[Q_2/K_1 - (1 + Q_1 - Q_3Q_4)K_1^{-1}\;\tan(\xi/2)\Big] \\ &\qquad - (Q_3 + Q_4)\,K_2^{-1}\;\arctan\Big[Q_2/K_2 + (1 - Q_1 + Q_3Q_4)K_2^{-1}\;\tan(\xi/2)\Big]\,,\end{aligned} \tag{3.96a}$$

---

[22] Since $\Omega_p \sim aM/r^3$, we have $T_\Omega \sim \Omega_p/\dot{\Omega}_p \sim r/\dot{r}$, i.e., Ω_p changes over the radiation reaction time scale: $T_\Omega \sim r^4/\mu M^2$. The normal $\hat{\boldsymbol{L}}$ to the orbital plane precesses around the black-hole spin with period $T_p = 2\pi/\Omega_p \sim r^3/aM \sim M^2/a$. The ratio between the two $T_\Omega/T_p \sim (a/M)(M/\mu)(r/M)^4 > (a/M)(M/\mu)$. When consider a typical IMRI with $M/\mu \gtrsim 100$ and IMBH with moderate spin $a/M \gtrsim 0.1$, we have $T_\Omega/T_p \gtrsim 10$.

where

$$K_1 = \sqrt{(1 - Q_3 Q_4)^2 - Q_1^2 - Q_2^2} = \left|\cos\lambda_L - \cos\theta_N \cos\theta_S - \cos(\phi_N - \phi_S)\sin\theta_N \sin\theta_S\right|, \quad (3.96b)$$

$$K_2 = \sqrt{(1 + Q_3 Q_4)^2 - Q_1^2 - Q_2^2} = \left|\cos\lambda_L + \cos\theta_N \cos\theta_S + \cos(\phi_N - \phi_S)\sin\theta_N \sin\theta_S\right|. \quad (3.96c)$$

3.C Orbital energy and orbital angular frequency for circular inclined orbits

In this appendix, we shall consider circular inclined geodesics in Kerr spacetime and derive the relations (i) between the total conserved orbital energy E and the orbital radius r, and (ii) between the orbital radius r and the orbital angular velocity Ω. Our results are based on the calculation of Shibata et al. [38] and will be valid for small inclination angles. These results are useful for computing the waveform phase Ψ_c in Sec 3.3.3 of this chapter [see Eq. (3.45) and (3.47) above].

Geodesic motion in the Kerr spacetime is governed by a set of first-order differential equations (see, e.g. Refs. [45, 58]):

$$\Sigma\frac{dr}{d\tau} = \pm\sqrt{V_r}, \quad (3.97a)$$

$$\Sigma\frac{d\theta}{d\tau} = \pm\sqrt{V_\theta}, \quad (3.97b)$$

$$\Sigma\frac{d\phi}{d\tau} = V_\phi, \quad (3.97c)$$

$$\Sigma\frac{dt}{d\tau} = V_t, \quad (3.97d)$$

where the various "potentials" are defined by

$$V_r = \left[E(r^2 + a^2) - L_z a\right]^2 - \Delta\left[r^2 + (L_z - aE)^2 + Q\right], \quad (3.98a)$$

$$V_\theta = Q - \cos^2\theta\left[a^2(1 - E^2) + \frac{L_z^2}{\sin^2\theta}\right], \quad (3.98b)$$

$$V_\phi = \frac{L_z}{\sin^2\theta} - aE + \frac{a}{\Delta}\left[E(r^2 + a^2) - L_z a\right], \quad (3.98c)$$

$$V_t = a\left(L_z - aE\sin^2\theta\right) + \frac{r^2 + a^2}{\Delta}\left[E(r^2 + a^2) - L_z a\right]. \quad (3.98d)$$

Here, $\Sigma = r^2 + a^2\cos^2\theta$, and $\Delta = r^2 - 2Mr + a^2$. The constants E, L_z, Q are the three constants of the motion: E is the total conserved orbital energy; L_z is the projection of the orbital angular momentum along the black hole's spin axis; and Q is known as the "Carter constant".

Shibata et al. have studied circular inclined geodesics in the Kerr spacetime. They defined an orbital inclination parameter by (equation (2.64) in [38])

$$y \equiv \frac{Q}{L_z^2 + a^2(1-E^2)^2} \,. \tag{3.99}$$

In the Newtonian limit, this parameter (which we presume to be small) can be identified as $y = \lambda_L^2$ [47], where λ_L is the orbital inclination angle (see Fig. 3.7 in Appendix B). From definition (3.99), we can express Q in terms of y, L_z, E and insert the result into the right hand side of Eq. (3.98). For circular inclined orbits, we must have $V_r = 0$ and $dV_r/dr = 0$. Solving these two equations for E and L_z and keeping terms up to first order in y, we obtain

$$\begin{aligned} E/\mu \;&=\; 1 - \frac{s^2}{2} + \frac{3s^4}{8} - \left(1 - \frac{y}{2}\right) q s^5 + \left[\frac{27}{16} + \frac{q^2}{2}(1-y)\right] s^6 - \frac{9}{2}\left(1 - \frac{y}{2}\right) q s^7 \\ &\quad + \left[\frac{675}{128} + \frac{q^2}{4}(15 - 23y)\right] s^8 - \left[\frac{135}{16}(2-y) + q^2(1-5y)\right] q s^9 + \mathcal{O}(s^{10}) \,, \end{aligned} \tag{3.100}$$

where $s = (M/r)^{1/2}$ and $q = a/M$ is the dimensionless spin. By Eq. (3.100), the orbital energy E is expressed as a function of the orbital radius.

We define the dimensionless orbital angular velocity as $\tilde{\Omega} = M\Omega$. It can be computed from

$$\tilde{\Omega} \;=\; \sqrt{(d\theta/dt)^2 + \sin^2\theta\,(d\phi/dt)^2} \,, \tag{3.101}$$

where $d\theta/dt$ and $d\phi/dt$ are to be solved for circular geodesics with small inclination angles. Their solution can be obtained from Eq. (2.72) and Eq. (2.73) in [38] respectively. Given these solutions, $\tilde{\Omega}$ can be written as (up to first order in y)

$$\tilde{\Omega} \;=\; s^3\left[1 + \frac{1}{2}q(-2+y)s^3 - \frac{3}{4}q^2 y s^4 + q^2(1-2y)s^6 + \frac{9}{4}q^3 y s^7 + \mathcal{O}(s^9)\right] , \tag{3.102}$$

Inverting the above equation, we have

$$\begin{aligned} s \;&=\; \tilde{\Omega}^{1/3}\Big[1 + \frac{1}{6}q(2-y)\tilde{\Omega} + \frac{1}{4}q^2 y\tilde{\Omega}^{4/3} + \frac{1}{9}q^2(2+y)\tilde{\Omega}^2 + \frac{1}{6}q^3 y\tilde{\Omega}^{7/3} + \frac{14}{81}q^3(1+3y)\tilde{\Omega}^3 \\ &\quad - \frac{1}{9}q^4 y\tilde{\Omega}^{10/3} + \frac{35}{243}q^4(1+7y)\tilde{\Omega}^4 - \frac{44}{81}q^5 y\tilde{\Omega}^{13/3} + \mathcal{O}(\tilde{\Omega}^5)\Big] \,. \end{aligned} \tag{3.103}$$

Equation (3.103) has essentially expressed the orbital radius as a function of the orbital angular velocity for small inclination angles. Equations (3.100), (3.102) and (3.103) are what we have used in the text of this chapter [i.e., Eq. (3.45)-(3.47) in Sec. 3.3.3].

Bibliography

[1] D. A. Brown, H. Fang, J. R. Gair, C. Li, G. Lovelace, I. Mandel, and K. S. Thorne, gr-qc/0612060.

[2] J. R. Gair, C. Li, G. Lovelace, I. Mandel, and H. Fang (2006), in preparation.

[3] B. Abbott et al., Phys. Rev. D **72**, 082001 (2005).

[4] B. Abbott et al., Phys. Rev. D **73**, 062001 (2006).

[5] K. S. Thorne, The Scientific Case for Mature LIGO Interferometers. `http://www.ligo.caltech.edu/docs/P/P000024-00.pdf`.

[6] P. E. Lindquist, Advanced LIGO—the next generation. `http://www.ligo.caltech.edu/docs/P/P030019-00/P030019-00.pdf`.

[7] T. Creighton, Advanced LIGO: Sources and astrophysics. `http://www.ligo.caltech.edu/docs/P/P030017-00.pdf`.

[8] M. C. Miller and E. J. M. Colbert, Int. J. Mod. Phys. **D13**, 1 (2004). astro-ph/0308402.

[9] J. R. Gair et al., Class. Quant. Grav. **21**, S1595 (2004).

[10] R. M. O'Leary, F. A. Rasio, J. M. Fregeau, N. Ivanova, and R. O'Shaughnessy, Astrophys. J. 637, 937 (2006), astro-ph/0508224.

[11] E. S. Phinney, private communication.

[12] I. Mandel, D. A. Brown, J. R. Gair, and M. C. Miller, arXiv:0705.0285v1 [astro-ph].

[13] M. Kesden et al., Phys. Rev. D **71**, 044015 (2005).

[14] A. Abramovici, K. S. Thorne, et. al., LIGO: The Laser Interferometer Gravitational Wave Observatory. Science, 256, 325–333 (1992).

[15] K. S. Thorne, ”Gravitational waves”, in *Proceedings of the Snowmass'94 Summer Study on Particle and Nuclear Astrophysics and Cosmology*, edited by E. W. Kolb and R. Peccei (World Scientific, Singapore, 1995).

[16] F. D. Ryan, Phys. Rev. D **52**, 5707 (1995).

[17] C. Li, in preparation.

[18] C. Li and G. Lovelace, gr-qc/0702146.

[19] Y. Mino, Phys. Rev. D **67**, 084027 (2003).

[20] S. Drasco and S. A. Hughes, Phys. Rev. D **69**, 044015 (2004).

[21] R. Geroch, J. Math. Phys. **11**, 2580 (1970).

[22] R. O. Hansen, J. Math. Phys. **15**, 46 (1974).

[23] K. S. Thorne, Rev. Mod. Phys. **52**, 299 (1980).

[24] W. Simon and R. Beig, J. Math. Phys. **24**, 1163 (1983).

[25] B. C. Xanthopulos, J. Phys. A **7**, 1025 (1979).

[26] B. C. Xanthopulos, J. Math. Phys. **22**, 1254 (1981).

[27] F. D. Ryan, Phys. Rev. D **56**, 1845 (1995).

[28] N. A. Collins and S. A. Hughes, Phys. Rev. D **69**, 124022 (2004).

[29] K. Glampedakis and S. Babak, Class. Quant. Grav. **23**, 4167 (2006).

[30] J. B. Hartle and K. S. Thorne, Astroph. J. **153**, 807 (1968).

[31] N. Yunes and J. A. González, Phys. Rev. D **73**, 024010 (2006).

[32] V. S. Manko and I. D. Novikov, Class. Quant. Grav. **9**, 2477 (1992).

[33] E. Guéron and P. S. Letelier, Phys. Rev. E **66**, 046611 (2002).

[34] D. A. Brown, in preparation.

[35] H. Tagoshi, S. Mano, and E. Takasugi, Prog. Theor. Phys., **98**, 829-850 (1997).

[36] T. A. Apostolatos, C. Curtler, G. J. Sussman and K. S. Thorne, Phys. Rev. D **49**, 6274 (1994).

[37] H. Tagoshi, M. Shibata, T. Tanaka, and M. Sasaki, Phys. Rev. D **54**, 1439 (1996).

[38] M. Shibata, M. Sasaki, H. Tagoshi, and T. Tanaka, Phys. Rev. D **51**, 1646 (1995)

[39] K. S. Thorne, in *300 Years of Gravitation*, edited by S. W. Hawkings and W. Israel (Cambridge University Press, Cambridge, England, 1987), p. 330–458.

[40] Numeric simulation data (equivalent strain noise versus frequency) for the advanced LIGO interferometer can be found at `http://emvogil-3.mit.edu/~pf/Bench/hvsf_silica.txt`

[41] B. J. Owen and B. S. Sathyaprakash, Phys. Rev. D **60**, 022002 (1999).

[42] A. Buonanno and Y. Chen, Class. Quant. Grav. **18**, L95 (2001).
A. Buonanno and Y. Chen, Phys. Rev. D **64**, 042006 (2001).
A. Buonanno and Y. Chen, Phys. Rev. D **65**, 042001 (2002).
A. Buonanno and Y. Chen, Class. Quant. Grav. **19**, 1569 (2002).
A. Buonanno and Y. Chen, Phys. Rev. D **67**, 062002 (2003).
A. Buonanno and Y. Chen, Phys. Rev. D **69**, 102004 (2004).

[43] C. Cutler and É. É. Flanagan, Phys. Rev. D **49**, 2658 (1994)

[44] L. S. Finn and K. S. Thorne, Phys. Rev. D **62**, 124021 (2000).

[45] J. M. Bardeen, W. H. Press, and S. A. Teukolsky, ApJ **178**, 347 (1972)

[46] S. A. Hughes, Phys. Rev. D **61**, 084004 (2000).
S. A. Hughes, Phys. Rev. D **64**, 064004 (2001).
K. Glampedakis and D. Kennefick, Phys. Rev. D **66**, 044004 (2002).

[47] K. Glampedakis, S. A. Hughes, and D. Kennefick, Phys. Rev. D **66**, 064005 (2002).

[48] Y. Mino, Phys. Rev. D **67**, 084027 (2003).

[49] S. A. Hughes, S. Drasco, É. É. Flanagan, and J. Franklin, Phys. Rev. Lett. **94**, 221101 (2005).

[50] S. Detweiler, Class. Quant. Grav. **22**, S681 (2005).

[51] L. Blanchet, G. Faye, B. R. Iyer, and B. Joguet, Phys. Rev. D **65**, 061501(R) (2002).
L. Blanchet, B. R. Iyer, and B. Joguet, Phys. Rev. D **71**, 129903(E) (2005).

[52] L. E. Kidder, C. M. Will, and A. G. Wiseman, Phys. Rev. D **47**, R4183 (1993).

[53] E. Poisson, Phys. Rev. D **57**, 5287 (1998).

[54] L. Blanchet, A. Buonanno, and G. Faye, Phys. Rev. D **74**, 104034 (2006).

[55] P. R. Brady, J. D. E. Creighton, and K. S. Thorne, Phys. Rev. D **58**, 061501 (1998).

[56] S. A. Teukolsky and W. H. Press, ApJ **193**, 443 (1972).

[57] S. Drasco and S. A. Hughes, Phys. Rev. D **73**, 024027 (2006).

[58] L. S. Finn, Phys. Rev. D **46**, 5236 (1992).

[59] D. Nicholson and A. Vecchio, Phys. Rev. D **57**, 4588 (1998).

[60] J. Mathews and R. L. Walker, *Mathematical Methods of Physics*, second edition. New York, W. A. Benjamin (1970).

[61] D. V. Gal'tsov, *Radiation reaction in the Kerr gravitational field*, J. Phys. A **15**, 3737 (1982).

[62] E. Berti, A. Buonanno, and C. M. Will, Phys. Rev. D **71**, 084025 (2005).

[63] L. Barack and C. Cutler, gr-qc/0612029.

[64] C. Hoenselaers, W. Kinnersley, and B. C. Xanthopoulos, J. Math. Phys. **20**, 2530 (1979).

[65] F. J. Ernst, Phys. Rev. **167**, 1175 (1968).

[66] H. P. Robertson and T. W. Noonan, *Relativity and Cosmology*. W.B. Saunders Co., Philadelphia (1938).

[67] *Solutions of Einstein's Equations: Techniques and Results*, edited by C. Hoenselaers and W. Dietz, Springer-Verlag (1984).

[68] H. Stephani, D. Kramer, M. Maccallum, C. Hoenselaers, and E. Herlt, *Exact Solutions of Einstein's Field Equations*, second edition, Cambridge University Press (2003).

[69] W. Kinnersley, J. Math. Phys. **18**, 1529 (1977) (I);
W. Kinnersley and D. M. Chitre, J. Math. Phys. **18**, 1538 (1977) (II);
W. Kinnersley and D. M. Chitre, J. Math. Phys. **19**, 1926 (1978) (III);
W. Kinnersley and D. M. Chitre, J. Math. Phys. **19**, 2037 (1978) (IV).

[70] R. Geroch, J. Math. Phys. **13**, 394 (1972).

[71] H. Quevedo, Phys. Rev. D **39**, 2904 (1989).

Chapter 4

Kludge Gravitational Waveforms for a Test Body Orbiting a Kerr Black Hole

One of the most exciting potential sources of gravitational waves (GWs) for low-frequency, space-based GW detectors such as the proposed Laser Interferometer Space Antenna (LISA) is the inspiral of compact objects into massive black holes in the centers of galaxies. The detection of waves from such "extreme mass ratio inspiral" systems (EMRIs) and extraction of information from those waves require template waveforms. The systems' extreme mass ratio guarantees that their waveforms can be determined accurately using black hole perturbation theory. Such calculations are computationally very expensive. There is a pressing need for families of approximate waveforms that can be generated cheaply and quickly but which still capture the main features of true waveforms. In this paper, we introduce a family of such "kludge" waveforms and describe ways to generate them. Different kinds of "kludges" have already been used to scope out data analysis issues for LISA. The models we study here are based on computing a particle's inspiral trajectory in Boyer-Lindquist coordinates, and subsequent identification of these coordinates with flat space spherical polar coordinates. A gravitational waveform may then be computed from the multipole moments of the trajectory in these coordinates, using well known solutions of the linearised gravitational perturbation equations in flat spacetime. We compute waveforms using a standard slow-motion quadrupole formula, a quadrupole/octupole formula, and a fast-motion, weak-field formula originally developed by Press. We assess these approximations by comparing to accurate waveforms obtained by solving the Teukolsky equation in the adiabatic limit (neglecting GW backreaction). We find that the kludge waveforms do extremely well at approximating the true gravitational waveform, having overlaps with the Teukolsky waveforms of 95% or higher over most of the parameter space for which comparisons can currently be made. Indeed, we find these kludges to be of such high quality (despite their ease of calculation) that it is possible they may play some role in the actual search of LISA data for EMRIs.

Adapted from the original manuscript [1] by S. Babak, H. Fang, J.R. Gair, K. Glampedakis, S.A. Hughes, *Kludge gravitational waveforms for a test-body orbiting a Kerr black hole*, published as Phys. Rev. D **75**, 024005 (2007).

4.1 Introduction

The proposed Laser Interferometer Space Antenna (LISA) [2], is expected to provide a variety of high-precision gravitational wave (GW) measurements. One of the most interesting targets for this space-based detector are the GWs generated by stellar-mass compact objects inspiralling into (super)massive black holes [(S)MBHs].[1] Accumulated astrometric observations provide strong support in favor of the existence of a "dark" compact object in the core of every galaxy (for which the central parsec region can be resolved) [3]. With masses ranging between 10^6 and $10^9 M_\odot$ these objects are believed to be massive Kerr black holes [4]. It is also believed that these holes are the "quiet" remnants of an older quasar population [5].

Multi-body interactions in the "cusp" stellar population surrounding these SMBHs can put stellar mass compact objects onto orbits that come close to the central black hole. If the object passes sufficiently close to the (S)MBH, it may be captured and subsequently spiral in by the emission of GWs [6, 7, 8]. Initially, the captured bodies are expected to be on "generic" orbits, i.e., eccentric (with eccentricity $e \approx 1$) and inclined with respect to the central black hole's equatorial plane [6, 9]. These orbits evolve adiabatically due to GW emission, decreasing in eccentricity and periastron while the inclination of the orbit remains approximately constant, but increases slightly (see [10, 11, 12] for approximate descriptions of the full inspiral).

For central black hole masses in the range $10^5 M_\odot \lesssim M \lesssim 10^7 M_\odot$, the GWs emitted during the inspiral will be at frequencies close to the floor of the LISA noise curve ($\sim$ 3 mHz). LISA will detect the bursts of radiation emitted near periapse throughout the inspiral, but these bursts will not be individually resolvable [13] unless they occur in our galaxy [14]. However, during the last few years of inspiral, when the small object is orbiting deep inside the SMBH's gravitational field, GWs are radiated continuously in the LISA band. During this phase, the residual eccentricity is typically at $e \lesssim 0.4$ [10, 11] and the orbital motion will exhibit extreme versions of relativistic effects (e.g., periastron and Lense-Thirring precession). As a consequence, the resulting GW signal will be strongly "colored" by these effects and will take a complicated form [15, 16]. By complicating the waveform, these strong-field effects potentially make data analysis difficult; but, they also encode a great deal of information about the strong field nature of the spacetime. By accurately measuring all of these effects, it is expected that we will be able to "map" the spacetime of the black hole [17], probing its multipolar structure and verifying that it obeys the constraints that general relativity imposes on black hole solutions [18, 19].

The expected amplitude of the signal from these extreme-mass-ratio inspirals (EMRIs) is about an order of magnitude below LISA's projected instrumental noise and, at low frequencies ($\lesssim$ 2 mHz), is several orders of magnitude below "confusion noise" produced by unresolved Galactic binaries [20]. However, the signals will be observed for $\sim 10^5$ waveform cycles, and matched filtering will therefore allow detection of these signals with moderately high signal-to-noise ratio (SNR) out to a redshift $z \sim 1$ [21]. Preliminary estimates

---

[1] LISA's sensitivity is primarily to events involving black holes on the low end of the mass spectrum seen in many galaxies—around 10^5 to (a few)$\times 10^7$ $M_\odot$. We emphasize this point because the name "supermassive black hole" is often taken to refer to a hole with mass in the range $10^7 - 10^9$ $M_\odot$. GW events from such black holes will typically be at frequencies too low for LISA's sensitivity.

suggest LISA could see as many as $\sim 10^3$ EMRI events during its lifetime [8, 21], using a suitable "semi-coherent" search algorithm and provided that confusion noise can be efficiently reduced in the real data.

Matched filtering algorithms require the correlation of the detector's output data stream with a bank of waveform templates, which describe the real signal with sufficient accuracy, covering the whole parameter space. The fact that we are dealing with a binary system of extreme mass ratio $\mu/M \ll 1$ means that the gravitational waveform can be computed accurately using black hole perturbation theory. The extreme mass ratio also guarantees that the orbital parameters evolve adiabatically under radiation reaction; i.e., they evolve on a much longer time scale than the orbital periods. This implies that within the radiation reaction time scale, the inspiral waveform can be approximated by "snapshot" waveforms—waveforms calculated by assuming that the small object is moving along a geodesic, neglecting backreaction for that short stretch of time. These snapshots are constructed using the Teukolsky equation [22], an equation that describes the first order change to the curvature tensor of a black hole due to some perturbing source. Accurate Teukolsky-based (TB) snapshot waveforms have been calculated for inclined-circular orbits [15], equatorial-eccentric orbits [16, 23, 24] and most recently, for a certain number of generic (inclined-eccentric) orbits [25]. The reader can find recent reviews on the modeling of EMRI waveforms and orbital dynamics in Refs. [12, 26].

TB waveforms are computationally expensive to generate as they require the numerical integration of the Teukolsky equation and summation over a large number of multipole modes. In this sense, these waveforms are not "user-friendly", especially when it comes to realistic data analysis calculations where one has to handle a bank, which contains $\sim 10^{12}$ of these waveforms [21]. Moreover, the Teukolsky formalism does not provide any information on "conservative" self-interaction effects. To compute these, one must use a self-force formalism. This approach is still under development and is very likely to be even more computationally expensive when it is completed (see [27] for a recent review).

These difficulties have led to a need for the construction of approximate families of waveforms that capture the main features of the true signals, but which can be generated quickly in large numbers. Such approximate waveforms are already being used for scoping out data analysis algorithms for the detection of EMRIs in LISA data [21], and may ultimately play some role as fiducial detection templates in the final data analysis. One possible approach is to construct post-Newtonian (PN) waveforms, which have the advantage of being analytic and therefore very easy to generate. Post-Newtonian EMRI waveforms have been computed in the Schwarzschild spacetime for both circular [28] and eccentric orbits [29], and in the spacetime outside a slowly rotating Kerr black hole for circular orbits [30].

Recently another class of approximate waveforms have become available, based on various "kludge" approaches [31]. Among them is Barak and Cutler's "analytic kludge" (AK) [32] (see also [33]). The principle of the kludges is to combine different prescriptions for the orbital evolution and the waveform emission (not necessarily in a self-consistent way). Historically, this idea of coupling a weak field formula with fully relativistic motion first appeared in papers by Sasaki and Ruffini [34, 35] and was then investigated more thoroughly for a test-body orbiting a Schwarzschild black hole by Tanaka et al. [24]. However, their main focus was to compute semi-relativistic energy fluxes, rather than gravitational waveforms. In the AK model developed by Barack and Cutler, the compact object in the EMRI system moves on a Keplerian orbit, amended to include first post-Newtonian effects of pericenter precession, Lense-Thirring precession, and inspiral from radiation reaction. The emitted gravitational waveforms are described by the lowest-order quadrupole formula.

In this paper, we consider an alternative way to construct kludge waveforms. This approach is much less amenable to analytic calculation, so we called it the "numerical kludge" (NK). The first step of the NK is to produce an inspiral trajectory in "phase space"—i.e. to specify (via some approximation to radiation reaction) the slowly changing constants of geodesic motion (orbital energy, axial angular momentum, and "Carter constant") which determine the orbit (up to initial conditions) [10, 11]. The second step is to numerically integrate the Kerr geodesic equations along this inspiral trajectory and hence obtain the Boyer-Lindquist coordinates of the inspiralling object as a function of time [36]. The final step is to construct a gravitational waveform from this inspiral trajectory.

The approach to waveform construction that we take is to identify the Boyer-Lindquist coordinates of the source with spherical polar coordinates in flat-space. There are several different expressions available in the literature for the gravitational waveforms from orbits in flat-space, and we apply these to our pseudo-flat-space trajectory to construct waveforms. Specifically, we look at the quadrupole formula [37], which is valid in the limit of weak-field (i.e., flat-space) and slow motion. We also examine the quadrupole-octupole formula of Bekenstein [38], as well as a formula derived by Press [39]. The Press formula is also a weak-field expression, but is not restricted to slow-motion or small sources, and contains radiation at orders higher than quadrupole and octupole.

The purpose of this paper is to establish and delimit the accuracy and reliability of waveforms constructed in these various ways. We do this by comparing to TB waveforms. TB waveforms are currently the most accurate EMRI waveforms available. In most cases, TB waveforms represent the emission from geodesic orbits—we mostly do not include the radiative evolution of the orbital parameters in this work.[2] We compare the various NK waveforms with TB waveforms using an overlap integral which weights the waveforms in frequency space by the expected LISA noise curve, and maximizes the overlap with respect to time offsets. This overlap is identical to the test used to evaluate the efficiency of model waveforms as detection templates.

We find that both quadrupole-octupole and Press NK waveforms are in remarkable agreement (overlaps $\gtrsim 0.95$) with TB waveforms for orbits with periastron $r_p \gtrsim 5M$. Most orbits in the final year of the inspiral satisfy this restriction, which means that NK waveforms are quite accurate over a considerable portion of the inspiral parameter space. For orbits that come below $r_p \simeq 5M$ (mostly prograde orbits around rapidly spinning holes), the agreement rapidly degrades (though NK waveforms remain more accurate than post-Newtonian or AK waveforms). This is not surprising—for such orbits the full TB waveform receives signifi-

---

[2] Complete TB inspirals exist for zero-eccentricity orbits [40]. For such orbits, we refer readers to Ref. [1] for a comparison between the TB inspiral waveforms and the NK inspiral waveforms.

cant contributions from higher multipoles and back-scattering off the spacetime curvature. These effects are *ab initio* absent in all the kludge prescriptions. In the high-agreement regions, waveforms generated using the Press formula generally perform better than the quadrupole-octupole prescription, because the Press formula includes contribution from higher harmonics which may not be negligible. The improvement in the relatively strong-field regime is only slight, however—we did not find any regime where the Press formula is a significant improvement on the quadrupole-octupole prescription. We therefore conclude that NK waveforms can accurately reproduce true gravitational waveforms in a large part of parameter space; but, there is little gain from going beyond the quadrupole-octupole prescription.

This paper is organised as follows. Section 4.2 provides a review of existing EMRI waveforms, paying special attention to the kludge semi-relativistic waveforms. In Section 4.3 we present details of how these waveforms can be generated. Section 4.4.1 discusses the overlap function between two waveforms, as this will be our main tool for comparison. Sections 4.4.2 and 4.4.3 contain the results from the comparison between kludge and Teukolsky-based waveforms. Finally, we present a concluding discussion in Section 4.5. Throughout the paper, we shall use greek letters (μ, ν, etc.) to denote spacetime indices, and latin letters (i, j, etc.) to denote spatial indices (unless explicitly stated otherwise). We also adopt geometric units $G = c = 1$.

4.2 Waveform inventory

Presently, several types of EMRI waveforms are available. In broad terms, these waveforms fall into three categories: (i) those calculated numerically within the framework of black hole perturbation theory (Teukolsky-based, or TB waveforms), (ii) analytic waveforms which result from self-consistent PN expansions of the GW equations *and* PN orbital motion, and (iii) approximate semi-relativistic waveforms, or “kludges”. This third category is the focus of this paper.

Kludge waveforms are constructed by combining a flat spacetime wave-emission formula with either a fully relativistic treatment of particle motion (resulting in the numerical kludge, or NK, waveforms), or some analytic approximation of this motion (leading to the analytic kludge, or AK, waveforms). We shall examine the construction of NK waveforms, comparing them to TB waveforms (the most accurate EMRI waveforms presently available). For completeness and background to this paper’s discussions, we now briefly discuss each of the above waveform families.

4.2.1 Teukolsky-based numerical waveforms

The primary framework for black hole perturbation theory in a Kerr background is the Teukolsky formalism [22], which encapsulates all gravitational radiative degrees of freedom in a single “master” wave equation—the “Teukolsky equation”—for the Weyl scalars ψ_0 and ψ_4. A key feature of this equation is that it admits separation of variables in the frequency domain, which effectively reduces it to a pair of ordinary differential equations. There are extensive results in the literature on solutions of the Teukolsky equation, starting from Teukolsky and Press [41], Detweiler [42] and Sasaki and Nakamura [43]. More recent work uses the Teukolsky-Sasaki-Nakamura formalism; see Refs. [12, 26] for detailed discussions and references on the subject.

To date, the Teukolsky equation has been solved in the frequency domain for circular-inclined orbits [15], eccentric-equatorial orbits [16] and most recently for a handful of generic (eccentric-inclined) orbits [25]. We make use of the waveforms generated by these various authors in this paper to assess the quality of our NK waveforms. Recently, the Teukolsky equation has also been solved directly in the time domain [44, 45]. Time-domain calculations have the great advantage of speed, since they avoid the need for Fourier decomposition and summation over orbital frequency harmonics. However, these calculations are not yet mature enough to provide accurate waveforms from Kerr orbits, because of the difficulty of representing the various δ-functions appearing in the energy-momentum tensor of a point particle.

As a final remark, we should mention again that in all the above TB calculations (either in the frequency or the time domain) the motion of the small object is taken to be strictly geodesic. This is a reasonable first approximation since for an EMRI system the orbital evolution is adiabatic, i.e., over a time interval of several orbits the motion is geodesic to high precision. However, for longer stretches of time ($\sim M^2/\mu$) the effects of gravitational back-reaction become significant and cannot be ignored anymore. Waveforms that take into account an evolving orbit (and the conservative self-interaction) require computation of the gravitational self-force (see [46] for an up-to-date review and a full list of references). However, self-force waveforms are not yet available and are unlikely to be for the next few years. Moreover, it is very likely that self-force calculations will remain quite computationally intensive; as such, it is very likely that it will not be possible to generate self-force based waveforms in sufficient numbers to be used for LISA data analysis. It is therefore essential to investigate approximate, easy-to-use waveform models.

4.2.2 Analytic waveforms

Most available analytic waveforms are based on post-Newtonian expansions of the orbital dynamics and of wave emission, expansions that are of greatest relevance when the bodies are widely separated. These waveforms are typically constructed for a specific object or for restricted orbital motion. A significant amount of work has been done on modeling waveforms from two spinning bodies with comparable masses orbiting in precessing quasi-circular orbits (a key GW source for both ground- and space-based detectors). Kidder [47] has investigated the effects of spin-spin and spin-orbital coupling on the waveform from inspiralling binaries. The most recent investigations of PN waveforms (and their application to data analysis) for spinning binary systems can be found in Refs. [48, 49, 50] (see also references therein). Another promising approach is described in [51], which is the first attempt to extend the “effective-one-body” method [52] to spinning compact objects. In parallel to modeling spinning binaries in quasi-circular orbits, there has been significant progress in the construction of waveforms for eccentric, comparable mass binaries [53, 54, 55]. Presently, there are no post-Newtonian waveforms which include both eccentricity of the orbit and spins of the orbiting bodies.

Post-Newtonian models are ultimately not very useful for modeling EMRIs, since most of the GWs observable to LISA are generated from a strong field region ($r \sim$ a few M), where the PN expansion is unlikely to be reliable. One can, however, construct PN waveforms in the EMRI limit, accepting their certain unreliability as a way to develop a very "quick and dirty" set of tools for studying these waves. PN EMRI waveforms are available for systems of a test mass in a quasi-circular [28] or eccentric [29] orbit around a Schwarzschild black hole, or in a quasi-circular orbit around a slowly rotating Kerr black hole [30].

More recently, a class of approximate PN waveforms has been developed by Barack and Cutler [32]. These "analytic kludge" (AK) waveforms are essentially phenomenological waveforms—they are constructed using the classic quadrupole waveforms for eccentric Keplerian orbits derived in [56], but with the relativistic effects of pericenter precession, Lense-Thirring precession, and inspiral imposed. Though not as accurate as the NK waveforms described in this paper, the AK are very quick to generate, and have proven to be useful for computing the Fisher information matrix in investigations of parameter measurement with EMRI GWs [32].

The overlap between AK and NK waveforms is high in the very weak field, but degrades as the orbital periapse is decreased [21]. Even for geodesic orbits, AK and NK waveforms with the *same physical parameters* drift out of phase quickly, since the frequency structure of the two waveform families is different. This arises because the AK uses a Keplerian orbital parameterisation, compared to the geodesic parameterisation used in the NK. For an equatorial orbit with semi-latus rectum $p = 30M$ and eccentricity $e = 0.3$ around a $10^6 M_\odot$ black hole of spin $a = 0.8$, the azimuthal frequency of the NK waveform is 0.196mHz compared to 0.216mHz for the AK. These orbits will therefore be one cycle out of phase within $\sim$ 6 hours. AK waveforms will thus not be particularly *faithful* templates. The problems can be mitigated by adjusting the orbital parameters of the AK waveform to improve the match with the NK, and the AK waveforms do capture the main features of true EMRI waveforms. For this reason, they may be quite *effectual* templates, but this has not yet been properly assessed. In the future, the effectualness of the AK waveforms as detection templates will be investigated by using banks of AK templates to search for more accurate NK or TB waveforms embedded in noise.

4.2.3 Semi-relativistic numerical kludge waveforms

The idea behind the numerical kludge (NK) waveforms is to combine a particle trajectory that is exact (up to inaccuracies in the phase space trajectory and conservative self-force terms) with an approximate expression for the GW emission. By including the particle dynamics accurately, we hope to capture the main features of the waveform accurately, even if we are using an approximation for the waveform construction.

The computation of NK waveforms proceeds in three steps. The first is to construct an inspiral trajectory in "phase space"—that is, to specify in some way the radiation-reaction induced time evolution of the constants of motion: E (energy), L_z (axial angular momentum) and Q (Carter constant), which characterize Kerr black hole orbits up to initial conditions. The construction of the phase space trajectory has been described in previous work [10, 11]. (In this paper we shall, in most cases, ignore the evolution of E, L_z and Q. The procedure for waveform construction including orbital evolution is identical to that for constant E, L_z, Q given in this paper.) The second step is to integrate the Kerr geodesic equations along the inspiral trajectory and hence obtain the Boyer-Lindquist coordinates of the inspiraling object as a function of time [36]. The final step is to construct a gravitational waveform from this inspiral trajectory. We do this by identifying the Boyer-Lindquist coordinates (r, θ, ϕ, t) with spherical polar coordinates in flat-space and then evaluating a flat-space emission formula for the corresponding flat-space source orbit.

4.3 Generation of numerical kludge waveforms

In this section, we describe the two stages of waveform generation (ignoring radiation-reaction): (i) the computation of a trajectory, and (ii) the computation of a gravitational waveform from an arbitrary trajectory.

4.3.1 Construct orbital trajectory

The first step in constructing a numerical kludge waveform is to compute the trajectory that the inspiraling body follows in the Boyer-Lindquist coordinates of the Kerr spacetime of the central black hole. Ignoring radiation reaction, this path is a Kerr geodesic. Geodesic motion in the Kerr spacetime is well known [57, 58] and is governed by a set of first-order differential equations:

$$\Sigma\frac{dr}{d\tau} = \pm\sqrt{V_r}, \tag{4.1a}$$

$$\Sigma\frac{d\theta}{d\tau} = \pm\sqrt{V_\theta}, \tag{4.1b}$$

$$\Sigma\frac{d\phi}{d\tau} = V_\phi, \tag{4.1c}$$

$$\Sigma\frac{dt}{d\tau} = V_t, \tag{4.1d}$$

where the various "potentials" are defined by

$$V_r = \left[E(r^2+a^2) - L_z a\right]^2 - \Delta\left[r^2 + (L_z - aE)^2 + Q\right], \tag{4.2a}$$

$$V_\theta = Q - \cos^2\theta\left[a^2(1-E^2) + \frac{L_z^2}{\sin^2\theta}\right], \tag{4.2b}$$

$$V_\phi = \frac{L_z}{\sin^2\theta} - aE + \frac{a}{\Delta}\left[E(r^2+a^2) - L_z a\right], \tag{4.2c}$$

$$V_t = a\left(L_z - aE\sin^2\theta\right) + \frac{r^2+a^2}{\Delta}\left[E(r^2+a^2) - L_z a\right]. \tag{4.2d}$$

Here, $\Sigma = r^2 + a^2\cos^2\theta$, and $\Delta = r^2 - 2Mr + a^2$. The constants E, L_z, Q are the three first integrals of the motion: E is the orbital energy; L_z is the projection of the orbital angular momentum along the black hole's spin axis; and Q is known as the "Carter constant". This last constant is the relativistic generalization of the "third integral" used to separate the equations which describe orbits in a Newtonian axisymmetric gravitational potential (a result which is particularly well known in the literature describing orbits in galactic potentials [59]). In the spherical (i.e., Schwarzschild) limit, Q reduces to the square of the orbital angular momentum projected into the equatorial plane; see [10] and references therein for discussion.

For a given E, L_z and Q, the roots of V_r determine the turning points of the radial motion—the periastron r_p, and apastron r_a. From these, one can define an orbital eccentricity e, and semi-latus rectum p, using the conventional Keplerian definitions

$$\begin{aligned} & r_p = \frac{p}{1+e}, \qquad r_a = \frac{p}{1-e}, && \text{(4.3a)} \\ \Rightarrow \qquad & p = \frac{2\, r_a\, r_p}{r_a + r_p}, \qquad e = \frac{r_a - r_p}{r_a + r_p}. && \text{(4.3b)} \end{aligned}$$

We also replace the Carter constant by an "inclination angle", defined by

$$\tan^2 \iota = \frac{Q}{L_z^2}. \tag{4.4}$$

To aid numerical integration, one can work in terms of two angular variables, ψ and χ, instead of r and θ. We define ψ by the equation

$$r = \frac{p}{1 + e\cos\psi}\ , \tag{4.5}$$

with ψ increasing monotonically along the orbit. We define χ by the equation

$$z = \cos^2\theta = z_- \cos^2\chi\,, \tag{4.6a}$$

where z_- is given by

$$\beta(z_+ - z)(z - z_-) = \beta z^2 - z\left[Q + L_z^2 + a^2(1 - E^2)\right] + Q\,. \tag{4.6b}$$

Here $\beta = a^2(1 - E^2)$ and $z_- \leq z_+$; χ, like ψ, varies monotonically along the orbit. Expanding the radial potential as

$$V_r = (1 - E^2)\,(r_a - r)\,(r - r_p)\,(r - r_3)\,(r - r_4)\,, \tag{4.7}$$

we find evolution equations for ψ and χ of the form

$$\begin{aligned} \frac{\mathrm{d}\psi}{\mathrm{d}t} &= M\sqrt{1 - E^2}\,[(p - r_3(1 - e)) - e(p + r_3(1 - e)\cos\psi)]^{1/2} \\ &\times \left[\gamma + a^2\, E\, z(\chi)\right]^{-1} (1 - e^2)^{-1}\,[(p - r_4(1 + e)) + e(p - r_4(1 + e)\cos\psi)]^{1/2}\ , && \text{(4.8)} \\ \frac{\mathrm{d}\chi}{\mathrm{d}t} &= \sqrt{\beta\,[z_+ - z(\chi)]}\left[\gamma + a^2\, E\, z(\chi)\right]^{-1}\ , && \text{(4.9)} \end{aligned}$$

where $\gamma = E[(r^2 + a^2)^2\,\Delta^{-1} - a^2] - 2\,M\,r\,a\,L_z\,\Delta^{-1}$. In terms of the variables ϕ, ψ and χ, the geodesic equations are well behaved at the turning points of the motion, which facilitates numerical integration (as discussed in [36]).

Although we currently ignore the radiation reaction and focus only on geodesic waveforms in this paper, it is quite straightforward to include the radiation reaction using the same procedure described above . To do so, one first computes an inspiral trajectory through phase space by writing

$$\begin{aligned}
\frac{\mathrm{d}E}{\mathrm{d}t} &= f_E(a, M, m, p, e, \iota), && (4.10a)\\
\frac{\mathrm{d}L_z}{\mathrm{d}t} &= f_L(a, M, m, p, e, \iota), && (4.10b)\\
\frac{\mathrm{d}Q}{\mathrm{d}t} &= f_Q(a, M, m, p, e, \iota). && (4.10c)
\end{aligned}$$

The functions f_E, f_L and f_Q in our work are derived from well-known post-Newtonian results, augmented by additional corrections. The leading order part of f_E is given by [10]

$$\dot{E} = -\frac{32}{5}\frac{\mu^2}{M^2}\left(\frac{M}{p}\right)^5 (1-e^2)^{3/2}\left[f_1(e) - \frac{a}{M}\left(\frac{M}{p}\right)^{3/2} f_2(e)\cos\iota\right]. \tag{4.11}$$

(For the full expressions see Ref. [11]). Since the parameters a, M and m are constant, and p, e and ι are directly related to E, L_z and Q via Eqs. (4.3)-(4.4), equations (4.10) can be integrated to give the phase space trajectory. That is, the values of E, L_z and Q (or equivalently p, e and ι) are determined as functions of time. To obtain the trajectory of the inspiralling particle, these time dependent expressions can be substituted into the right hand sides of Eqs. (4.1c), (4.1d), (4.8) and (4.9). The resulting set of ODEs can then be integrated to give the inspiral trajectory. In the following, we will only consider waveforms from geodesic trajectories (setting $f_E \equiv f_L \equiv f_Q \equiv 0$), and refer the reader to Refs. [10, 11] for more details on the construction of inspirals.

Once a trajectory has been obtained in this manner, one constructs an "equivalent" flat-space trajectory by projecting the Boyer-Lindquist coordinates onto a fictitious spherical polar coordinate grid and defining the corresponding Cartesian coordinate system:

$$\begin{aligned}
x &= r\sin\theta\cos\phi, && (4.12a)\\
y &= r\sin\theta\sin\phi, && (4.12b)\\
z &= r\cos\theta. && (4.12c)
\end{aligned}$$

Here $\{r, \theta, \phi\}$ are the Boyer-Lindquist coordinates; the corresponding Cartesian coordinates $\{x, y, z\}$ are treated as if they were the same as true flat-space Cartesian coordinates (see Sec. 4.3.2). We use the resulting flat-space trajectory as input to a wave generation formula. This is a "bead on a wire" prescription—by putting the trajectory in flat-space, we remove the background that is causing the curvature of the geodesic path and hence we are forcing the particle to move along a curved path like a bead moving on a wire. This leads to obvious inconsistencies in the approach—e.g., the non-conservation of the flat-space energy-momentum tensor of the particle motion since we are not including the energy-momentum of "the wire" along which the particle moves.

4.3.2 Compute gravitational waveforms from particle trajectory

Having constructed the particle orbit in our pseudo-flat-space, we now apply a flat-space wave generation formula. We consider the weak-field situation and write down the spacetime metric as $g_{\mu\nu} = \eta_{\mu\nu} + h_{\mu\nu}$, where $\eta_{\mu\nu}$ is the flat metric and $h_{\mu\nu}$ are small perturbations. We define the *trace-reversed* metric perturbation as $\bar{h}^{\mu\nu} \equiv h^{\mu\nu} - (1/2)\eta^{\mu\nu}h$, where $h = \eta^{\mu\nu}h_{\mu\nu}$. Imposing the Lorentz gauge condition $\bar{h}^{\mu\alpha}{}_{,\alpha} = 0$, we write the linearized Einstein field equations as

$$\Box\bar{h}^{\mu\nu} = -16\pi\mathcal{T}^{\mu\nu}, \tag{4.13}$$

in which $\Box$ denotes the usual flat-space wave operator and the effective energy-momentum tensor $\mathcal{T}^{\mu\nu}$ satisfies

$$\mathcal{T}^{\mu\nu}{}_{,\nu} = 0\,. \tag{4.14}$$

Here a comma subscript denotes partial derivative ($f_{,\mu} = \partial f/\partial x^{\mu}$). Note that our source conservation equation uses a partial rather than a covariant derivative. This is because we would hope, in a self-consistent approach, to choose coordinates so that the energy momentum tensor is flat-space conserved. Finally, when observing GWs at large distances, we are really only interested in the transverse and traceless parts of the spatial components of $\bar{h}^{\alpha\beta}$; a projection of these components will be necessary.

Taking coordinates centered at the black hole, we denote the position of the observer by $(t, \mathbf{x})$ and the position of the particle by $(t_p, \mathbf{x}_p)$. The wave equation (4.13) has the familiar retarded time solution

$$\bar{h}^{jk}(t,\mathbf{x}) = 4\int \frac{\mathcal{T}^{jk}(t-|\mathbf{x}-\mathbf{x}'|,\mathbf{x}')}{|\mathbf{x}-\mathbf{x}'|}\ \mathrm{d}^3x'. \tag{4.15}$$

The additional coordinate $\mathbf{x}'$ is the integration variable, which goes over every possible space location where the effective energy-momentum tensor $\mathcal{T}^{\mu\nu}(t',\mathbf{x}')$ is nonzero. If the source motion is only negligibly influenced by gravity, then $\mathcal{T}^{\mu\nu}$ may be taken to equal $T^{\mu\nu}$, the energy-momentum tensor of the matter source. In Ref. [39], Press derived a formula valid for extended, fast motion sources. This was obtained by substituting Eq. (4.14) into Eq. (4.15) repeatedly. The result is[3]

$$\bar{h}^{jk}(t,\mathbf{x}) = \frac{2}{r}\frac{\mathrm{d}^2}{\mathrm{d}t^2}\int \left[\left(\mathcal{T}^{00} - 2\mathcal{T}^{0l}n_l + \mathcal{T}^{lm}n_l n_m\right)x'^j x'^k\right]_{t'=t-|\mathbf{x}-\mathbf{x}'|}\mathrm{d}^3x', \tag{4.16}$$

in which $r^2 = \mathbf{x}\cdot\mathbf{x}$ and $\mathbf{n} = \mathbf{x}/r$. In the slow motion limit, the Press formula reduces to the usual quadrupole

---

[3] Equation (4.16) is in a slightly different form from the original Press paper.

formula (hereafter, an overdot denotes a time derivative)

$$\bar{h}^{jk}(t,\mathbf{x}) = \frac{2}{r}\left[\ddot{I}^{jk}(t')\right]_{t'=t-r}, \tag{4.17}$$

where

$$I^{jk}(t') = \int x'^{j} x'^{k} T^{00}(t',\mathbf{x}')d^3x' \tag{4.18}$$

is the source's mass quadrupole moment. Including the next order terms, we obtain the quadrupole-octupole formula (see Refs. [38, 39] for details),

$$\bar{h}^{jk} = \frac{2}{r}\left[\ddot{I}^{jk} - 2n_i\ddot{S}^{ijk} + n_i\dddot{M}^{ijk}\right]_{t'=t-r}, \tag{4.19}$$

with[4]

$$S^{ijk}(t') = \int x'^{j} x'^{k} T^{0i}(t',\mathbf{x}')d^3x', \tag{4.22}$$

$$M^{ijk}(t') = \int x'^{i} x'^{j} x'^{k} T^{00}(t',\mathbf{x}')d^3x'. \tag{4.23}$$

Note that in both Eqs. (4.17) and (4.19), the retarded time is $t-r$ instead of the more complicated expression appearing in (4.16). If desired, it is a straightforward (but increasingly tedious) task to include more terms in the slow-motion expansion of (4.16). In the present work we shall make use of Eq. (4.17) (the "quadrupole formula"), Eq. (4.19) (the "quadrupole-octupole" formula) and the full Press formula Eq. (4.16).

The waveform in the standard transverse-traceless (TT) gauge is given by the TT projection of the above expressions. We define an orthonormal spherical coordinate system via

$$\mathbf{e}_r = \frac{\partial}{\partial r}, \quad \mathbf{e}_\Theta = \frac{1}{r}\frac{\partial}{\partial\Theta}, \quad \mathbf{e}_\Phi = \frac{1}{r\sin\Theta}\frac{\partial}{\partial\Phi}. \tag{4.24}$$

The angles $\{\Theta,\Phi\}$ denote the observation point's latitude and azimuth respectively. The waveform in transverse-

---

[4] Here M^{ijk} is the mass-octupole moment. Note that formally, the current-quadrupole moment is usually defined as (Eq. (5.19b) in Ref. [60]):

$$\mathcal{S}_{ab} = \left[\int \epsilon_{apq} x_p (-\mathcal{T}_{0q}) x_b \, d^3x\right]^{\rm STF}. \tag{4.20}$$

Here the superscript "STF" stands for "symmetric and trace-free". The corresponding current quadrupole moment contribution to the radiation field is (Eq. (4.8) in [60])

$$h^{\rm TT}_{jk} = \left[\frac{8x_q}{3r^2}\epsilon_{pq(j}\ddot{\mathcal{S}}_{k)p}\right]^{\rm TT}. \tag{4.21}$$

It can be verified that the $n_i\ddot{S}^{ijk}$ term in Eq. (4.19), with S^{ijk} defined by Eq. (4.22), is equivalent to the right hand side of Eq. (4.21).

traceless gauge is then given by

$$h^{jk}_{TT} = \frac{1}{2}\begin{pmatrix} 0 & 0 & 0 \\ 0 & h^{\Theta\Theta} - h^{\Phi\Phi} & 2h^{\Theta\Phi} \\ 0 & 2h^{\Theta\Phi} & h^{\Phi\Phi} - h^{\Theta\Theta} \end{pmatrix}, \tag{4.25}$$

with

$$h^{\Theta\Theta} = \cos^2\Theta\left[h^{xx}\cos^2\Phi + h^{xy}\sin 2\Phi + h^{yy}\sin^2\Phi\right] + h^{zz}\sin^2\Theta - \sin 2\Theta\left[h^{xz}\cos\Phi + h^{yz}\sin\Phi\right], \tag{4.26a}$$

$$h^{\Phi\Theta} = \cos\Theta\left[-\frac{1}{2}h^{xx}\sin 2\Phi + h^{xy}\cos 2\Phi + \frac{1}{2}h^{yy}\sin 2\Phi\right] + \sin\Theta\left[h^{xz}\sin\Phi - h^{yz}\cos\Phi\right], \tag{4.26b}$$

$$h^{\Phi\Phi} = h^{xx}\sin^2\Phi - h^{xy}\sin 2\Phi + h^{yy}\cos^2\Phi. \tag{4.26c}$$

The usual “plus” and “cross” waveform polarizations are given by $h_+ = \frac{1}{2}(h^{\Theta\Theta} - h^{\Phi\Phi})$ and $h_\times = h^{\Theta\Phi}$ respectively. The expressions (4.16), (4.17) and (4.19) are valid for a general extended source in flat-space. If we specialize to the case of a point-mass μ moving along a trajectory $x'_p(\tau)$, then the energy-momentum tensor in flat spacetime is given by

$$T^{\mu\nu}(t', \mathbf{x}') = \mu\int_{-\infty}^{\infty}\frac{\mathrm{d}x'^{\mu}_p}{\mathrm{d}\tau}\frac{\mathrm{d}x'^{\nu}_p}{\mathrm{d}\tau}\delta^4\left(x' - x'_p(\tau)\right)\ \mathrm{d}\tau = \mu\frac{\mathrm{d}\tau}{\mathrm{d}t'_p}\frac{\mathrm{d}x'^{\mu}_p}{\mathrm{d}\tau}\frac{\mathrm{d}x'^{\nu}_p}{\mathrm{d}\tau}\delta^3\left(\mathbf{x}' - \mathbf{x}'_p(t')\right), \tag{4.27}$$

where τ is the proper time along the trajectory. It is related to the particle's coordinate time by $\mathrm{d}\tau = (1 - v^2/c^2)^{1/2}\,\mathrm{d}t'$, where $v^2 = |\mathrm{d}\mathbf{x}'_p/\mathrm{d}t'_p|^2$. On the right hand side of Eq. (4.27) is a term $\mathrm{d}t'_p/\mathrm{d}\tau = 1 + O(v^2/c^2)$. Expressions (4.17) and (4.19) are slow-motion expansions, and at the order of these expansions we should replace $\mathrm{d}t'_p/\mathrm{d}\tau$ by 1 for consistency. The Press formula (4.16) is a fast-motion expression, and therefore we do include this term. The presence of a δ-function in $T^{\mu\nu}$ facilitates the simplification of the various moments in Eqs. (4.17) and (4.19):

$$I^{jk} = \mu x'^{j}_p x'^{k}_p\,, \tag{4.28}$$

$$S^{ijk} = v^i\, I^{jk} = \mu\, v^i x'^{j}_p x'^{k}_p\,, \tag{4.29}$$

$$M^{ijk} = x'^{i}_p\, I^{jk} = \mu\, x'^{i}_p x'^{j}_p x'^{k}_p\,. \tag{4.30}$$

Here $v^a \equiv \mathrm{d}x'^a/\mathrm{d}t'_p$. The Press formula similarly simplifies to

$$\bar{h}^{jk}(t, \mathbf{x}) = \frac{2\mu}{r}\frac{\mathrm{d}^2}{\mathrm{d}t^2}\left[(1 - n_a v^a)\, x'^{j}_{p} x'^{k}_{p}\left(\frac{\mathrm{d}t'_p}{\mathrm{d}\tau}\right)\right]_{t'_p = t - |\mathbf{x} - \mathbf{x}'_p|}. \tag{4.31}$$

The square-bracketed expression is to be evaluated at a time t'_p given implicitly by $t = t'_p + |\mathbf{x} - \mathbf{x}'_p(t'_p)|$. In a numerical implementation, we evaluate the expression (4.31) as a function of the time t'_p along the particle's path. In order to obtain a time series that is evenly spaced in t and compute the right hand side of Eq. (4.31) by finite differencing, we adjust the spacing of the sampling at the particle, $\delta t'_p$, such that

$$\delta t = (1 - n_a v^a)\, \delta t'_p\,. \tag{4.32}$$

With a delta function source (4.27), the retarded-time solution (4.15) can be evaluated directly [34]:

$$\bar{h}^{jk}(t, \mathbf{x}) = \left[\frac{4\mu}{r} \left(\frac{\mathrm{d}t'_p}{\mathrm{d}\tau} \right) \frac{\mathrm{d}x'^j_p}{\mathrm{d}t'_p} \frac{\mathrm{d}x'^k_p}{\mathrm{d}t'_p} \frac{1}{1 - n_a v^a} \right]_{t'_p = t - |\mathbf{x} - \mathbf{x}'_p|}\,. \tag{4.33}$$

Naively, one could suppose that (4.33) will perform better than (4.16), since it is derived using only one of the two (invalid) flat-space equations, rather than both. In fact, we find that the retarded integral expression (4.33) performs much worse than either (4.17), (4.19) or (4.16) when compared to TB waveforms. The reason appears to be that the manipulations which lead to the quadrupole, quadrupole-octupole, and Press formulae ensure that the actual source terms—mass motions—are on the right hand side. This is to be contrasted with the retarded integral expression (4.15), which identifies the dominant GW on the left hand side with weak spatial stresses terms in T^{ij}.

We must emphasize that the NK prescription is clearly inconsistent—we are binding the particle motion to a Kerr geodesic while assuming flat spacetime for GW generation and propagation. This is manifested by the fact that the energy-momentum tensor (4.27) is not flat-space conserved, $\partial_\nu T^{\mu\nu} \neq 0$. However, the spirit of this calculation is *not* a formal and consistent approximation to EMRI waveforms; it is rather a "phenomenological" approach which takes into account those pieces of physics we believe are the most crucial—in particular, the exact Kerr geodesic motion. By including the exact source trajectory, we ensure that the spectral components of the kludge waveforms are at the correct frequencies, although their relative amplitudes will be inaccurate. As we shall see, this line of thinking is validated *post facto* by the remarkable agreement between the kludge and TB waveforms (see Section 4.4).

It is important to underline the physical assumptions that have been made in the derivation of the quadrupole formula (4.16), the quadrupole-octupole formula (4.17) and the Press formula (4.19), in order to understand their generic limitations. First of all, the assumed absence of any background gravitational field means that our kludge waveforms are unable to capture any features related to back-scattering. This effect is known to first appear at 1.5PN level (i.e., at $\mathcal{O}(v^3)$; see, e.g., Ref. [61]). Such "tails" of waves are particularly prominent in the strong-field TB equatorial "zoom-whirl" waveforms [16] and in the waveforms from plunging or parabolic orbits [62]. In all these cases, the hole's quasinormal mode ringing, produced by back scattering, adorns the emitted signal.

The slow-motion nature of expressions (4.17) and (4.19) suggests that they might be bad models for waveforms generated by orbits venturing deep inside the central BH's spacetime. Indeed, these formulas poorly reproduce the rich multipole structure of the true waveform from such orbits, as they (and any other slow-motion approximation) essentially truncate the sum over multipoles. The Press formula (4.16) includes contributions at all multipoles and so might be expected to handle these contributions quite well. However, it turns out not to perform much better than the quadrupole-octupole waveform in this regime. While it includes contributions at all multipoles, the lack of background curvature in the waveform model *might* cause the amplitudes of the higher modes to be much lower than for true EMRI waveforms.

Fortunately, these two deficiencies become important for the same class of orbits—those that allow the body to approach very close to the black hole. As a rule of thumb we shall find that NK waveforms are reliable (in terms of the overlap discussed in the next section) as long as the closest orbital approach (periastron) is $r_p \gtrsim 5M$.

4.4 Kludge waveforms: Results and comparison

In this Section we compare NK waveforms (using the overlap function defined in Sec. 4.4.1) to a variety of TB waveforms from inclined-circular, equatorial-eccentric and some generic Kerr orbits with time-independent E, L_z and Q. The TB waveforms are treated here as "exact" (though this is not strictly the case as discussed in Section 4.2). Our comparison rule is that the waveforms are generated using the same Kerr orbit with identical initial conditions. We label these orbits by the triad of orbital elements $\{p, e, \iota\}$ defined in Eqs. (4.3)–(4.4).

4.4.1 The overlap between waveforms

We start by giving a brief description of the measure used for the quantitative comparison between NK and TB waveforms. The main motivation for the computation of accurate EMRI waveforms is to carry out matched filtering for detection of the GWs. For the purpose of signal detection and parameter estimation, a bank of templates is constructed which covers the desired parameter space with sufficient resolution. The detector output is then filtered through each template. The measured strain amplitude in the detector, $x(t) = s(t) + n(t)$, consists of a (possibly present) signal $s(t)$, and the detector noise $n(t)$. We define the Fourier representation of these time series as

$$\tilde{x}(f) = \int_{-\infty}^{\infty} x(t) e^{-i2\pi t f} dt. \tag{4.34}$$

The signal-to-noise ratio (SNR) can be expressed in terms of an inner product defined on the vector space of possible signals. Given two vectors (time series), $x(t), h(t)$, we define the overlap $(x|h)$ by the equation [63, 64]

$$(x|h) = 2 \int_{0}^{+\infty} \frac{\tilde{x}(f)\tilde{h}^*(f) + \tilde{x}^*(f)\tilde{h}(f)}{S_h(f)} df, \tag{4.35}$$

where $S_h(f)$ is the detector's one-sided noise power spectral density (PSD) (in this case, the noise PSD for the LISA detector) and an asterisk denotes complex conjugation. Considering $h(t, \lambda^\alpha)$ as a template with parameters λ^α we can approximate the SNR by [63]

$$\frac{S}{N}\Big[h(\lambda^\alpha)\Big] = \frac{\langle (s|h) \rangle_n}{\sqrt{\langle (n|h)^2 \rangle_n}} = \frac{(s|h)}{\sqrt{(h|h)}} \ . \tag{4.36}$$

The notation $\langle f \rangle_n$ means to ensemble average the function f over all possible noise realizations n. The PSD in the denominator of Eq. (4.35) serves to suppress those frequency components of the signal at which the detector noise is large.

The main tool which will be used in this paper is not the SNR, but rather the overlap function $\mathcal{O}$. The overlap is defined as an inner product between two normalized vectors/signals:

$$\mathcal{O} = (\hat{s}|\hat{h}) \ . \tag{4.37}$$

The normalization is chosen so that $(\hat{s}|\hat{s}) = (\hat{h}|\hat{h}) = 1$. The overlap can be regarded as the inner product between two unit vectors; it varies within $[-1, 1]$. The overlap is equal to 1 if the two waveforms are identical, and it equals zero if the two waveforms are orthogonal (for example, cosine and sine signals). The overlap is an appropriate measure of "goodness-of-fit" since we are interested in knowing how well the NK approximate the behavior of TB EMRI waveforms. In this context, it is important to include the noise properties of the detector since it is no problem if a template has poor performance at frequencies where detector noise is large.

For a fair comparison, we should choose the signal (TB waveform) and template to have the same parameters.[5] In practice, the start times of our signals and templates were slightly mismatched, so we allow for maximisation over starting time ("time of arrival"). This maximization is commonly done in GW data analysis, and can be accomplished very efficiently in the Fourier transform, since the time offset corresponds to a phase shift in the frequency domain. Accordingly, we modify the inner product $(x|h)$ slightly:

$$(x|h) = \max_t \left(\mathrm{Re} \int_0^\infty \frac{4\tilde{x}(f)\tilde{h}^*(f)}{S_h(f)} e^{i2\pi f t} df \right) \tag{4.38}$$

where t corresponds to the time difference. We find that the maximum usually occurs with a time offset close to zero (typically a few frequency bins).

We conclude our discussion of the overlap by describing our approximation to the LISA noise $S_h(f)$. We have used an analytic approximation to the numerically generated sensitivity curve given in Ref. [66]. The agreement between these two curves is excellent as clearly illustrated in Fig. 4.1. Our approximate $S_h(f)$ function can be easily calculated according to the following simple prescription. Define $u = 2\pi f \tau$, where

---

[5] Note that here we study not the fitting factors but the faithfulness of the NK waveforms as compared to TB-based ones, i.e., how well an approximate waveform with given parameters reproduces the "true" waveform with the *same* physical parameters. A faithful bank of waveforms could be used for parameter estimation, while for detection all that is required is an "effectual" template bank, i.e., one in which every true waveform is well represented by one template, even if that template has very different parameters [65].

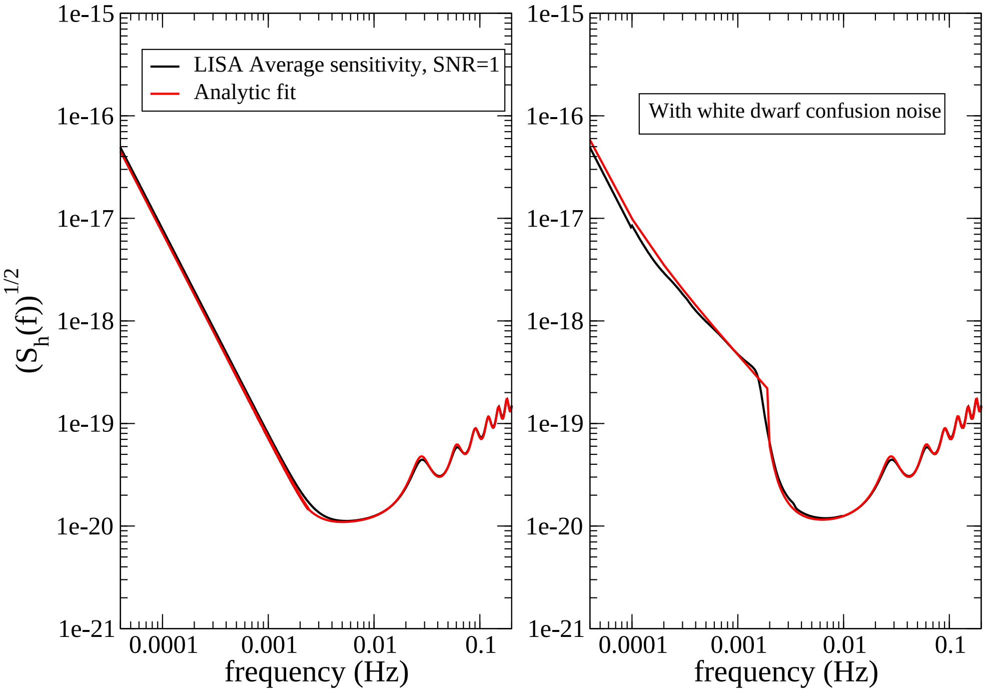

Figure 4.1: Expected sensitivity curve $\sqrt{S_h(f)}$ for LISA; black curve: numerical curve as generated in [66], red curve: analytic approximation used in this paper; see text for details.

f is frequency and $\tau = (5 \times 10^6\,\mathrm{km})/c = 50/3$ sec is the light travel time down one of LISA's arms. For $u < u_{\rm trans} = 0.25$ we set

$$S_h(f) = \left[\frac{8.08 \times 10^{-48}}{(2\pi f)^4}\mathrm{Hz}^4 + 5.52 \times 10^{-41}\right] \mathrm{Hz}^{-1}, \tag{4.39}$$

while for $u \geq u_{\rm trans}$,

$$S_h(f) = \frac{1}{R}\left(\frac{2.88 \times 10^{-48}}{(2\pi f)^4}\mathrm{Hz}^4 + 5.52 \times 10^{-41}\right) \mathrm{Hz}^{-1}, \tag{4.40a}$$

where

$$R = \frac{1}{u^2}\left[(1 + \cos^2(u))\left(\frac{1}{3} - \frac{2}{u^2}\right) + \sin^2(u) + \frac{4\sin(u)\cos(u)}{u^3}\right]. \tag{4.40b}$$

Note that LISA's characteristics are incorporated in the light travel time τ and in the numerical constants in the above expressions, so a similar mission but with different noise characteristics would still be described by the functional form defined by Eqs. (4.39) – (4.40).

In Fig. 4.1, we have also included noise from a confused population of galactic white dwarf binaries following the prescription outlined in [32].

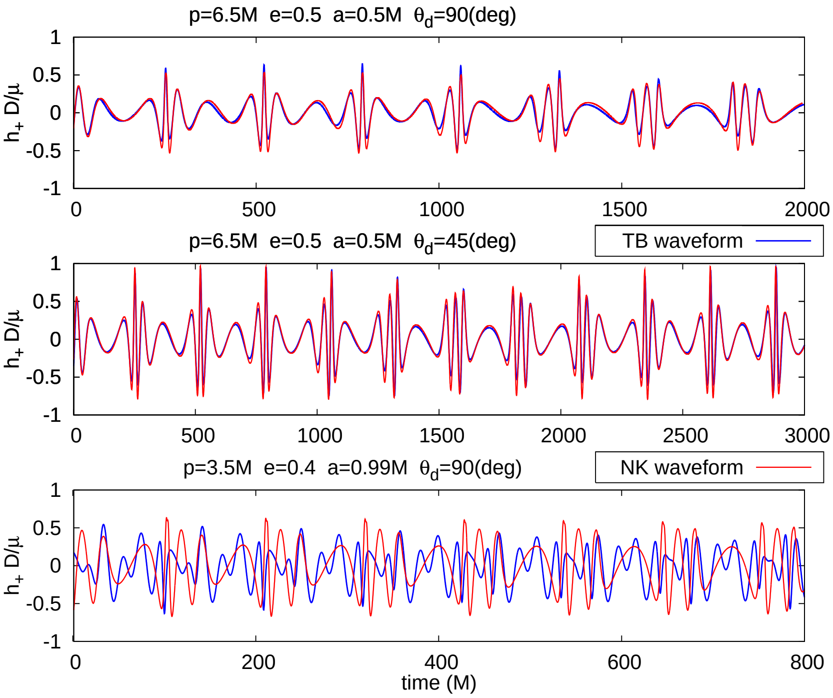

Figure 4.2: Comparing TB and NK (Press-formula numerical kludge) waveforms (black and red curves, respectively) for equatorial orbits and for an observer at a latitudinal position $\theta = 45°$ or $90°$. Orbital parameters are listed above each graph. The waveforms are scaled in units of D/μ where D is the radial distance of the observation point from the source and μ is the test-body's mass. The x-axis measures retarded time (in units of M) and we are showing the "+" polarization of the GW in each case. The overlaps between the NK and TB waveforms are $0.979, 0.990, 0.507$ going from the top figure down.

4.4.2 Time-domain comparison

Figures 4.2, 4.3, and 4.4 show time-domain waveforms for a selection of orbits in the moderate and strong field regions. The NK waveforms plotted in these figures were generated using the Press formula (4.19) (for similar figures with quadrupole-octupole waveforms, see [1]). The results for "plus" and "cross" polarizations are essentially the same, so in the figures we show only the "plus" polarization. For all of the figures, we have assumed an observation point located at $\Phi = 0°$ and $\Theta = 45°$ or $90°$ (as indicated).

Direct visual inspection of the waveforms gives some indication of how well the NK and TB waveforms match. In each of the cases illustrated, the kludge waveforms manage to capture the overall wave pattern, and for the orbits with $p > 8M$ (not shown here) they almost exactly match the TB waveforms. For ultra-relativistic orbits (e.g., with $p \lesssim 5M$ and $1 - a \ll 1$ as in bottom panel of Fig. 4.2), the finer structure in the TB waveforms is clearly not reproduced by the NK waveforms. As we have discussed, these features are the imprints of higher multipole components in the radiation which are amplified by back-scattering, and thus are not expected to appear in the NK waveforms. Comparing with quadrupole and quadrupole-octupole waveforms, waveforms generated using the Press formula do have some finer features due to the presence of higher multipole components, as we might have hoped, but they are not nearly as complicated in structure as

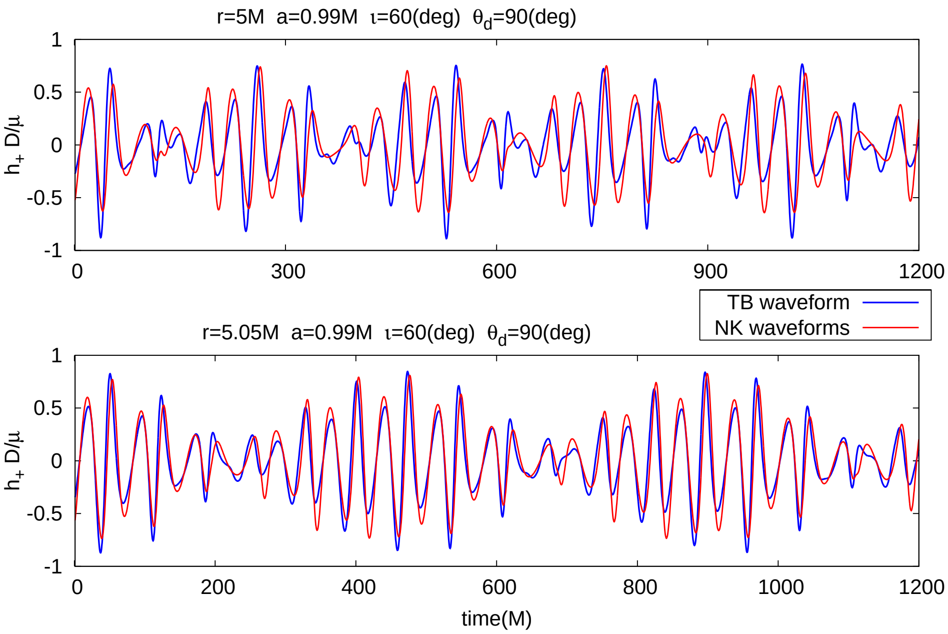

Figure 4.3: Comparing TB and NK (Press-formula numerical kludge) waveforms (black and red curves, respectively) for circular-inclined orbits and for an observer at a latitudinal position $\theta = 90°$. Orbital parameters are listed above each graph. The waveforms are scaled in units of D/μ where D is the radial distance of the observation point from the source and μ is the test-body's mass. The x-axis measures retarded time (in units of M) and we again show the plus polarization of the GW. The overlaps between the NK and TB waveforms are 0.888 for the top figure and 0.961 for the bottom figure.

the TB waveforms.

One also notices that for certain parts of the waveforms (e.g., Fig. 4.3), there is a disagreement in the amplitude while the phase is accurately reproduced. This amplitude discrepancy is periodic, i.e., the points where the amplitude is poorly reproduced occur at regular intervals. This phenomenon exists for all NK waveforms (quadrupole, quadudrupole-octupole, and Press), but is less pronounced in the Press waveforms. The amplitude disagreement suggests that NK waveforms are missing some periodic components, which again can be attributed to the truncated expansions in multipole moments (for quadrupole and quadrupole-octupole waveforms), as well as the lack of back-scattering and other strong gravity features in all NK waveforms. Nevertheless, in order to construct templates that have a high overlap with the true signals, it is much more important that the waveform phase is faithfully reproduced than the waveform amplitude. The waveform phase is determined by the orbit generating the gravitational radiation. The fact that the kludge waveforms are based on true geodesic orbits is presumably the reason that we find, *post facto*, such impressively high overlaps with TB waveforms, especially for those from circular-inclined orbits.

A comprehensive set of data for the overlaps between NK and TB waveforms is given in Tables 4.1, 4.2 and 4.3. These were computed using the overlap function described in Section 4.4.1 and assuming a central black hole mass of $M = 10^6 M_\odot$. This was chosen since preliminary event rate estimates suggest the inspirals

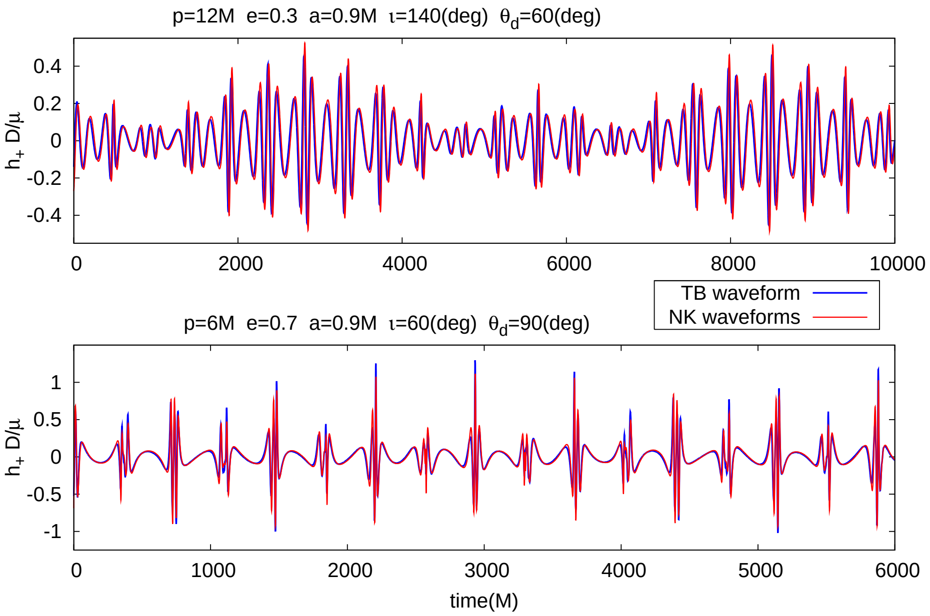

Figure 4.4: Comparing TB and NK (Press-formula numerical kludge) waveforms (black and red curves, respectively) for generic orbits. Orbital parameters are listed above each graph. The waveforms are scaled in units of D/μ where D is the radial distance of the observation point from the source and μ is the test-body's mass. The x-axis measures retarded time (in units of M). The overlaps between the NK and TB waveforms are 0.994 and 0.970 for the top and bottom figures respectively.

of $\sim 10M_\odot$ BHs into $\sim 10^6 M_\odot$ SMBHs will dominate the LISA detection rate [21]. These tables indicate that if the orbital periastron is $r_p \gtrsim 5M$, the overlap between TB waveforms and both the quadrupole-octupole and Press waveforms stays above ~ 0.95. We also find that both these expressions have better performance than the pure quadrupole waveforms (4.17), but there is little difference between the quadrupole-octupole and Press waveforms. The NK and TB waveforms begin to deviate significantly for strong-field, ultra-relativistic orbits with $r_p \lesssim 4M$, with the overlap dropping to $\sim 50\%$ for orbits that come very close to the horizon. Disappointingly, the Press waveforms do not seem to do much better than the quadrupole-octupole waveforms in this strong field regime, despite the inclusion of additional multipole components. The Press waveforms do perform consistently better for circular orbits and weak-field eccentric orbits, but the difference between the two approaches is usually small. We therefore conclude that the quadrupole-octupole waveform model is sufficient and there is not much gain from using the computationally more intensive Press formula.[6]

To summarize, we find that NK waveforms are accurate—and very quick to generate—substitutes for TB waveforms for all orbits around a Schwarzschild black hole with $e \lesssim 1/3$ right up until the final plunge. This result follows from applying the condition $r_p \gtrsim 5M$ at the Schwarzschild separatrix $p_S = (6+2e)M$. Compu-

---

[6] For detection purpose, one important practical reason for not using the Press formula has to do with the separation of intrinsic and extrinsic parameters. In [21], by employing a pure quadrupole gravitational waveform, the source orientation angles and the azimuthal phase of the inspiraling body can be treated as extrinsic parameters, which do not affect the intrinsic radiation of the source, but only how it projects onto the detector. By constrast, the Press formula [Eq. (4.16), (4.31)], which is valid for an extended source, inherently contains those parameters via n^a and the retarded time expression $t'_p = t - |\mathbf{x} - \mathbf{x}'_p|$, making them "more expensive" to search over.

p/M[1]	e[2]	ι[3] (deg)	a/M[4]	Θ[5] (deg)	overlap(+)[6]			overlap with WD (+)			duration(M)[8]
					Quad	Quad-Oct	Press	Quad	Quad-Oct	Press	
1.7	0.1	0	0.99	90	0.84	0.772	0.741				2000
1.7	0.3	0	0.99	90	0.76	0.557	0.500				700
1.9	0.5	0	0.99	90	0.544	0.570	0.547				700
1.9	0.5	0	0.99	90	0.523	0.484	0.445				2000
2.11	0.7	0	0.99	45	0.562	0.566	0.562				700
2.2	0.7	0	0.99	90	0.526	0.496	0.458				700
2.5	0.1	0	0.99	90	0.906	0.853	0.827				2000
2.5	0.5	0	0.99	90	0.671	0.665	0.651				700
3.5	0.4	0	0.99	90	0.588	0.524	0.507				2000
3.5	0.4	0	0.99	45	0.624	0.598	0.593				5000
5.1	0.5	0	0.5	90	0.856	0.962	0.967	0.856	0.961	0.968	700
5.5	0.5	0	0.5	90	0.864	0.964	0.973	0.862	0.962	0.973	2000
6.0	0.4	0	0.5	90	0.871	0.970	0.980	0.864	0.967	0.979	2000
6.0	0.5	0	0.5	90	0.858	0.966	0.974	0.855	0.963	0.973	2000
6.5	0.5	0	0.5	90	0.870	0.970	0.979	0.864	0.968	0.978	2000
6.5	0.5	0	0.5	45	0.937	0.987	0.990	0.932	0.986	0.990	8000
10.0	0.3	180	0.99	90	0.864	0.961	0.966	0.806	0.943	0.954	8000
10.0	0.3	180	0.99	45	0.922	0.971	0.969	0.883	0.957	0.956	8000
10.4	0.5	180	0.99	0	0.998	0.998	0.999	0.997	0.999	0.998	2000
10.5	0.5	180	0.99	90	0.878	0.975	0.982	0.856	0.968	0.978	2000
15.0	0.4	0	0.5	90	0.824	0.963	0.968	0.60	0.878	0.881	8000
15.0	0.4	0	0.99	90	0.824	0.961	0.963	0.603	0.874	0.860	8000

Table 4.1: Numerical data for overlaps between TB and kludge waveforms: Equatorial-eccentric Kerr orbits. Data is not shown with WD confusion noise for the ten orbits in the very strong field regime. In this regime, none of the kludge waveforms reproduce the TB waveforms very well, and this is compounded when the dominant harmonics are suppressed by white dwarf confusion noise. The overlaps are uniformly poor and uninformative, so we do not include them.

---

[a] semi-latus rectum

[b] eccentricity

[c] inclination angle

[d] spin

[e] observation point, $\phi = 0$ always

[f] overlap between "+" polarization of TB waveform with quadrupole ("Quad"), quadrupole-octupole ("Quad-Oct") and Press ("Press") kludge waveforms

[g] overlap between "×" polarizations

[h] waveform duration

p/M	e	ι (deg)	a/M	Θ (deg)	overlap(+)			overlap($\times$)			overlap with WD ($\times$)			duration(M)
					Quad	Quad-Oct	Press	Quad	Quad-Oct	Press	Quad	Quad-Oct	Press	
5.0	0	30	0.5	45	0.944	0.984	0.990	0.946	0.984	0.990	0.945	0.984	0.990	3000
5.0	0	30	0.5	90	0.899	0.974	0.984	0.891	0.971	0.984	0.89	0.969	0.983	3000
5.0	0	30	0.99	45	0.929	0.969	0.975	0.93	0.969	0.975	0.927	0.967	0.974	3000
5.0	0	30	0.99	90	0.904	0.958	0.964	0.9	0.957	0.966	0.895	0.954	0.965	3000
5.05	0	60	0.5	45	0.924	0.967	0.973	0.922	0.969	0.977	0.922	0.968	0.976	3000
5.05	0	60	0.5	90	0.91	0.955	0.961	0.911	0.963	0.973	0.907	0.961	0.972	3000
5.0	0	60	0.99	45	0.857	0.912	0.917	0.86	0.917	0.925	0.857	0.913	0.921	3000
5.0	0	60	0.99	90	0.854	0.882	0.888	0.87	0.912	0.925	0.862	0.907	0.922	3000
10.0	0	30	0.5	45	0.93	0.989	0.995	0.936	0.99	0.994	0.751	0.957	0.975	8000
10.0	0	30	0.5	90	0.89	0.981	0.990	0.901	0.981	0.990	0.63	0.93	0.969	7000
10.0	0	30	0.99	45	0.92	0.98	0.986	0.93	0.98	0.986	0.674	0.92	0.946	8000
10.0	0	30	0.99	90	0.884	0.974	0.982	0.915	0.975	0.983	0.371	0.892	0.963	7000
10.0	0	45	0.7	45	0.932	0.980	0.981	0.936	0.983	0.987	0.75	0.935	0.953	8000
10.0	0	45	0.7	90	0.922	0.972	0.972	0.92	0.98	0.987	0.68	0.929	0.969	8000
10.0	0	60	0.5	45	0.914	0.981	0.987	0.912	0.982	0.990	0.691	0.937	0.969	8000
10.0	0	60	0.5	90	0.945	0.98	0.981	0.932	0.981	0.986	0.732	0.925	0.948	7000
10.0	0	60	0.99	45	0.873	0.953	0.958	0.875	0.957	0.965	0.611	0.875	0.906	8000
10.0	0	60	0.99	90	0.923	0.941	0.937	0.915	0.959	0.965	0.675	0.86	0.893	7000
20.0	0	30	0.5	45	0.934	0.987	0.982	0.938	0.989	0.989	0.957	0.987	0.902	50000
20.0	0	30	0.5	90	0.889	0.970	0.922	0.893	0.974	0.962	0.92	0.984	0.900	30000
20.0	0	30	0.99	45	0.93	0.98	0.951	0.94	0.988	0.992	0.951	0.987	0.977	50000
20.0	0	30	0.99	90	0.895	0.968	0.907	0.914	0.979	0.988	0.933	0.979	0.951	30000
20.0	0	60	0.5	45	0.92	0.975	0.966	0.916	0.981	0.995	0.952	0.958	0.990	50000
20.0	0	60	0.5	90	0.95	0.973	0.958	0.934	0.976	0.972	0.95	0.967	0.957	30000
20.0	0	60	0.99	45	0.895	0.963	0.962	0.892	0.967	0.973	0.934	0.951	0.896	50000
20.0	0	60	0.99	90	0.954	0.96	0.938	0.937	0.972	0.978	0.963	0.946	0.943	30000

Table 4.2: Numerical data for overlaps between TB and kludge waveforms: Inclined-circular Kerr orbits.

p/M	e	ι (deg)	a/M	Θ (deg)	overlap(+)			overlap(×)			overlap with WD (×)			duration(M)
					Quad	Quad-Oct	Press	Quad	Quad-Oct	Press	Quad	Quad-Oct	Press	
6.0	0.1	20.1364	0.9	90	0.912	0.982	0.993	0.91	0.984	0.996	0.894	0.98	0.995	15000
6.0	0.1	20.1364	0.9	60	0.935	0.988	0.996	0.939	0.99	0.997	0.929	0.989	0.997	15000
6.0	0.1	20.1364	0.9	30	0.972	0.995	0.998	0.972	0.995	0.998	0.968	0.995	0.998	15000
6.0	0.5	20.103	0.9	90	0.89	0.967	0.973	0.89	0.972	0.980	0.875	0.968	0.979	15000
6.0	0.5	20.103	0.9	60	0.916	0.975	0.980	0.912	0.978	0.982	0.913	0.976	0.981	15000
6.0	0.5	20.103	0.9	30	0.958	0.985	0.985	0.959	0.985	0.986	0.955	0.984	0.985	15000
6.0	0.1	60.1461	0.9	90	0.951	0.989	0.993	0.941	0.988	0.995	0.933	0.987	0.995	10000
6.0	0.1	60.1461	0.9	60	0.958	0.989	0.994	0.95	0.988	0.995	0.946	0.987	0.996	10000
6.0	0.1	60.1461	0.9	30	0.943	0.986	0.996	0.942	0.987	0.996	0.941	0.986	0.996	10000
6.0	0.5	60.1108	0.9	90	0.934	0.975	0.980	0.919	0.974	0.982	0.912	0.971	0.981	15000
6.0	0.5	60.1108	0.9	60	0.939	0.974	0.982	0.927	0.972	0.984	0.924	0.97	0.984	15000
6.0	0.5	60.1108	0.9	30	0.917	0.971	0.978	0.916	0.971	0.979	0.915	0.971	0.979	15000
6.0	0.7	60.0755	0.9	90	0.926	0.966	0.970	0.911	0.967	0.974	0.906	0.966	0.975	20000
6.0	0.7	60.0755	0.9	60	0.928	0.967	0.971	0.919	0.966	0.974	0.916	0.966	0.974	20000
6.0	0.7	60.0755	0.9	30	0.897	0.963	0.966	0.897	0.963	0.967	0.897	0.963	0.968	20000
12.0	0.1	119.9586	0.9	90	0.916	0.987	0.994	0.911	0.988	0.998	0.627	0.922	0.985	15000
12.0	0.1	119.9586	0.9	60	0.926	0.988	0.991	0.92	0.989	0.998	0.634	0.926	0.985	15000
12.0	0.1	119.9586	0.9	30	0.9	0.983	0.994	0.899	0.986	0.994	0.577	0.91	0.956	15000
12.0	0.5	119.9686	0.9	90	0.938	0.988	0.992	0.934	0.988	0.995	0.889	0.979	0.993	15000
12.0	0.5	119.9686	0.9	60	0.942	0.988	0.993	0.936	0.987	0.994	0.889	0.977	0.991	15000
12.0	0.5	119.9686	0.9	30	0.924	0.984	0.993	0.924	0.986	0.994	0.862	0.971	0.988	15000
12.0	0.7	119.9786	0.9	90	0.935	0.986	0.992	0.933	0.987	0.993	0.904	0.981	0.991	25000
12.0	0.7	119.9786	0.9	60	0.940	0.987	0.992	0.934	0.985	0.992	0.904	0.978	0.990	25000
12.0	0.7	119.9786	0.9	30	0.926	0.983	0.992	0.924	0.983	0.990	0.884	0.973	0.986	25000
12.0	0.3	139.9597	0.9	90	0.9	0.985	0.992	0.891	0.984	0.996	0.751	0.955	0.991	15000
12.0	0.3	139.9597	0.9	60	0.938	0.991	0.994	0.931	0.99	0.997	0.827	0.972	0.993	15000
12.0	0.3	139.9597	0.9	30	0.948	0.992	0.994	0.949	0.993	0.998	0.859	0.979	0.994	15000
12.0	0.1	159.9728	0.9	90	0.836	0.973	0.992	0.838	0.974	0.993	0.494	0.887	0.968	15000
12.0	0.1	159.9728	0.9	60	0.881	0.984	0.995	0.889	0.987	0.998	0.549	0.926	0.990	15000
12.0	0.1	159.9728	0.9	30	0.947	0.994	0.997	0.947	0.995	0.997	0.726	0.96	0.968	15000
12.0	0.5	159.9793	0.9	90	0.876	0.976	0.991	0.877	0.977	0.995	0.808	0.961	0.993	15000
12.0	0.5	159.9793	0.9	60	0.912	0.985	0.994	0.919	0.988	0.996	0.862	0.977	0.994	15000
12.0	0.5	159.9793	0.9	30	0.961	0.994	0.996	0.962	0.995	0.998	0.932	0.991	0.996	15000

Table 4.3: Numerical data for overlaps between TB and kludge waveforms: Generic Kerr orbits.

tations of inspirals into Schwarzschild black holes [11] indicate that, in many cases, the residual eccentricity at plunge will be small, so that kludge waveforms will be suitable for the majority of Schwarzschild inspirals. For retrograde orbits around Kerr black holes ($90° \leq \iota \leq 180°$), the periapse moves out to even larger radii, so that even weaker restrictions can be imposed on the eccentricity. In contrast, for prograde orbits ($0° \leq \iota \leq 90°$), an increased black hole spin allows stable orbits to exist much deeper in the strong field. As $a \rightarrow M$, the separatrix of equatorial orbits asymptotically goes to $p_K^{\rm pro}(e) = (1+e)M$ [16]. Kludge waveforms are not very good in this regime, with overlaps $\sim 50\%$; fortunately, this corresponds to a comparatively small region of parameter space.

If the overlap between a given signal and the best-fit template in a search bank is less than 1, this leads to a decrease in the maximum distance to which that signal can be detected, and a corresponding reduction in event rate. For the purposes of detection, overlaps as low as 50% might be considered good enough, if the astrophysical event rate is sufficiently large [21]; but for very rare events it is conventional to seek overlaps of 97% or higher (rate losses of no more than 10%). For the purposes of parameter estimation, overlaps $\gtrsim 95\%$ will be required in general. It is clear from the results in this paper that overlaps $\gtrsim 97\%$ or 95% are only partially achievable by the existing family of kludge waveforms. Nonetheless, these waveforms might be useful for LISA data analysis as search or detection templates over some (perhaps a large part) of the astrophysically relevant portion of the $\{a/M, p, e, \iota\}$ parameter space. The waveforms may also provide sufficiently accurate estimation of the source parameters (in certain regions of parameter space) that they could be used as the first stage in a hierarchical search. The purpose of such a search would be to identify "interesting" regions of parameter space for follow up with more accurate waveforms.

One should bear in mind, however, that the regions where kludge waveforms are good enough must be identified more carefully than in this paper by comparison to accurate *inspiral* waveforms. As we have discussed earlier, the flat-space emission formulas used in the construction of the NK waveforms ignore all effects of scattering from the background curvature. These "tail" terms make a significant contribution to the waveform structure, and build up over the course of an inspiral. Although we have found good overlaps with geodesic waveforms here (see [1] for overlap between circular-inclined inspiral waveforms), comparisons to generic inspiral orbits are required to properly assess the importance of the tail terms. Accurate, self-force waveforms for such orbits will not be available for a few years and only then will it be possible to firmly demarcate the regime of usefulness of the present, or further improved, NK waveforms.

4.4.3 Frequency-domain comparison

To better understand the overlaps quoted Tables 4.1-4.3, we consider here the integrand of Eq. (4.38) [ignoring the constant factor of "4"]

$$\frac{\tilde{x}(f)\tilde{h}^*(f)}{S_h(f)} e^{i2\pi f t}, \tag{4.41}$$

with t fixed at the value which maximizes the overlap. In Figure 4.5 we plot the real part of this function for the generic orbit $p = 12M$, $e = 0.1$, $\iota = 120°$ and $a = 0.9M$. For the signal $\tilde{x}(f)$ we use the TB waveform and correlate it with templates $\tilde{h}(f)$. As templates we use the TB waveform itself (black solid line), the Press NK waveform (squares), the quadrupole-octupole NK waveform (crosses) and the quadrupole NK waveform (circles). We have deliberately chosen a case for which including higher harmonics significantly ($> 10\%$) improves the overlap, especially in the presence of white dwarf confusion noise (see Table 4.3).

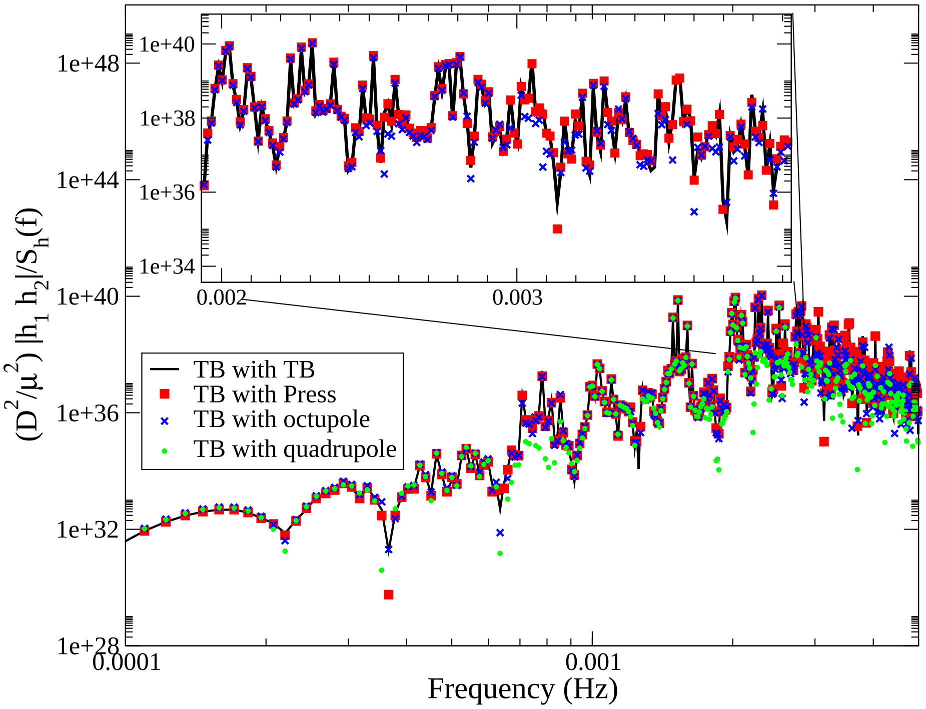

Figure 4.5: Comparison of the integrand of the SNR in the frequency domain $\mathrm{Re}\{\tilde{x}(f)\tilde{h}^*(f)e^{i2\pi f t_{\max}}/S_h(f)\}$ [see Eq. (4.41)], where $\tilde{x}(f)$ is determined from the quadrupole, quadrupole-octupole or Press waveform, and $\tilde{h}(f)$ is determined from the TB waveform. We have chosen orbital parameters $p = 12M$, $e = 0.1$, $\iota = 120°$ and spin $a = 0.9M$. Each point is at a specific frequency obtained by beating the fundamental frequencies Ω_ϕ, Ω_θ, Ω_r against each other. One can see that the Press waveform performs better than quadrupole-octupole waveform at high frequencies.

One can see that the main contributions to the overlap come from several dominant harmonics. For a circular equatorial orbit the main harmonic would correspond to twice the orbital frequency, but in general the main harmonics depend on eccentricity [32]. Besides the harmonics coming from the azimuthal motion, there are many additional components coming from beating between harmonics of the fundamental frequencies of the ϕ-, θ- and r-motion: $\Omega_\phi, \Omega_\theta, \Omega_r$ (see [67] for a Fourier decomposition of the orbital motion). Depending on the mass M of the central black hole, the dominant harmonics may lie in the most sensitive part of LISA's frequency range or they may be suppressed by confusion noise. In the latter case the higher harmonics, although smaller in amplitude, are effectively enhanced by the inverse power spectral density and therefore play an important role in SNR accumulation. Looking at the inlaid box in Figure 4.5 we can compare the quadrupole-octupole and Press waveforms at high frequency. Here the Press waveform does perform better – e.g., at ∼3mHz the quadrupole-octupole NK waveform has failed to reproduce some harmonics in the TB signal, whereas the Press waveform does so pretty well.

4.5 Concluding discussion

In this paper we have provided a simple, "easy-to-use" prescription for approximating the gravitational waveforms generated by test-bodies inspiraling into Kerr black holes. These "kludge" waveforms are constructed by combining familiar flat-spacetime wave equations with true geodesic trajectories in the Kerr spacetime. Despite its formal inconsistency this hybrid approximation results in remarkably accurate waveforms, as we have established by comparison to more rigorous, Teukolsky-based, perturbative waveforms. We find an impressive overlap between the kludge and TB waveforms for particles on geodesic orbits (i.e., ignoring radiation-reaction). This overlap is $> 95\%$ over a significant portion of the relevant orbital parameter space. Large degradation (overlap reduced to $\lesssim 50\%$) occurs for strong field orbits around rapidly spinning black holes. For such cases, the contribution of the radiation backscattered from the background spacetime is sizable; this effect is not included in the present formulation of the kludge waveforms. As a rough (but reliable) rule of thumb, we have found that kludge waveforms work well for Kerr orbits with periapse distance $r_p \gtrsim 5M$, irrespective of the black hole spin.

We have experimented with three different types of kludge waveforms generated using three different solutions of the flat-spacetime gravitational wave equation: quadrupole, quadrupole-octupole and the Press waveforms [39]. The latter choice includes contributions from all multipole moments of the orbiting body and bears the greatest resemblance to the Teukolsky-based waveforms.

The area where these kludge waveforms will find most use is in the development of EMRI data analysis for LISA. The combination of accuracy and simplicity of generation has already made these waveforms invaluable tools for the study of data analysis issues. It seems quite plausible that the waveforms may also play a role in actual searches of the LISA data. One use could be for estimation of observed waveform parameters as the first stage in a hierarchical search. The high faithfulness of these waveforms suggest that they may be able to set fairly tight bounds on the parameters of the emitting system. This will be extremely useful input for the second stage of the search where the system parameters will be refined using more accurate waveforms.

We can also use the kludge waveforms to estimate the fluxes of energy and angular momentum carried away in GWs from geodesic orbits, and use these as estimates of the energy and angular momentum lost from the orbit in a true inspiral. The energy and angular momentum content of a TT GW field, h^{jk}_{TT}, propagating in flat-space at large distances from the source, is determined from the Isaacson energy-momentum tensor of the wave field [68, 69]

$$T^{\mu\nu}_{GW} = \frac{1}{32\pi} \left\langle h^{jk,\mu}_{TT} h^{jk,\nu}_{TT} \right\rangle . \tag{4.42}$$

Integration of this expression gives the energy and angular momentum loss rates due to GW emission (equations (4.13) and (4.22′) of [60]) as

$$\dot{E} = \frac{1}{16\pi}\int \left\langle h^{jk,t}_{TT} h^{jk,t}_{TT} \right\rangle r^2\, \mathrm{d}\Omega\,, \tag{4.43}$$

$$\dot{L}_i = \frac{1}{16\pi}\int \left\langle \epsilon_{ipq} h^{pa}_{TT} h^{aq,t}_{TT} - \frac{1}{2}\epsilon_{ipq} x_p h^{ab,q}_{TT} h^{ab,t}_{TT} \right\rangle r^2 \mathrm{d}\Omega\,. \tag{4.44}$$

The angle brackets in expressions (4.42)–(4.44) mean "average over several gravitational wavelengths". In Figure 4.6 we show the angular distribution of the gravitational radiation from an EMRI orbit of given p and e, for several different orbital inclinations, ι. This picture is more or less typical of the majority of orbits. The variation of the energy flux with the sky position of the observer is indicative of beaming. This is strongest for equatorial orbits and decreases as the orbital inclination is increased. Equatorial orbits are restricted to a single plane, while inclined orbits wander through more of the spacetime. This wandering averages out the beaming over the sky. The larger the orbital inclination, the more of the phase space the body explores, the more averaging occurs and the more homogeneous the sky distribution of the energy flux.

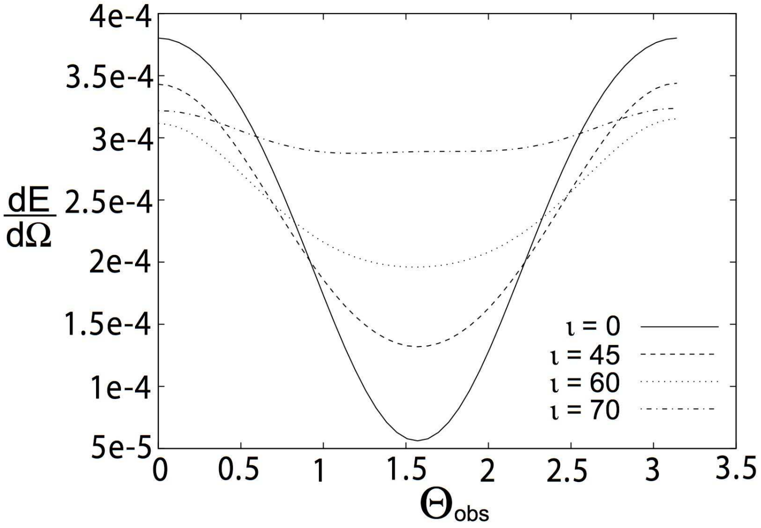

Figure 4.6: Angular radiation pattern: Energy radiated per unit solid angle as a function of the colatitude of the observer, Θ_{obs}, for orbits with $p = 5M$, $e = 0.4$, $a = 0.9M$ and a sequence of inclinations, as labelled.

Since the inspiral trajectory and waveform construction are considered separately, kludge GWs carry a different amount of energy and angular momentum to infinity than the inspiraling particle loses. The kludge fluxes computed from Eqs. (4.43)-(4.44) allow us to assess the inconsistency of the approximations which go into the kludge construction. This assessment has been carried out in [1]. There it was found that the kludge fluxes typically compare well to the best available PN formulas in the weak field—e.g., post-Newtonian based expressions described in [11]—but are not as accurate for evolving inspirals as the latter. For strong field orbits, the kludge fluxes provide a somewhat better estimate than PN formulas, when compared to TB results. Such comparison of fluxes (TB, PN, and NK) provide us with an estimate of the error when using NK waveforms for SNR calculations. The results in [1] suggest the NK waveforms will tend to underestimate the true SNRs.

Within the adiabatic approximation, one can also apply our NK scheme to calculate full inspiral kludge waveforms by taking into account radiation-reaction-induced orbital evolution. This realistic scenario requires an additional "kludge" for describing the orbital evolution itself [10, 11]: exact geodesic orbital dynamics coupled with radiation reaction based on PN-based expressions for the fluxes. Such inspiral waveforms for circular-inclined orbits have been computed in [1] and turn out to have high overlaps with the available TB inspirals. The overlap is $\gtrsim 75\%$ even when the inspiral terminates in the strong field region, indicating the kludge will be a very useful tool for generating inspiral waveforms. However, as we have discussed above, the kludge waveforms at present do not include some important physical features (backscatters, high harmonics, self-forces) that we expect in true inspirals. Only when accurate "Teukolsky + self-force-based waveforms" are available for generic inspiral orbits will we be able to fully quantify the range of validity and level of accuracy of the kludge waveforms.

A further possible application of kludge waveforms is to the study of non-Kerr EMRIs. It is hoped that LISA observations will allow "spacetime-mapping" of black holes [17, 70], and thereby test the no-hair theorem. To carry out such tests quantitatively will require waveform templates, which incorporate the deviation from Kerr in the spacetime structure by a set of suitable parameters (e.g., multipole moments [17]). The development of rigorous non-Kerr EMRI waveforms is a very difficult task, since generic stationary and axisymmetric spacetimes lack the Killing-tensor symmetry and algebraically special properties that underly the Teukolsky framework for the Kerr spacetime. One way to make progress is to construct kludge waveforms in non-Kerr spacetimes along the lines outlined in this paper. Our results for the Kerr spacetime suggest that such kludge waveforms may be sufficiently accurate for qualitative, and even quantitative studies of non-Kerr EMRIs. All that is required is the integration of the geodesic equation in the non-Kerr spacetime, followed by the same kludge waveform generation as for Kerr. Thus kludge waveforms provide a computationally quick and easy tool to study "bumpy" and "quasi-Kerr" spacetime mapping [18, 19].

The kludge waveforms presented in this and a companion paper [11] can be considered as "second generation", an improvement on the original simple version of quadrupole waveforms [31] and inspirals [10]. Certainly, there is space for further improvement. The inclusion of conservative self-force effects on the inspiral is an obvious next step. Reference [1] has discussed how this can be achieved by calculating the relevant orbital frequency shifts for circular Schwarzschild orbits. We can also further improve waveform generation by including the back-scattering effects arising from the propagation of the GWs in a curved spacetime.

In summary, given the present level of performance of our kludge waveforms and inspirals and their prospects of improvement, we believe that they should remain valuable tools for LISA source modeling for the coming years.

Bibliography

[1] S. Babak, H. Fang, J. R. Gair, K. Glampedakis and S. A. Hughes, preprint gr-qc/0607007.

[2] K. Danzman et al., LISA – Laser Interferometer Space Antenna, Pre-Phase A Report. Max-Planck-Institute fur Quantenoptic, Report MPQ 233 (1998).

[3] D. Merritt and L. Ferrarese, in *The Central Kpc of Starbursts and AGN*, edited by J. H. Knapen et al., San Francisco: A.S.P., p. 335 (2001). See also astro-ph/0107134.

[4] M. Sarzi et al., ApJ **567**, 237 (2002).

[5] M. J. Rees, in *Black Holes and Relativistic Stars*, Proceedings of S. Chandrasekhar Memorial Conference (University of Chicago Press, Chicago, 1998). See also astro-ph/9701161.

[6] S. Sigurdsson, Class. Quant. Grav. **14**, 1425 (1997).

[7] M. J. Rees, Class. Quant. Grav. **14**, 1411 (1997).

[8] S. Sigurdsson and M. J. Rees, Mon. Not. R. Astron. Soc. **284**, 318 (1997).

[9] M. Freitag, Class. Quant. Grav. **18**, 4033 (2001); Astrophys. J. Lett. **583**, L21 (2003).

[10] K. Glampedakis, S. A. Hughes, and D. Kennefick, Phys. Rev. D **66**, 064005 (2002).

[11] J. R. Gair and K. Glampedakis, Phys. Rev. D **73**, 064037 (2006).

[12] K. Glampedakis, Class. Quant. Grav. **22**, S605 (2005).

[13] L. Barack and C. Cutler, Phys. Rev. D **70** 122002 (2004).

[14] L. J. Rubbo, K. Holley-Bockelmann, and L. S. Finn, astro-ph/0602445.

[15] S. A. Hughes, Phys. Rev. D **61**, 084004 (2000); Phys. Rev. D **64**, 064004 (2001).

[16] K. Glampedakis and D. Kennefick, Phys. Rev. D **66**, 044002 (2002).

[17] F. D. Ryan, Phys. Rev. D **52**, 5707 (1995).

[18] N. A. Collins and S. A. Hughes, Phys. Rev. D **69**, 124022 (2004).

[19] K. Glampedakis and S. Babak, Class. Quant. Grav. **23**, 4167 (2006).

[20] G. Nelemans, L. R. Yungelson, and S. F. Portegies Zwart, Astron. and Astrophys. **375**, 890 (2001).

[21] J. R. Gair, L. Barack, T. Creighton, C. Cutler, S. L. Larson, E. S. Phinney, and M. Vallisneri, Class. Quant. Grav. **21**, S1595 (2004).

[22] S. A. Teukolsky, ApJ **185**, 635 (1973).

[23] C. Cutler, D. Kennefick, and E. Poisson, Phys. Rev. D **50**, 3816 (1994).

[24] T. Tanaka, M. Shibata, M. Sasaki, H. Tagoshi, and T. Nakamura, Prog. Theor. Phys. **90**, 65 (1993).

[25] S. Drasco and S. A. Hughes, Phys. Rev. D **73** 024027 (2005).

[26] Y. Mino, M. Sasaki, M. Shibata, H. Tagoshi, and T. Tanaka, Prog. Theor. Phys. Suppl. **128**, chapter 1 (1998).

[27] Poisson, E., "The Motion of Point Particles in Curved Spacetime", *Living Rev. Relativity* 7, (2004), 6. `http://www.livingreviews.org/lrr-2004-6`.

[28] E. Poisson, Phys. Rev. D **47**, 1497 (1993);
E. Poisson and M. Sasaki, Phys. Rev. D **51**, 5753 (1995).

[29] J. Levin, R. O'Reilly, and E. J. Copeland, Phys. Rev. D **62**, 024023 (2000).

[30] E. Poisson, Phys. Rev. D **48**, 1860 (1993).

[31] Material on a variety of LISA and EMRI topics can be found at the following www address: `http://www.tapir.caltech.edu/list/index.html`.

[32] L. Barack and C. Cutler, Phys. Rev. D **69**, 082005, (2004).

[33] C. Moreno-Garrido, E. Mediavilla and J. Buitrago, Mon. Not. R. Astron. Soc. **274**, 115 (1995).

[34] R. Ruffini and M. Sasaki, Prog. Theor. Phys. **66**, 1627 (1981).

[35] M. Sasaki, Prog. Theor. Phys. **69**, 815 (1983).

[36] T. Creighton, J. R. Gair, S. A. Hughes, and M. Vallisneri, in preparation.

[37] C. W. Misner, K. S. Thorne and J. A. Wheeler, *Gravitation*, (San Francisco:Freeman, 1973).

[38] J. D. Bekenstein, ApJ **183**, 657, (1973).

[39] W. H. Press, Phys. Rev. D **15**, 965 (1977).

[40] S. A. Hughes, Phys. Rev. D **64**, 064004 (2001).

[41] S. A. Teukolsky and W. H. Press, ApJ **193**, 443 (1974).

[42] S. L. Detweiler, Astrophys. J. **225**, 687 (1978).

[43] M. Sasaki and T. Nakamura, Prog. Theor. Phys. **67**, 1788 (1982).

[44] E. Poisson, gr-qc/0407050; K. Martel, Phys. Rev. D **69**, 044025 (2004); K. Martel and E. Poisson, Phys. Rev. D **66**, 084001 (2002).

[45] R. Lopez-Aleman, G. Khanna, and J. Pullin, Class. Quant. Grav. **20**, 3259 (2003).

[46] E. Possion, Class. Quant. Grav. **21**, R153 (2004).

[47] L. Kidder, Phys. Rev. D **52**, 821 (1995).

[48] A. Buonanno, Y. Chen, and M. Vallisneri, Phys. Rev. D **67**, 104025 (2003). ,

[49] Y. Pan, A. Buonanno, Y. Chen, and M. Vallisneri, Phys. Rev. D **69**, 104017 (2004).

[50] L. Blanchet and A. Buonanno, gr-qc/0605140.

[51] T. Damour, Phys. Rev. D **64**, 124013 (2001).

[52] A. Buonanno and T. Damour, Phys. Rev. D. **59**, 084006 (1999) and **62**, 064015 (2000); T. Damour, P. Jaranowski and G. Shafer, Phys. Rev. D **62**, 084011 (2000).

[53] A. Gopakumar and B. Iyer, Phys. Rev. D **65**, 084011 (2002).

[54] T. Damour, A. Gopakumar, and B. Iyer, Phys. Rev. D **70** 064028 (2004).

[55] R. Memmesheimer, A. Gopakumar, and G. Schaefer, Phys. Rev. D **70** 104011 (2004).

[56] P. C. Peter and J. Mathews, Phys. Rev. **131**, 435 (1963); P. C. Peter, Phys. Rev. **136**, B1224 (1964).

[57] J. M. Bardeen, W. H. Press, and S. A. Teukolsky, ApJ **178**, 347 (1972).

[58] S. Chandrasekhar, *The Mathematical Theory of Black Holes* (Oxford Univ. Press, 1983).

[59] J. Binney and S. Tremaine, *Galactic Dynamics* (Princeton University Press, Princeton, NJ, 1987), chapter 3.

[60] K. S. Thorne, Rev. Mod. Phys. **52**, 299 (1980).

[61] L. Blanchet, T. Damour, and B. Iyer, Phys. Rev. D **51**, 5360 (1995).

[62] Y. Kojima and T, Nakamura, Prog. Theor. Phys. **72**, 494 (1984).

[63] C. Cutler and E. Flanagan, Phys. Rev. D **49**, 2658 (1994).

[64] R. Balasubramanian, B. S. Sathyaprakash, and S. Dhurandhar, Phys. Rev. D **53**, 3033 (1996).

[65] T. Damour, B. R. Iyer, and B. Sathyaprakash, Phys. Rev. D **57** 885 (1998).

[66] `http://www.srl.caltech.edu/~shane/sensitivity/MakeCurve.html`, S. L. Larson, W. A. Hiscock, and R. W. Hellings, Phys. Rev. D **62**, 062001 (2000).

[67] S. Drasco and S. A. Hughes, Phys. Rev. D. **69** 044015 (2004).

[68] R. A. Isaacson, Phys. Rev. **166** 1263 (1968).

[69] R. A. Isaacson, Phys. Rev. **166** 1272 (1968).

[70] C. Cutler and K. Thorne, gr-qc/0204090.

Chapter 5

Frame Dragging, Gravity Probe B, and Mach's Principle

General relativity predicts that the Earth's rotation drags inertial frames into a (very slow) tornado-like rotational motion relative to the "distant stars". This frame-dragging effect is being tested by Gravity Probe B, a set of four superconducting gyroscopes in an Earth-orbiting satellite. In this paper we explain frame dragging by two physical descriptions: that of space behaving like a fluid dragged into motion by the Earth's spin, and that of a magnetic-like component to the Earth's gravitational field (gravitomagnetism); and we give a simple demonstration of the equivalence of these two descriptions. We then discuss the simplest version of Mach's Principle—that the angular velocities of inertial frames near Earth is determined by the rotation of matter in the distant universe. We explore Mach's Principle using a simple model in which our universe is idealized as an enormous, expanding and slowly rotating sphere, surrounded by vacuum. This model predicts that, when the universe is very young and its outer boundary is far beyond our cosmological horizon, inertial frames near earth are dragged into almost perfect lock-step rotation with the universe. As the universe expands, this frame dragging weakens, and at late times inertia near Earth breaks free of the grip of the universe's rotating matter. An apparent paradox—that this breaking free begins before we have causal contact with the outer edge of the universe—is explained, and is used to elucidate the contrast between frame dragging and signal propagation.

Preliminary form of a manuscript, coauthored by H. Fang and K. S. Thorne, to be submitted to American Journal of Physics.

5.1 Introduction and overview

In Newtonian physics there is a universal standard of rotational inertia—a global set of Cartesian axes with respect to which one sees no Coriolis force. Newton's laws of physics take their simplest, standard form when written in a coordinate system tied to these *inertial axes*. These axes can be identified experimentally by ideal (perfect) gyroscopes: gyroscopic spin directions remain always fixed relative to the inertial axes; the spins do not precess.

In general relativity, moving matter drags the inertial axes into inhomogeneous rotation relative to distant stars. The nearer the moving matter, the greater the rotation, so we must replace the idea of global inertial axes by tiny, individual inertial axes, one set of axes at each location in space. Moreover, because the very concept of space depends on the observer's velocity, we must think of each observer as carrying a set of (rotational) inertial axes—axes tied to the directions of gyroscopes that the observer carries. These inertial axes are sometimes called inertial frames, a poor terminology since "inertial frame" also means "freely falling frame". To avoid confusion, we shall use the phrase "inertial axes" when discussion rotation, and "inertial frames" when discussing translation—with one exception: the phrase "frame dragging" is widely interpreted by physicists as referring to rotational dragging, not translational dragging, so we shall sometimes use it to mean "dragging of inertial axes".

A specific, important example of the general relativistic dragging of inertial axes (frame dragging) is the influence of the spin of the Earth or any other body with weak enough gravity that space around it can be regarded as nearly Euclidean and the flow of time as nearly uniform. As viewed in such a body's rest frame, inertial axes and gyroscopic spins outside the body rotate relative to distant stars (i.e. relative to inertial frame at radial "infinity") with the frame-dragging angular velocity

$$\vec{\omega}_{\rm drag} = \frac{G}{c^2}\left[\frac{-\vec{J} + 3(\vec{J}\cdot\vec{e}_r)\vec{e}_r}{r^3}\right] . \tag{5.1}$$

Here G is Newton's gravitation constant, c is the speed of light, $\vec{J}$ is the body's spin angular momentum, r is the radial distance from the body's center, and $\vec{e}_r$ is the unit radial vector.

This frame-dragging effect was discovered, in general relativity, by J. Lense and H. Thirring (1918) [1] and so is called the Lense-Thirring effect. Its magnitude near the Earth is exceedingly small. Since the Earth's spin angular momentum is $J \sim MR^2\Omega_{\rm earth}$ (with M, R and $\Omega_{\rm earth}$ the Earth's mass, radius, and rotational angular velocity), Eq. (5.1) predicts

$$\omega_{\rm drag} \sim \left(\frac{GM/c^2}{R}\right)\left(\frac{R^3}{r^3}\right)\Omega_{\rm earth} \sim 0.03\,{\rm arcsec/yr} . \tag{5.2}$$

Note that $2GM/c^2$ is the Schwarzschild radius (horizon radius) of a non-rotating black hole with the same mass as the Earth. Evidently, the weakness of the Earth's frame dragging is due to the Earth's huge size compared to the equivalent black hole: $R \sim 10^4$ km $\gg 2GM/c^2 \sim 1$ cm. For spinning neutron stars, with $R_{\rm NS} \sim 3 \times 2GM_{\rm NS}/c^2$, frame dragging can be fast; and for a spinning black hole, with $R_{\rm BH} \simeq 2GM_{\rm BH}/c^2$, it can be faster still—and can have major astrophysical consequences (see, e.g. Box 15.1 of Ref. [2]).

In 1960 Leonard Schiff proposed testing this frame-dragging prediction using gryroscopes flown in an Earth-orbiting satellite. Schiff's idea has now been realized: Four satellite-borne, superconducting gyroscopes (*Gravity Probe B*) were launched into a polar orbit on April 20, 2005. The directions of the gyroscopes' spins were monitored relative to a distant star, and the data are now being analyzed, with a planned release of results in spring 2007. The goal is a test of frame dragging to one per cent accuracy. For details see Ref. [3] and references cited therein. For discussions of other experiments or proposals to test frame dragging see, e.g., [4, 5, 6].

The frame dragging formula (5.1) is normally derived, in general relativity, in two steps: First, one derives from Einstein's equations a metric function

$$\omega = \frac{2G}{c^2}\frac{J}{r^3} \tag{5.3}$$

(*not to be confused with* $\omega_{\rm drag}$!) that describes the influence of the Earth's spin on the spacetime metric,

$$ds^2 = -c^2dt^2 + dr^2 + r^2d\theta^2 + r^2\sin^2\theta(d\phi - \omega dt)^2 \; . \tag{5.4}$$

(Here, for simplicity, we have omitted the tiny influence of the Earth's mass on the metric, and the term quadratic in ω is at the level of errors in this approximation so should be ignored.) Second, one insists that a gyroscope always keep its spatial direction fixed relative to the local standard of inertia embodied in this spacetime metric—i.e., one "parallel transports" the gyroscope's spin (or, if the gyroscope is not freely falling, one "Fermi-Walker" transports it); the result is Eq. (5.1). For details, see general relativity textbooks, e.g., Sec. 40.7 of [7]. Later in the paper we will need the metric (5.4), reexpressed in Cartesian coordinates x^j; it takes the form

$$ds^2 = -c^2dt^2 + \delta_{jk}(dx^i + \gamma^j dt)(dx^k + \gamma^k dt) \; , \tag{5.5a}$$

$$\vec{\gamma} = -\omega r \sin\theta\, \vec{e}_\phi = -\frac{2G}{c^2}\frac{1}{r^2}\vec{J}\times\vec{e}_r \; . \tag{5.5b}$$

There are several other, simpler ways to deduce and understand the gyroscopic frame-dragging equation (5.1). One rather sophisticated way, based on graviton/elementary-particle couplings, has been presented in this journal previously [8]. A second way uses ideas from fluid mechanics: just as the flow of water in a river, which is slower near the bank and faster near the center, drags a leaf on the water's surface into rotation, so *space flows around the Earth* in a tornado-like way, faster near Earth and slower farther away, and this flow drags a gyroscope's spin into rotation (precession). A third way uses ideas from electromagnetic theory: the Earth's spin creates a gravitational analog of a magnetic field, and the gyroscope precesses around this *gravitomagnetic field* in the same manner as a magnetized spinning body precesses around a true magnetic field. In Sec. 5.2, we will present and discuss these second and third descriptions of frame dragging and will show, by a very simple argument, that they are completely equivalent, despite their very different physical depictions.

Einstein has written [9] that one of his principal motivations in formulating general relativity was the idea of Mach, that local standards of inertia are determined fully by the mean motion of matter in the distant universe. This idea, which has come to be called *Mach's Principle*, was rather vague in Mach's writings [10], and has triggered a large number of more precise formulations, with a wide range of mathematical and physical content [11]. The simplest and most straightforward version of Mach's Principle states that, when there are no nearby, massive spinning bodies (such as the Earth, a neutron star, or a black hole), inertial axes are tied to the mean rotational motion of the matter that fills the distant universe.

Does general relativity satisfy this simple version of Mach's Principle? The order-of-magnitude frame-dragging formula (5.2) suggests that it might. In order of magnitude, the universe's Hubble distance (the size of our cosmological horizon) is equal to the Schwarzschild radius of all the matter within that distance, so Eq. (5.2) with $R \sim 2GM/c^2$ and $r \sim R$ suggests that (far from heavy spinning bodies, such as the Earth or Sun) inertial axes might rotate with the same angular velocity as the mean motion of our universe's matter, $\omega_{\rm drag} \sim \Omega_{\rm universe}$—which could account for the observed fact that inertial axes are tied to distant stars.

Many mathematical models of our universe have been developed to explore whether this is so. Perhaps the simplest and most compelling was a 1966 study by Brill and Cohen [12], in which the universe's matter is idealized as contained in a thin, spherical shell that rotates slowly with respect to inertial frames far outside it (at radial infinity). If the shell is arbitrarily close to its own Schwarzschild radius (analogous to the situation with our universe), the shell fully controls the inertial axes inside it: they turn in lock-step rotation with the shell. If the shell is very large compared to its Schwarzschild radius (by contrast with our universe), the standard of inertia at spatial infinity controls the interior inertial axes; they point toward ”stars” at rest at spatial infinity regardless of the shell's rotation rate. As the shell is slowly shrunk from very large to its Schwarzschild radius, the inertial axes slowly transition from control by “infinity” to control by the shell.

This 1966 study added credence to the hope that General Relativity might incorporate Mach's Principle in a very clean and compelling way. However, subsequent studies, using more realistic models of the universe, have revealed a more complicated and less satisfying picture [13, 14, 15, 16, 17, 18]. In Sec. 5.3 of this paper we present a simple and pedagogically illuminating variant of these types of studies.

5.2 Frame dragging: The space-drag and gravitomagnetic descriptions

5.2.1 Fluid like space-drag description

In formulating our fluid description of frame dragging, we begin with general relativity's metric $ds^2 = -c^2dt^2 + dr^2 + r^2d\theta^2 + r^2\sin^2\theta(d\phi - \omega dt)^2$ [Eq. (5.4)] for spacetime outside the spinning Earth or other body. We ask, What is the physical meaning of the metric function $\omega = (2G/c^2)J/r^3$? To answer this, consider a thought experiment involving a large laser gyroscope: an optical fiber that encircles the Earth at fixed radius r and polar angle θ, and that (for pedagogical simplicity) has unit index of refraction, so light travels in it at vacuum speed. When a photon is sent through the fiber clockwise, from a laser at rest relative to the distant stars (ϕ = constant), its time to travel around the fiber and return to the laser can be deduced by setting $ds^2 = -c^2dt^2 + r^2\sin^2\theta(d\phi - \omega dt)^2 = 0$ along its path. (This is the only property of the general relativistic metric that we shall need: as in special relativity, so in general relativity, the interval ds^2 vanishes along photon trajectories.) Solving for dt and integrating ϕ from 0 to 2π, we find for the clockwise travel time $\Delta t = 2\pi r\sin\theta/(c - \omega r\sin\theta)$. By contrast, if the photon travels counter-clockwise, its round-trip travel time is $\Delta t = 2\pi r\sin\theta/(c + \omega r\sin\theta)$.

To ensure that the travel times clockwise and counterclockwise are the same, we must set the laser into rotational motion with angular velocity $d\phi/dt = \omega$. A straightforward calculation based on $ds^2 = 0$ then reveals equal round-trip travel times. Correspondingly, the laser gyroscope identifies $d\phi/dt = \omega$ as a nonrotating motion, so far as inertia of photons is concerned.

It is convenient and fruitful to interpret this result as telling us that *the Earth's spin drags space into rotational motion relative to the distant stars (relative to inertial frames at radial "infinity") with angular velocity* $d\phi/dt = \omega = (2G/c^2)J/r^3$; and a laser gyroscope with its laser at rest with respect to this space sees clockwise and counter-clockwise light travel as taking the same round trip time. In other words, this laser gyroscope reveals to us (i.e. defines for us) the rotational state of space in the vicinity of the Earth.

One might object that Lorentz invariance (or, in general relativity, local Lorentz invariance) insists that the laws of physics cannot pick out any preferred state of motion, so it should not be possible or sensible to speak of space as having some preferred motion. This is certainly true of *translational* motion in special relativity and local translational motion in general relativity. However, it is *not* true of rotational motion in special relativity, or in axially symmetric situations like ours in general relativity. Rotational motion is very different from translational motion. Our laser gyroscope demonstrates this: it readily picks out a preferred "rest frame" for space, so far as rotational motion is concerned.

Note that the rotational angular velocity $\omega = (2G/c^2)J/r^3$ of space relative to the distant stars depends on radius. It is greater near the Earth than far away, and its associated linear velocity [which is the same as the function $-\vec{\gamma}$ in the Cartesian version (5.5) of the spacetime metric]

$$\vec{v}_{\text{space}} = -\vec{\gamma} = \omega r\sin\theta\,\vec{e}_\phi = \frac{2G}{c^2}\frac{1}{r^2}\vec{J}\times\vec{e}_r \tag{5.6}$$

is also greater near Earth than far away. This is similar to the velocity of the air in a tornado or the water in a whirlpool: greater near the center than far away. This analogy is more than heuristic. It can be made quantitative:

In the reference frame of any local observer who moves with the fluid, the velocity field of nearby fluid can be decomposed into three physically distinct parts: an isotropic expansion (volume change), a shear, and a local rotation (see textbooks on fluid mechanics, e.g. Chap. 12 of [19] and Sec. 6.4 of [20]). The angular velocity of the local rotation is equal to half the fluid's vorticity, i.e., $\frac{1}{2}\vec{\nabla}\times\vec{v}$. A small, isotropic object (leaf, chip of wood, etc) placed in the fluid is dragged by the fluid into rotation with precisely this angular velocity.

Similarly, it is reasonable to expect that above the spinning Earth, any object whose orientation is inertially controlled (e.g. a gyroscope or a small nonspinning rock) will be dragged by the flow of space into rotation with a “frame-dragging” angular velocity given by

$$\vec{\omega}_{\text{drag}} = \frac{1}{2}\vec{\nabla} \times \vec{v}_{\text{space}} \ . \tag{5.7}$$

By inserting expression (5.6) for $\vec{v}_{\text{space}}$, we obtain precisely the frame-dragging angular velocity predicted by general relativity, Eq. (5.1).

5.2.2 Gravitomagnetic description

When gravity is weak (linearized) and the velocities of all gravitating matter and test matter are small compared to the speed of light in the gravitating matter’s mean rest frame (slow motion), then the equations of general relativity can be rewritten in a language and notation that resembles Maxwell’s electromagnetic theory. For full details see, e.g., Refs. [21, 4, 6] and papers cited therein.

This Maxwell-like formulation of slow-motion, linearized general relativity entails writing the slow-motion geodesic equation for a test particle $dv_j/dt = -\Gamma_{j00} - 2\Gamma_{j0k}(v_k/c)$ [with $\Gamma_{j0k} = \frac{1}{2}(\gamma_{j,k} - \gamma_{k,j})$] in Lorentz force notation:[1]

$$\frac{d\vec{v}}{dt} = \frac{m}{m}\left(\vec{g} + \frac{\vec{v}}{c} \times \vec{H}\right) = \vec{g} + \frac{\vec{v}}{c} \times \vec{H} \,, \qquad \text{where } \ \vec{H} = \vec{\nabla} \times \vec{\gamma} \,. \tag{5.8}$$

Evidently, the Newtonian gravitational acceleration $\vec{g}$ is the analog of the electric field (it is sometimes called the gravitoelectric field), and $\vec{H}$ is the analog of the magnetic field (and so is called the gravitomagnetic field). In electromagnetism the right hand side is multipled by the particle’s charge-to-mass ratio e/m. In the gravitational case the analog of charge is mass, so the right hand side is multiplied by $m/m = 1$.

Just as the ordinary magnetic field is the curl of a vector potential $\vec{A}$ which (as dictated by Maxwell’s equations) is generated by the motion of electric charge, i.e. by the electric current density $\vec{j}$,

$$\vec{B} = \vec{\nabla} \times \vec{A} \,, \quad \nabla^2 \vec{A} = -4\pi \vec{j} \,, \tag{5.9}$$

so the gravitomagnetic field is the curl of a vector potential $\vec{\gamma}$ which (as dictated by Einstein’s equations) is generated by the motion of mass, i.e. by the mass current density $\rho\vec{v}$ (where ρ is mass density and $\vec{v}$ is the mass’s velocity):

$$\vec{H} = \vec{\nabla} \times \vec{\gamma} \,, \quad \nabla^2 \vec{\gamma} = +16\pi\rho\vec{v} \,. \tag{5.10}$$

The sign difference in the magnetic (5.9) and gravitomagnetic (5.10) source terms is due to the gravitational

---

[1] The geodesic equation can be written as $du^\alpha/d\tau = -\Gamma^\alpha_{\beta\gamma} u^\beta u^\gamma$. In slow-motion, linearized gravity, the 4-velocity takes its Newtonian limit $u^0 = 1$, $u^j = u_j = v_j$, the proper time τ goes to Minkowski time t, and $\Gamma^j_{k0} \simeq \Gamma_{jk0}$. Therefore to first order in $\vec{v}$, the geodesic equation becomes $dv_j/dt = -\Gamma_{j00} - 2\Gamma_{j0k}(v_k/c)$.

force between like particles being attractive by contrast with the repulsive electromagnetic force; the factor 4 can be traced to the "spin-2" nature of weak gravity, viewed as a canonical field theory, by contrast with the spin-1 nature of electromagnetism.

Just as a spinning, charged sphere generates a dipolar magnetic field via Eq. (5.9), so the spinning Earth generates a dipolar magnetic field via Eq. (5.10):

$$\vec{\gamma} = -\frac{2G}{c^2}\frac{1}{r^2}\vec{J} \times \vec{e}_r\,, \qquad \vec{H} = -\frac{2G}{c}\left[\frac{-\vec{J} + 3(\vec{J}\cdot\vec{e}_r)\vec{e}_r}{r^3}\right], \tag{5.11}$$

where $\vec{J}$ is the spin angular momentum (i.e., the current dipole moment) and is defined as $\vec{J} = \int \vec{r}\,' \times \rho\vec{v}\, d^3\vec{r}\,'$. Since the gravitomagnetic force on a mass element inside a gyroscope has the standard Lorentz-force form $(\vec{v}/c) \times \vec{H}$, the spin of a gyroscope precesses around a gravitomagnetic field in the same manner as a spinning particle with a magnetic dipole moment precesses around an ordinary magnetic field [22]. Translating the magnetic precession equation to the gravitomagnetic case,[2] we obtain for the gyroscopic precessional angular velocity

$$\vec{\omega}_{\text{drag}} = -\frac{1}{2c}\vec{H} = \frac{G}{c^2}\left[\frac{-\vec{J} + 3(\vec{J}\cdot\vec{e}_r)\vec{e}_r}{r^3}\right], \tag{5.12}$$

which agrees with the standard general relativistic prediction (5.1) and with the fluid like dragging-of-space prediction (5.7).

5.2.3 Relation of space-drag and gravitomagnetic descriptions of frame dragging

The relation between the space-drag and gravitomagnetic descriptions of frame dragging becomes clear when one ties them both to relativity's curved-spacetime description. The tie is through the off-diagonal components $g_{0j} = \gamma_j$ of the frame-dragging metric (5.5): The velocity of space dragging is $\vec{v}_{\text{space}} = -\vec{\gamma}$, and the gravitomagnetic vector potential is $\vec{\gamma}$; so $\vec{v}_{\text{space}}$ and $-\vec{\gamma}$ are the same quantities but viewed in two very different physical pictures. Correspondingly, the vorticity of the flow of space $\vec{\nabla} \times \vec{v}_{\text{space}}$ is the same as the negative of the gravitomagnetic field $-\vec{H} = -\vec{\nabla} \times \vec{\gamma}$. And finally, the physical fact that a gyroscope is dragged by the flow of space into precession with angular velocity $\vec{\omega}_{\text{drag}} = \frac{1}{2}\vec{\nabla} \times \vec{v}_{\text{space}}$ is completely equivalent to the precession of the gyroscope around the gravitomagnetic field with angular velocity $\vec{\omega}_{\text{drag}} = -\frac{1}{2}\vec{H}$.

---

[2] A magnetic dipole $\vec{\mu}$ is defined as $\vec{\mu} \equiv \frac{1}{2}\int \vec{r}\,' \times \vec{j}\, d^3\vec{r}\,'$, where $\vec{j}$ is the electric current density (analogous to $\rho\vec{v}$). In a magnetic field $\vec{B}$, a small particle with magnetic dipole moment $\vec{\mu}$ feels a torque $\vec{\mu} \times \vec{B}$ (which follows from the Lorentz force law). Similarly in the gravitational case, the Lorentz-force-like geodesic equation (5.8) dictates that a gyroscope with spin $\vec{S}$ feels a torque given by $\frac{1}{2}\vec{S} \times \vec{H}/c$. The gyroscope's spin angular momentum is changed by this torque: $d\vec{S}/dt = \frac{1}{2}\vec{S} \times \vec{H}/c$; i.e. $\vec{S}$ rotates with the "gravitomagnetic" angular velocity $\vec{\omega}_{\text{GM}} = -\vec{H}/2c$.

5.3 Mach's Principle

5.3.1 Overview

Turn, now, from frame dragging outside the rotating Earth or other rotating body to frame dragging inside a rotating universe, i.e. to Mach's principle. As we discussed near the end of Sec. 5.1 (the Brill-Cohen model problem [12]), a spinning, massive, spherical shell that is arbitrarily close to its Schwarzschild radius drags inertial axes inside itself into lock-step rotation with its own spin. In this sense, general relativity incorporates Mach's principle. But a spinning, massive shell is an extremely crude model of our universe. In this section we explore a much better model.

We begin in Sec. 5.3.2 by treating our universe as spatially homogeneous and filled with pressureless matter (i.e. we ignore the tiny amount of radiation and the large amount of "dark energy" that fill the real universe, and we average over density fluctuations due to planets, stars, and galaxies). We set this model universe into extremely slow[3] and completely *rigid* rotation relative to local inertial axes, i.e., we give its matter a homogeneous vorticity. (Note: this is vorticity of the matter relative to local inertial axes, by contrast with the "vorticity of space" relative to radial infinity invoked in Sec. 5.2.1.) We verify that, as in Newtonian theory, there is no "center of rotation" for this universe: by transforming to spatial coordinates that move linearly with respect to the original coordinates, we change the apparent center of rotation but leave the vorticity unchanged everywhere. This is very satisfying.

We then allow our rotating, homogeneous universe to expand in a manner governed by Einstein's equations, and we explore how its vorticity evolves. In the authors' opinion, the most satisfying result would be a discovery that Einstein's equations force the vorticity to vanish. This is because only then would the inertial axes be tied, everywhere, into lock-step rotation with the matter. (Such lock-step rotation everywhere should be possible when the vorticity is spatially constant, as it is in this model.)

Our calculation in Sec. 5.3.2, however, does *not* reveal a vanishing vorticity. Instead, we can specify any (small) value we wish for the homogeneous vorticity at some initial moment of time, and the Einstein equations then dictate that the vorticity remain homogeneous, but decay in magnitude at the same rate as it would in Newtonian physics: vorticity $\propto 1/a^2$. Here a is the "expansion factor" of the universe, i.e. (up to a multiplicative constant) the distance between any two particles of matter in the universe when the tiny rotation is neglected. Evidently, general relativity does *not* incorporate Mach's principle in the way that we would find most satisfying.

To explore the influence of the universe's matter in greater detail, in Sec. 5.3.3 we give our model universe an outer edge, beyond which is vacuum and asymptotically flat spacetime. Then, as in the Brill-Cohen, rotating-shell problem, the inertial influence of the universe's matter must compete with the inertial influence of the distant, empty spacetime (of spatial "infinity"). By analogy with the rotating-shell result, it is

---

[3] We require slow rotation so we can perform an analysis using perturbation theory, expanding to first order in the rotational angular velocity.

reasonable to expect the following, at the center of this idealized universe :

- Very soon after the big-bang expansion begins (when the cosmological horizon is tiny compared to the radius of the universe's outer edge, so an observer at the center can see only a tiny fraction of the distance to the edge), the universe's matter will almost completely control the inertial axes at its center; i.e., the angular velocity ω_c of the central inertial axes (relative to radial infinity) will be almost identical to the angular velocity Ω_c of the central matter's rotation: $(\Omega_c - \omega_c)/\Omega_c \ll 1$.
- As the universe expands, the inertial grip of its rotating matter will weaken and the inertial influence of the external empty space (radial "infinity") will correspondingly grow, causing the fractional slippage of the inertial axes from the universe's grasp, $(\Omega_c - \omega_c)/\Omega_c$, to increase, approaching unity as the universe becomes very large and its cosmological horizon becomes enormously larger.

Indeed, this is what our calculation in Sec. 5.3.3 reveals, though there is a complicated subtlety: in a dynamically expanding spacetime such as this one, we must find a preferred way to "map" angular positions at radial infinity (in the asymptotically flat, vacuum region outside the universe) onto angular positions $\bar{\varphi}$ at the center, so that the angular velocity $\Omega_c = d\bar{\varphi}/d\tau$ of the central matter with respect to radial infinity (with τ = proper time as measured by the matter) will be well defined, and so will be ω_c.[4] We achieve this preferred mapping via a preferred family of spacelike geodesics introduced by Schmid [18], which connect the center of the universe to radial infinity (see Appendix 5.A for details). With this choice of mapping, our results are gauge-invariant and take a very simple and elegant form [Eq. (5.41)]. Figure 5.1 shows the corresponding fractional slippage of the inertial axes, $(\Omega_c - \omega_c)/\Omega_c$.

Notice that the slippage at the universe's center begins immediately after the big bang and long before the center has had any causal contact with the universe's edge—i.e., before the cosmological horizon has been reached. How is this possible? At such early times there is no way, through electromagnetic or any other light-speed observations, for a central observer to discover that the universe has an edge. The observer sees only a homogeneous universe with small, homogeneous vorticity. But frame dragging *appears* to tell the observer that the universe is finite.

This appearance is an illusion. Since the central observer cannot see out into the external universe, there is no way for that observer to learn what the standard of rotational inertia is out there and correspondingly, no way to learn how the angular coordinate $\bar{\varphi}$ at the center should be chosen so as to tie it to inertia at infinity. As a result, there is no way for the observer to know what $\Omega = (d\bar{\varphi}/d\tau)_{\mathrm{matter}}$ is (nor what is the frame-dragging angular velocity ω). The only thing the central observer can measure is the matter's vorticity, i.e. (twice) the angular velocity of the matter relative to local gyroscopes. [In our spatially homogeneous model, this turns out, not surprisingly, to be $2(\Omega - \omega)$.]

Even though the central observer cannot measure Ω or ω individually at early times, we as physicists probing this model mathematically can calculate them; and they show a remarkably smooth slippage as a

---

[4] The difference $\Omega_c - \omega_c$ is uniquely defined independent of any such mapping. It is half the vorticity of the matter, i.e. it is the spatially constant angular velocity of the matter relative to local inertial axes.

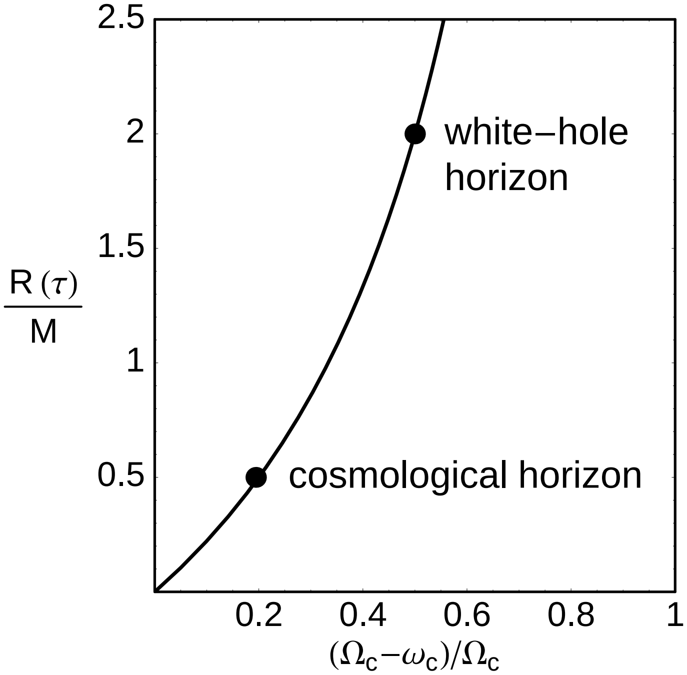

Figure 5.1: The fractional slippage of the inertial axes at the center of a model universe with a spherical edge, $(\Omega_c - \omega_c)/\Omega_c$ at time τ, plotted against the radius $R(\tau)$ of the expanding universe's outer edge (which depends on time τ) in unit of its mass M [see Eq. (5.41)]. Here τ is proper time measured in the rest frame of the universe's slowly rotating matter, Ω_c is the angular velocity $(d\phi/d\tau)_c$ of the matter at the center relative to inertial frames at infinity, ω_c is the corresponding angular velocity of inertial axes at the center, and (it turns out) their difference $\Omega_c - \omega_c$ is half the (locally measurable) vorticity of the matter, i.e. it is the (spatially homogeneous) locally measured angular velocity of the matter relative to gyroscopes. This figure assumes the mapping of angles, between the center of the universe and infinity, that is embodied in the matching of the 3-metric (5.34)–(5.35) and the extrinsic curvature (5.37)–(5.38). The radius marked "cosmological horizon" corresponds to the moment when an observer at the center of the universe can first see out to the universe's edge and discover there *is* an edge [see Eq. (5.42) and surrounding discussion]. The radius marked "white-hole horizon" corresponds to the moment when the universe's surface passes through its Schwarzschild radius, $R = 2M$.

function of time: no lock-step rotation $[(\Omega_c - \omega_c)/\Omega_c = 0]$ before causal contact with the universe's edge is achieved; no sudden change when causal contact is reached. This seems rather non-Machian.

This non-Machian behavior is intimately tied to a truly non-causal aspect of frame dragging. In any spherically symmetric situation, such as this one, the frame-dragging angular velocity ω (viewed as a vector when its direction is taken into account) has a dipolar angular dependence; and in general relativity, dipolar fields are not radiative, i.e. they do not obey wave equations. This remarkable fact is tied to the spin-two nature of the graviton: only fields with quadrupolar and higher-order angular forms (i.e. with angular order greater than or equal to the graviton spin $s = 2$) are governed by wave equations.

The frame-dragging angular velocity ω, like the non-propagating, spherical coulomb field of a charge distribution in electromagnetic theory, is laid down at some initial time and evolves forward thereafter in a nonradiative manner. For a detailed general relativistic analysis and discussion of how the matter's angular momentum distribution governs the evolution of ω, see Refs. [16, 18] and references therein.

The most serious way in which our model problem differs from the physical universe is in its neglect of "dark energy", which constitutes today about 65% of the universe's energy density. In Sec. 5.3.4, we rectify this neglect by inserting dark energy into our universe-with-edge model. We assume (as is somewhat likely) that the dark energy takes the mathematical form of a cosmological constant in Einstein's equations.

By contrast with the matter, we cannot cut off this dark energy at an outer edge for the universe. It extends out of the universe into the vacuum exterior, undiminished, i.e. with a continuing-constant cosmological term in Einstein's equations. This radically alters the geometry of spacetime outside the universe: the geometry is no longer asymptotically flat and so no longer has the asymptotic inertial properties and influence familiar from special relativity. Instead, the geometry is asymptotically that of the DeSitter solution to Einstein's equations, and it has an asymptotic "DeSitter horizon". Despite this change of spacetime geometry, we find that the fractional slippage of the inertial axes, $(\Omega_c - \omega_c)/\Omega_c$, remains qualitatively the same as in the absence of dark energy [Eq. (5.57) and Fig. 5.2 of Sec. 5.3.4 below].

5.3.2 Spatially homogeneous model universe that rotates slowly and rigidly

We now turn to the mathematical details of frame dragging in a spatially flat, spatially infinite, homogeneous model universe that rotates slowly and rigidly, i.e. with uniform vorticity; and we explore the impact of Einstein's equations on the value (nonzero!) and evolution of the vorticity ($\propto 1/a^2$) . Before setting the model universe into slow rotation, we shall first look at the non-rotating case, which is an essential preliminary. In our formulae we will use subscript "$-$" to emphasize that this is the interior of the universe, and later we will use subscript "+" for the exterior, beyond the universe's edge. We will use geometric units with $G = c = 1$ for the rest of this paper.

The interior spacetime of a homogeneous, spatially-flat universe can be described by the Friedmann-Robertson-Walker (FRW) metric (with its vanishing spatial curvature term, "$k = 0$"). In comoving coordinates $x_-^\alpha = \{\tau, \bar{r}, \bar{\theta}, \bar{\varphi}\}$, the universe's spacetime metric can be written as

$$ds_-^2 = -d\tau^2 + a^2(\tau)\left(d\bar{r}^2 + \bar{r}^2 d\bar{\theta}^2 + \bar{r}^2 \sin^2\bar{\theta}\, d\bar{\varphi}^2\right). \tag{5.13}$$

Here $a(\tau)$ is the scale factor, whose form is determined by the field equations. The density of the universe satisfies $\rho a^3 = \rho_o a_o^3 =$ constant, where the subscript "o" indicates quantities evaluated at some reference time τ_o. We presume that the universe has negligible pressure so its energy-momentum tensor takes the form $T^{\alpha\beta} = \rho u_-^\alpha u_-^\beta$, where u_-^α is the 4-velocity of its fluid. Since the fluid elements are at rest with respect to the spatial coordinates $(\bar{r}, \theta, \phi)$, the components of u_-^α are $(1, 0, 0, 0)$. Given this $T^{\alpha\beta}$ and the metric (5.13), the Einstein field equations yield

$$\dot{a}^2 = \frac{8\pi}{3}\rho a^2 = \frac{8\pi}{3}\frac{\rho_o a_o^3}{a}\ , \tag{5.14}$$

where dots indicate derivative with respect to τ. The solution to Eq. (5.14) is

$$a(\tau) = a_o(\tau/\tau_o)^{2/3}. \tag{5.15}$$

Now set the universe into slow rotation so that the fluid elements, instead of being at rest in the coordinates $(\bar{r}, \bar{\theta}, \bar{\varphi})$, move with angular velocity

$$\frac{d\bar{\varphi}}{d\tau} = \Omega(\bar{r}, \tau)\ . \tag{5.16}$$

We seek a solution to the Einstein field equations, accurate to first order in Ω, that has the following metric

$$ds_-^2 = -d\tau^2 + a^2\left[d\bar{r}^2 + \bar{r}^2 d\bar{\theta}^2 + \bar{r}^2 \sin^2\bar{\theta}(d\bar{\varphi} - \omega d\tau)^2\right]. \tag{5.17}$$

Here $\omega = \omega(\bar{r}, \tau)$ is the angular velocity of local inertial frames with respect to the coordinates and $a(\tau)$ takes the unperturbed form (5.15). The term quadratic in ω in Eq. (5.17) should be ignored. The energy-momentum tensor that goes with this metric is still that of a pressureless fluid : $T^{\alpha\beta} = \rho u_-^\alpha u_-^\beta$, in which ρ is the *rest* mass density and u_-^α now takes the values $(1, 0, 0, \Omega)$. The energy-momentum conservation law leads to the following first-order nontrivial equation:

$$T^{\phi\beta}{}_{;\beta} = \frac{1}{a^3}\frac{d}{d\tau}\left[a^5\rho(\Omega - \omega)\right] = 0\ . \tag{5.18}$$

Since $\rho a^3 =$ constant [Eq. (5.14)], equation (5.18) implies

$$\Omega - \omega = \left(\frac{a_o}{a}\right)^2 \varpi_o(\bar{r})\ , \tag{5.19}$$

where ϖ_o is an arbitrary function of $\bar{r}$, representing the difference between Ω and ω at time τ_o. It can be verified that Eq. (5.19) is consistent with the geodesic equation for the fluid elements and with the conservation of angular momentum per unit mass for each fluid element. It can also be verified that, if $(\Omega - \omega)$ is independent of $\bar{r}$, then the vorticity is $2(\Omega - \omega) = 2(a_o/a)^2\varpi_o$.

In general relativity, as in Newtonian theory, the local angular velocity of rotation of a fluid element relative to local inertial frames is equal to half its vorticity.[5] We shall impose the homogeneity condition that the universe fluid rotates uniformly relative to local inertial frames, i.e., its vorticity is the same everywhere. This implies that the vorticity is

$$\text{vorticity} = 2(\Omega - \omega) = 2\varpi_o\left(\frac{a_o}{a}\right)^2 , \tag{5.20}$$

and so it decays in magnitude at the same rate as it would in Newtonian physics: vorticity $\propto 1/a^2$. At time τ_o, the vorticity of the fluid is simply $2\varpi_o$.

Next we compute and solve the Einstein field equations to determine the relationship between ω and Ω. The non-trivial components of the field equations are found to be

$$\tau\phi: \qquad 16\pi\rho a^2\bar{r}(\omega - \Omega) = 4\omega_{,\bar{r}} + \bar{r}\omega_{,\bar{r}\bar{r}} , \tag{5.21a}$$

$$\bar{r}\phi: \qquad \sqrt{24\pi\rho}\,\omega_{,\bar{r}} + \omega_{,\bar{r}\tau} = 0 . \tag{5.21b}$$

Equation (5.19) can be inserted into Eq. (5.21a), and the resulting differential equation has the following solution for ω

$$\omega(\bar{r},\tau) = \left[-\frac{8\pi}{5}\rho\bar{r}^2 + \zeta_1(\tau) - \frac{\zeta_2(\tau)}{\bar{r}^3}\right]\varpi_o .$$

Here ζ_1 and ζ_2 are two dimensionless functions of τ to be determined. Since the $1/\bar{r}^3$ term diverges at the origin, we shall set $\zeta_2(\tau) \equiv 0$, which makes ω satisfy Eq. (5.21b) automatically and gives

$$\omega(\bar{r},\tau) = \left[-\frac{8\pi}{5}\rho\bar{r}^2 + \zeta_1(\tau)\right]\varpi_o . \tag{5.22}$$

Since $\varpi_o = (a/a_o)^2(\Omega - \omega)$, this is the desired relation between ω and Ω.

To help in the next subsection, we elucidate the nature of the coordinates $(\tau, \bar{r}, \bar{\theta}, \bar{\varphi})$ used in defining the angular velocity $\Omega = d\bar{\varphi}/d\tau = (\partial\bar{\varphi}/\partial\tau)_{\bar{r},\bar{\theta}}$ of the universe's fluid. The interior metric (5.13) shows that the 3-surfaces of constant τ are homogeneous and have a flat 3-metric, and that radial lines of constant $(\tau, \bar{r}, \bar{\theta})$ are geodesics in the homogeneous 3-surfaces, and also spacelike geodesics of the 4-dimensional spacetime. These radial, spacelike geodesics $\mathcal{G}$ can be thought of as carrying the angular coordinates $(\bar{\theta}, \bar{\varphi})$ from the origin outward, throughout the universe; i.e., they can be thought of as mapping the angles $(\bar{\theta}, \bar{\varphi})$ from the origin to other points in the universe. Schmid [18] has shown that this mapping of of angles by means of spacelike geodesics $\mathcal{G}$ gives rise to a remarkably simple and elegant description of frame dragging not only when the vorticity is uniform (as in our model universe) but also when it is nonuniform. In Sec. 5.3.3, when

---

[5] In the local rest frame of a fluid element, the velocities of neighboring fluid elements are small compared to the speed of light, so the general relativistic viewpoint on fluid motions and inertia reduces to the Newtonian viewpoint. For a Newtonian proof that the local fluid angular velocity relative to local inertial frames is half its vorticity, see Sec. 6.4 of [20].

giving our universe an edge, we will extend these radial spacelike geodesics $\mathcal{G}$ into the vacuum exterior and onward to spacelike infinity, use them to carry our angular coordinates out to infinity, and thereby use them to define the angular velocity of our universe's fluid with respect to infinity.

5.3.3 Universe with an outer edge

To explore the influence of the universe's matter (pressureless fluid) in greater detail, we now give our model universe a spherical outer boundary, beyond which is vacuum and asymptotically flat spacetime. Then, as in the Brill-Cohen, rotating-shell problem, the inertial influence of the universe's matter must compete with the inertial influence of the distant, empty spacetime; this competition gives rise to the unknown function $\zeta_1(\tau)$ in Eq. (5.22)—i.e., it determines the frame dragging angular velocity $\omega(\bar{r}, \tau)$.

5.3.3.1 No rotation

We begin with the rotation turned off. The boundary of the *non-rotating* universe, call it Σ, is a hypersurface located at constant $\bar{r} = \bar{r}_{\circledcirc}$. To ensure a smooth transition between the universe and the exterior vacuum region, we impose the Darmois-Israel junction conditions [23], which require that the intrinsic metric and extrinsic curvature at the boundary surface Σ be continuous. Taking the metric (5.13) for the non-rotating universe and setting $\bar{r} = \bar{r}_{\circledcirc}$, we obtain the 3-metric on Σ as

$$ {}^{(3)}ds_-^2 = -d\tau^2 + a^2 \bar{r}_{\circledcirc}^2 \left(d\bar{\theta}^2 + \sin^2\bar{\theta}\, d\bar{\varphi}^2 \right) . \tag{5.23} $$

The exterior spacetime of the *non-rotating* universe is described by the Schwarzschild metric. Written in Schwarzschild coordinates $x_+^\alpha = \{t, r, \theta, \varphi\}$, it is

$$ ds_+^2 = -(1-\mathcal{A})dt^2 + \frac{dr^2}{1-\mathcal{A}} + r^2(d\theta^2 + \sin^2\theta\, d\varphi^2) , \tag{5.24a} $$

where

$$ \mathcal{A}(r) = \frac{2M}{r} , \tag{5.24b} $$

and M is the total mass of the universe, as measured gravitationally by observers far outside it. Being pressureless, any fluid element on the surface of the universe Σ must follow a radial geodesic $r = R(\tau)$ and $t = T(\tau)$ in the outer Schwarzschild spacetime. Here τ is the proper time measured on Σ and thus is the same as the comoving time coordinate used in the interior region. The 3-metric on Σ, calculated from the exterior, is

$$ {}^{(3)}ds_+^2 \;=\; \left[-(1-\mathcal{A}_R)\left(\frac{dT}{d\tau}\right)^2 + \frac{(dR/d\tau)^2}{1-\mathcal{A}_R} \right] d\tau^2 + R^2\left(d\theta^2 + \sin^2\theta\, d\varphi^2\right), \tag{5.25} $$

in which $\mathcal{A}_R = \mathcal{A}(R)$. Notice that the term in square brackets in Eq. (5.25) is equal to the inner product of the 4-velocity of the fluid element, i.e., -1. To match this 3-metric with the one computed from the interior, Eq. (5.23), we must let $R(\tau) \equiv a\bar{r}_{\circledcirc}$. This amounts to selecting, from a family of radial geodesics, a solution that has the same τ dependence as $a\bar{r}_{\circledcirc} \sim \tau^{2/3}$. This solution can be found, e.g., in Ref. [7] Eq. (25.38) with time reversed:

$$R(\tau) = 2M\left(\frac{3\tau}{4M}\right)^{2/3} . \tag{5.26}$$

Equating $R(\tau)$ (5.26) and $a\bar{r}_{\circledcirc}$ (5.15), we obtain

$$M = \frac{4\pi}{3}\rho_o(a_o\bar{r}_{\circledcirc})^3 , \tag{5.27}$$

in which we have used the relation $\tau_o^2 = 1/(6\pi\rho_o)$. [This can be obtained by combing the second equation in (5.14) with Eq. (5.15).] The corresponding expression for $T(\tau)$ is

$$T(\tau) = \tau + 4M\left(\frac{R}{2M}\right)^{1/2} + 2M\log\left|\frac{(R/2M)^{1/2} - 1}{(R/2M)^{1/2} + 1}\right| . \tag{5.28}$$

Note that in matching Eq. (5.25) with Eq. (5.23), we must also identify the angular coordinates as $\theta = \bar{\theta}$, $\varphi = \bar{\varphi}$. These angular coordinates match up smoothly at the boundary because of the spherical symmetry throughout the interior universe and the exterior vacuum region.

It remains to check that the extrinsic curvature of Σ is the same as computed using the interior and exterior 4-metrics. In Appendix 5.B, we verify that this is indeed so.

5.3.3.2 Exterior of the rotating universe

When we set our model universe into slow rotation, the exterior spacetime is dragged by its motion, giving rise to a frame dragging angular velocity $\sigma(r)$ in the metric

$$ds_+^2 \quad = \quad -(1-\mathcal{A})\,dt^2 + \frac{dr^2}{1-\mathcal{A}} + r^2 d\theta^2 + r^2\sin^2\theta\,(d\varphi - \sigma dt)^2 \tag{5.29}$$

[cf. Eq. (5.4)]. The vacuum field equation for σ, to first order in σ, is (e.g. Eq. (9) in Ref. [24])

$$r^{-4}\frac{d}{dr}\left(r^4\frac{d\sigma}{dr}\right) = 0 , \tag{5.30}$$

which implies $\sigma = \text{const.}/r^3$. Comparing this with the standard asymptotic form for the metric far from a source (e.g. Eq. (19.5) of Ref. [7]), we see that the constant is $2J$, where J is the spin angular momentum of the slowly rotating universe (as measured via frame dragging by distant observers):

$$\sigma = \frac{2J}{r^3} . \tag{5.31}$$

The frame dragging prevents the azimuthal coordinate φ in the exterior from matching up smoothly at Σ with the interior azimuthal coordinate $\bar{\varphi}$, and it also aggravates the coordinate singularity at $r = 2M$ ($\mathcal{A} = 0$) in the exterior. To achieve a smooth match at Σ and remove the singularity at $\mathcal{A} = 0$, we use the radial spacelike geodesics $\mathcal{G}$ described at the end of Sec. 5.3.2 to define new exterior azimuthal and time coordinates $\tilde{\varphi}$ and $\tilde{t}$. Specifically, we extend the radial geodesics $\mathcal{G}$ from the universe's interior into the exterior and on outward to radial infinity. Then we carry our angular azimuthal coordinate $\bar{\phi}$ from the interior into and throughout the exterior, along the geodesics $\mathcal{G}$ (giving it the name $\tilde{\phi}$ in the exterior); and we carry our new time coordinate $\tilde{t}$ inward from infinity (where we set it equal to the Schwarzschild t coordinate) to Σ. In Appendix 5.A we carry out this geometric construction, thereby arriving at the following relationship between the Schwarzschild (φ, t) and the new coordinates $(\tilde{\varphi}, \tilde{t})$:

$$d\varphi = d\tilde{\varphi} + \frac{2J}{r^3}\frac{\sqrt{\mathcal{A}_R}}{1-\mathcal{A}}\frac{dr}{\sqrt{1-\mathcal{A}+\mathcal{A}_R}}\,, \tag{5.32a}$$

$$dt = d\tilde{t} + \frac{\sqrt{\mathcal{A}_R}}{1-\mathcal{A}}\frac{dr}{\sqrt{1-\mathcal{A}+\mathcal{A}_R}}\,, \tag{5.32b}$$

where $\mathcal{A}_R \equiv \mathcal{A}(R)$. In terms of the new, geometrically defined coordinates, the exterior metric takes the form

$$ds_+^2 = -(1-\mathcal{A})\,d\tilde{t}^2 - 2\left(\frac{\mathcal{A}_R}{1-\mathcal{A}+\mathcal{A}_R}\right)^{1/2} d\tilde{t}dr + \frac{dr^2}{1-\mathcal{A}+\mathcal{A}_R} + r^2 d\theta^2 + r^2\sin^2\theta\left(d\tilde{\varphi} - \frac{2J}{r^3}d\tilde{t}\right)^2\,, \tag{5.33}$$

In this coordinate system, each spacelike geodesic $\mathcal{G}$, starting orthogonal to the surface of the universe, travels along fixed $(\tilde{t}, \theta, \tilde{\varphi})$; just like it travels along fixed $(\tau, \bar{\theta}, \bar{\varphi})$ inside the universe.

5.3.3.3 Matching interior and exterior of rotating universe

For the slowly rotating universe, the hypersurface Σ swept out by its moving boundary is still at the interior coordinate location $\bar{r} = \bar{r}_{\circledcirc}$ (to first order in the rotation) and is described by the same geodesic functions, Eq. (5.26) and (5.28). However, since we have adopted $(\tilde{t}, \tilde{\varphi})$ coordinates in the exterior region, $T(\tau)$ [Eq. (5.28)] must be transformed into $\tilde{T}(\tau)$ using Eq. (5.32b) with $r = R(\tau)$. By imposing continuity of the intrinsic 3-metric and extrinsic curvature across Σ, we will obtain the unknown function $\zeta_1(\tau)$ and the constant ϖ_o in the frame dragging equation (5.22).

Calculated from the exterior metric [Eq. (5.33)], the 3-metric of the hypersurface Σ is

$${}^{(3)}ds_+^2 = -d\tau^2 + R^2\left(d\theta^2 + \sin^2\theta\, d\tilde{\varphi}^2\right) - \frac{4J}{R}\sin^2\theta\, d\tilde{\varphi}d\tau\,. \tag{5.34}$$

Calculated from the interior metric [Eq. (5.17)], the 3-metric is

$${}^{(3)}ds_-^2 = -d\tau^2 + (a\bar{r}_{\circledcirc})^2\left(d\bar{\theta}^2 + \sin^2\bar{\theta}\, d\bar{\varphi}^2\right) - 2\omega(a\bar{r}_{\circledcirc})^2\sin^2\bar{\theta}\, d\bar{\varphi}d\tau\,, \tag{5.35}$$

where ω is to be evaluated at $\bar{r}_{\circledcirc}$. Setting $\tilde{\varphi} = \bar{\varphi}$ everywhere on Σ (for all τ), and correspondingly matching the $d\tilde{\varphi}d\tau$ term in Eq. (5.34) to the $d\bar{\varphi}d\tau$ term in Eq. (5.35), we obtain

$$\omega(\bar{r}_{\circledcirc}, \tau) = \frac{2J}{R^3(\tau)} \,. \tag{5.36}$$

To compute the extrinsic curvature on Σ, we follow the prescription given in Appendix 5.B. The result is:

$$\begin{aligned} K^{-}_{ij}dx^i dx^j &= -a\bar{r}_{\circledcirc}\left(d\bar{\theta}^2 + \sin^2\bar{\theta}^2\, d\bar{\varphi}^2\right) + a\bar{r}_{\circledcirc}\left(2\omega + \bar{r}_{\circledcirc}\omega_{,\bar{r}}\right)\sin^2\bar{\theta}\, d\bar{\varphi}d\tau \,, && (5.37)\\ K^{+}_{ij}dx^i dx^j &= -R\left(d\theta^2 + \sin^2\theta^2 d\tilde{\varphi}^2\right) - \frac{2J}{R^2}\sin^2\theta\, d\tilde{\varphi}d\tau \,. && (5.38)\end{aligned}$$

Note that ω and $\omega_{,\bar{r}}$ in Eq. (5.37) should be evaluated at $\bar{r}_{\circledcirc}$. The matching of the $d\bar{\varphi}d\tau$ and $d\tilde{\varphi}d\tau$ terms leads to

$$\left(2\omega + \bar{r}\omega_{,\bar{r}}\right)\Big|_{\bar{r}_{\circledcirc}} = -\frac{2J}{R^3} \,. \tag{5.39}$$

Inserting Eq. (5.22) into Eq. (5.36) and (5.39), we can determine the two unknowns ζ_1 and ϖ_o in ω [Eq. (5.22)]:

$$\begin{aligned} \omega(\bar{r}, \tau) &= -\frac{3J}{R^3}\left(\frac{\bar{r}}{\bar{r}_{\circledcirc}}\right)^2 + \frac{5J}{R^3} \,, && (5.40a)\\ \Omega(\bar{r}, \tau) &= \omega + \varpi_0/a^2 = \omega + \frac{5J}{2MR^2} \,. && (5.40b)\end{aligned}$$

Note that their dependence on τ is entirely contained in $R(\tau)$ and $\mathcal{A}_R = 2M/R(\tau)$.

The frame dragging can be manifested by calculating the ratio of $(\Omega - \omega)$ [the angular velocity of the fluid as measured by local inertial-guidance gyroscopes] to Ω [the angular velocity of the fluid relative to inertial frames at infinity]. This ratio χ_c is to be evaluated at the center of the universe $\bar{r} = 0$:

$$\chi_c \equiv \left(\frac{\Omega_c - \omega_c}{\Omega_c}\right) = \frac{1}{1 + 2M/R} \,. \tag{5.41}$$

At very early times, when $R(\tau)/M \to 0$, the ratio χ_c vanishes and the frame dragging is perfect: the spin direction of a gyroscope is locked to the rotational motion of the universe's fluid. At very late times, χ_c becomes unity, so the universe's rotation has no significant influence on gyroscopes. Figure 5.1 depicts the evolution of χ_c as the universe expands. Two special times are shown on the graph: (i) The crossing of the cosmological horizon happens at the time τ, at which an observer at the center can first see out to the universe's edge; that is, when a null ray emitted from the edge at $\tau = 0$ reaches the center. This horizon crossing time $\tau_{\rm HC}$ is determined mathematically by

$$\int_0^{\tau_{\rm HC}} \frac{d\tau}{a(\tau)} = \int_0^{\bar{r}_s} d\bar{r} \,, \tag{5.42}$$

with $a(\tau)$ given by Eq. (5.15). The radius of the universe at that time is $R_{\rm HC} = a(\tau_{\rm HC}) \times \bar{r}_s = M/2$. (ii) The second special time τ is the one at which the edge of the universe passes through the white-hole horizon: $R = 2M$. For a discussion of Fig. 5.1, see Sec. 5.3.1 above.

5.3.4 Universe with dark energy and an outer edge

In this section, we add dark energy to our universe-with-edge model. We assume the dark energy takes the mathematical form of a cosmological constant in Einstein's equations both inside the universe and in the vacuum exterior. Again we shall lay the foundation for our calculations by first examining a non-rotating universe. Then we shall explore the influence of frame dragging by setting the model universe into slow rotation. For an introduction to cosmological models with dark energy, see, e.g., Ref. [2] (Chapter 18), Ref. [25] (Chapter 8), Ref. [26] (Chapter 12), and Ref. [27].

5.3.4.1 Non-rotating universe and exterior

The metric for the *non-rotating* universe takes the same form as in Eq. (5.13), but it now satisfies the Einstein field equations with a Λ term, where Λ is the cosmological constant:

$$\mathcal{R}_{\mu\nu} - \frac{1}{2} g_{\mu\nu} \mathcal{R} + \Lambda g_{\mu\nu} = 8\pi T_{\mu\nu} \ . \tag{5.43}$$

This interior spacetime is the (flat) Friedmann-Lemaître (FL) universe. The solution of (5.43) for the scale factor $a(\tau)$ takes the form (cf., e.g., Eq. (12.77) in Ref. [26])

$$a(\tau) = \left(\frac{\rho_{m_0}}{\rho_\Lambda} \right)^{1/3} \sinh^{2/3} \left(\frac{\tau}{\tau_\Lambda} \right) . \tag{5.44}$$

Here ρ_{m_0} is the matter density of the universe today and

$$\rho_\Lambda \equiv \frac{\Lambda}{8\pi} , \qquad \tau_\Lambda \equiv \frac{2}{\sqrt{3\Lambda}} . \tag{5.45}$$

In the exterior, the metric satisfying the vacuum Einstein field equations with a cosmological constant is that of the Schwarzschild-de Sitter (SdS) spacetime [28]:

$$ds_+^2 = -(1 - \mathcal{B}) dt^2 + \frac{1}{1 - \mathcal{B}} dr^2 + r^2 \left(d\theta^2 + \sin^2 \theta d\varphi^2 \right) , \tag{5.46a}$$

where

$$\mathcal{B} = \frac{2M}{r} + \frac{\Lambda}{3} r^2 . \tag{5.46b}$$

The metric component g_{rr} diverges when $\mathcal{B} \to 1$. For $M\Lambda^{1/2} < 1/3$, $\mathcal{B} = 1$ has two real positive roots, r_h and $r_{\rm SdS}$ ($r_{\rm SdS} > r_h > 0$), corresponding to the location of the white-hole horizon and the "Schwarzschild-de

Sitter" cosmological horizon respectively [29]:

$$r_{h,\mathrm{SdS}} = \frac{1}{\Lambda^{1/2}} \sin\left[\frac{1}{3}\sin^{-1}(3M\Lambda^{1/2}) + \ell\frac{2\pi}{3}\right], \qquad \ell = 0,\, 1\,. \tag{5.47}$$

The matching of the 3-metric and extrinsic curvature at the boundary of the universe can be done in the same manner as in Sec. 5.3.3: The fluid element on the boundary sphere follows a radial geodesic of the SdS spacetime, which must be matched to the proper radius of the universe $R(\tau) = a(\tau)\bar{r}_{\circledcirc}$. Then the 3-dimensional hypersurface Σ swept out by the moving boundary sphere is determined and it is straightforward to compute ${}^{(3)}ds^2_{\pm}$ and $\mathcal{K}^{\pm}_{ij}$ and verify they match each other on Σ.

Let **u** be the 4-velocity of the universe's surface in the exterior SdS geometry and let **n** be the unit normal vector. Since the surface follows a radial timelike geodesic, only the time and radial components of **u** and **n** are nonzero and they satisfy the following four equations

$$\begin{aligned} -E &= u_t = -(1-\mathcal{B})\,u^t\,, & \text{(5.48a)}\\ -1 &= \mathbf{u}\cdot\mathbf{u} = -(1-\mathcal{B})(u^t)^2 + (1-\mathcal{B})^{-1}(u^r)^2\,, & \text{(5.48b)}\\ 0 &= \mathbf{u}\cdot\mathbf{n} = -(1-\mathcal{B})\,u^t n^t + (1-\mathcal{B})^{-1}u^r n^r\,, & \text{(5.48c)}\\ 1 &= \mathbf{n}\cdot\mathbf{n} = -(1-\mathcal{B})(n^t)^2 + (1-\mathcal{B})^{-1}(n^r)^2\,, & \text{(5.48d)} \end{aligned}$$

where E is a constant (the conserved total energy along the timelike geodesic). From (5.48), the solution for u^r can be found: $u^r = \sqrt{E-(1-\mathcal{B})}$. Computed from the interior, the radial component of the 4-velocity is

$$\dot{R} = \dot{a}\,\bar{r}_{\circledcirc} = \bar{r}_{\circledcirc}\left(\frac{\rho_{m_0}}{\rho_\Lambda}\right)^{1/3}\frac{d}{d\tau}\left[\sinh^{2/3}\left(\frac{\tau}{\tau_\Lambda}\right)\right] = \sqrt{\frac{2M}{R} + \frac{\Lambda}{3}R^2}\,, \tag{5.49}$$

where we have used the definition of ρ_Λ and τ_Λ, and the relation $(4\pi/3)\rho_{m_0}\bar{r}^3_{\circledcirc} = M$. Comparing Eq. (5.49) with the solution for u^r, we infer $E^2 = 1$.

5.3.4.2 Slowly rotating universe and its exterior

Following the same procedure as in Sec. 5.3.2, we now set the fluid elements in the universe into slow rotation with angular velocity $\Omega = d\bar{\varphi}/d\tau$. The metric describing the slowly rotating universe takes the same form as Eq. (5.17) with $a(\tau)$ now given by Eq. (5.44). Our goal is to solve the Einstein field equations with a cosmological constant [Eq. (5.43)] to detemine the frame-dragging angular velocity $\omega(\bar{r},\tau)$.

Similar to Eq. (5.21), the non-trival components of the field equations are given by

$$\begin{aligned} \tau\tau: &\quad \rho_{m_0}a_0^3 = \rho_m\,a^3\,, & \text{(5.50a)}\\ \tau\phi: &\quad 16\pi\rho_m a^2\,\bar{r}\,(\omega-\Omega) = 4\omega_{,\bar{r}} + \bar{r}\omega_{,\bar{r}\bar{r}}\,, & \text{(5.50b)}\\ \bar{r}\phi: &\quad \sqrt{3\Lambda + 24\pi\rho_m}\;\omega_{,\bar{r}} + \omega_{,\bar{r}\tau} = 0\,. & \text{(5.50c)} \end{aligned}$$

The solution to the field equations for ω in this case is also similar to that in Sec. 5.3.2 [i.e., similar to Eq. (5.22); the only difference is the exact form of the scale factor $a(\tau)$]:

$$\omega(\bar{r},\tau) = \left[-\frac{8\pi}{5}\left(\frac{\rho_{m_0}a_o^3}{a^3}\right)\bar{r}^2 + \zeta_1(\tau)\right]\varpi_o \, . \tag{5.51}$$

In the exterior vacuum, the SdS metric picks up a correction term $\sim J$. [In the asymptotically de Sitter spacetime, J no longer bears the meaning of a spin angular momentum as measured at infinity.]

$$ds_+^2 = -(1-\mathcal{B})dt^2 + \frac{1}{1-\mathcal{B}}dr^2 + r^2 d\theta^2 + r^2\sin^2\theta\left(d\varphi - \frac{2J}{r^3}dt\right)^2 \, . \tag{5.52}$$

Similar to Sec. 5.3.3.2, we transform into $(\tilde{t},\tilde{\varphi})$ coordinates, which are constant along spacelike geodesics $\mathcal{G}$ orthogonal to the universe's surface:

$$\begin{aligned} d\varphi &= d\tilde{\varphi} + \frac{2J}{r^3}\frac{\sqrt{\mathcal{B}_R}}{1-\mathcal{B}}\frac{dr}{\sqrt{1-\mathcal{B}+\mathcal{B}_R}} \, , && \text{(5.53a)} \\ dt &= d\tilde{t} + \frac{\sqrt{\mathcal{B}_R}}{1-\mathcal{B}}\frac{dr}{\sqrt{1-\mathcal{B}+\mathcal{B}_R}} \, . && \text{(5.53b)} \end{aligned}$$

Then the exterior metric takes the form

$$ds_+^2 = -(1-\mathcal{B})\,d\tilde{t}^2 - 2\left(\frac{\mathcal{B}_R}{1-\mathcal{B}+\mathcal{B}_R}\right)^{1/2} d\tilde{t}dr + \frac{dr^2}{1-\mathcal{B}+\mathcal{B}_R} + r^2 d\theta^2 + r^2\sin^2\theta\left(d\tilde{\varphi} - \frac{2J}{r^3}d\tilde{t}\right)^2 \, . \tag{5.54}$$

Similar to Eq. (5.36) and (5.39), the matching of the 3-metric and extrinsic curvature yields the following relation at the boundary of the slowly rotating universe:

$$\begin{aligned} \omega(\bar{r}_{\circledcirc},\tau) &= \frac{2J}{R^3(\tau)} \, , && \text{(5.55a)} \\ (2\omega + \bar{r}\omega_{,\bar{r}})\big|_{\bar{r}_{\circledcirc}} &= -\frac{2J}{R^3} \, . && \text{(5.55b)} \end{aligned}$$

By combining with Eq. (5.51), the solutions for ω and Ω can be determined [compare with Eq. (5.40)]:

$$\begin{aligned} \omega(\bar{r},\tau) &= -\frac{3J}{R^3}\left(\frac{\bar{r}}{\bar{r}_s}\right)^2 + \frac{5J}{R^3} \, , && \text{(5.56a)} \\ \Omega(\bar{r},\tau) &= \omega + \varpi_0/a^2 = \omega + \frac{5J}{2MR^2} \, . && \text{(5.56b)} \end{aligned}$$

Note that ω and Ω take exactly the same form as in the absence of dark energy (Sec. 5.3.3.3)—though $R = R(\tau)$ now has a different dependence on τ [Eq. (5.44)]. As before we define the ratio $\chi_c = (\Omega_c - \omega_c)/\Omega_c$ and find

$$\chi_c \equiv \left(\frac{\Omega_c - \omega_c}{\Omega_c}\right) = \frac{1}{1+2M/R} \, . \tag{5.57}$$

Again χ_c takes the same simple form as without dark energy [Eq. (5.41)], but its time evolution (τ-dependence) is differently specified by Eq. (5.44).

Equation (5.57) shows that, although dark energy influences the time evolution of frame dragging via the expansion rate of the universe, it does not bring any fundamental change to the initial, or the long-term asymptotic behavior of χ_c. Figure 5.2 depicts the behavior of χ_c in Eq. (5.57).

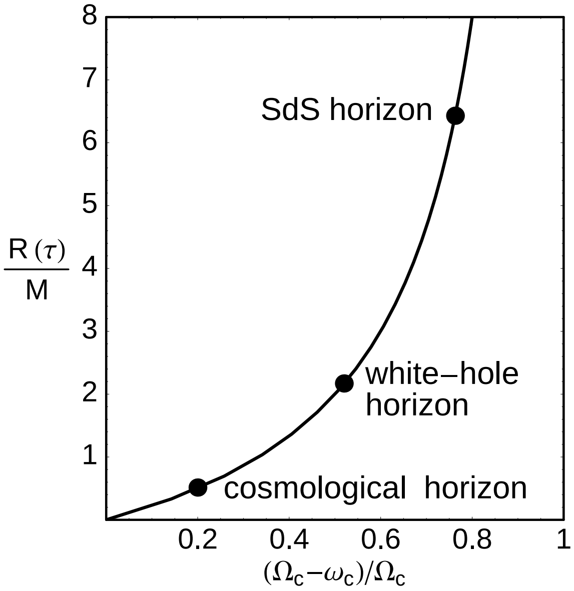

Figure 5.2: The fractional slippage of the inertial axes at the center of a model universe with a spherical edge, $(\Omega_c - \omega_c)/\Omega_c$, as a function of the dimensionless radius of the universe's edge $R(\tau)/M$ [see Eq. (5.55)]. We have assumed the existence of dark energy in our model universe as well as in an exterior vacuum region. We assume the dark energy takes the mathematical form of a cosmological constant Λ in Einstein's field equations. In this figure, the cosmological constant is taken to be $\Lambda = 1/(20M^2)$.[†] The radius marked "white-hole horizon" corresponds to the moment when the universe's surface passes through its Schwarzschild radius. The radius marked "SdS horizon" corresponds to the moment when the universe's surface passes through the "Schwarzschild-de Sitter" radius [Eq (5.47)].

[†] The Friedmann equation for the Friedmann-Lemaître universe is $H^2 = (\Lambda/3) - (k/a^2) + (8\pi\rho/3)$, where H is the Hubble paramter, the parameter k describes the spatial curvature, and ρ is the pressure-free matter density. Observations suggest that our universe is nearly flat ($k \simeq 0$), and that the ratio between the dark-energy component and matter is $(\Lambda/3)/(8\pi\rho/3) \simeq 7/3$. If we take the radius of the universe to be $1/H$, then this leads to $M^2\Lambda = (4\pi/3H^3)^2\rho^2\Lambda \simeq 1/20$.

Appendices

5.A Spacelike geodesics

In Sec. 5.3.2, we set our spatially homogeneous model universe into slow and rigid rotation, with respect to a family of radial spacelike geodesics $\mathcal{G}$ characterized by $(\tau, \bar{\theta}, \bar{\varphi}) = \text{const.}$ (see the discussion at the end of Sec. 5.3.2). These geodesics arrive at the surface of the universe Σ from the interior, and hit that surface orthogonally. In this appendix, we shall continue their journey into the exterior Schwarzschild spacetime by starting them out orthogonal to Σ, and shall use them to map our azimuthal angle (with respect to $\mathcal{G}$) throughout the spacetime.

We start by finding the unit normal vector to the surface Σ. The boundary of the slowly rotating universe is the hypersurface

$$\mathscr{B}(t,r) = \frac{4M}{3}\left(\frac{r}{2M}\right)^{3/2} + 4M\left(\frac{r}{2M}\right)^{1/2} + 2M\log\left|\frac{(r/2M)^{1/2}-1}{(r/2M)^{1/2}+1}\right| - t = 0. \tag{5.58}$$

This is obtained by combining the geodesic functions $R(\tau)$ [Eq. (5.26)] and $T(\tau)$ [Eq. (5.28)]. The normal 1-form to this hypersurface can be identified as $\mathbf{n}_+ \propto d\mathscr{B}$, from which we can determine the unit normal vector (in Schwarzschild coordinates):

$$n_+^{\lambda}(r) \quad = \quad \left\{\frac{\sqrt{\mathcal{A}}}{1-\mathcal{A}}, 1,\ 0,\ \frac{2J}{r^3}\frac{\sqrt{\mathcal{A}}}{1-\mathcal{A}}\right\}, \tag{5.59}$$

where $\mathcal{A} = 2M/r$. When the exterior spacetime is Schwarzschild-de Sitter (Sec. 5.3.4), it is difficult to obtain a compact expression for the hypersurface function $\mathscr{B}(t,r)$. However, $\mathscr{B}(t,r)$ and its 1-form vector $\mathbf{n}_+$ remain the same for a non-rotating and a slowly rotating universe. Therefore we can take the alternative approach of solving $\mathbf{n}_+$ from Eq. (5.48).

Let $\mathbf{k}$ be the tangent vector to the spacelike geodesics $\mathcal{G}$ in the exterior region. Its contravariant components can be solved for from the following three equations:

$$\begin{aligned} k_\varphi &= g_{\varphi\varphi}k^\varphi + g_{\varphi t}k^t = 0\,, && (5.60a)\\ k_t &= g_{tt}k^t + g_{t\varphi}k^\varphi = -E\,, && (5.60b)\\ 1 &= g_{\alpha\beta}k^\alpha k^\beta\,. && (5.60c)\end{aligned}$$

Equation (5.60a) is the conservation of angular momentum (it is zero because $\mathcal{G}$ has zero angular momentum in the interior); Equation (5.60b) is the conservation of energy E. We must choose E according to the initial condition for $\mathcal{G}$ on the starting surface Σ. Finally Eq. (5.60c) specifies $\mathbf{k}$ to be spacelike with unit norm. The solutions to (5.60) are

$$k^t = \frac{E}{1-\mathcal{A}}\,, \qquad k^r = \sqrt{1-\mathcal{A}+E^2}\,, \qquad k^\varphi = \frac{2J}{r^3}\frac{E}{1-\mathcal{A}}\,. \tag{5.61a}$$

We choose E so that $\mathbf{k}(R) = \mathbf{n}_+(R)$—this guarantees that the spacelike geodesics start out orthogonal to Σ. This implies that

$$E = \sqrt{\mathcal{A}_R} = \sqrt{2M/R}\,. \tag{5.62}$$

Now we can define a set of new coordinates that are constant along the geodesic $\mathcal{G}$:

$$\begin{aligned} \tilde{\varphi} &= \varphi + \int_r^\infty \left(\frac{d\varphi}{dr'}\right)dr' = \varphi + \int_r^\infty \left(k^\varphi/k^{r'}\right)dr'\,, && (5.63a)\\ \tilde{t} &= t + \int_r^\infty \left(\frac{dt}{dr'}\right)dr' = t + \int_r^\infty \left(k^t/k^{r'}\right)dr'\,. && (5.63b)\end{aligned}$$

Inserting expressions (5.61) into Eq. (5.63) and taking the differentials, we obtain

$$\begin{aligned} d\tilde{\varphi}(\varphi,r) &= d\varphi - \frac{2J}{r^3}\frac{\sqrt{\mathcal{A}_R}}{1-\mathcal{A}}\frac{dr}{\sqrt{1-\mathcal{A}+\mathcal{A}_R}}\,, && (5.64a)\\ d\tilde{t}(\varphi,r) &= dt - \frac{\sqrt{\mathcal{A}_R}}{1-\mathcal{A}}\frac{dr}{\sqrt{1-\mathcal{A}+\mathcal{A}_R}}\,. && (5.64b)\end{aligned}$$

Applying the transformation (5.64) to the exterior metric of our slowly rotating universe (5.29), we bring the exterior metric into the form (5.33), in which the spacelike geodesics $\mathcal{G}$ are characterized by fixed coordinate lines: $(\tilde{t},\theta,\tilde{\varphi})$ = constant. Hence any rotation described in these coordinates is referenced to the geometric quantities $\mathcal{G}$.

The above procedure also applies to slowly rotating Schwarzschild-de Sitter spacetime, where we obtain a similar coordinate transformation given by Eq. (5.53).

5.B Matching of extrinsic curvature

To ensure a smooth connection between our model universe and the exterior vacuum region, we impose the so-called Darmois-Israel junction conditions [23], which require the continuity of the intrinsic metric and extrinsic curvature on the boundary (the hypersurface Σ in our problem). In Sec. 5.3.3.1, in the case when there is no rotation, we have shown how to calculate the intrinsic metric on Σ from both the interior and exterior regions. In Sec. 5.3.3.3, for the slowly rotating universe, we give expressions for the intrinsic metric [Eq. (5.34) and (5.35)] , and use them to determine the metric function ω on the hypersurface Σ [Eq. (5.36)]. In this appendix, we will focus on the calculation of the extrinsic curvature and will match it across Σ.

The extrinsic curvature of a 3-dimensional hypersurface describes how the slice is embedded in the 4-dimensional spacetime. Let n^α be the unit normal vector of the hypersurface, and define the *induced 3-metric*:

$$\gamma_{\alpha\beta} \equiv g_{\alpha\beta} - n_\alpha n_\beta \,. \tag{5.65}$$

Note that the 3-metrics ${}^{(3)}ds^2_\pm$ given in Eq. (5.23) and (5.25) are nothing other than $\gamma_{\alpha\beta}dx^\alpha dx^\beta$ expressed in the intrinsic coordinates of Σ: $(\tau, \bar\theta, \bar\varphi)$ (we have identified $\bar\theta$ with θ and $\bar\varphi$ with φ in these two equations). Given the above definition, the extrinsic curvature can be written as the Lie-derivative of the induced metric along the unit normal vector [30]:[6]

$$K_{\alpha\beta} = -\frac{1}{2}\mathscr{L}_{\mathbf{n}}\gamma_{\alpha\beta} = -\frac{1}{2}\left(\gamma_{\alpha\beta,\lambda}n^\lambda + \gamma_{\alpha\lambda}n^\lambda{}_{,\beta} + \gamma_{\lambda\beta}n^\lambda{}_{,\alpha}\right) \,. \tag{5.66}$$

As an example to illustrate the calculation of extrinsic curvature, we turn back to Sec. 5.3.3.1 and examine the case when the universe is non-rotating and has an outer edge: the spacetime of the non-rotating universe is described by the metric (5.13) and the exterior vacuum region is described by the Schwarzschild metric (5.24).

To find the unit normal vector $n^\lambda_\pm$ from both regions, we must solve the equations

$$\mathbf{n}\cdot\mathbf{n} = 1 \quad \text{and} \quad \mathbf{n}\cdot\mathbf{u} = 0\,, \tag{5.67}$$

where $\mathbf{u}$ is the 4-velocity of the fluid element on the surface and is given by

$$u^\alpha_- = (1,0,0,0)\,, \quad u^\alpha_+ = (dT/d\tau, dR/d\tau, 0, 0) \,. \tag{5.68}$$

Here $R(\tau)$ and $T(\tau)$ are a solution to the geodesic equation in the exterior Schwarzschild spacetime, and are

---

[6] The definition of $\gamma_{\alpha\beta}$ [Eq. (5.65)] and the expression for $K_{\alpha\beta}$ [Eq. (5.66)] are consistent as long as Σ is a timelike hypersurface (which is the case in our problem).

given by Eq. (5.26) and Eq. (5.28) respectively. Combining (5.67) and (5.68), we obtain **n**:

$$\begin{aligned} n^\lambda_- &= \left\{0, a^{-1}(\tau), 0, 0\right\} , && (5.69a)\\ n^\lambda_+ &= \left\{\sqrt{2M/R}\,(1-2M/R)^{-1}, 1, 0, 0\right\} . && (5.69b) \end{aligned}$$

It is now straightforward to compute $\gamma^\pm_{\alpha\beta}$ and $K^\pm_{\alpha\beta}$, and transform the latter into intrinsic coordinates:

$$K^\pm_{\alpha\beta} dx^\alpha_\pm dx^\beta_\pm\Big|_\Sigma \rightarrow \quad K^-_{ij}(\tau, \bar{\theta}, \bar{\varphi}) dx^i dx^j \ , \ K^+_{ij}(t, \theta, \varphi) dx^i dx^j \ . \tag{5.70}$$

It turns out that the nonzero components of the extrinsic curvature are

$$\begin{aligned} K^-_{ij} dx^i dx^j &= -a\bar{r}_\circledcirc \left(d\bar{\theta}^2 + \sin^2\bar{\theta}^2 d\bar{\varphi}^2\right), && (5.71a)\\ K^+_{ij} dx^i dx^j &= -R\left(d\theta^2 + \sin^2\theta^2 d\varphi^2\right). && (5.71b) \end{aligned}$$

Hence $K^-_{ij} = K^+_{ij}$. It therefore confirms our statement at the end of Sec. 5.3.3.1.

In the case of a slowly rotating universe (Sec. 5.3.3.3), the unit normal vector becomes

$$\begin{aligned} n^\lambda_- &= \left\{0, a^{-1}(\tau), 0, 0\right\}, && (5.72a)\\ n^\lambda_+ &= \left\{\frac{\sqrt{\mathcal{A}} - \sqrt{\mathcal{A}_R/(1-\mathcal{A}+\mathcal{A}_R)}}{1-\mathcal{A}}, \ 1, \ 0\,, \ \frac{2J}{r^3}\,\frac{\sqrt{\mathcal{A}} - \sqrt{\mathcal{A}_R/(1-\mathcal{A}+\mathcal{A}_R)}}{1-\mathcal{A}}\right\} . && (5.72b) \end{aligned}$$

Note that the components of n^λ_+ are expressed in coordinates $(\tilde{t}, r, \theta, \bar{\varphi})$, which are attached to spacelike geodesics described in Appendix 5.A. Following the same procedure as in the non-rotating case, the extrinsic curvature on Σ is obtained:

$$\begin{aligned} K^-_{ij} dx^i dx^j &= -a\bar{r}_\circledcirc \left(d\bar{\theta}^2 + \sin^2\bar{\theta}^2 d\bar{\varphi}^2\right) + a\bar{r}_\circledcirc\,(2\omega + \bar{r}_\circledcirc \omega_{,\bar{r}})\sin^2\bar{\theta}\, d\bar{\varphi} d\tau \ , && (5.73a)\\ K^+_{ij} dx^i dx^j &= -R\left(d\theta^2 + \sin^2\theta^2 d\tilde{\varphi}^2\right) - \frac{2J}{R^2}\left(1 - \frac{2\mathcal{A}_\mathrm{R}}{1+\sqrt{\mathcal{A}_\mathrm{R}}}\right)\sin^2\theta\, d\tilde{\varphi} d\tau \ . && (5.73b) \end{aligned}$$

Bibliography

[1] H. Thirring and J. Lense, Phys. Z. **19**, 156 (1918).

[2] J. B. Hartle, *Gravity: An Introduction to Einstein's General Relativity* (Addison-Wesley, San Francisco, 2003).

[3] `http://einstein.stanford.edu`.

[4] V. B. Braginsky, C. M. Caves, and K. S. Thorne, Phys. Rev. D **15**, 2047 (1977).

[5] I. Ciufolini and E. C. Pavlis, Nature (London) **431**, 958 (2004);
L. Iorio, New Astronomy **10**, 603 (2005);
V. B. Braginsky, A. G. Polnarev, and K. S. Thorne, Phys. Rev. Lett. **56**, 863 (1984).

[6] Section 3 of M. L. Ruggiero and A. Tartaglia, Nuovo Cimento B **117**, 743 (2002).

[7] C. W. Misner, K. S. Thorne, and J. A. Wheeler, *Gravitation* (W. H. Freeman, San Francisco, 1973).

[8] B. R. Holstein, Am. J. Phys. **69**, 1248 (2001).

[9] See Sec. 2 of A. Einstein, Annalen der Physik, 1916, p. 49; English translation in H.A. Lorentz, A. Einstein, H. Minkowski, and H. Weyl, *The Principle of Relativity* (Methuen, London, 1923); Reprinted (Dover, New York, 1952).
See also chapter 4 of J. Eisenstaedt, *The Curious History of Relativity* (Princeton University Press, Princeton NJ, 2006).

[10] E. Mach, *Die Mechanik in ihrer Entwickelung: Historisch-kritisch dargestellt*, (Brockhaus, Leipzig, 1883); English translation *The Science of Mechanics: A Critical and Historical Account of its Development* (Open Court, La Salle, IL, 1960).

[11] See, e.g., J. B. Barbour and H. Pfister, eds. *Mach's Principle: From Newton's Bucket to Quantum Gravity* (Birkhaeuser, Boston, 1995); also Sec. 21.12 of [7].

[12] D. R. Brill and J. M. Cohen, Phys. Rev. **143**, 1011 (1966).

[13] L. S. Kegeles, Phys. Rev . D **18**, 1020 (1978).

[14] R. J. Wiltshire, Gen. Rel. Grav. **35**, 175 (2003).

[15] D. Lynden-Bell, J. Katz, and J. Bicak, Mon. Not. R. Astron. Soc. **272** 150 (1995); 1600(E) (1995).

[16] J. Bicak, D. Lynden-Bell, and J. Katz, Phys. Rev. D **69**, 064011 (2004).

[17] C. Schmid, gr-qc/0201095.

[18] C. Schmid, Phys. Rev. D **74**, 044031 (2006).

[19] R. D. Blandford and K. S. Thorne, *Applications of Classical Physics*, `http://www.pma.caltech.edu/Courses/ph136/yr2006/`.

[20] D. J. Tritton, *Physical Fluid Dynamics*, 2nd edition. Oxford University Press, Oxford, 1988.

[21] R. L. Forward, Proc. IRE **49**, 892 (1969).

[22] See, e.g., page 328 in *Quantum Optics, Experimental Gravitation, and Measurement Theory*, edited by P. Meystre and M. O. Scully. Plenum Press, New York (1983).

[23] Darmois, G., 1927. *Mémorial des Sciences Mathématiques*, vol. 25, (Paris: Gautier-Villars).
W. Israel, Nuovo Cimento B44, 1 (1966); Errata: Nuovo Cimento B48, 463 (1967).

[24] J. B. Hartle and K. S. Thorne, Aastrophys. J. **153**, 807 (1968).

[25] S. M. Carroll, *Spacetime and Geometry: an Introduction to General Relativity* (Addison Wesley, San Francisco, 2004).

[26] Øyvind Grøn and Sigbjørn Hervik, *Einstein's General Theory of Relativity*, available online at `http://www.fys.uio.no/~sigbjorh/gravity.pdf`.

[27] Zel'dovich, Yakov Borisovich, and Novikov, Igor Dmitrivich, *Relativistic Astrophysics Volume 2: The Structure and Evolution of the Universe*. University of Chicago Press, 1983.

[28] K. Kottler, Ann. Phys. (Leipzig) **56**, 410 (1918).

[29] D. Markovic and S. L. Shapiro, Phys. Rev. D **61**, 084029 (2000).

[30] T. W. Baumgarte and S. L. Shapiro, Phys. Rept. **376**, 41 (2003).